CFD Modelling of Outflow and Ductile Fracture Propagation in Pressurised Pipelines

A thesis submitted to University College London for the degree of Doctor of Philosophy

By

Solomon Fisher Brown

Department of Chemical Engineering
University College London
Torrington Place
London WC1E 7JE

July 2011

I, Solomon Fisher Brown confirm that the work presented in this thesis is my own. Where information has been derived from other sources, I confirm that this has been indicated in the thesis.

Abstract

This thesis describes the fundamental extension, development and testing of a mathematical model for predicting the transient outflow following the failure of pressurised pipelines. The above encompasses improvements to the theoretical basis and numerical stability, reduction in the computational runtime and the modelling of fracture propagation with particular reference to CO_2 pipelines.

The basic model utilises the homogeneous equilibrium model (HEM), where the constituent phases in two-phase mixtures are assumed to be in thermodynamic and mechanical equilibrium. The resultant system of conservation equations are solved numerically using the Method of Characteristics (MOC) coupled with a suitable Equation of State to account for multi-component hydrocarbon mixtures.

The first part of the study involves the implementation of the Finite Volume Method (FVM) as an alternative to the MOC. In the case of gas and two-phase hydrocarbon pipeline ruptures, both models are found to be in excellent accord producing good agreement with the published field data. As compared to the MOC, the FVM shows considerable promise given its significantly shorter computation runtime and its ability to handle non-equilibrium or heterogeneous flows.

The development, testing and validation of a Dynamic Boundary Fracture Model (DBFM) coupling the fluid decompression model with a widely used fracture model based on the Drop Weight Tear Test technique is presented next. The application of the DBFM to an hypothetical but realistic CO_2 pipeline reveals the profound impacts of the line temperature and types of impurities present in the CO_2 stream on the pipeline's propensity to fracture propagation. It is found that the pure CO_2 and the post-combustion pipelines exhibit very similar and highly temperature dependent propensity to fracture propagation. An increase in the line temperature from 20 – 30 ^{o}C results in the transition from a relatively short to a long running propagating facture. The situation becomes progressively worse in moving from the pre-combustion to the oxy-fuel

stream. In the latter case, long running ductile fractures are observed at all the temperatures under consideration. All of the above findings are successfully explained by examining the fluid depressurisation trajectories during fracture propagation relative to the phase equilibrium envelopes.

Finally, two of the main shortcomings associated with previous work in the modelling of pipeline ruptures are addressed. The first deals with the inability of Oke's (2004) steady state model to handle non-isothermal flow conditions prior to rupture by accounting for both heat transfer and friction. The second removes the rupture plane instabilities encountered in Atti's (2006) model when simulating outflow following the rupture of ultra high pressure pipelines. Excellent agreement between the new non-isothermal model predictions and the published data for real pipelines is observed.

Acknowledgements

I wish to thank the following people and organisations who have contributed so much in many ways to facilitate the completion of this thesis.

To the ESPRC for their financial support of my project. Thank you for everything.

My supervisor, Prof. Haroun Mahgerefteh for the opportunity given me to study in this field and your excellent supervision.

To my family: Thank you for your support and guidance.

To my fiancé Patricia Wood, thank you for your understanding and support throughout my studies.

My office mates Maria, Aisha, Peng, Sergey, Shirin, Navid, Alex and Vikram it has been a pleasure meeting and working with you all.

The technical and admin. staff of the Department of Chemical engineering, UCL.

Finally, to Dr. Garfield Denton. Thank you for friendship and advice through the course of my time at UCL.

Table of Contents

Chapter 1: Introduction

The global demand for energy is predicted to increase by 36 % from 2008 to 2035 (International Energy Agency, 2011). Despite increased investment in renewable energy sources, fossil fuels such as coal, oil and natural gas, are expected to account for 50 % of the demand for this additional energy. By far the most prevalent method of transportation of these fuels is through pressurised pipelines. The length of such pipelines continues to increase, with an estimated 90,000 miles either in construction or planning in 2010 alone (Tubb, 2010).

Given the highly flammable nature of the inventories conveyed coupled with the high pressures involved (typically above 100 bara) pipeline failures have on many occasions led to catastrophic consequences both in terms of fatalities and environmental damage. Even in the US, which has some of the most stringent pipeline safety regulations in the developed world, data published by the Office of Pipeline Safety (PHMSA, 2010) indicates 5600 serious pipeline failure incidents between 1990 and 2009. These have resulted in 365 fatalities and over £3.3 m damage to property.

Given the above, an essential part of the safety assessment for pressurised pipelines involves the prediction of the discharge rate and its variation with time in the event of pipeline failure. Such data is central to assessing all the consequences associated with pipeline failure including fire, explosion, atmospheric dispersion and emergency planning. Even the pipeline's susceptibility to catastrophic long propagating fractures following a puncture is related to the rate of loss of the inventory (Mahgerefteh et al., 2006).

The safety of pressurised pipelines (see for example Bilio et al. (2009)) has recently attracted renewed attention given that this mode of transportation is now widely accepted as the most practical way of conveying the captured CO_2 from fossil fuel power plants for subsequent sequestration. At concentrations greater than 10 % v/v the gas is likely to be instantly fatal (Kruse and Tekiela, 1996). As such, the consequences of a CO_2 pipeline failure are an important issue.

Given the above, the development of accurate, robust and computationally efficient mathematical models for predicting discharge rates following pipeline failure has been the focus of considerable attention.

The success of these models invariably depends on their ability to capture all the important processes and their complex interactions taking place during depressurisation. These include expansion wave propagation, phase and flow dependent heat transfer and friction effects. Finally, the use of a reliable Equation of State is required to correctly predict phase equilibrium.

The starting point for all robust pipeline outflow models is the formulation of the mass, momentum and energy conservation equations. The coupling of the conservation equations with appropriate correlations for predicting the fluid thermo-physical and hydrodynamic properties during the pipeline depressurisation results in a set of hyperbolic equations. Given that these can only be solved using a numerical technique, their resolution can often be exceptionally computationally demanding. This is especially so for punctures; the most common type of pipeline failure (Oke et al., 2003).

For example, the computational runtime for the simulation of the complete depressurisation of a 100 km, 0.8 m pipeline conveying natural gas at 100 bara following a 15 cm puncture is 18 hours using a relatively high specification (e.g. 2.66

GHz, 3.0 GB RAM) personal computer. This is despite significant progress in the development of fast solution algorithms such as nested grid systems (Mahgerefteh et al., 1999; Oke et al., 2003), interpolation techniques (Mahgerefteh et al., 2007) and the more fundamental approaches involving the formulation of the conservation equations using different combinations of primitive variables (Mahgerefteh et al., 2006).

In the main, two different approaches are adopted. The more rigorous models (see for example Bendiksen et al., 1991; Nordsveen and Haerdig, 1997) account for thermal as well as mechanical non-equilibrium effects such as phase slip between the constituent phases during rapid depressurisation. Such so called two-fluid models were initially developed in the early seventies in the nuclear industry for the analysis of steam/water flow in the core of a nuclear reactor (Peterson et al., 1985).

The dynamic two-fluid model OLGA (Bendiksen et al., 1991), for example, has been specifically developed for prediction of steady state pressure drop, liquid hold-up and flow regime transitions for hydrocarbon pipelines. However, very limited progress has been made in extending OLGA to the highly unsteady state flows involving the rupture of hydrocarbon pipelines (Shoup et al., 1998). This is due to OLGA's reliance on the availability of empirical data such as the transition between the various flow regimes, bubble nucleation and evolution dynamics as well as the numerical simulation's instability problems. Also, there is little information regarding the formulation of the choking conditions at the rupture plane, critical for the correct modelling of such highly transient flows. Finally, the fact that separate conservation equations are required for each constituent phase means that such two-fluid models are in principle extremely computationally demanding. The two-fluid model PLAC (Hall et al., 1993) on the other hand, sharing similar underlying theory to OLGA has been shown to produce poor agreement with release data obtained based on the rupture of real hydrocarbon pipelines (Chen et al., 1995).

Chen et al. (1995a, b) partly overcame such problems by developing a Marginally Stable Model based on extending the Geurst's variation principle (Geurst, 1986). The model accounts for phase slip but ignores non-equilibrium thermal effects. Based on comparison with real pipeline rupture data (Richardson and Saville, 1996), the authors showed that non-equilibrium effects are only important in the case of short pipelines. For long pipelines (>100m), both phase slip and inter-phase thermal stratification may be ignored, hence the far simpler and more robust homogenous equilibrium model (HEM) becomes applicable.

During the past decade, Mahgerefteh and co-workers at UCL (see for example Mahgerefteh et al., 2008; Oke et al., 2003; Wong and Mahgerefteh, 1999) have developed a numerical model for simulating the fluid dynamics following the rupture of pressurised pipelines. Based on the HEM assumption, the model accounts for the important processes taking place during depressurisation, including real fluid behaviour, frictional effects, radial and axial flow in the proximity of puncture as well as the accompanying rapid pressure and thermal transients. The comparative results between the model and real data show very good agreement leading to significant industrial applications.

The aim of this study is the fundamental improvement followed by testing and where possible validation against published real data of UCL pipeline rupture model. The objectives are:

- Addressing some of the main limitations the model's theoretical basis
- Reduction in the computational runtime
- Extension to modelling ductile fracture propagation in CO_2 pipelines.

This thesis is divided into 8 chapters:

Chapter 2 is a review of the mathematical models available in the open literature for simulating pipeline failures. This includes the evaluation of their strengths and weaknesses in terms of robustness, computational efficiency and accuracy as compared to any available real data.

In chapter 3, the main theoretical basis for the UCL pipeline outflow model employed in this work is presented. This commences with the main assumptions and the justifications employed in the formulation of the mass, momentum and energy conversation equations governing the ensuing flow. This is followed by the presentation of the Peng-Robinson Equation of State employed for predicting the relevant liquid/vapour phase equilibrium data and the appropriate two-phase thermodynamic equations and hydrodynamic correlations for predicting speed of sound, heat transfer and friction effects.

Chapter 4 presents a review of the Method of Characteristics (MOC) employed for resolving the conservative equations along side the appropriate boundary conditions required to simulate the outflow from a multiple pipeline following failure. The solution of the compatibility equations using the Method of Specified Time intervals, the Euler predictor-corrector technique to improve the accuracy of the numerical results and their coupling with the relevant boundary conditions are given next. The latter include a closed valve or dead-ended pipe (intact end point), a centrifugal pump (at the flow source), full-bore rupture/puncture and in the case of the multi-segment pipelines, the junction (bends or connector) between two pipelines.

Chapter 5 presents the formulation and validation of a Finite Volume Method (FVM) developed as an alternative to the MOC for the numerical solution of the conservation equations in order to reduce computational runtime. The derivation of an appropriate FVM based on a deterministic re-formulation of the staggered grid Random Choice Method (Gottlieb, 1988) is presented. The outflow predictions obtained using both methods for hypothetical and published real pipeline rupture scenarios are compared and contrasted. The hypothetical failure scenarios tested involve gas, liquid and two-phase pipeline inventories. The performance of the two numerical solution methods is

assessed based on stability, degree of agreement with the real pipeline rupture data and computational runtime.

In chapter 6 the HEM based outflow model is coupled with a well-established Drop Weight Tear Test energy fracture model (Makino et al., 2001) to simulate ductile fracture propagation in CO_2 pipelines. This is in view of the recent significant interest in the use of pressurised pipelines for transporting captured CO_2 from fossil fuel power plants for subsequent sequestration as part of the Carbon Capture and Sequestration Chain.

Following its validation against published real pipeline fracture data, the fully coupled fracture model is applied to hypothetical pipelines of given fracture toughness in order to test the pipeline's propensity to fracture propagation as a function of the line temperature, pressure and different types of stream impurities. The latter correspond to those encountered based on pre-combustion, post-combustion and oxy-fuel capture technologies. All of the observed trends are explained by examining the feed mixtures depressurisation trajectories during fracture propagation relative to the corresponding phase equilibrium envelopes.

Chapter 7 presents the methodologies for addressing two of the main shortcomings in the theoretical formulation of the UCL HEM pipeline rupture model. The first deals with the assumption of isothermal flow prior to rupture which becomes invalid in situations when the feed and ambient temperatures are different. Also this assumption ignores frictionally induced fluid/wall heat transfer effects. The second addresses the rupture plane numerical instabilities encountered at ultra high line pressures.

Chapter 8 deals with general conclusions and suggestions for future work.

.

Chapter 2: Literature Review

2.1 Introduction

In the UK, the Pipeline Safety Regulations 1996 (HSE, 1996) require that the risks associated with the construction and operation of major accident hazard (MAH) pipelines are as low as reasonably practicable (ALARP). An essential step in determining the risks associated with MAH pipelines is the prediction of the fluid release rate and its variation with time following pipeline failure. This information forms the basis for assessing all the consequences of pipeline failure including fire, explosion and toxic release.

Denton (2009) presented an extensive review of the most widely used commercially available and academic outflow models for pipeline ruptures. A large body of new work has since been published on the modelling of various aspects of pipeline failure/blowdown and its numerical simulation. In addition, some of the models reviewed by Denton (2009) have since been compared with new experimental data or extended to account for new flow phenomena.

In this chapter, seven of the current state of the art models for simulating outflow following pipeline failure are reviewed. Where possible, results relating to the validation of the models in comparison with available real data are presented. The models reviewed include:

1. OLGA (Bendiksen et al., 1991)
2. University College London models (Mahgerefteh et al.,1997-2008; Atti, 2006; Oke et al., 2003; Oke, 2004)
3. SLURP (Cleaver et al., 2003; Cumber, 2007)
4. Botros et al. (2004-2010)
5. Terenzi (2005)

6. Popescu (2009)
7. Makino et al. (2001).

2.2 OLGA (Bendiksen et al., 1991)

The first version of OLGA was developed for the hydrocarbon industry by Statoil in 1983 to simulate the slow transients associated with terrain-induced slugging, pipeline start-up, shut-in and variable production rates. Its physical model was at first based on small diameter data for low-pressure air/water flow. Initially, OLGA could successfully simulate bubble/slug flow regime but it was incapable of modelling stratified/annular flow regime. Bendiksen et al. (1991) addressed this problem as well as extending the model to deal with hydrocarbon mixtures.

In OLGA, separate conservation equations are applied for gas, liquid bulk and liquid droplets, which may be coupled through interfacial mass transfer. Two momentum equations are used:

1. A combined equation for the gas and possible liquid droplets
2. An equation for the liquid film.

Heat transfer through the pipe wall is accounted for by a user specified heat transfer coefficient. Different frictional factors are used for the various flow regimes. The pertinent conservation equations are solved using an implicit finite difference numerical scheme giving rise to numerical diffusion of sharp slug fronts and tails thus failing to predict correct slug sizes (Nordsveen and Haerdig, 1997). This problem was addressed in a later version (Nordsveen and Haerdig, 1997) by introducing a Langrangian type-front tracking scheme.

According to Chen et al. (1993), due to the inherent limitations in the numerical methods and two phase models in OLGA, proper phase behaviour is not modelled.

Validation of OLGA

OLGA was validated under transient conditions by Shoup et al. (1998). The simulation results obtained were then compared with field data obtained by Deepstar for 'slow' and 'rapid' blowdown of a 5.28 km, 0.102 m i.d. onshore gas condensate pipeline at 4.8 MPa (700 psi) discharging through 1.27 cm (slow blowdown) and 2.54 cm (rapid blowdown) choke openings. The precise mixture composition used was not given. In order to simulate blowdown it was assumed that release occurs through a valve situated at the end of the pipeline.

Figures 2.1 and 2.2 respectively show the variation of pressure with time at Sites 3 and 6. The figures show that reasonable agreement is obtained during slow blowdown, but the model performs relatively poorly when simulating rapid blowdown.

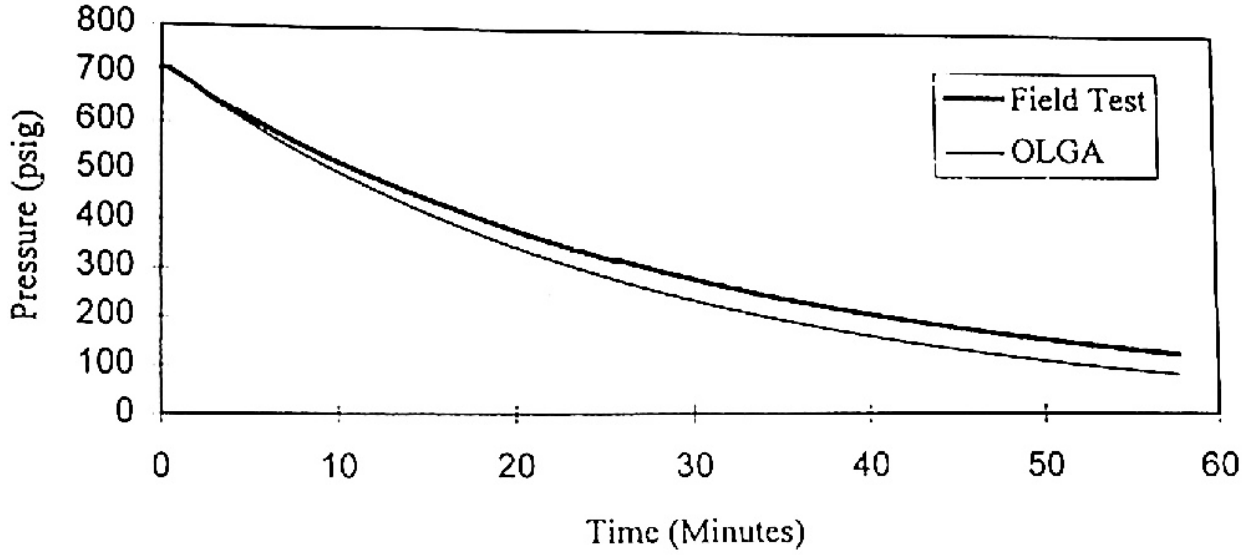

Figure 2.1: Slow Blowdown – Pressure at Site 3. OLGA Simulations versus Field Test (Shoup et al., 1998).

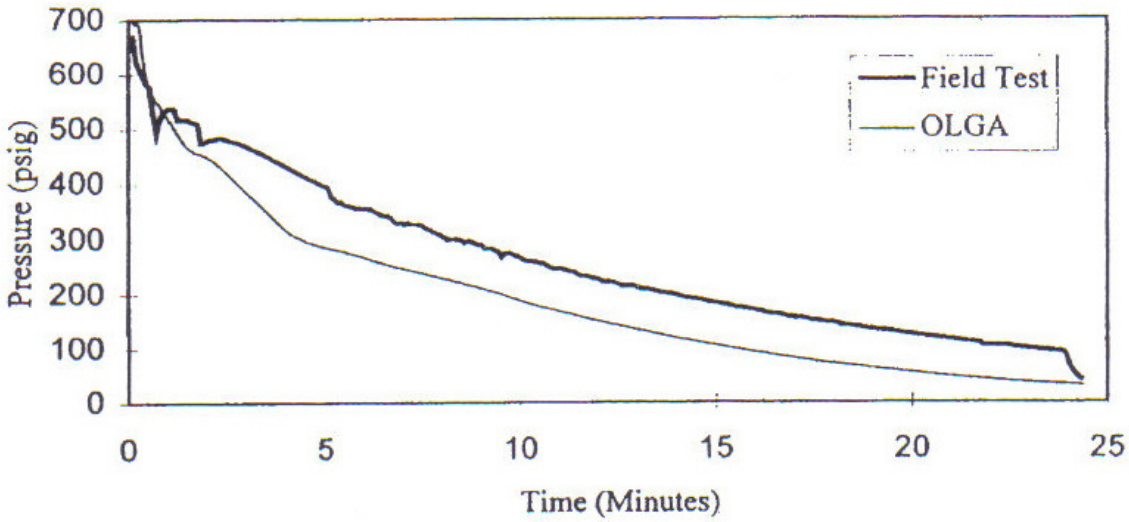

Figure 2.2: Rapid Blowdown – Pressure at Site 6. OLGA Simulations versus Field Test (Shoup et al., 1998).

More recently, OLGA was validated against experimental decompression data by Botros et al. (2007). The decompression tests were conducted at the TCPL Gas Dynamic Test Facility (GDTF) in Didsbury, Canada. The tests were performed using a 172 m long, 49.5 mm i.d. instrumented shock-tube rig containing inventories ranging from pure nitrogen to typical rich gas mixtures. The decompression of the pipeline was initiated upon failure of a rupture disc.

Figure 2.3 shows the variation of pressure with time for Case 2, at an initial pressure and temperature of 105.8 bara and -25.6 ^{o}C respectively at distances of 23.1 m (P14), 47.1 m (P19) and 71.1 m (P24) from the rupture point. The pipeline contained an inventory indicative of a rich gas mixture containing ca. 95.6 % methane. As was observed by Botros et al. (2007), the delay in the initial pressure drop predicted by OLGA as compared to the measured data implies that the speed of the front of the decompression wave is under predicted. It is also clear that the predicted pressure drop is greater than that observed in the experimental measurements. These observations are in accord with the under-prediction of the outflow pressure in figure 2.2 (shown above).

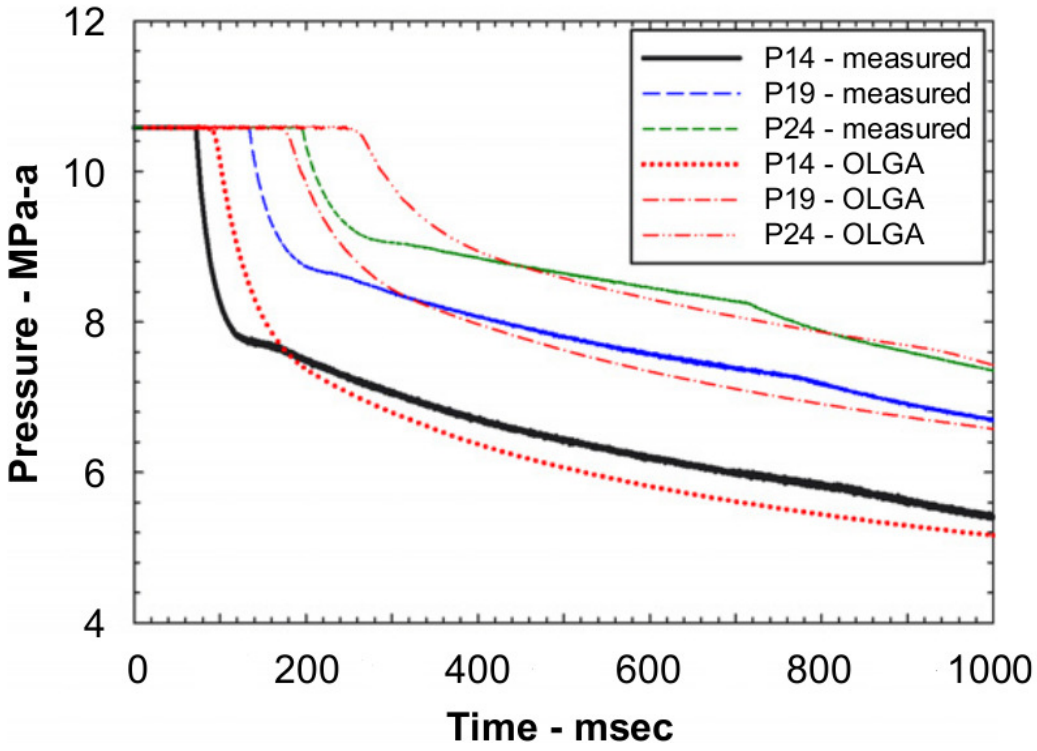

Figure 2.3: Comparison between OLGA and experimental data for Case 2 at P14, P19 and P24 (Botros et al., 2007).

2.3 University College London models (Mahgerefteh et al., 1997-2008; Atti, 2006; Oke et al., 2003; Oke, 2004)

Between 1997 and 2003, Mahgerefteh et al. published four papers relating to the modelling of the transient outflow following rupture of pressurised hydrocarbon pipelines. The following is a review of the main features.

Mahgerefteh et al. (1997) developed a pipeline rupture outflow model using a single mass, momentum and energy equation for one-dimensional flow based on the classical inverse marching Method of Characteristics (Zucrow and Hoffman, 1975). The model was applied to simulate the dynamic response of check and ball valves during emergency isolation. In order to illustrate the various dynamic effects in a gas transmission pipeline and simplify the modelling requirements the inventory was treated as an ideal gas.

The check valve closure was assumed to be instantaneous. In the case of the ball valve closure, Mahgerefteh et al. (1997) accounted for the variation of flow rate as a function of time during valve closure.

Dynamic valve response following emergency isolation was modelled based on a real North Sea pipeline of length and diameter 145 km and 0.87 m respectively containing methane. The initial flow velocity was 10 m/s and the line pressure and temperature were 133 bar and 283 K respectively. Under such conditions, the inventory remained in the gaseous phase following rupture. The pipeline was assumed to be partially insulated with a heat transfer coefficient of 5 W/m^2K.

Mahgerefteh et al. (1997) investigated the effect of valve proximity to the rupture plane on the total amount of inventory released. Figure 2.4 shows the variation of inventory loss with distance of valve from the rupture plane in the case of a ball valve and a check valve. The ball valve is assumed to activate closure at a pressure of 10 bar below the normal working pressure and close at a rate of 2.54 cm/s. The check valve on the other hand is assumed to close upon the detection of flow reversal. It is clear from the figure that for valves positioned in close proximity (up to 5 km) to the rupture plane, a check valve offers a much better degree of protection in terms of limiting the total amount of inventory released. However, for valves positioned at larger distances the difference in performance becomes negligible.

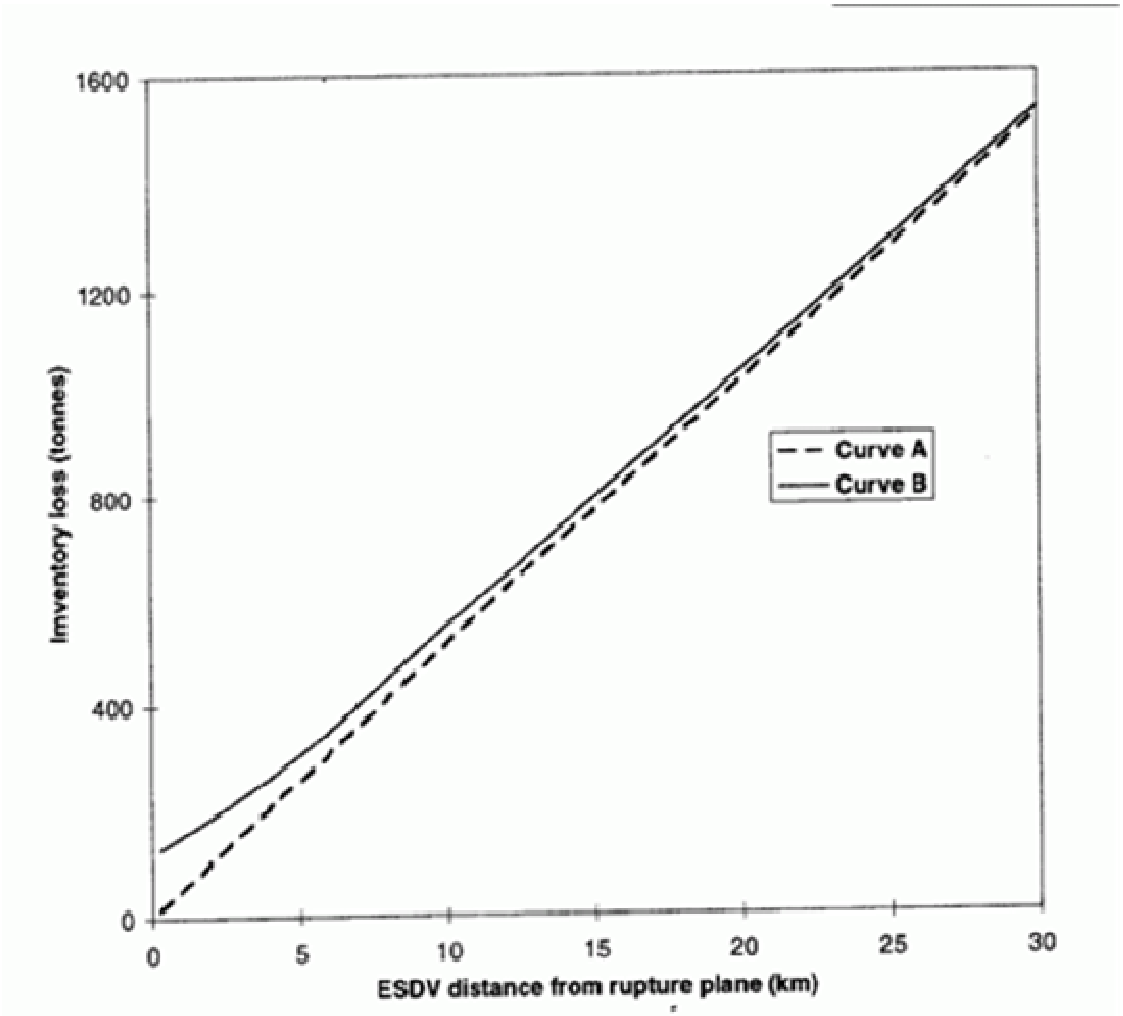

Figure 2.4: The variation of inventory loss as a function of ESDV proximity to the rupture plane.

Curve A: Check valve

Curve B: Ball valve (Mahgerefteh et al., 1997)

Mahgerefteh et al. (1999) extended the above model (Mahgerefteh et al., 1997) to account for real fluid behaviour using the Peng-Robinson Equation of State (PR EoS) (Peng and Robinson, 1976). Two-phase fluid flow is accounted for using the homogeneous equilibrium model (HEM) (Chen et al., 1995a, b) where the constituent phases are assumed to be at thermal and mechanical equilibrium. In addition, curved characteristics were employed, replacing the characteristic lines with parabolas. The latter was claimed to overcome the errors introduced as a result of using linear characteristics, which assumes linear variation of the flow parameters between the grid points.

The long computational runtimes associated with the simulation of long pipelines were partly addressed by using a Compound Nested Grid System (CNGS) in which successively coarser discretisation grids were used away from the rupture plane. Mahgerefteh et al.'s (1999) pipeline outflow model was validated against intact end pressure data recorded for the rupture of the Piper Alpha to MCP-01 subsea line (Cullen, 1990) as well as two sets of test results (P40 and P42) obtained from the Isle of Grain depressurisation tests (Richardson and Saville, 1996).

Figure 2.5 shows the variation of pressure with time at the intact end of pipeline following the full bore rupture (FBR) of the Piper Alpha to MCP-01 sub-sea line. Curve A shows the measured data whereas curve B shows the predictions using the Compound Nested Grid System Method of Characteristics (CNGS-MOC). Curve C shows the corresponding data (CNGS-ideal) generated based on the ideal gas assumption, as described previously (Mahgerefteh et al., 1997). As it may be observed, accounting for real fluid behaviour results in improved agreement with field data. However this is at the cost of a significant increase in the computational runtime (c.f. 1.5 minutes for ideal gas compared with 6 days based on real fluid behaviour).

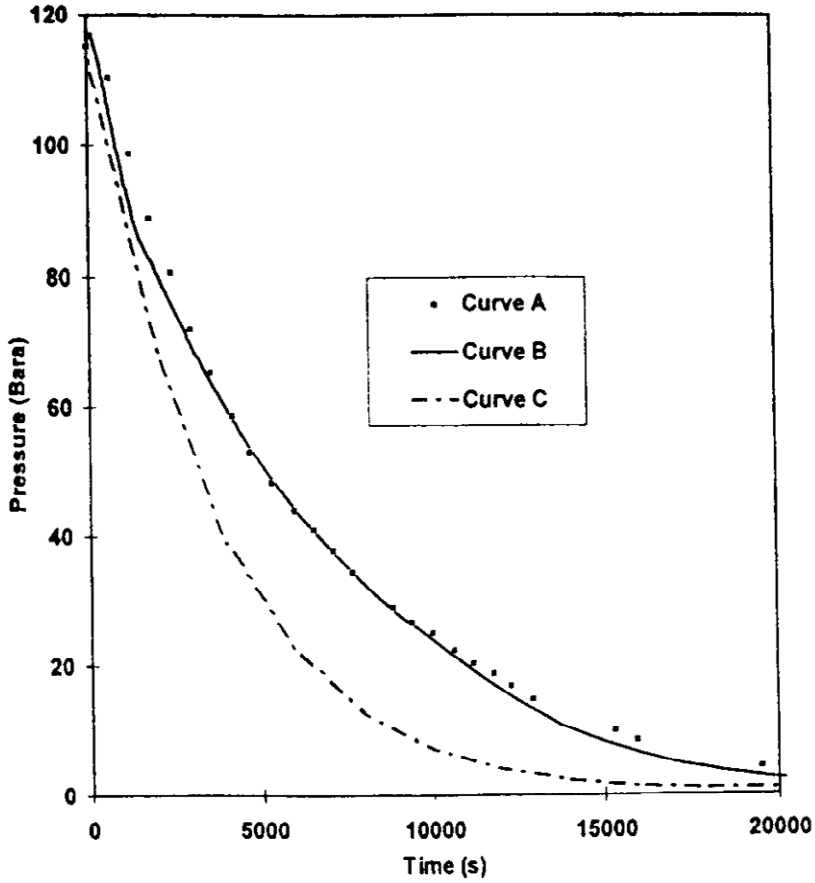

Figure 2.5: Intact end pressure vs. time profiles for the Piper Alpha to MCP pipeline (Mahgerefteh et al., 1999).

Curve A: Field Data

Curve B: CNGS-MOC, CPU runtime = 6 days

Curve C: CNGS-MOC ideal gas, CPU runtime = 1.5 min

In a later publication, using the MOC, Mahgerefteh et al. (2000) employed a real fluid model to predict the effect of phase transition on the dynamic behaviour of emergency shutdown valves. Based on their findings, the authors concluded that a transition from gas to two-phase leads to a delay of valve shutdown activation as well as a higher discharge rate and a greater loss of inventory as compared to a permanent gas.

The pipeline outflow model developed by Oke et al. (2003) and Oke (2004) dealt with the flow following the puncture and/or rupture in pipeline networks. The model is based on the MOC and assumes homogeneous equilibrium between phases. In order to assess

the impact on computational runtime and simulation accuracy, three different combinations of the formulation of the conservation equations were employed. These included pressure (P), enthalpy (H) and velocity (U) (PHU); pressure, entropy (S) and velocity (PSU); as well as the pressure, density (D) and velocity (PDU) with the latter formulation used by previous workers (for example Mahgerefteh et al., 1997). The effect of adopting quadratic interpolation along the space co-ordinate, as opposed to linear interpolation was also investigated.

The PDU, PHU and PSU based conservation equations were used by Oke (2004) to simulate the Isle of Grain rupture P40 test. Figure 2.6 shows the measured variation of the discharge pressure with time compared to the simulated results. Oke (2004) concluded that the PHU model performed best in terms of accuracy, respectively followed by the PSU and PDU based models. The PHU model also resulted in the least CPU runtime. The computational runtimes required corresponded to 12, 13 and 86 mins for the PHU, PSU and PDU based models respectively on an IBM Pentium IV 2.4 MHz PC. Although the use of quadratic as opposed to linear interpolation marginally improved the model predictions, it also resulted in longer simulation runtime.

In each case, good agreement between predicted and field data was obtained for the Piper Alpha simulation. The reported execution time using the PHU formulation was ca. 28 hours.

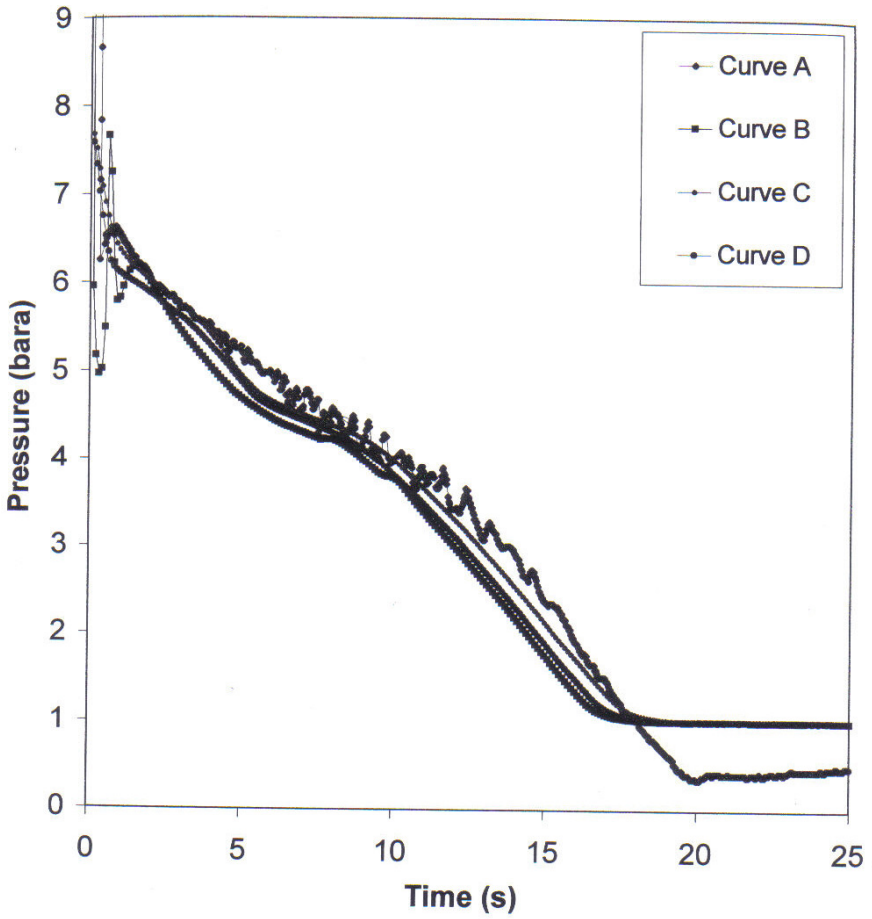

Figure 2.6: FBR pressure vs. time profiles at the open end for test P40 (LPG) showing the effect of primitive variables on simulated results (Oke, 2004).

Curve A: Open end measurement

Curve B: Open end simulation results using the PDU model

Curve C: Open end simulation results using the PHU model

Curve D: Open end simulation results using the PSU model

Oke et al. (2003) presented a model for simulating the transient fluid flow following the puncture of a pipeline. The model was used to simulate an hypothetical 16 km long pipeline, conveying a condensable hydrocarbon mixture with an initial flow rate of 0.3 m^3/s. A centrifugal pump was used to sustain this flow rate for 90 s following rupture. The PHU model was used in the simulation with the pipeline assumed to be isolated downstream upon puncture. Figure 2.7 shows a pictorial timeline simulation of the fluid flow pattern following puncture as presented by Oke et al. (2003).

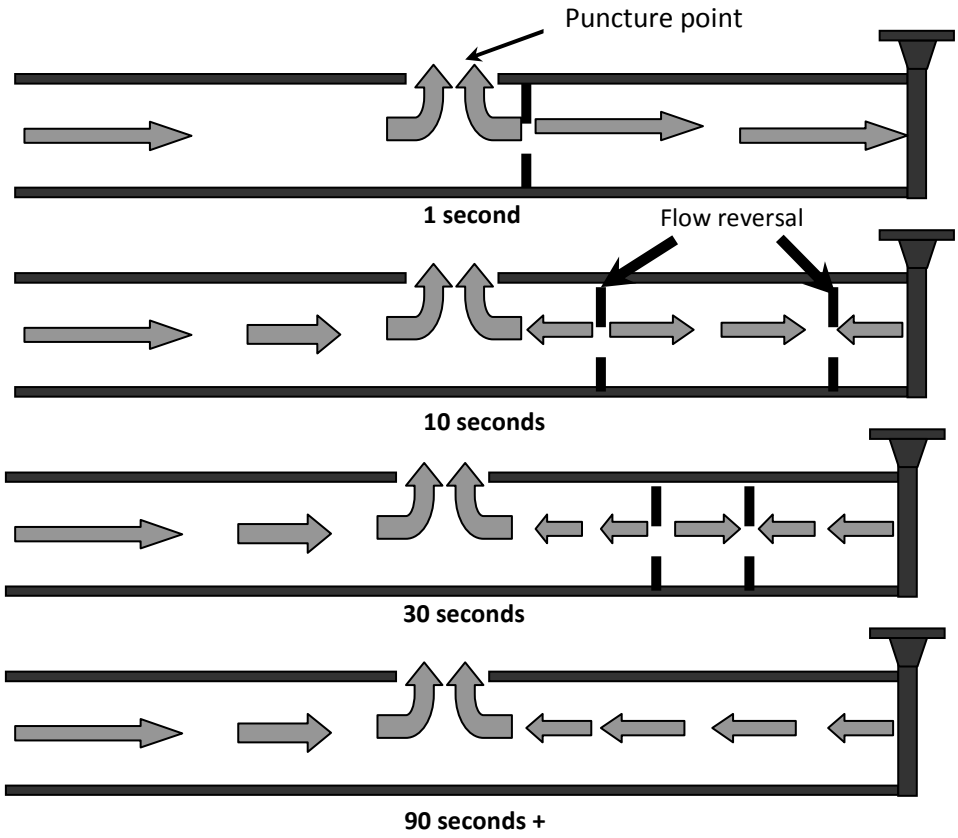

Figure 2.7: Schematic representation of flow patterns in the pipeline following puncture (Oke et al., 2003).

Atti (2006) developed an interpolation technique for Oke's (2004) HEM model to reduce the computational runtime. The conservation equations were formulated using the pressure, enthalpy and velocity (PHU) (Oke, 2004) and solved in conjunction with P-H (pressure-enthalpy) flash calculations.

The interpolation scheme involved first determining the maximum and minimum fluid enthalpies (H_{max}, H_{min}) at the likely fluid pressure (P_{max}, P_{min}) and temperature (T_{max}, T_{min}) ranges. P_{max} and P_{min} were taken as the inlet and ambient pressures respectively. T_{max} is the greater of the feed and the ambient temperatures, and T_{min} is determined by ignoring pipe wall/ambient heat transfer and performing an isentropic flash from P_{max} and T_{max} to P_{min}. Figure 2.8 shows the corresponding interpolation space domain.

The interpolation scheme is performed in two stages. The initial sweep involves determining the intermediate values of Z at points a, b and c corresponding to the enthalpy, h* by interpolating between points Z_{11}-Z_{13}, Z_{21}-Z_{23} and Z_{31}-Z_{33}, respectively.

The second step involves determining Z* by interpolating between Z(a), Z(b) and Z(c) along the pressure axis.

Atti (2006) states that the application of the interpolation scheme to a range of representative fluids such as permanent gases, two-phase mixtures, flashing liquids and permanent liquids reveals a maximum 0.01 % difference between the predicted fluid properties based on interpolation as compared to direct flash calculations. This finite difference is found to have a negligible effect on the predicted fluid flow profiles such as pressure, discharge velocity, mass flow rate and discharge temperature following pipeline rupture.

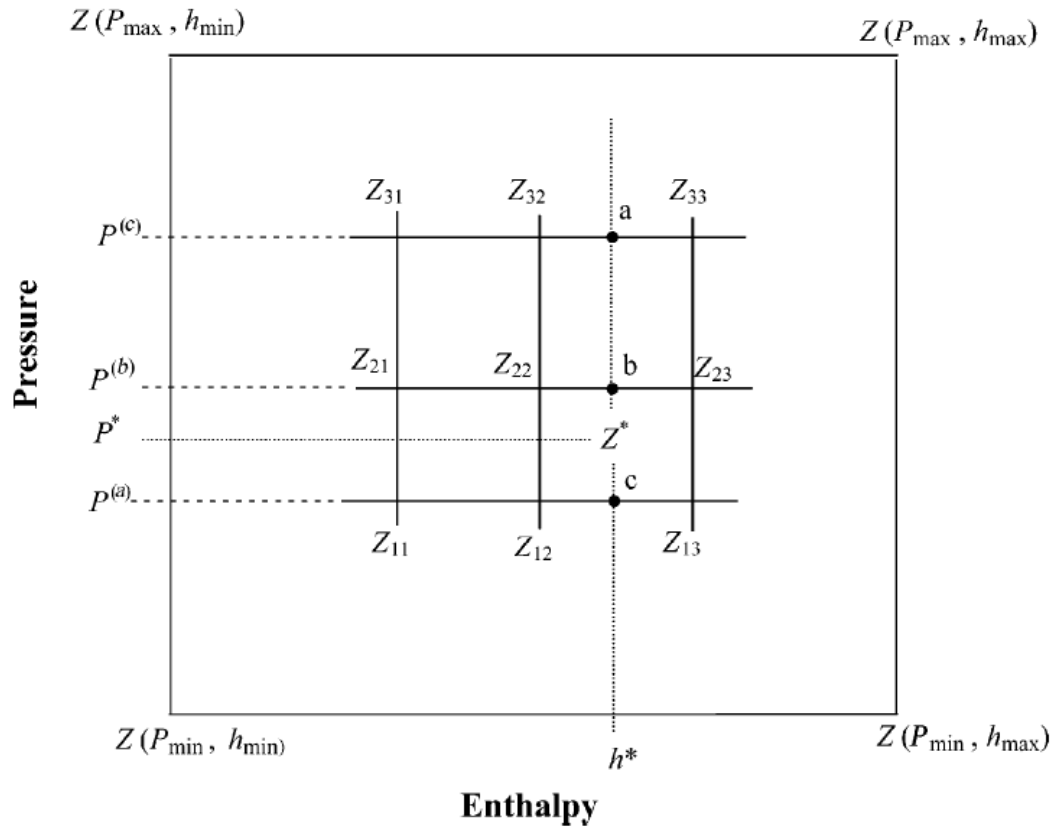

Figure 2.8: **Schematic representation of the depressurizing fluid pressure/enthalpy interpolation domain Atti (2006).**

The model was validated by comparison against the results of the Isle of Grain rupture tests as well as the closed end data relating to the MCP-01 riser rupture during the Piper Alpha disaster.

Figure 2.9 shows the variation of fluid pressure at the rupture plane for the P40 Isle of Grain test. The measured data is represented by curve A. Curves B and C on the other hand respectively represent the simulation results with and without the interpolation scheme.

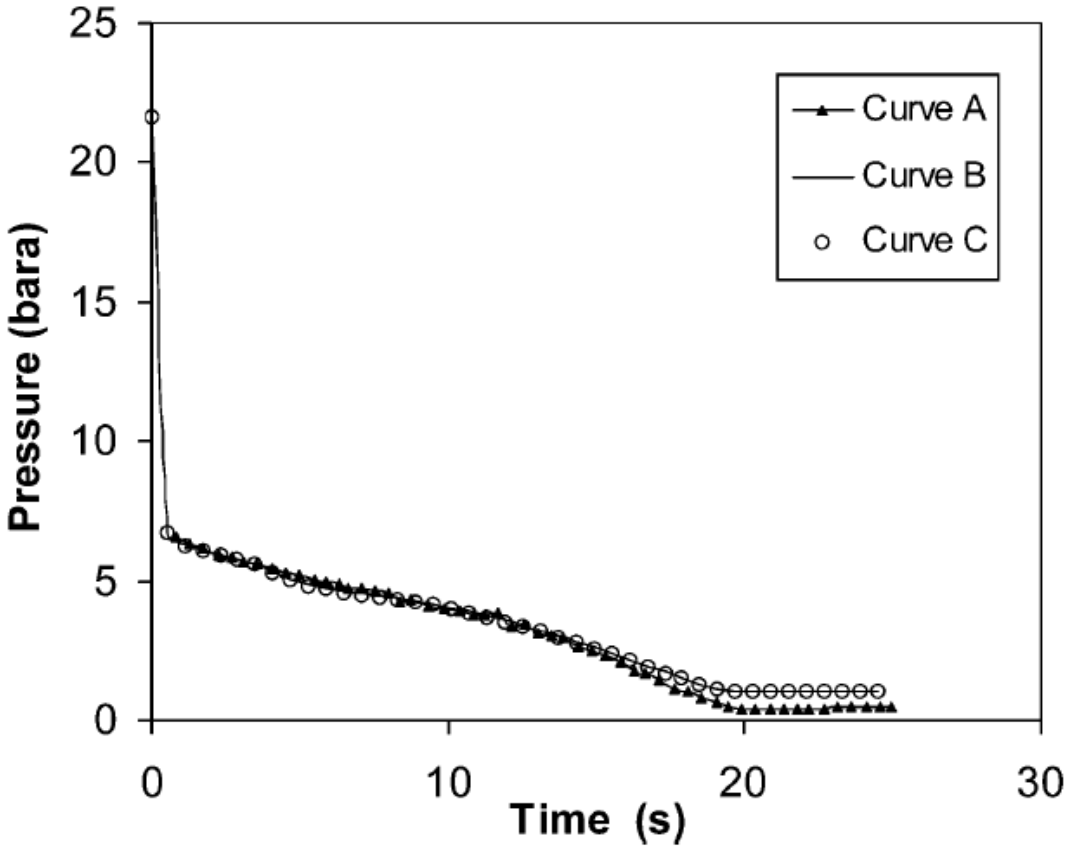

Figure 2.9: Pressure vs. time profiles at open end for test P40 (LPG) (Mahgerefteh et al., 2007).

Curve A: Measurement (Chen et al., 1995a, b)

Curve B: Simulation data without the interpolation scheme: CPU runtime = 12 min

Curve C: Simulation data employing the interpolation scheme: CPU runtime = 3.5 min

As it may be observed from figure 2.9, the simulated data (curves B and C) are identical and in good accord with the test data. The use of the interpolation scheme (curve B) results in a 70 – 80 % reduction in the computational runtime for the cases presented.

Mahgerefteh et al. (2008) developed a hybrid outflow model to address the failure of the homogeneous equilibrium model (HEM) to account for the post depressurisation liquid discharge in ruptured pipelines containing two-phase or condensable gas mixtures.

Figure 2.10 shows a schematic representation of a declined (downward sloping) pipeline containing a liquid/vapour mixture following depressurisation to the ambient pressure. In this case the HEM model does not account for the discharge of the remaining liquid in the pipeline. Mahgerefteh et al. (2008) simulate the subsequent liquid discharge rate by performing an energy balance over the entire length of the pipeline based on the assumption that any remaining liquid will disengage from the vapour.

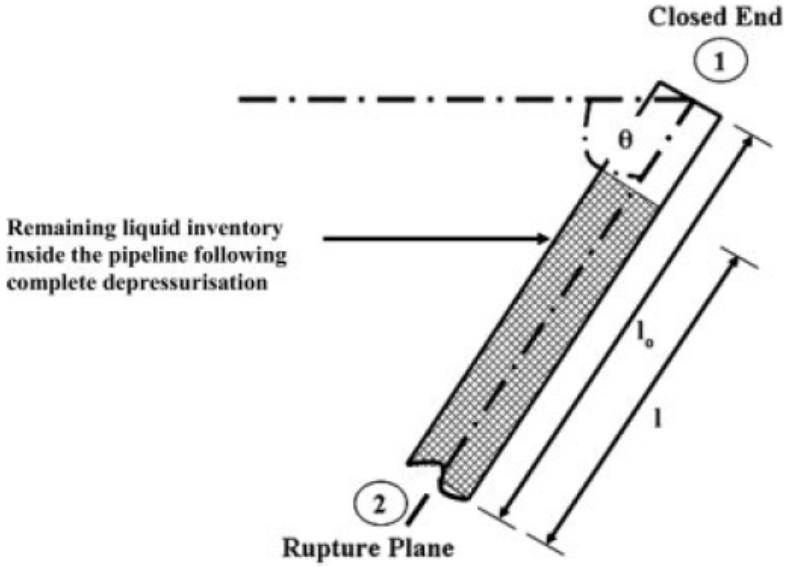

Figure 2.10: Schematic representation of a pipeline declined at an angle θ (Mahgerefteh et al., 2008).

Figure 2.11 shows a comparison of the variation of mass released with time between Atti's (2006) HEM and the Mahgerefteh et al. (2008) hybrid model for a hypothetical 100 m long, 0.154 m i.d. pipeline containing an inventory of 100 % hexane as a permanent liquid at 21 bara and 20 ^{o}C. Curves A and B respectively show Atti (2006) and Mahgerefteh et al. (2008) hybrid model predictions. As it may be observed, Atti's (2006) model (curve A) significantly underestimates the cumulative mass discharge as it does not account for post-depressurisation outflow.

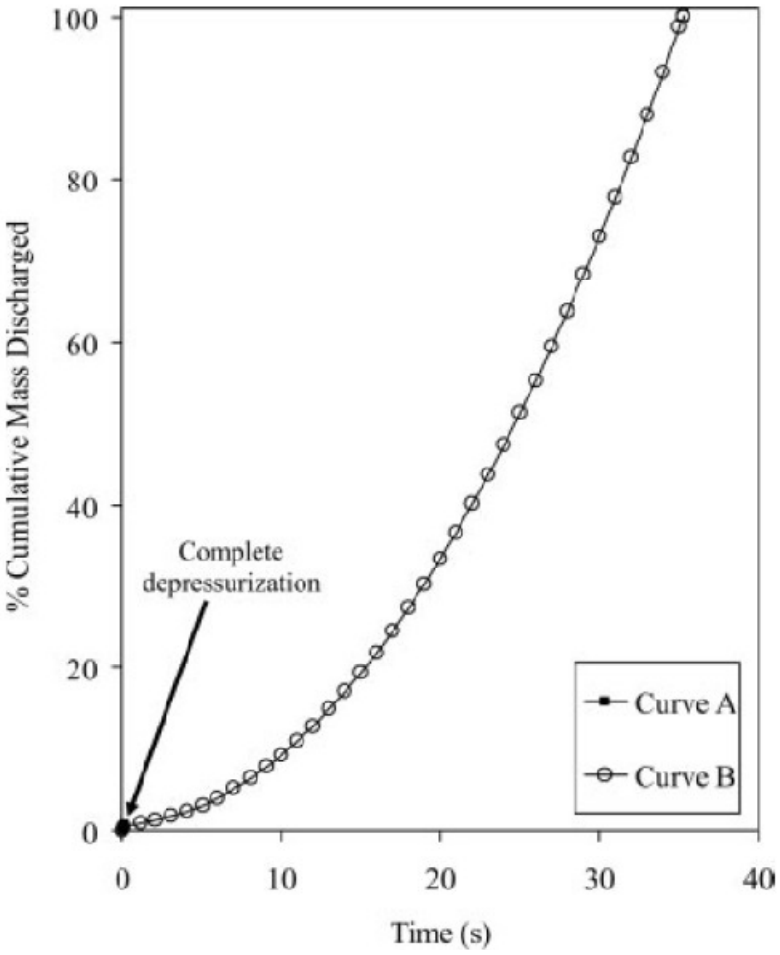

Figure 2.11: Variation of % cumulative mass discharged with time for a pipeline transporting 100 % hexane at a decline angle of -10 ^{o} following FBR (Mahgerefteh et al., 2008).

Curve A: Atti (2006)

Curve B: Hybrid model

2.4 SLURP (Cleaver et al., 2003; Cumber, 2007)

Cleaver et al. (2003) developed SLURP for simulating the outflow rate from ruptured pipelines transporting compressed volatile liquids. The mathematical basis of SLURP is the same as that originally developed by Morrow (1982) with the further extension of the thermodynamic property model to account for a wide range of fluids with a consistent degree of accuracy (Cleaver et al., 2003).

The main assumptions in SLURP include; for a failure along the pipe length the ruptured pipe ends are sufficiently remote from each other that the outflow is unaffected, the pipeline is infinitely long and the outflow from the pipeline is always choked.

SLURP's physical model is separated into three sub-models (Cleaver et al., 2003):

1. A critical discharge flow model for calculating the pressure close to the pipe exit
2. A relationship for the pressure gradient in the two-phase section of the pipe
3. A model for the voidage within the pipe.

According to the authors, physical property predictions in SLURP are determined from curves fitted using the PR EoS (Peng and Robinson, 1976) and the COSTALD method for the prediction of liquid densities (Thomson et al., 1982).

Cleaver et al. (2003) validated SLURP by comparing the predicted inventories and mass flow rates with outflow measurements taken from the Isle of Grain LPG experiments (Tam and Higgins, 1990) and the predicted outflow data calculated using the general two-phase pipeline model PROFES (Hyprotech, 2003). The Isle of Grain tests used in the validation were Tests T61, T63, T65 and T66. Tests T61 and T65 were full bore rupture tests while Tests T63 and T66 were blowdown tests through a circular and triangular orifice respectively. The inventory used in the tests comprised primarily of LPG (ca. 95 mole% propane and 5 mole% butane). A discharge coefficient of 0.8 as suggested by Haque et al. (1992) was used to simulate test T63 (Cleaver et al., 2003). No information was given by Cleaver et al. (2003) about the comparison between SLURP and test T66 experimental results.

Table 2.1 gives a summary of the Isle of Grain test conditions used in the validation.

Table 2.1: Subset of tests from the Isle of Grain experiments used in the validation of SLURP (Cleaver et al., 2003).

Test	Initial conditions		Orifice diameter (mm)	Orifice shape
	Pressure (bar abs)	Temperature (°C)		
T61	21.2	Unknown	51	Circular
T63	22.5	18.4	35	Circular
T65	11.6	13.8	51	Circular
T66	21.8	13.3	35	Triangular

Figures 2.12 to 2.14 present the variations of total pipeline inventory with time for tests T61, T63 and T65 respectively. As can be seen in the figures, SLURP performs poorly during the latter stages of depressurisation (figures 2.12 and 2.13 respectively). Cleaver et al. (2003) attributed this to the finite length of the pipeline, as the assumption of an infinitely propagating two-phase region is no longer valid. For test T65 (figure 2.14) there are significant discrepancies between the test and simulated data. Cleaver et al. (2003) suggest that this is due to the delay in the fluid flashing to two-phase upon pipeline failure.

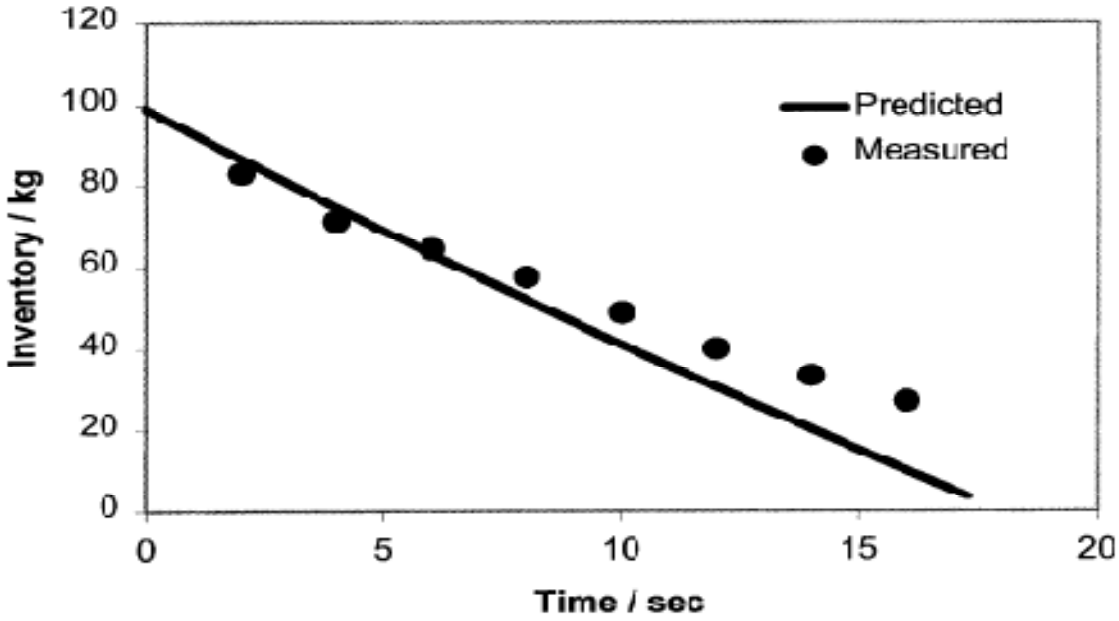

Figure 2.12: Comparison between SLURP model and measured variation of pipeline inventory with time for test T61 (Cleaver et al., 2003).

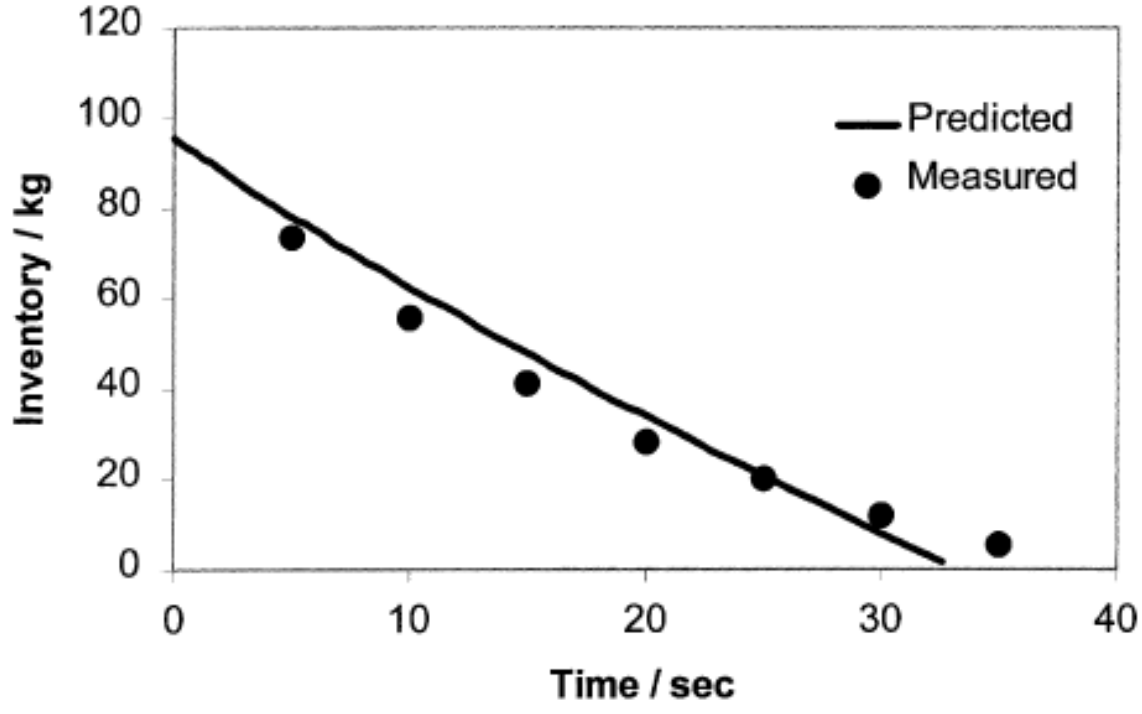

Figure 2.13: Comparison between SLURP model and measured variation of pipeline inventory with time for test T63 (Cleaver et al., 2003).

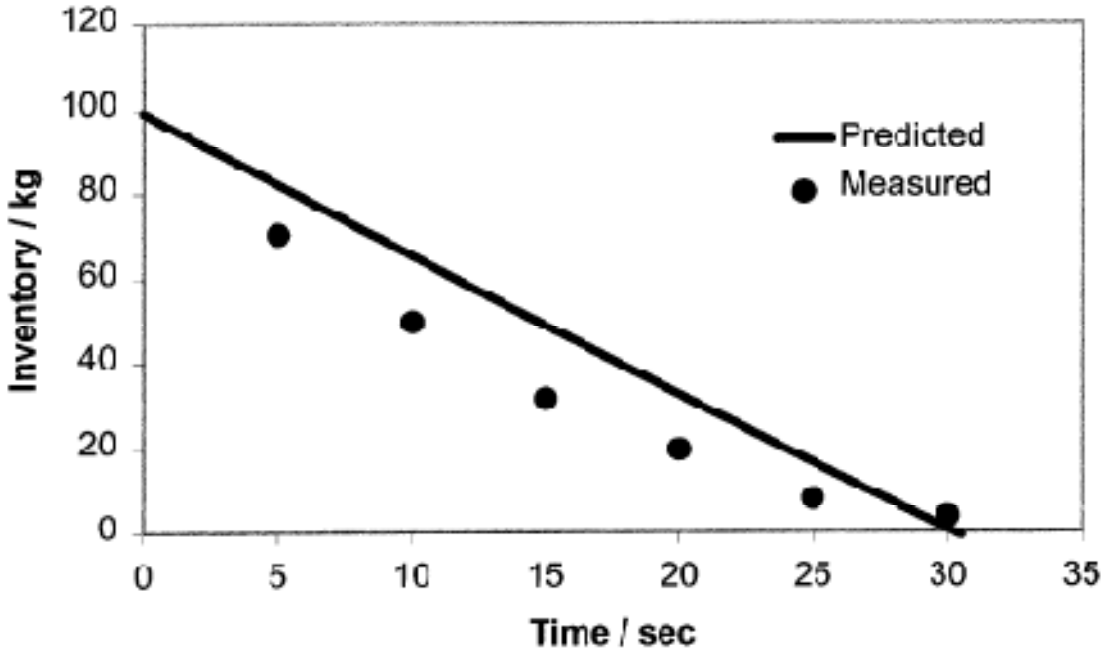

Figure 2.14: Comparison between SLURP model and measured variation of pipeline inventory with time for test T65 (Cleaver et al., 2003).

Cumber (2007) extended SLURP (SLURP_FAUSKE) by reverting to the homogeneous equilibrium flow assumption (SLURP_HEM) by assuming no phase slip and accounting for fluid/wall heat transfer (SLURP_HEM_HT).

To study the impact of these extensions to SLURP, a number of propane outflow scenarios were modelled and the results compared against PROFES predictions. Table 2.2 shows the failure scenarios examined.

Table 2.2: Failure scenarios used in the comparison of predicted outflow calculated using SLURP and PROFES for a pipeline at an initial temperature of 15 ^{o}C containing carrying an inventory of 100 % propane.

Case	Initial pressure (bar gauge)	Pipe diameter (mm)
P1	45	250
P2	70	250
P3	20	250

Figure 2.15 shows the comparison of the variation of mass flow rate with time for case P1. As it may be observed, the SLURP models predict a higher flow rate than that given by PROFES with the original SLURP model (SLURP_FAUSKE) giving closest agreement. The figure also shows that the inclusion of heat transfer effects (SLURP_HEM_HT) has little impact on the predicted outflow. Cumber (2007) stated that this was consistent with the findings of Webber et al. (1999) where including wall heat transfer tended to improve predictions of temperature and pressure profiles but not the discharge rate as compared to measured data.

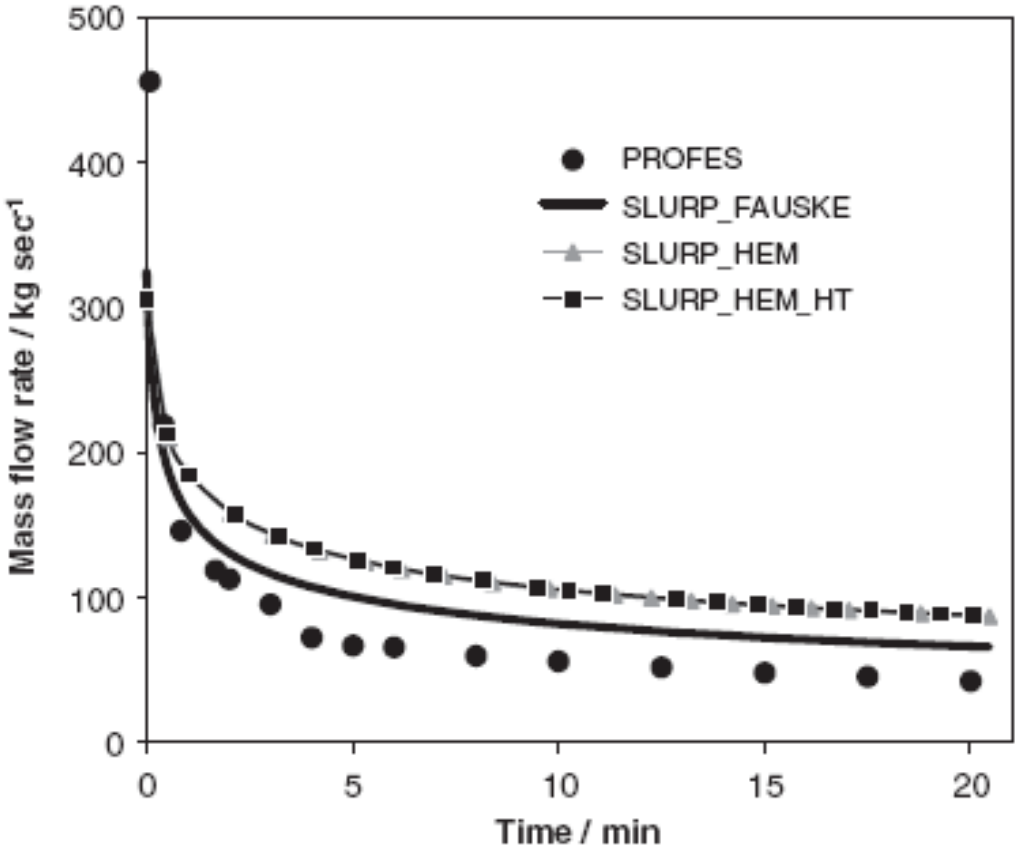

Figure 2.15: Comparison of predicted release rate for a propane pipeline at an initial pressure of 46 bara and 15 ^{o}C (Cumber, 2007).

2.5 Botros et al. (2004-2010)

Botros et al. (2004) performed a series of shock tube depressurisation tests using the NPS 2 stainless steel expansion tube test rig shown in figure 2.16 at the TCPL Gas Dynamic Test Facility (GDTF) in Didsbury, Canada.

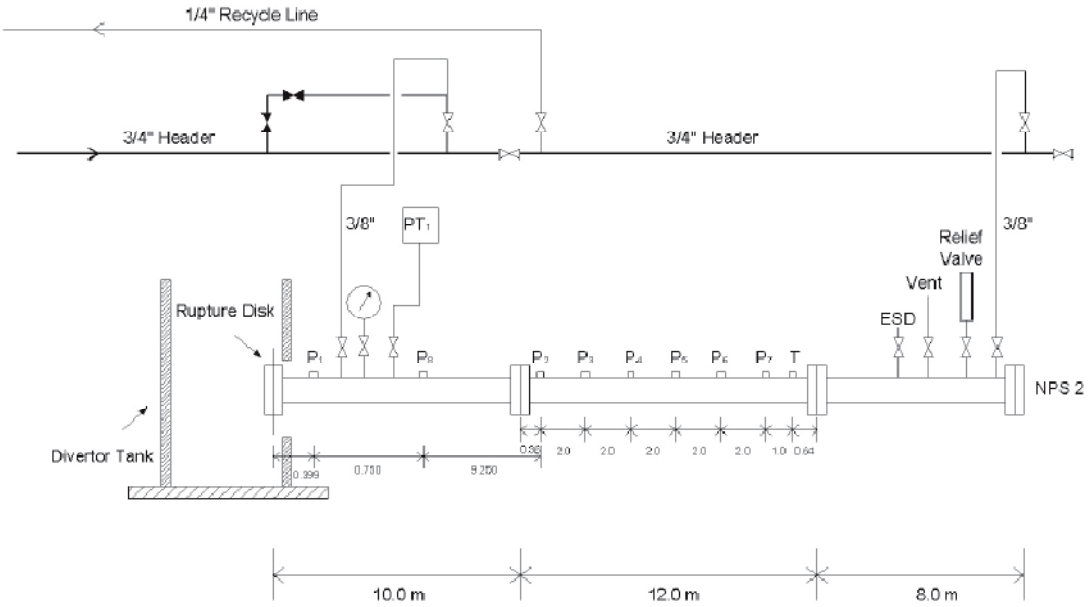

Figure 2.16: Schematic representation of the experimental setup for TCPL Gas Dynamic shock tube tests (Botros et al., 2004).

The main test section was a 30 m long seamless tube (i.d. = 49.325 mm) with an internal surface honed to a roughness of approximately 0.10 mm. A rupture disc was placed at one end of the tube, which upon rupturing, initiated a decompression wave propagating upstream of the test pipe. Eight dynamic high frequency pressure transducers (P1 to P8, see figure 2.16) together with a temperature transducer were mounted along the decompression tube test section to capture the expansion waves propagation.

A total of 12 tests were conducted with various gas compositions and different initial pressures ranging from 10 to 21.5 MPa. Tables 2.3 and 2.4 respectively give the initial pressures and gas compositions used in the decompression tests.

For each test, the authors compared the experimentally obtained decompression wave speeds against those predicted from of the decompression models GASDECOM (Eiber et al., 1993) and AGA-8-DECOM (Botros et al., 2001).

GASDECOM and AGA-8-DECOM predict decompression wave behaviour by calculating the speed of sound and the outflow velocity using incremental pressures and densities. The models use the Benedict-Webb-Rubin-Starling (BWRS EoS) (Starling, 1973) and the AGA-8 Equations of State (Starling and Savidge, 1992) respectively to describe the thermodynamic state of the fluid. The outflow velocity at any pressure is taken to be the sum of all the previous velocity changes. The simplifying assumptions behind both models are:

- The fluid is homogeneous with an average mixture density in the two-phase region
- The speed of sound in two-phase mixtures is calculated for thermodynamic equilibrium; no droplet effects
- No velocity slip between vapour and liquid phases
- Flat liquid/vapour interface, no droplets; one-dimensional isentropic flow model and no friction in pipe.

Table 2.3: Initial pressures for shock tube tests (Botros et al., 2004).

Gas mixture	Initial Pressure		
	10 MPa	14MPa	20 MPa
Base	File-21	File-18	File-15
Medium	File-20	File-23	File-19
Rich	File-22	File-17	File-16
Very Rich	File-26	File-25	File-24

Figures 2.17 and 2.18 respectively show the comparison of the variation of pressure with decompression wave speed and the decompression trajectories relative to the phase envelope predicted by GASDECOM and AGA-8-DECOM for file-21 test.

Table 2.4: Mixture compositions for shock tube tests (Botros et al., 2004).

	File-15	File-18	File-21	File-19	File-23	File-20
C1	92.757	93.020	92.955	81.383	83.220	82.738
C2	4.075	3.876	4.076	12.640	11.357	11.544
C3	0.861	0.909	0.800	4.056	3.481	3.765
i-C4	0.103	0.108	0.099	0.095	0.088	0.096
n-C4	0.146	0.158	0.137	0.138	0.123	0.141
I-C5	0.053	0.059	0.066	0.051	0.059	0.052
n-C5	0.027	0.026	0.073	0.023	0.065	0.023
N2	0.699	0.647	0.697	0.566	0.624	0.575
CO2	1.279	1.197	1.097	1.048	0.982	1.065
	File-16	File-17	File-22	File-24	File-25	File-26
C1	77.991	76.884	77.271	70.763	70.770	70.947
C2	15.298	16.137	15.971	17.898	17.946	17.681
C3	4.772	5.067	4.955	9.688	9.633	9.717
i-C4	0.087	0.086	0.082	0.075	0.075	0.075
n-C4	0.123	0.121	0.114	0.104	0.104	0.104
I-C5	0.044	0.044	0.055	0.050	0.050	0.050
n-C5	0.023	0.022	0.061	0.056	0.056	0.056
N2	0.588	0.580	0.579	0.531	0.531	0.532
CO2	1.075	1.060	0.912	0.835	0.835	0.837

Referring to figure 2.17, as it may be observed, the measured data for P1 and P8 show an almost linear decline in the pressure ratio to approximately 0.55. At this pressure ratio, a slight plateau of constant pressure with decreasing decompression wave speed is observed indicating an instantaneous drop in the speed of sound corresponding to a phase transition from vapour to a two-phase mixture. The same data taken from all of the pressure transducers shows a slightly slower wave speed towards the end of the depressurisation process. While initially in reasonably good agreement with the measured data, neither model predicts the pressure plateau. This is despite the decompression trajectories crossing the phase envelope, as may be seen in figure 2.18.

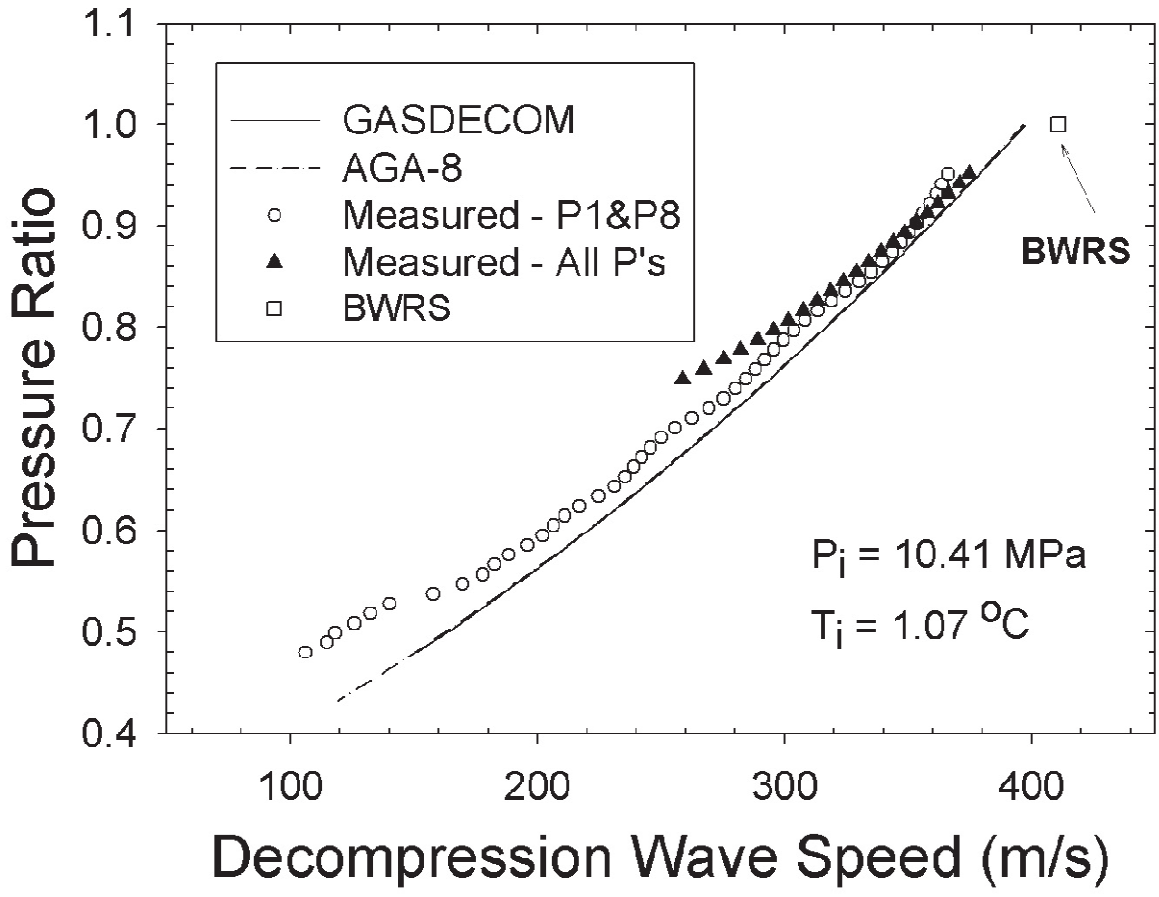

Figure 2.17: Measured and calculated decompression wave speed results of file-21 test (Botros et al., 2004).

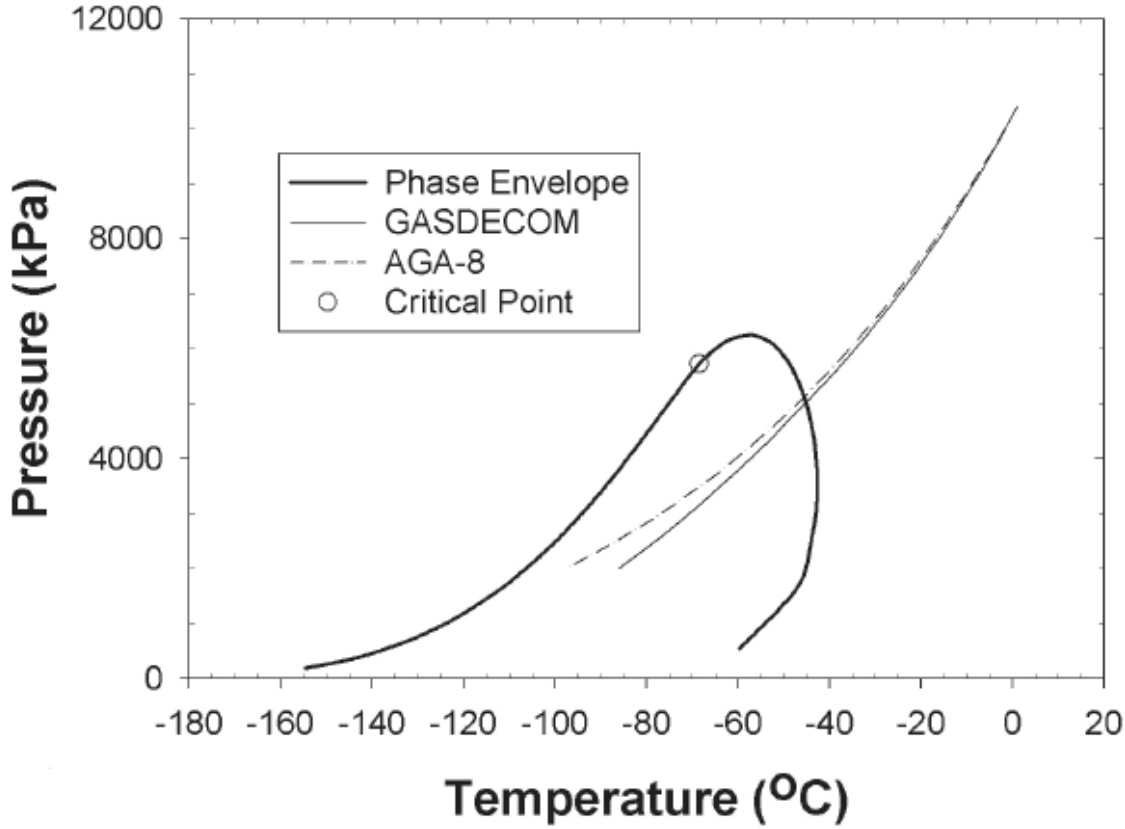

Figure 2.18: Predicted decompression Pressure-Temperature trajectories relative to phase envelope for file-21 test (Botros et al., 2004).

Figure 2.19 shows the variation of the ratio of choked exit pressure and pressure behind the decompression wave to the initial pressure with distance travelled behind the decompression wave. The predicted results were obtained assuming ideal steady Fanno flow (Shapiro, 1953), while the measured data represents the pressure minima at each pressure transducers from file-15, file-18 and file-21. The Fanning friction factor for the test cases was estimated to be around 0.00232 corresponding to a hydraulically smooth pipe with mean flow Reynolds' number in the range 4 to 8 x 10^7 based on the pipe diameter.

As can be seen in figure 2.19, the Fanno flow model is in good agreement with the experimental data for test case file-15 (Pi = 20 MPa). However, the Fanno flow model under-predicts the pressure behind the wave in test cases file-18 (Pi = 13.8 MPa) and file-

21 (Pi = 10.41 MPa). Botros et al. (2004) attributed this to the higher rate of condensation and the larger impact of friction caused by the lower initial pressure and the transient nature of the flow respectively.

Botros et al. (2010a) performed a similar series of tests to those described above (Botros et al., 2004) on a 42 m long stainless steel test rig consisting of four spool pieces at pressures up to 370 bara. A schematic representation of the test rig used by Botros et al. (2010a) is shown in figure 2.20. The four spool pieces were internally honed to a roughness of less than 0.636 μm. A total of 16 dynamic pressure transducers were mounted along the length of the rupture tube. Table 2.5 gives the position of the pressure transducers relative to the rupture disc. Two fast response temperature transducers were located on spools 1 and 2 and a static temperature probe on spool 3. A total of five tests were conducted with various gas compositions and different initial temperatures and pressures as given in table 2.6.

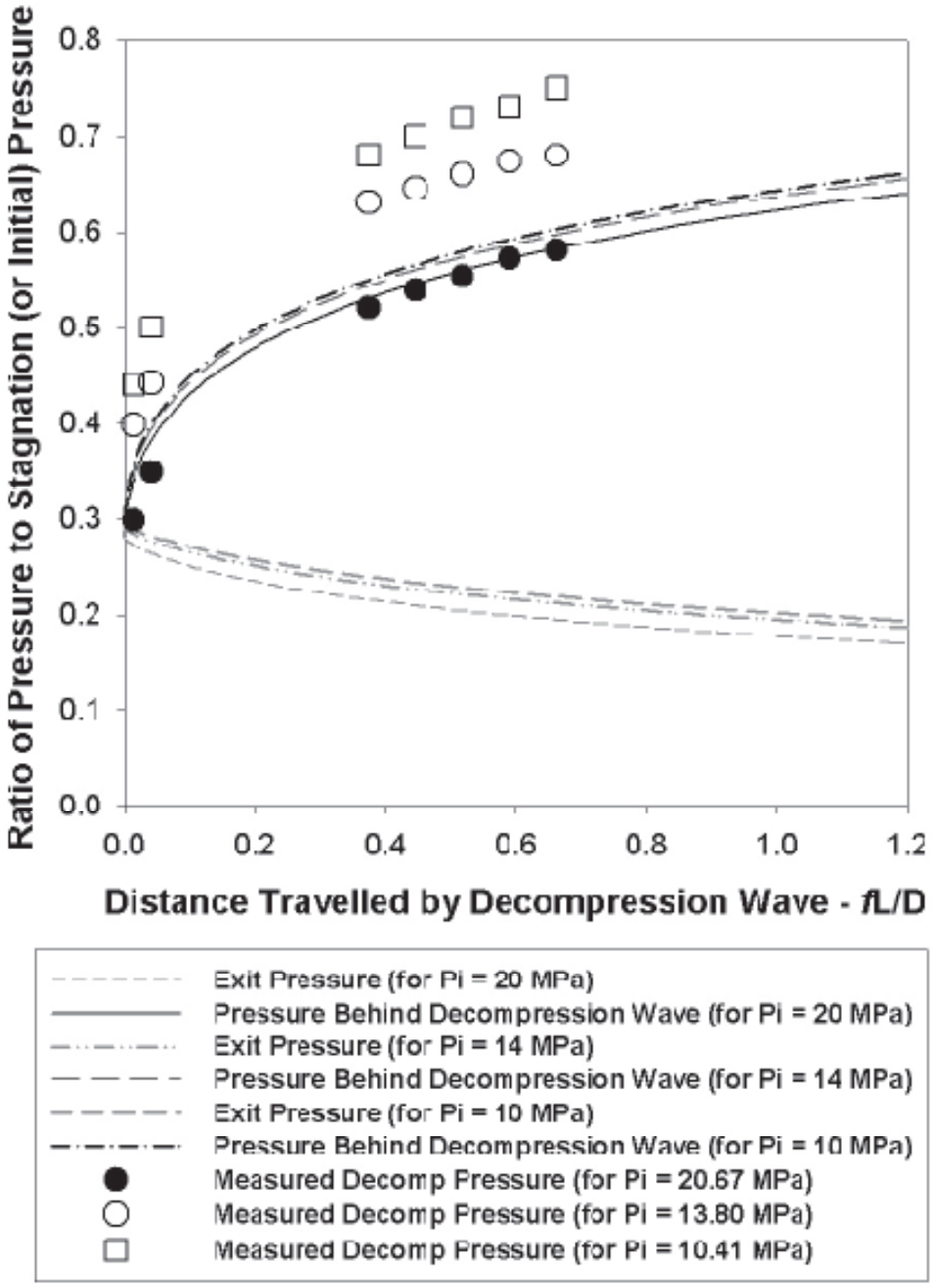

Figure 2.19: Comparison of measured and predicted dimensionless pressure ratios vs. distance travelled by decompression wave for the base gas mixture (Botros et al., 2004).

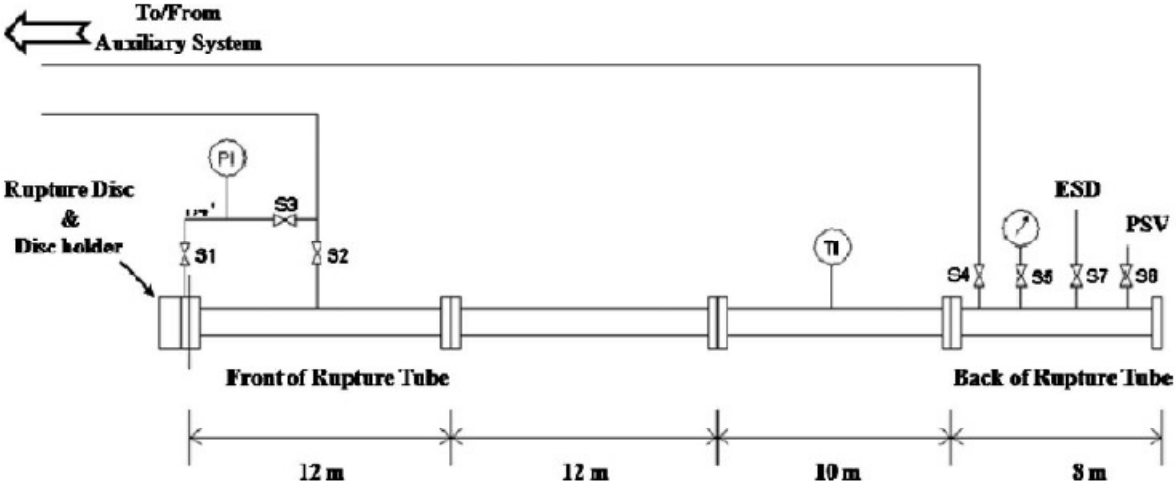

Figure 2.20: Schematic representation of the experimental setup for shock tube tests (Botros et al., 2010a).

Table 2.5: Location of pressure transducers relative to the rupture disc (Botros et al., 2010a).

	Location	Distance from previous PT (mm)	Distance from choked location (mm)	Distance from previous PT (D)	Distance from choked location (D)
First spool	(Flange RF)	0	0	0.00	0.00
	PT1	29.5	29.5	0.77	0.77
	PT1A	62.9	92.4	1.65	2.43
	PT1B	10.4	102.8	0.27	2.70
	PT2	97.2	200	2.55	5.25
	PT3	150	350	3.94	9.19
	PT4	150	500	3.94	13.12
	PT5	200	700	5.25	18.37
	PT6	200	900	5.25	23.62
	PT7	200	1,100	5.25	28.87
	PT8	2000	3,100	52.49	81.36
	PT9	2000	5,100	52.49	133.86
	PT10	2000	7,100	52.49	186.35
	PT11	2000	9,100	52.49	238.85
Second spool	PT12	3900	13,000	102.36	341.21
	PT13	6000	19,000	157.48	498.69
Third spool	PT14	6000	25,000	157.48	656.17

Table 2.6: Mixture compositions and initial conditions (Botros et al., 2010a).

	Test 1	Test 2	Test 3	Test 4	Test 5
Pi (kPa-a)	36195.2	36333.6	36114.0	33377.0	35658.0
Ti (°C)	26.50	20.50	67.90	21.20	21.20
		Gas composition (mole %)			
C1	91.1099	83.1579	83.1355	76.4542	80.6894
C2	5.3291	4.3151	4.9189	9.3231	7.7610
C3	1.4813	5.7600	5.5617	6.0851	5.5969
iC4	0.1562	0.9862	0.9764	1.4975	0.9729
nC4	0.2119	1.9957	1.8895	3.3347	1.8834
iC5	0.0496	1.4712	1.4019	0.8439	1.0027
nC5	0.0378	0.6350	0.5925	0.8289	0.5101
C6+	0.0413	0.3017	0.2741	0.4420	0.3469
N2	0.5768	0.5687	0.4847	0.5150	0.5171
CO2	1.0060	0.8084	0.7647	0.6756	0.7196
Sum	100.00	100.00	100.00	100.00	100.00

The measured results were compared to the decompression wave predictions of GASDECOM and PIPEDECOM (Philips and Robinson, 2005). PIPEDECOM uses the same underlying assumptions as GASDECOM. In order to account for non-equilibrium conditions PIPEDECOM artificially alters the phase transition temperature by a specified amount, referred to as the delay.

Figure 2.21 shows the comparisons of GASDECOM and PIPEDECOM (with delays of 0 ^{o}C, 1 ^{o}C and 2 ^{o}C respectively) pressure versus decompression wave speed predictions against the measured data for Test 1. From the figure it can be seen that regardless of the delay temperature applied, PIPEDECOM predicts a higher decompression wave velocity than is seen experimentally. GASDECOM in contrast under-predicts the initial wave velocity, but shows good agreement with the experimental data between 20 to 10 MPa. For the latter stages of the pressure drop GASDECOM shows similar behaviour to PIPEDECOM. Botros et al. (2010a) attributed the differences observed in the predictions of GASDECOM and PIPEDECOM to the slight difference in the methodologies used to calculate the propagation velocities.

Botros et al. (2010a) found that in general the PIPEDECOM with the 1 ^{o}C delay showed the best prediction of the measured pressure plateaus.

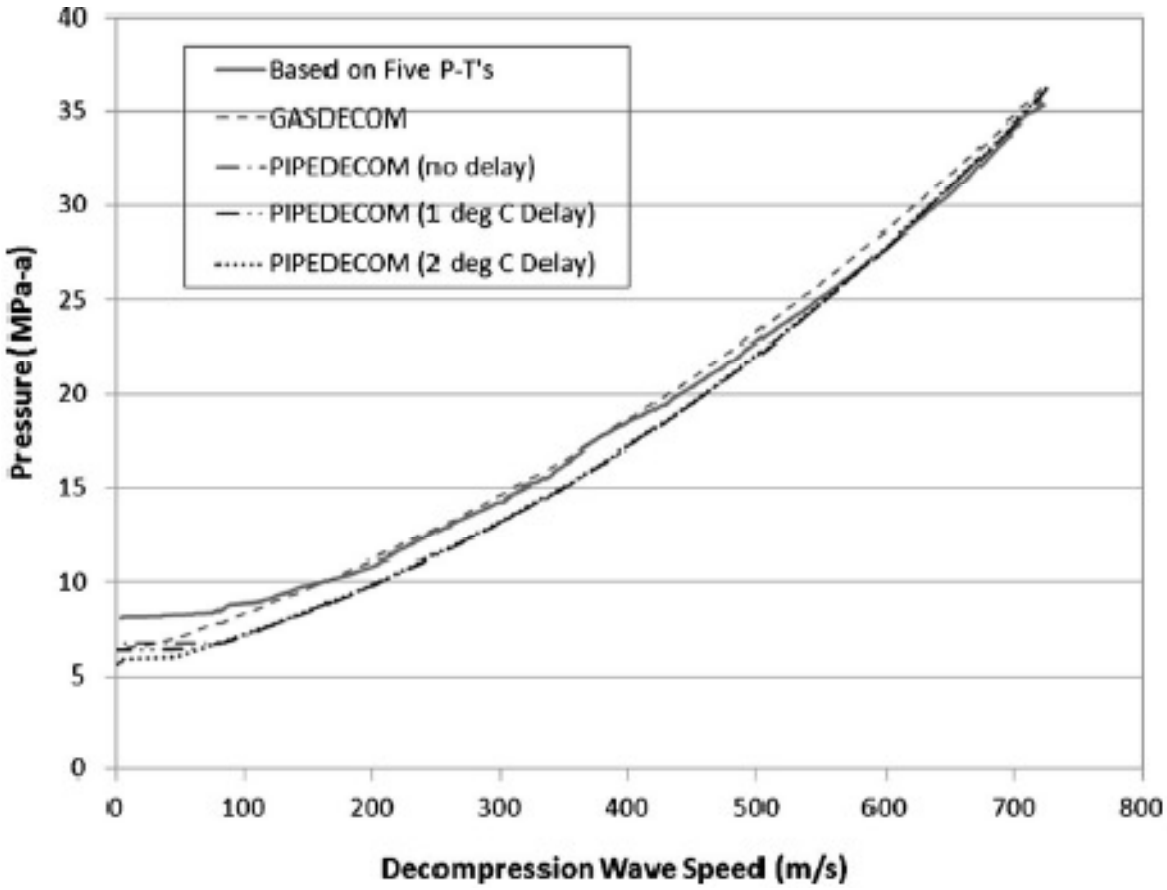

Figure 2.21: Measured and calculated decompression wave speed results of Test 1 for a conventional gas mixture from an initial pressure = 10 MPa (Botro et al., 2010a).

The same test rig shown as in figure 2.20 was used by Botros et al. (2010b) to quantify the effects of pipe diameter and wall friction on the decompression wave speed predictions of GASDECOM. Due to safety and space limitations at the TCPL Gas Dynamic Test Facility, Botros et al. (2010b) simulated the behaviour of larger pipes by keeping the shock tube diameter constant (i.d. 38.1 mm) while adjusting the ratio of the internal surface roughness to pipe diameter of the first spool from 1.6×10^{-6} (smooth) to 1×10^{-4} (rough). Tables 2.7 and

2.8 give the initial conditions and mixture compositions for Tests 1 to 6 in the smooth and rough tubes respectively.

Table 2.7: Mixture compositions and initial conditions of the tests conducted with the smooth tube (Botros et al., 2010b).

	Reference-Smooth	Test 1-Smooth	Test 2-Smooth	Test 3-Smooth	Test 4-Smooth	Test 4R-Smooth	Test 5-Smooth	Test 6-Smooth
Pi (kPa-a)	18,537	18,584	10,188	14,182	19,771	18,175	21,171	21,344
Ti (°C)	16.74	21.50	20.50	12.20	11.50	11.90	−3.51	−14.01
				Mole %				
	Dry	Medium rich			Rich			Ultra-rich
C1	98.6864	87.9168	85.8463	80.4083	82.2015	81.6402	82.9164	79.3017
C2	0.5822	6.5522	7.6575	7.3598	6.8193	7.2071	6.6487	10.0013
C3	0.0193	3.1044	3.8710	7.3078	7.4616	7.4769	7.0287	6.1103
iC4	0.0000	0.2557	0.3638	0.8173	0.7052	0.7497	0.6657	1.3280
nC4	0.0000	0.4785	0.7346	1.0930	0.8856	0.9701	0.8908	1.7365
iC5	0.0000	0.0000	0.0000	0.0000	0.0000	0.0000	0.0000	0.0000
nC5	0.0000	0.0000	0.0000	0.0000	0.0000	0.0000	0.0000	0.0000
C6+	0.0000	0.0000	0.0000	0.0013	0.0014	0.0000	0.0000	0.0000
N_2	0.5600	0.5062	0.4748	0.4619	0.4657	0.4668	0.4733	0.4500
CO_2	0.1521	1.1862	1.0520	2.5507	1.4598	1.4893	1.3765	1.0723
Sum	100.0000	100.0000	100.0000	100.0000	100.0000	100.0000	100.0000	100.0000

Table 2.8: Mixture compositions and initial conditions of the tests conducted with the rough tube (Botros et al., 2010b).

	Reference-Rough	Test 1-Rough	Test 2-Rough	Test 3-Rough	Test 4-Rough	Test 4R-Rough	Test 5-Rough	Test 6-Rough
Pi (kPa-a)	18,438	18,107	9,841	14,419	19,837	19,708	21,237	21,451
Ti (°C)	17	20.30	21.10	10.95	11.37	11.15	−4.50	−10.19
	Mole %							
	Dry	Medium rich			Rich			Ultra-rich
C1	97.27541	87.62877	84.98462	79.93636	82.30301	81.86064	83.75912	78.75135
C2	1.436511	6.62011	8.461556	7.678089	6.867478	7.070905	6.394818	10.47236
C3	0.266926	3.133182	3.909766	7.216741	7.133507	7.144299	6.47354	5.990389
iC4	0.032076	0.265379	0.370734	0.895606	0.752414	0.800358	0.667776	1.392736
nC4	0.043216	0.557908	0.879323	1.209697	0.985874	1.039705	0.994521	1.863462
iC5	0.010148	0.008298	0.010009	0.006298	0.006679	0.007647	0.007704	0.005962
nC5	0.007487	0.005409	0.007329	0.004462	0.004745	0.005597	0.005497	0.004345
C6+	0.009185	0.011607	0.008428	0.006158	0.00637	0.007098	0.007268	0.005953
N_2	0.555543	0.627095	0.487948	0.463562	0.474295	0.46962	0.480017	0.44478
CO_2	0.363498	1.142273	0.880287	2.583022	1.465631	1.594125	1.209743	1.068667
Sum	100.0000	100.0000	100.0000	100.0000	100.0000	100.0000	100.0000	100.0000

Figures 2.22 and 2.23 show the comparisons of GASDECOM pressure versus decompression wave speed predictions against the measured data for Test 1 in the smooth and rough tubes respectively. Referring to figure 2.22, it can be seen that good agreement is obtained between GASDECOM's predictions and experimental data.

The differences in the initial conditions and composition for the rough tube test (figure 2.23) resulted in a marked difference in the observed phase transition pressure. The predicted phase transition pressure of ca. 7 MPa-a is significantly lower than the experimentally observed value of ca. 7.8 MPa-a. In practice, this would result in an under-prediction of the pipeline toughness required to arrest a fracture.

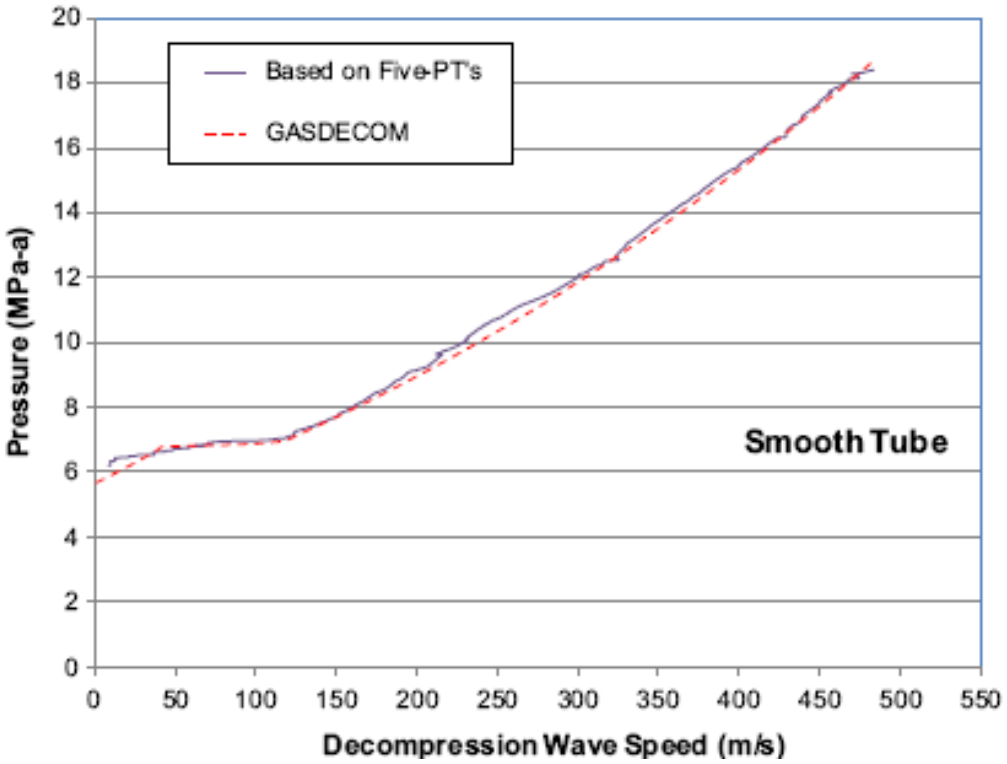

Figure 2.22: Measured and calculated decompression wave speed results of Test 1 for a medium rich gas mixture from an initial pressure = 18.1 MPa-a (Botros et al., 2010b).

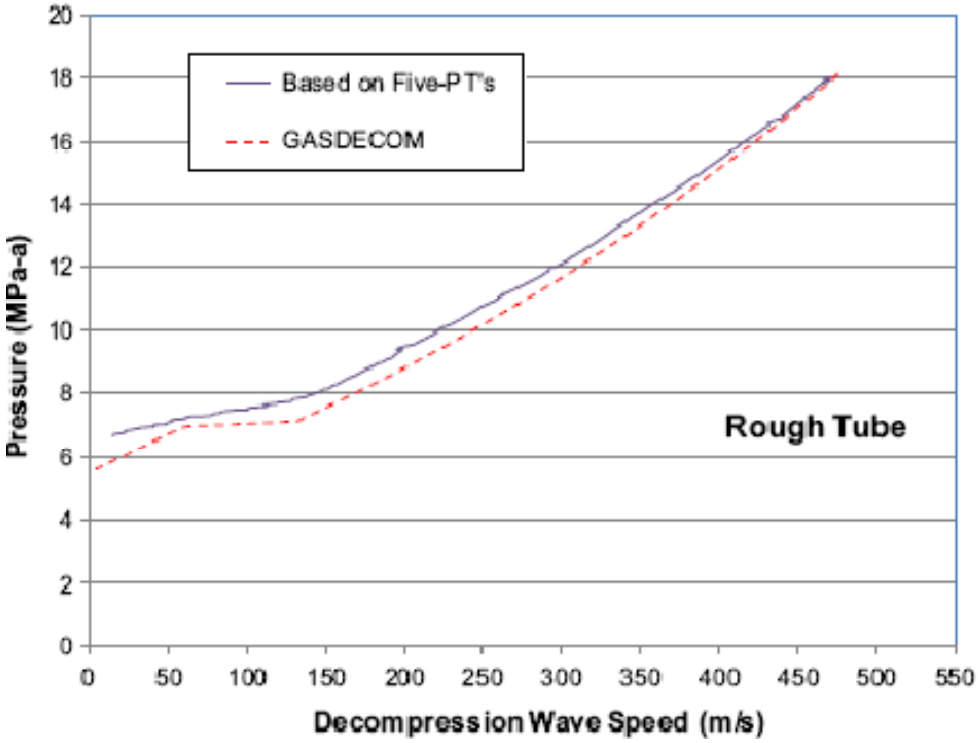

Figure 2.23: Measured and calculated decompression wave speed results of Test 1 for a medium rich gas mixture from an initial pressure = 18.1 MPa-a (Botros et al., 2010b).

To account for pipe friction, Botros et al. (2010b) applied a simple perturbation method to include a friction related term in their expression for the decompression wave speed. Both this model, named Rough GASDECOM and the original GASDECOM were used as a basis for the design of four hypothetical pipelines in terms of resistance to fracture propagation. A comparison of the predicted decompression wave speed versus pressure data showed that accounting for friction required an increase of up to 19 % in toughness in order to arrest a fracture.

Given the above, it is clear that GASDECOM is restricted to the prediction of the initial pressure drop along the pipeline. Moreover the model neglects fluid/wall heat transfer and does not account for the effect of friction at a fundamental level through coupling with an energy conservation equation (Mahgerefteh et al. (2006) or see equation 3.3, chapter 3).

2.6 Terenzi (2005)

Terenzi (2005) presented Machnet (Machnet_Real) developed to investigate the impact of real gas behaviour on the interaction between pipeline decompression and ductile fracture propagation. Homogeneous equilibrium is assumed between gas and liquid. Thermodynamic properties, such as the void fraction, are determined by linear interpolation using a look up table with the density and specific internal energy as independent variables. Fluid/wall heat transfer is calculated by solving the Fourier equation in cylindrical geometry between the external environment and the fluid. The Colebrook-White correlation (Keenan and Nuemann, 1946) is used to account for frictional effects along the pipeline. The resulting governing system of equations is resolved using Roe's (1981) approximate Riemann solver in an explicit Finite Volume Godunov-type scheme.

Terenzi (2005) also developed a model for the decompression of a pipeline transporting an ideal gas (Machnet_Ideal) by assuming zero heat transfer and frictionless flow to derive a similarity solution for the pressure at the exit plane and the speed of the rarefaction wave.

Machnet_Ideal and Machnet_Real's predictions were tested by comparison with the results of tests conducted at the Foothills Pipelines Northern Alberta Burst Test Facility (NABT) (Picard and Bishnoi, 1988). These tests involved the release of natural gas (ca. 85 % methane) from pipelines with respective pipeline internal diameters, pressures and temperatures in the ranges of 1219 to 1422 mm, 7.5 to 8.7 MPa and -18 to +18 ^{o}C.

Figure 2.24 shows the variation of the ratio of pressure to initial pressure and void fraction with expansion wave velocity. The simulated results obtained from Machnet_Ideal and Machnet_Real utilising the PR and Soave-Redlich-Kwong (SRK) Equations of State were compared with experimental data. As may be observed, Machnet_Real coupled with either the PR or SRK shows similar behaviour, while Machnet_Ideal over-predicts the wave speed throughout the decompression process. Additionally, the fluid void fraction falls slightly from unity when the pressure ratio

reaches ca. 0.55. At this point Machnet_Real predictions using the PR and SRK Equations of State begin to diverge from the experimental data.

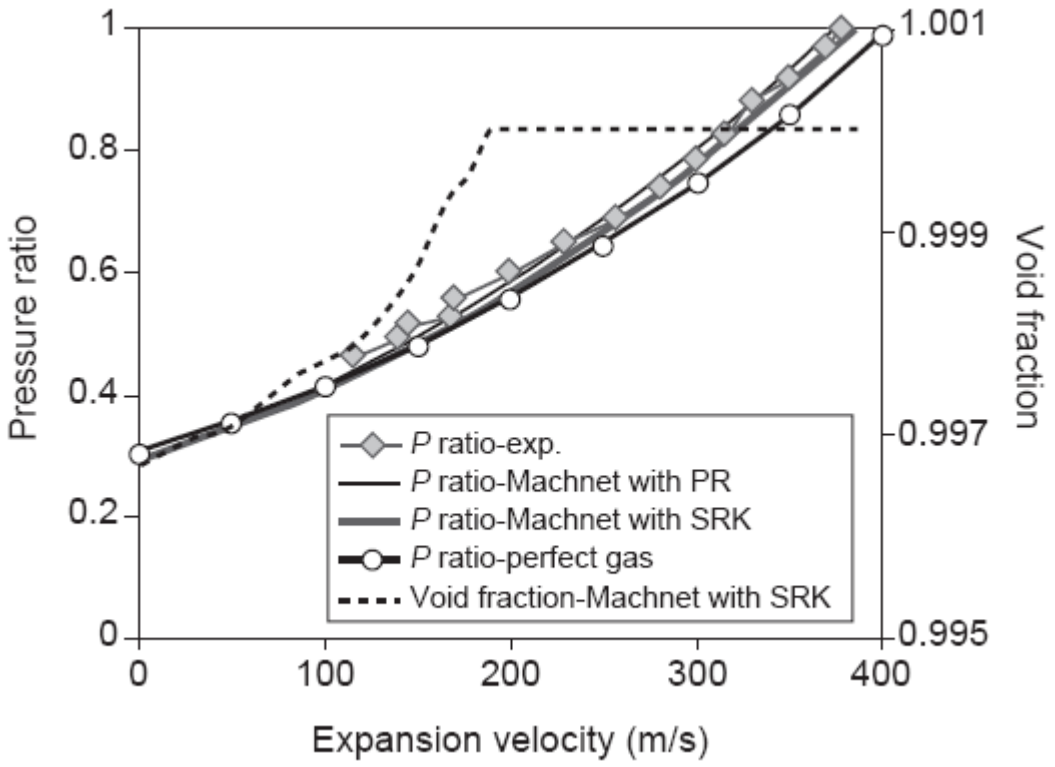

Figure 2.24: Measured and calculated decompression wave speed results of NABT Test 5 (Picard and Bishnoi, 1988).

Based on the above data it is clear that the fluid flow model is capable of simulating the decompression wave initiated upon pipeline failure. However, the authors did not a present a similar comparison relating to the release characteristics. As such, the efficacy of the model with regards to the prediction of outflow cannot be verified.

2.7 Popescu (2009)

Popescu (2009) developed a model for analysing the high-pressure release from a pipeline during ductile fracture propagation. The model separates the pipeline into two sections:

1. Ahead of the crack tip (i.e. remaining enclosed inventory within the pipeline)
2. Behind the moving crack.

For the portion of the pipeline ahead of the crack tip, one-dimensional conservation equations for mass, momentum and energy are applied. The model accounts for friction through the inclusion of a viscous stress term and couples the conservation equations with the ideal gas Equation of State.

Behind the crack the flow is assumed to be negligible in the axial direction and that all flow is through the crack tip opening. In this region the continuity equation is integrated over the release plane and is combined with the ideal gas choked flow equation (Greenshields et al., 2000).

The model for the flow ahead of the crack tip was validated using the experimental results from two decompression tests. The first test was performed using a 11.5 m pipeline containing methane. The second test used a 34.5 m pipeline containing hydrogen. Both pipelines were instrumented with pressure sensors at 1 and 3 m from the middle of the pipeline. No details about the failure type, ambient conditions, feed temperature or pipeline characteristics were given by Popescu (2009).

Figures 2.25 and 2.26 show the comparisons of the predicted and experimental pressure transients for test 1 (11.5 m) and test 2 (34.5 m) respectively. The figures show that the model gives good agreement with experimental data following pipeline failure. However, the speed at which the front of the decompression wave arrives at the probe locations is slightly over-predicted. This is indicated by the faster pressure drop from the initial value.

Although good agreement is obtained in the pressure profiles presented, the assumption of ideal gas behaviour means that the model is not applicable to non-ideal or two-phase mixtures. Further, this assumption leads to an incorrect prediction of the speed of sound which is essential for the tracking of the expansion wave. In addition, the performance of the internal flow model is uncertain with respect to long pipelines, where it is likely that heat transfer and friction may be significant.

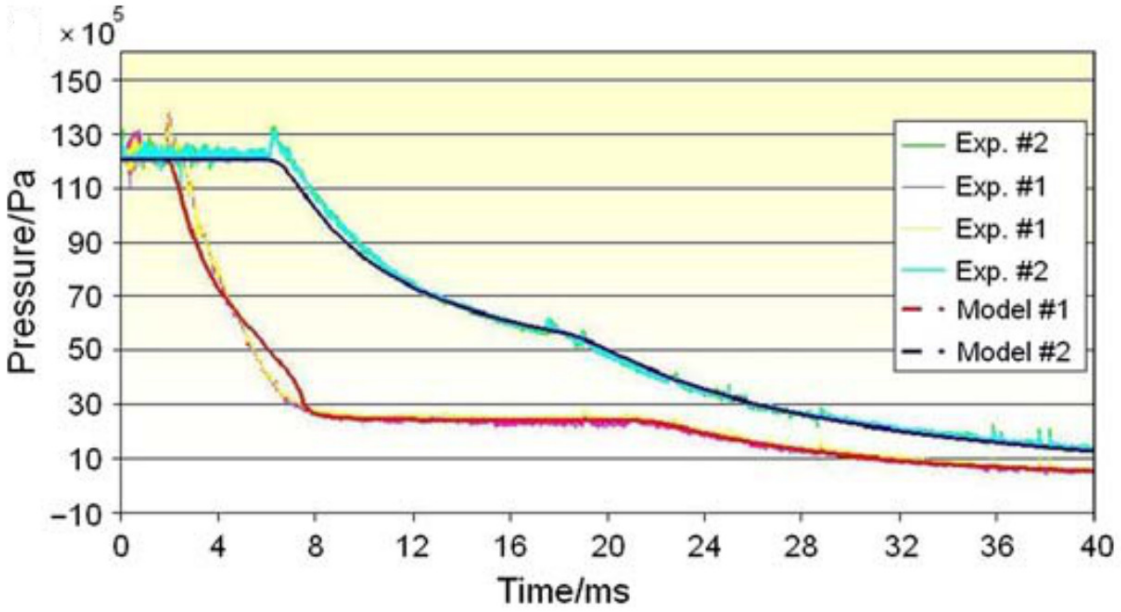

Figure 2.25: Comparison of the variation of pressure with time between predicted and experimental for a 11.5 m pipeline containing methane (Popescu, 2009).

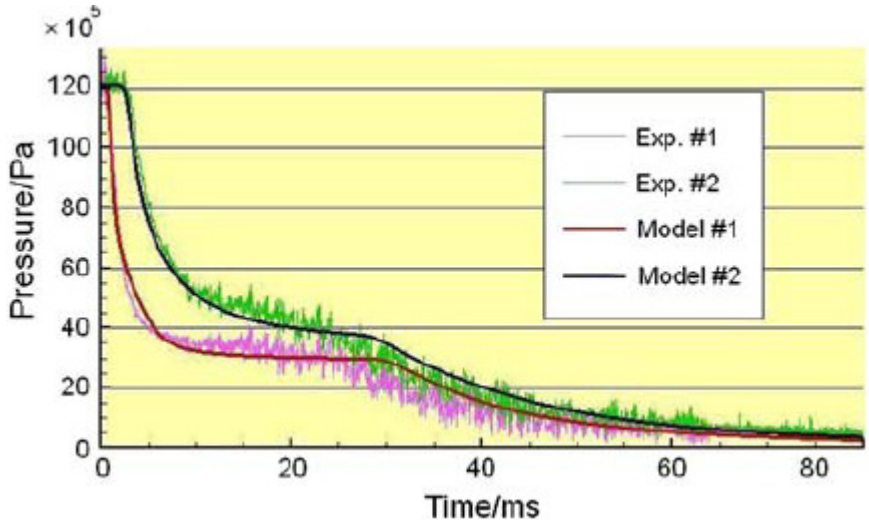

Figure 2.26: Comparison of the variation of pressure with time between predicted and experimental for a 34.5 m pipeline containing hydrogen (Popescu, 2009).

2.8 Makino et al. (2001)

Makino et al. (2001) presented two models to calculate the two-phase decompression curves for natural gas. The first combined the British Gas Model (DECAY) (Jones and Gough, 1981) and the BWRS Equation of State (Starling, 1973). The second model solves the one-dimensional compressible flow equations using a Flux Difference Splitting (FDS) scheme coupled with the BWRS Equation of State. Both models assume homogeneous equilibrium between gas and liquid droplets and neglect heat transfer and frictional effects.

The simulation results of the two models were compared for the decompression of test C2 (High-Strength Line Pipe (HLP) Committee) (Sugie et al, 1987). In this experiment an instrumented 163 m long, 1182 mm i.d. natural gas (ca. 90 % methane) pipeline was depressurised following the detonation of an explosive charge at the pipeline midpoint.

Figure 2.27 shows a comparison of the pressure against decompression velocity using the two models. As it may be observed both predictions are in accord, slightly deviating near the end of the depressurisation process.

Neither model predictions were compared with experimental data. As such their efficacy cannot be verified.

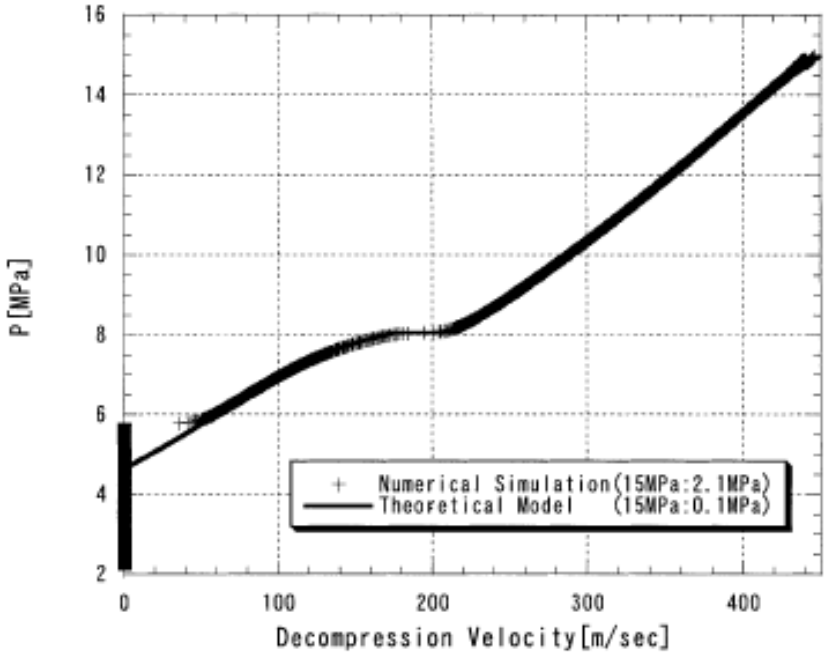

Figure 2.27: Comparison of the variation of pressure with decompression wave speed between numerical and the British Gas Decay based model (Makino et al., 2001) for the C2 test.

2.9 Concluding Remarks

Based on the above review, it's clear that considerable progress has been made in improving the model accuracy and the reduction of computational runtime in simulating outflow following pressurised pipeline failure. However, there exists significant scope for improving the pipeline failure models reported in the open literature.

For example, of the models presented, the homogenous equilibrium based models by Mahgerefteh et al. (1999) and Atti (2006) are the most robust with the latter performing best in terms of accuracy and computational runtime when compared to experimental data (Atti, 2006). Nonetheless, when simulating the complete blowdown of long pipelines (>100 km) the long computational runtimes make the use of these models in the design of pipelines impracticable. Hence, ways of further reducing the computational runtime need to be investigated.

Given the catastrophic consequences of running ductile fractures and the important role that the fluid pressure plays in their propagation it is perhaps unsurprising that a number of studies have focussed on pipeline decompression behaviour rather than outflow. However, the majority of models developed neglect both heat transfer and frictional effects on the expansion wave initiated by the sudden exposure to the ambient pressure. As the work of Botros et al. (2010b) highlights, these non-isentropic effects can have a dramatic impact on whether a crack propagates or arrests.

Additionally, those models that do account for non-isentropic effects, for example Makino et al. (2001), Popescu (2009) and Terenzi (2005), are limited to the analysis of fixed length pipelines. In practice the propagation of a fracture will rapidly expose an increasing amount of the pipeline inventory to the ambient atmosphere. Neglecting the increased pressure drop may result in an over-prediction of the final crack length.

Chapter 3: Background Theory for Modelling Transient Flow in Pipelines

3.1 Introduction

A robust mathematical model for predicting the transient outflow from a pressurised pipeline following its failure must account for the following:

- The rapid fluid transients, through the derivation of equations governing conservation laws for mass, momentum and energy allowing for single or two-phase flows
- The thermo-physical behaviour of the fluid mixture through the application of an appropriate Equation of State (EoS) and hydrodynamic relations
- Interaction of the fluid with the enclosing pipe wall, in the form of frictional effects and heat transfer with the ambient atmosphere.

Once the governing physical model has been derived, the computational time required to resolve the system of equations should be minimised. The dominant characteristics of the particular flow may mean that some terms may have a negligible effect on the final solution and so may be safely ignored. Following such simplification the resulting system of conservation equations may be linear, quasi-linear or non-linear, parabolic or hyperbolic in nature. As a consequence, the method of numerical resolution must be selected appropriately.

This chapter presents the governing model assumptions and the mathematical formulation of the outflow model developed in this study taking account of all of the above phenomena.

3.2. Model Assumptions

The main assumptions made in the development of the pipeline outflow model study are:

- Steady state flow exists prior to rupture
- The flow is predominantly one-dimensional, that is the rate of change of the flow variables normal to the axial direction is negligible relative to those along the axial direction. However, in the case of a puncture in the pipe wall, the flow is resolved in the normal and axial directions in the proximity of the orifice
- In the case of full bore rupture (FBR), the Homogeneous Equilibrium Model (HEM) is applicable where the constituent phases are in both thermal (i.e. same temperature) and mechanical (i.e. same velocity) equilibrium. This is based on previous studies by Chen et al. (1995) and Mahgerefteh et al. (1999) showing good agreement between HEM based outflow predictions against real data recorded following the full bore rupture of long pipelines (>100 m) containing flashing liquids and condensable gas mixtures
- Each pipeline segment is rigidly clamped, of uniform cross sectional area, pipelines in a network are assumed to be rigidly clamped, possess inelastic walls, and are time and space invariant with respect to cross-sectional area.

3.3 Formulation of the Governing Conservation Equations

The governing equations for generalised unsteady one-dimensional fluid flow may be expressed in terms of a combination of several primitive parameters e.g. pressure, entropy, density. As described in the previous chapter, Oke et al. (2003) determined that the pressure, enthalpy and fluid velocity combination required the least computational runtime for their numerical solution as well as producing the most accurate predictions when compared to real pipeline rupture data. The corresponding mass, momentum and energy conservation are respectively given by (Oke et al., 2003):

$$(\rho T + \varphi)\left(\frac{\partial P}{\partial t} + u\frac{\partial P}{\partial x}\right) - \rho\varphi\left(\frac{\partial h}{\partial t} + u\frac{\partial h}{\partial x}\right) + \rho^2 a^2 T\frac{\partial u}{\partial x} = 0 \quad \textbf{(3.1)}$$

$$\rho\frac{\partial u}{\partial t} + \rho u\frac{\partial u}{\partial x} + \frac{\partial P}{\partial x} = \beta_x - \rho g\sin(\theta) \quad \textbf{(3.2)}$$

$$\rho\left(\frac{\partial h}{\partial t} + u\frac{\partial h}{\partial x}\right) - \left(\frac{\partial P}{\partial t} + u\frac{\partial P}{\partial x}\right) = Q_h - u\beta_x \quad \textbf{(3.3)}$$

Where, ρ, u, P, h, T, a and φ are the density, velocity, pressure, specific enthalpy, temperature, speed of sound and isochoric thermodynamic function (see section 3.5.3) of the homogeneous fluid as function of time, t, and space, x. Q_h and θ are the heat transferred through the pipe wall to the fluid and the angle of inclination of the pipeline to the horizontal respectively. β_x is the frictional force term given by:

$$\beta_x = -\frac{2\rho u|u|f_w}{D} \quad \textbf{(3.4)}$$

Where, f_w is the Fanning friction factor and D is the pipeline diameter. In section 3.8, the system of equations comprising (3.1) to (3.3) is shown to be hyperbolic (Prasad and Ravindran, 1985).

3.4 Cubic Equations of State

In this study, the Peng-Robinson EoS (PR EoS) (Peng and Robinson, 1976) and the Modified Peng-Robinson (MPR EoS) (Wu and Chen, 1997) are employed for obtaining the relevant fluid thermodynamic and phase equilibrium data. The PR EoS equation has been widely applied to high-pressure hydrocarbon mixtures producing good agreement with real data (see for example Walas, 1985). While the MPR EoS has been shown (Mahgerefteh et al., 2008) to produce generally good agreement with the well-established but computationally demanding GERG-2004 EoS (Kunz et al., 2007) for CO_2 and its mixtures.

The PR EoS (Walas, 1985) and MPR EoS (Wu and Chen, 1997) are respectively given by:

$$P = \frac{RT}{V - b_V} - \frac{a_V \alpha}{V^2 + 2b_V V - (b_V)^2} \quad \textbf{(3.5)}$$

$$P = \frac{RT}{V - b_V} - \frac{a_V \alpha}{V(V + b_V) + 0.645 b_V (V - b_V)} \quad \textbf{(3.6)}$$

Where:

$$a_V = 0.45724 \frac{R^2 T_c^2}{P_c^2} \quad \textbf{(3.7)}$$

$$b_V = 0.07780 \frac{RT_c}{P_c} \quad \textbf{(3.8)}$$

For mixtures:

$$a_V \alpha = \sum \sum y_i y_j (a_V \alpha)_{ij} \quad \textbf{(3.9)}$$

$$(a_V \alpha)_{ij} = \left(1 - K_{ij}\right) \sqrt{(a_V \alpha)_i (a_V \alpha)_j} \quad \textbf{(3.10)}$$

$$b_V = \sum y_i b_{V\,i} \quad \textbf{(3.11)}$$

Where, P_c, T_c and V are the critical pressure (kN/m^2), critical temperature (K) and molar volume (m^3/kmol) respectively. In addition, R and α are the universal gas constant (kJ/(kmol-K)) and alpha function, while K_{ij}, y_i and y_j are the binary interaction parameter and component mole fractions respectively.

Given the fluid molecular weight (M_W) (kg/kmol), the fluid density is given by:

$$\rho = \frac{M_W}{V} \quad \textbf{(3.12)}$$

The form of the generalised alpha function used in conjunction with both the PR and MPR EoS is that given by Soave (1972):

$$\alpha = \left(1 + \kappa \left(\frac{T}{T_c}\right)^{0.5}\right)^2 \quad \textbf{(3.13)}$$

Where:

$$\kappa = 0.48 + 1.574\omega - 0.175\omega^2 \quad \textbf{(3.14)}$$

ω is the accentric factor.

3.5 Hydrodynamic and Thermodynamic Relations for the HEM

The following section presents the main equations and correlations employed for determining the two-phase mixture density, speed of sound, the heat transferred to the fluid (Q_h) and the pertinent hydrodynamic relations.

3.5.1 Two-phase Mixture Density

Based on the HEM assumption the pseudo-mixture density is given by:

$$\rho = \frac{\rho_g \rho_l}{\rho_g(1-\chi) + \rho_l \chi} \quad \textbf{(3.15)}$$

Where ρ_l and ρ_g are the liquid and gas densities in turn determined from:

$$\rho_g = \frac{PM_g}{Z_g RT} \quad \textbf{(3.16)}$$

$$\rho_l = \frac{PM_l}{Z_l RT} \quad \textbf{(3.17)}$$

χ is the fluid quality, defined as the mass of vapour per unit mass of the bulk fluid. Z is the fluid compressibility.

3.5.2 Single and Two-phase Speed of Sound (Atti, 2006)

For single-phase real fluids, the speed of sound, a in the fluid may be expressed analytically as (Picard and Bishnoi, 1987):

$$a^2 = \frac{\gamma}{\kappa\rho} \quad \textbf{(3.18)}$$

Where, γ is the ratio of specific heats, and κ is the isothermal coefficient of volumetric expansion both respectively given by (Walas, 1985):

$$\gamma = \frac{C_P}{C_V} \tag{3.19}$$

$$\kappa = -\rho\left(\frac{\partial V}{\partial P}\right)_T \tag{3.20}$$

Where, C_P and C_V are the specific heats at constant pressure and volume respectively. V is the specific volume of the fluid and the term $\left(\frac{\partial V}{\partial P}\right)_T$ in equation (3.20) can be obtained by differentiating the PR and MPR EoS respectively (equation (3.5) and (3.6) resp.):

$$\left(\frac{\partial V}{\partial P}\right)_T = \left(\frac{-RT}{(V-b_V)^2} - \frac{2a_V\alpha(V+b_V)}{(V^2+2b_VV-(b_V)^2)^2}\right)^{-1} \tag{3.21}$$

$$\left(\frac{\partial V}{\partial P}\right)_T = \left(\frac{-RT}{(V-b_V)^2} - \frac{a_V\alpha(2V+1.645b_V)}{\left(V(V+b_V)+0.645b_V(V-b_V)\right)^2}\right)^{-1} \tag{3.22}$$

For two-phase flows, equation (3.18) is evaluated numerically (Mahgerefteh et al., 2000):

$$a^2 = \left(\frac{\Delta P}{\rho(T,P)-\rho(T^*,P-\Delta P)}\right)_s \tag{3.23}$$

Where, the subscript, s, denotes a constant entropy condition and ΔP denotes an incremental change in the fluid pressure ($\Delta P = 1\times10^{-6}$ bar). T^* represents the corresponding fluid temperature obtained from a pressure-entropy flash at the incremented pressure.

3.5.3 Evaluation of the Thermodynamic Function φ

The isochoric thermodynamic function, φ in equation (3.1), for single-phase fluids is given by (Picard and Bishnoi, 1987):

$$\varphi = \left(\frac{\partial P}{\partial s}\right)_\rho = \frac{\rho\xi T a^2}{C_P} \tag{3.24}$$

Where, ξ is the isobaric coefficient of volumetric expansion = $\frac{1}{V}\left(\frac{\partial V}{\partial T}\right)_P$. In the case of two-phase flows φ is calculated numerically in the following manner. Given that:

$$\varphi = \left(\frac{\partial P}{\partial s}\right)_\rho \overset{\text{def}}{=} \left(\frac{\partial P}{\partial s}\right)_V \tag{3.25}$$

Using one of Maxwell's relations (Walas, 1985):

$$\left(\frac{\partial P}{\partial s}\right)_\rho = -\left(\frac{\partial T}{\partial V}\right)_S \tag{3.26}$$

Since $V = {}^1/_\rho$:

$$\frac{dV}{d\rho} = -\frac{1}{\rho^2} \tag{3.27}$$

Equation (3.26) becomes:

$$\left(\frac{\partial P}{\partial s}\right)_\rho = \rho^2\left(\frac{\partial T}{\partial \rho}\right)_S \tag{3.28}$$

Hence, from equation (3.25):

$$\varphi = \rho^2\left(\frac{\partial T}{\partial \rho}\right)_S = \rho^2\left(\frac{\Delta T}{\Delta \rho}\right)_S \tag{3.29}$$

Equation (3.29) may then be solved using the same numerical algorithm as that used for the solution of equation (3.23).

3.5.4 Fanning Friction Factor, f_w

The fanning friction factor, f_w, is required for calculating the frictional force in the momentum equation (equation (3.4)). For transitional and turbulent flows in rough pipes f_w is determined from Chen (1979):

$$\frac{1}{\sqrt{f_w}} = 3.48 - 1.7372\ln\left(\frac{\varepsilon}{r_{in}} - \frac{16.2446}{Re}\ln A\right) \tag{3.30}$$

Where:

$$A = \frac{\left(\frac{\varepsilon}{r_{in}}\right)^{1.0198}}{6.0983} + \left(\frac{7.149}{Re}\right)^{0.8981} \tag{3.31}$$

ε, r_{in} and Re represent the pipe roughness, pipe inner radius and Reynolds' number respectively.

For turbulent flow in smooth pipelines Rohsenow et al. (1998) recommend the following correlation proposed by Techo (1965) for determining f_w by:

$$\frac{1}{\sqrt{f_w}} = 1.7372 \ln \frac{Re}{1.964 \ln Re - 3.8215} \quad \textbf{(3.32)}$$

According to Rohsenow et al. (1998), the above correlation gives predictions within 2 % of experimental data.

The fanning friction factor for laminar fully developed flow is given by (Rohsenow et al., 1998):

$$f_W = \frac{16}{Re} \quad \textbf{(3.33)}$$

3.5.5 Thermal Conductivity and Viscosity Calculations

The vapour thermal conductivity and viscosity needed for determining the Nusselt, Reynolds and Prandtl numbers are calculated using the principle of corresponding states using methane as a reference fluid method as described by Ely and Hanley (1981, 1983) for non-polar gases. It is claimed (Assael et al., 1996) that Ely and Hanley's (1981) method is one of the few schemes that is able to predict the viscosity and thermal conductivity for a wide range of non-polar components with reasonable accuracy.

In the case of liquid mixtures containing alkanes, viscosities and thermal conductivities are determined from a semi-empirical scheme presented by Assael et al. (1996). The range of applicability of the scheme is between 280 K to 400 K and pressures from saturation up to 990 atm where the uncertainty in the predictions is less than 5 % (Assael et al., 1996).

For mixtures containing two-phase fluids, correlations proposed by the Design Institute for Physical Property Data (DIPPR) (Daubert and Danner, 1990) are applied due to their

claimed accuracy. For two-phase fluids, the mixture thermal conductivity and viscosity is given by:

$$\frac{1}{c_m} = \frac{\chi}{c_g} + \frac{1-\chi}{c_l} \quad \textbf{(3.34)}$$

Where, c_m is the mixture property to be determined and c_g and c_l are the gas and liquid properties respectively.

3.6 Fluid/Wall Heat Transfer (Atti, 2006)

In the case of flow in pipelines, heat transfer to the fluid during flow is entirely due to exchange with the enclosing wall. However, except in the case of a perfectly insulated pipeline, this will also be influenced by wall and ambient properties/conditions.

Newton's cooling law (Fairuzov, 1998; Mahgerefteh et al., 1999) is commonly employed for determining the heat transferred to a fluid flowing in a pipe. It is given by:

$$Q_h = \frac{4}{D_{in}} U_h \left(T_{amb} - T_f\right) \quad \textbf{(3.35)}$$

Where U_h, D_{in}, T_{amb} and T_f denote the overall heat transfer coefficient, the pipeline inner diameter, the ambient and fluid temperatures respectively.

The transient energy balance used by Atti (2006) is employed in this study to model the transient heat transfer process at the fluid/pipe wall interface. Full details of the model are given in the same publication hence only a brief account is given here.

The method applies an energy balance out across the fluid-wall-ambient surfaces based on a lumped body approach (Myers, 1987). The wall temperatures are then updated for a given time step, thus estimating the heat input to the fluid in the next time interval. Figure 3.1 shows a schematic representation of the important heat transfer parameters.

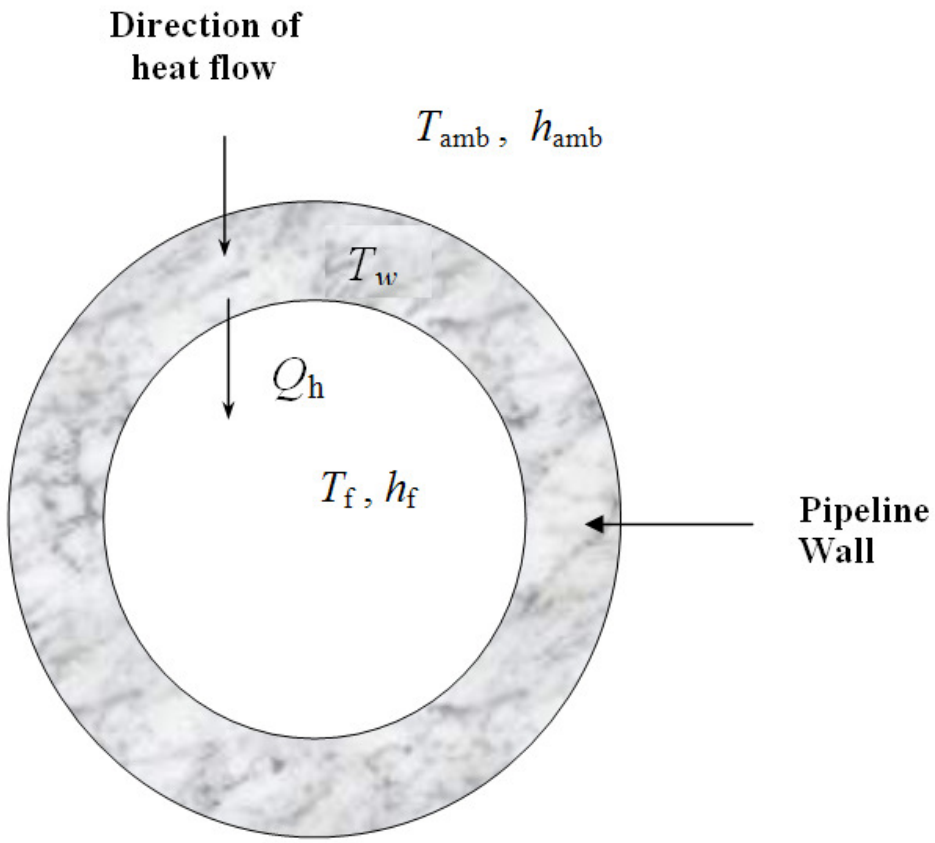

Figure 3.1: Schematic representation of the heat flow across the cross-section of a pipeline wall based on the lumped body approach (Atti, 2006).

Where T_{amb}, h_{amb} and T_w respectively represent the ambient temperature, heat transfer coefficient of the ambient and wall temperature. T_f, h_f and Q_h respectively represent the fluid's temperature, fluid heat transfer coefficient and the quantity of heat transferred to the fluid.

The following assumptions are made in the lumped body approach:

- The heat transfer coefficient between the pipe wall and either the ambient (h_{amb}) or the flowing fluid (h_f) is constant over a given time step and are determined from the properties at the beginning of the time step
- The wall density (ρ_w), specific heat capacity (C_{pw}) and thermal conductivity (κ_w) are constant with respect to time and space
- The ambient and fluid temperature employed in the energy balance are constant over a given time step

- Heat transfer occurs predominantly in the radial direction across the pipeline wall. Heat flow from conduction in the longitudinal and tangential directions inside the pipe wall is neglected.

Applying Newton's cooling law, the heat transferred to the fluid (Q_h) in a given time step may be approximated by (Atti, 2006):

$$Q_h = \frac{4}{D_{in}} h_f (T_w - T_f) \quad \textbf{(3.36)}$$

3.7 The Steady State Isothermal Flow Model (Oke, 2004)

In this section the steady state isothermal flow model developed by Oke (2004) is presented. The model is based on the one-dimensional continuity and momentum equations presented in section 3.3.

From equation (3.1), the steady state expression is obtained by setting the time derivatives to zero and can be written as:

$$\frac{\partial \rho u}{\partial x} = 0 \quad \textbf{(3.37)}$$

Integrating equation (3.37), gives (Oke, 2004):

$$\rho_i u_i = \rho_{i-1} u_{i-1} \quad \textbf{(3.38)}$$

Where the subscripts i-1 and i respectively represent the penultimate and current grid point under consideration. Equation (3.38) is the governing equation for mass conservation at steady state for flow in a uni-diameter pipeline.

From equation (3.2), the steady state momentum equation in one-dimension can be expressed as:

$$\rho u \frac{du}{dx} = -\frac{dP}{dx} - \rho g \sin(\theta) + \beta \quad \textbf{(3.39)}$$

Where, the steady state frictional force term β is given by equation (3.4). The correlations required in calculating the fanning wall friction factor (f_W) have already been discussed in section 3.5.4.

Substituting the expression for β into equation (3.39) and rearranging gives (Oke, 2004):

$$\rho dP - (\rho u)^2 \frac{d\rho}{\rho} = -\left(\frac{2f_w(\rho u)^2}{D} + \rho^2 g \sin(\theta)\right) dx \quad \textbf{(3.40)}$$

The above equation can be expressed as

$$\rho dP + K_1 \frac{d\rho}{\rho} = (K_2 + \rho^2 K_3) dx \quad \textbf{(3.41)}$$

Where,

$$K_1 = -(\rho u)^2 \quad \textbf{(3.42)}$$

$$K_2 = -\frac{2f_w(\rho u)^2}{D} \quad \textbf{(3.43)}$$

$$K_3 = -g \sin(\theta) \quad \textbf{(3.44)}$$

Rearranging equation (3.41) and taking the limits results in (Oke, 2004):

$$\int_{P_{i-1}}^{P_i} \frac{\rho}{(K_2 + \rho^2 K_3)} dP + K_1 \int_{\rho_{i-1}}^{\rho_i} \frac{\rho}{\rho(K_2 + \rho^2 K_3)} d\rho = \int_{x_{i-1}}^{x_i} dx \quad \textbf{(3.45)}$$

The final form of equation (3.45) after resolving the integrals on the LHS is given by (Oke, 2004):

$$\frac{1}{2}\left[\frac{\rho}{(K_2 + \rho^2 K_3)_{P_i}} + \frac{\rho}{(K_2 + \rho^2 K_3)_{P_{i-1}}}\right] + \frac{K_1}{2K_2}\left[2ln\left(\frac{\rho_i}{\rho_{i-1}}\right) - ln\left(\frac{(K_2 + \rho_i^2 K_3)}{(K_2 + \rho_{i-1}^2 K_3)}\right)\right] = x_i - x_{i-1} \quad \textbf{(3.46)}$$

The following outlines the algorithm used for calculating the isothermal steady state drop (as summarised by Denton (2009)):

1. Collate data at pipeline inlet such as fluid pressure, temperature, velocity, etc.
2. Divide the pipeline into sections (grids) with the distance between the grids being $\Delta = x_i - x_{i-1}$
3. Guess the downstream pressure at the next grid point i.e. P_i
4. In conjunction with an Equation of State, evaluate the expression on the LHS of equation (3.46)
5. If equation (3.46) is satisfied, then the guessed downstream pressure is adopted as the solution. The fluid velocity u_i can then be obtained by applying equation (3.38). If the equation is not satisfied, go back to step 3 and update the guessed P_i
6. Update the flow properties at this grid point and calculate the pressure drop at the next grid using steps 3-5 until the variables at the final grid is calculated.

3.8 Hyperbolicity of the Governing Conservation Equations

The partial differential equations (PDEs) pertaining to the conservation of mass, momentum and energy coupled with an appropriate EoS constitute a system of equations that are essentially the Euler equations with additional terms due to friction and heat transfer in the momentum and energy equations respectively.

The selection of an appropriate numerical technique for the solution of the governing partial differential equations is dependent on their mathematical nature. It is shown below that the system of conservation equations are quasilinear and hyperbolic.

A partial differential equation is said to be quasilinear if all derivatives of the dependent function $u(x,t)$ are linear, while their corresponding coefficients may contain non-linear terms (Prasad and Ravindran, 1985), i.e. it is in the following form:

$$a(x,t,u)u_t + b(x,t,u)u_x = c(x,t,u) \quad \textbf{(3.47)}$$

Where, u_t and u_x are the partial derivatives of the function u in terms of t and x respectively. The system of conservation, equations (3.1), (3.2) and (3.3) can be written as:

$$(\rho T + \varphi)\left(\frac{\partial P}{\partial t} + u\frac{\partial P}{\partial x}\right) - \rho\varphi\left(\frac{\partial h}{\partial t} + u\frac{\partial h}{\partial x}\right) + \rho^2 a^2 T\frac{\partial u}{\partial x} = 0 \quad \textbf{(3.48)}$$

$$\rho\left(\frac{\partial u}{\partial t} + u\frac{\partial u}{\partial x}\right) + \frac{\partial P}{\partial x} = \alpha \quad \textbf{(3.49)}$$

$$\rho\left(\frac{\partial h}{\partial t} + u\frac{\partial h}{\partial x}\right) - \left(\frac{\partial P}{\partial t} + u\frac{\partial P}{\partial x}\right) = \psi \quad \textbf{(3.50)}$$

Where:

$$\alpha = \beta_x - \rho g \sin(\theta) \quad \textbf{(3.51)}$$

And:

$$\psi = Q_h - u\beta_x \quad \textbf{(3.52)}$$

The conservation equations represented by equations (3.48) to (3.50) are clearly linear in the partial derivative terms. Furthermore, terms that are coefficients of the partial derivatives, such as the density (ρ) or the fluid speed of sound (a) are nonlinear functions of P, h and u. The governing equations are therefore quasilinear in structure.

The conservation equations (i.e. equations (3.48) to (3.50)) may be written in the general form:

$$A\frac{\partial U}{\partial t} + B\frac{\partial U}{\partial x} = C \quad \textbf{(3.53)}$$

Where, A, U, B and C are given by:

$$U = \begin{pmatrix} P \\ h \\ u \end{pmatrix} \quad \textbf{(3.54)}$$

$$A = \begin{pmatrix} \rho T + \varphi & -\rho\varphi & 0 \\ 0 & 0 & \rho \\ -1 & \rho & 0 \end{pmatrix} \quad \textbf{(3.55)}$$

$$B = \begin{pmatrix} (\rho T + \varphi)u & -\rho\varphi u & \rho^2 a^2 T \\ 1 & 0 & \rho u \\ -u & \rho u & 0 \end{pmatrix} \quad \textbf{(3.56)}$$

$$C = \begin{pmatrix} 0 \\ \alpha \\ \psi \end{pmatrix} \quad \textbf{(3.57)}$$

A system of partial differential equations as given by equation (3.53) is said to be hyperbolic if the eigenvalues, satisfying equation (3.58) given below, are real and distinct (Prasad and Ravindran, 1985):

$$|B - \lambda A| = 0 \quad \textbf{(3.58)}$$

Thus, for the conservation equations, the above equation may be expressed as:

$$|B - \lambda A| = \begin{vmatrix} (\rho T + \varphi)(u - \lambda) & \rho\varphi(\lambda - u) & \rho^2 a^2 T \\ 1 & 0 & \rho(u - \lambda) \\ \lambda - u & \rho(u - \lambda) & 0 \end{vmatrix} = 0 \quad \textbf{(3.59)}$$

Hence:

$$-(\rho T + \varphi)(u - \lambda)\rho^2(u - \lambda)^2 + \rho^2\varphi(\lambda - u)^2(u - \lambda) + \rho^3 a^2 T(u - \lambda) = 0 \quad \textbf{(3.60)}$$

Factorising equation (3.60) gives:

$$(u - \lambda)[-(\rho T + \varphi)\rho^2(u - \lambda)^2 + \rho^2\varphi(\lambda - u)^2 + \rho^3 a^2 T] = 0 \quad \textbf{(3.61)}$$

$$(u - \lambda)[-\rho^3 T(u - \lambda)^2 + \rho^3 a^2 T] = 0 \quad \textbf{(3.62)}$$

Dividing through by $\rho^3 T$ gives:

$$(u - \lambda)[a^2 - (u - \lambda)^2] = 0 \quad \textbf{(3.63)}$$

Solving equation (3.63) to obtain the roots gives:

$$\lambda_1 = u \quad \textbf{(3.64)}$$

$$\lambda_2 = u - a \quad \textbf{(3.65)}$$

$$\lambda_3 = u + a \quad \textbf{(3.66)}$$

It can be seen that the eigenvalues (λ_i) are real and distinct. Thus, the system of quasilinear partial differential equations for mass, momentum and energy conservation are hyperbolic. This implies that the behaviour of the physical system described by these equations will be dominated by wave-like phenomena (Prasad and Ravindran, 1985).

3.9 Conclusions

In this chapter the mass, momentum and energy conservation equations for the transient fluid flow in a pipeline following its failure were presented. These were expressed in terms of the dependent variables pressure, enthalpy and velocity due to their proven accuracy in simulating real data as well as computational efficiency. The governing system of conservation equations were shown to be quasi-hyperbolic in character.

The conservation equations coupled with a Cubic Equation of State represent the foundation of the transient fluid flow model. The various hydrodynamic and thermodynamic relations for predicting the pertinent fluid properties such as the fluid speed of sound, viscosity and phase dependent friction factor were presented.

In addition, the main features of the lumped body approach for modelling the fluid phase dependent heat transfer effects including, fluid/pipe wall and pipe wall/ambient were presented. Finally, the steady state isothermal model based on a real fluid was presented.

In chapter 4, the various numerical methods required to resolve the conservation equations are presented. Particular attention is paid to the Method of Characteristics as a solution methodology given its popularity due to its accuracy and robustness.

Chapter 4: Application of the Method of Characteristics (MOC) to the Simulation of Puncture/Full Bore Rupture of Multi-Segment Pipeline Networks

4.1 Introduction

The Euler equations (continuity, momentum and energy) for unsteady fluid flow were presented in chapter 3 (equations (3.1) to (3.3)). The resulting system of equations were shown to be quasilinear and hyperbolic in nature. As these equations contain terms that are unknown or non-linear functions of their dependent and independent variables they can only be solved numerically (see Flatt, 1986; Mahgerefteh et al., 1999). Their complete solution also requires the application of appropriate boundary conditions at the inlet and exit points of the fluid along the pipeline. These boundary conditions enable closure of the governing equations with their solutions establishing the fluid dynamic and thermo-physical properties in time and space along the pipeline.

Three numerical techniques are commonly employed for resolving hyperbolic partial differential equations. These are:

1. Finite Difference Methods (FDM)
2. Finite Volume Methods (FVM)
3. Method of Characteristics (MOC)

The FDM is a general mathematical technique that is widely applied to partial differential equations (PDEs). It involves discretising the spatial domain into a series of nodes forming a grid. Finite approximations are then substituted for the derivatives appearing in the PDEs taking values at the nodal points resulting in a system of algebraic equations. However, numerical diffusion associated with these methods makes

them unsuitable for modelling the transient flow following pipeline failure (Mahgerefteh et al., 2009).

Similarly, the FVM breaks the system up into a set of discrete cells. The integral of the PDEs over each cell is approximated to produce a system of algebraic relations. The application of the FVM to hyperbolic PDEs has received significant attention in recent years (see for example Leveque, 2002; Toro, 2009). The development of a FVM suitable for the resolution of governing conservation equations (equations (3.1) to (3.3)) is presented in chapter 5.

The MOC is a mathematical technique that is particularly suited to the solution of hyperbolic PDEs with two independent variables such as distance and time. The MOC resolves the system of PDEs into a system of ordinary differential equations (compatibility equations) through a particular co-ordinate change. These co-ordinates represent curves (characteristic lines) in the space-time plane along which the compatibility equations hold. The method is particularly suitable for systems containing complex boundary conditions, as each boundary condition may be applied individually to each characteristic curve moving into the computational domain.

In this chapter, the formulation and implementation of the MOC used to solve the conservation equations governing single/two-phase homogeneous flow in pipeline networks is outlined. The boundary conditions required to simulate the outflow from a multi-segment pipeline are also presented.

4.2 Mathematical Formulation of the MOC

4.2.1 The Method of Specified Time Intervals

There are two main grid discretisation methods for the MOC. These are the Characteristic Grid method (CG) which is also known as the Natural Method of Characteristics (Wylie and Streeter, 1993), and the Inverse Marching method or the Method of Specified Time Intervals (MST) (Flatt, 1986).

In the case of the CG method, the position of the new solution is not known *a priori*. This is determined by the intersection of the left and right running characteristics with the origins located at points where the solution is already known or obtained from the initial data. A free-floating grid is developed in the *x* - *t* plane as shown in figure **Error! Reference source not found.**. This method is particularly accurate as the solution progresses naturally along the characteristic lines. In the case where more than two characteristic lines are present, i.e. when an energy equation is solved, the intersection of the path line between the known initial points requires interpolation.

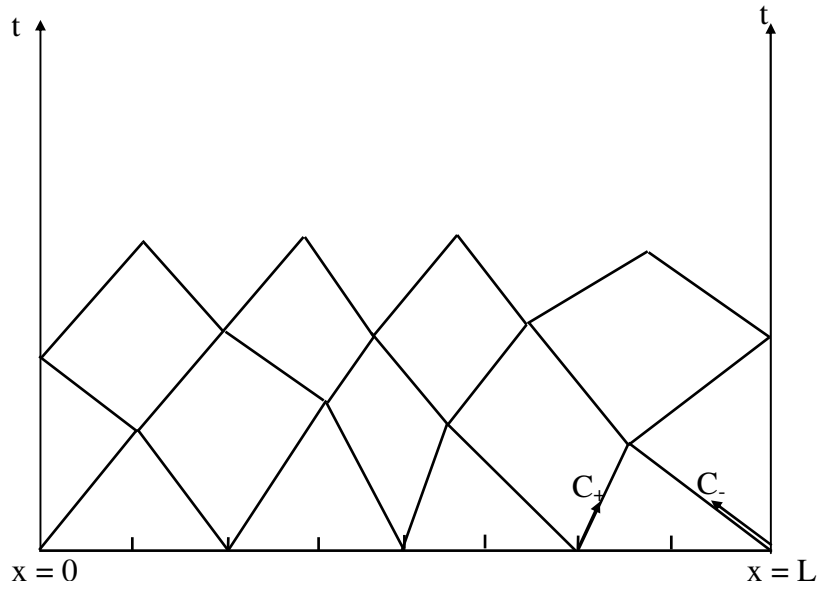

Figure 4.1: The Characteristic Grid.

In the MST (see figure **Error! Reference source not found.**) the location of the solution points in the space-time grid is specified *a priori* and the characteristic lines are traced backwards in time to their origin in the previous points. This method necessitates interpolation to locate the intersection of all three characteristic lines on the previous time line and as a result can lead to a greater loss of accuracy than the CG method.

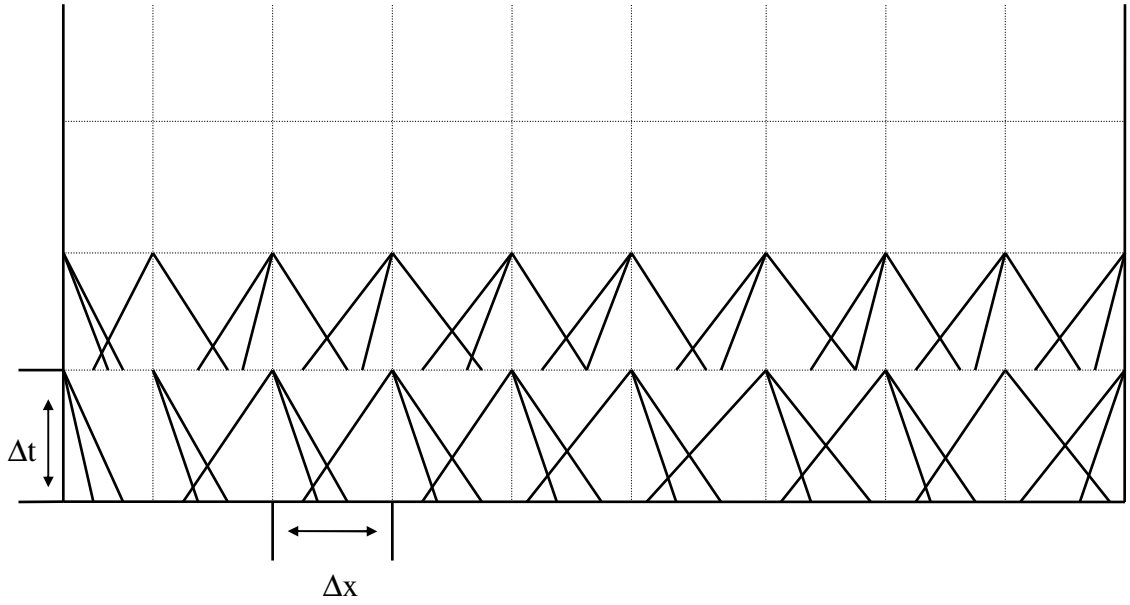

Figure 4.2: The Method of Specified Time Intervals.

While the CG method may be more accurate it does not allow for the introduction of boundary conditions at predefined times. In contrast, the MST method allows control of the time at which input variables are given at boundaries. This means that the implementation of models for systems that commonly prevail in reality such as valve closure or pump shutdown is much less cumbersome. For this reason, this method is adopted in this study.

4.2.2 Numerical Formulation of the MOC

The solution of PDEs using the MOC comprises two steps:

1. Conversion of the PDEs into a system of ordinary differential equations (ODEs) called the compatibility equations

2. Solution of the compatibility equations based on the MST method employing an Euler predictor-corrector technique (Zucrow and Hoffman, 1975).

Step 1: Conversion of PDEs to ODEs

The governing conservation equations (continuity, momentum and energy) for unsteady fluid flow were derived in chapter 3 and are repeated below.

$$(\rho T + \varphi)\left(\frac{\partial P}{\partial t} + u\frac{\partial P}{\partial x}\right) - \rho\varphi\left(\frac{\partial h}{\partial t} + u\frac{\partial h}{\partial x}\right) + \rho^2 a^2 T\frac{\partial u}{\partial x} = 0 \quad \textbf{(3.1)}$$

$$\rho\frac{\partial u}{\partial t} + \rho u\frac{\partial u}{\partial x} + \frac{\partial P}{\partial x} = \alpha \quad \textbf{(3.2)}$$

$$\rho\left(\frac{\partial h}{\partial t} + u\frac{\partial h}{\partial x}\right) - \left(\frac{\partial P}{\partial t} + u\frac{\partial P}{\partial x}\right) = \psi \quad \textbf{(3.3)}$$

Where α and ψ are given by equations (3.51) and (3.52) respectively.

Following Atti (2006), introducing $\frac{1}{\lambda}$ (see chapter 3; section 3.8) to represent the slope of the characteristic lines, the conservation equations may be replaced by three compatibility equations, which are valid along the respective characteristic curves. The three compatibility equations are given by (Atti, 2006):

$$\rho_0 d_0 h - d_0 P = \psi d_0 t \quad \textbf{(4.1)}$$

Along the path line characteristic (C_0):

$$\frac{d_0 t}{d_0 x} = \frac{1}{u} \quad \textbf{(4.2)}$$

$$d_+ P + \rho a d_+ u = \left(a\alpha + \frac{\varphi\psi}{\rho T}\right) d_+ t \quad \textbf{(4.3)}$$

Along the positive Mach line characteristic (C_+):

$$\frac{d_+ t}{d_+ x} = \frac{1}{u + a} \quad \textbf{(4.4)}$$

$$\rho a d_- u - d_- P = \left(a\alpha - \frac{\varphi\psi}{\rho T}\right) d_- t \quad \textbf{(4.5)}$$

Along the negative Mach line (C_-):

$$\frac{d_- t}{d_- x} = \frac{1}{u - a} \quad \textbf{(4.6)}$$

The positive (C_+) and negative (C_-) Mach lines govern the speed at which expansion and compression waves propagate, while the path line (C_0) dictates the rate of flow through any given point along the pipeline.

Step 2: Solution of the Compatibility Equations

As described above, the solution of the compatibility equations requires the tracing of the characteristic lines in a discretised $x - t$ plane as shown in figure **Error! Reference source not found.**.

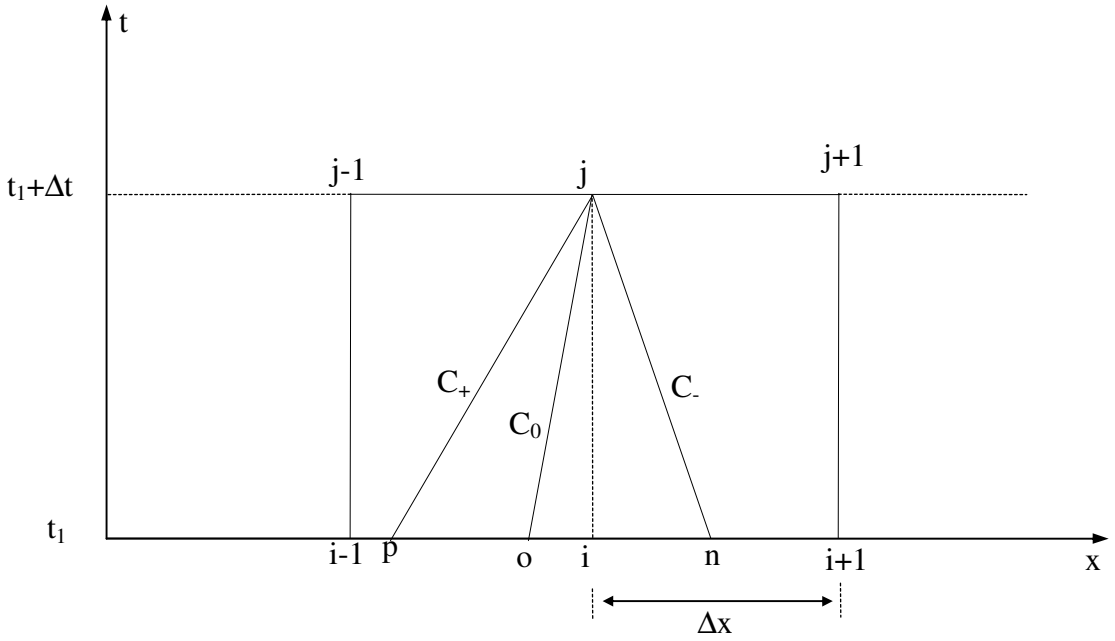

Figure 4.3: A schematic representation of Path line (C_0) and Mach lines (C_+, C_-) characteristics at a grid point along the time (*t*) and space (*x*) axes.

It is assumed that the fluid properties are already known at grid points *i-1*, *i* and *i+1* at time t_1. The initial conditions at the foot of each characteristic curve (i.e. points *p*, *o* and *n*) are evaluated by linear interpolation. The compatibility equations are solved by a finite difference method to obtain the flow variables *P*, *h* and *u* at the intersection point *j* at the next time step $t_1 + \Delta t_1$.

The time step (Δt) employed is pre-specified and are in turn calculated subject to the Courant-Friedrichs-Lewy (CFL) criterion (Courant et al., 1967; Mahgerefteh et al., 2009). This criterion is a requirement for the stability of the numerical scheme employed for the system under consideration. It is given by:

$$\Delta t \leq \frac{\Delta x}{|u+a|_{max}} \quad \textbf{(4.7)}$$

4.2.3 Finite Difference Solution of Compatibility Equations

A full description of the finite difference method used to resolve the compatibility equations is given elsewhere (e.g. Atti (2006)). Hence, only a brief description highlighting the salient points is given here.

An Euler predictor-corrector finite difference technique is used to numerically solve the compatibility and characteristic equations **Error! Reference source not found.** to **Error! Reference source not found.**. The method consists of an explicit predictor step, which is used as an estimate of the fluid properties at the solution point. The corrector step then uses this as an initial estimate for an implicit approximation of the time step.

First Order Approximation: Predictor Step

In the predictor step the compatibility equations **Error! Reference source not found.**, **Error! Reference source not found.** and **Error! Reference source not found.** are expressed in finite difference form as (Atti, 2006):

Path line compatibility:

$$\rho_0(h_j - h_0) - (P_j - P_0) = \psi_0(t_j - t_0) \quad \textbf{(4.8)}$$

Positive Mach line compatibility:

$$(\rho a)_p(u_j - u_p) + (P_j - P_p) = \left(a\alpha + \frac{\varphi\psi}{\rho T}\right)_p (t_j - t_p) \quad \textbf{(4.9)}$$

Negative Mach line compatibility:

$$(\rho a)_n(u_j - u_n) - (P_j - P_n) = \left(a\alpha - \frac{\varphi\psi}{\rho T}\right)_n (t_j - t_n) \quad \textbf{(4.10)}$$

The subscripts assigned to the various properties in equations **Error! Reference source not found.** to **Error! Reference source not found.** denote the location in space and time, as shown in figure **Error! Reference source not found.**. The points x_p, x_o and x_n

are calculated from a first order finite difference form of equations **Error! Reference source not found.**, **Error! Reference source not found.** and **Error! Reference source not found.**. The fluid properties are then linearly interpolated from those at the grid points *i-1*, *i* and *i+1* (Atti, 2006).

Second Order Approximation: Corrector Step

In order to improve the accuracy of the first order solution, a second order approximation to the compatibility equations is employed. The finite difference form of the compatibility equations **Error! Reference source not found.**, **Error! Reference source not found.** and **Error! Reference source not found.** can be expressed as (Atti, 2006):

Path line compatibility:

$$\frac{1}{2}\left(\rho_0+\rho_j\right)\left(h_j-h_0\right)-\left(P_j-P_0\right)=\frac{1}{2}\left(\psi_0+\psi_j\right)\left(t_j-t_0\right) \tag{4.11}$$

Positive Mach line compatibility:

$$\frac{1}{2}\left((\rho a)_p+(\rho a)_j\right)\left(u_j-u_p\right)+\left(P_j-P_p\right) = \frac{1}{2}\left(\left(a\alpha+\frac{\varphi\psi}{\rho T}\right)_p+\left(a\alpha+\frac{\varphi\psi}{\rho T}\right)_j\right)\left(t_j-t_p\right) \tag{4.12}$$

Negative Mach line compatibility:

$$\frac{1}{2}\left((\rho a)_n+(\rho a)_j\right)\left(u_j-u_n\right)-\left(P_j-P_n\right) = \frac{1}{2}\left(\left(a\alpha-\frac{\varphi\psi}{\rho T}\right)_n+\left(a\alpha-\frac{\varphi\psi}{\rho T}\right)_j\right)\left(t_j-t_n\right) \tag{4.13}$$

In a similar manner employed in the predictor step, the positions x_p, x_o and x_n are calculated from a second order finite difference form of equations **Error! Reference source not found.**, **Error! Reference source not found.** and **Error! Reference source not found.**. The fluid properties at these points are then found by linear interpolation, as

in the first order step. This calculation is repeated until a certain tolerance (ca. 10^{-5}) is satisfied for the three independent flow variables, i.e. P, h and u.

4.3 Boundary Conditions Required for Simulating the Failure of Pipeline Networks

In this section, the boundary conditions required to simulate the outflow from a multi-segmented pipeline following failure are presented. These include:

- Intact pipeline end
- Feed pump
- Full-bore rupture/orifice at pipeline end
- Puncture on the walls of a pipeline
- Junction of two pipelines (bends or connector) in a multiple segment pipeline network.

4.3.1 The Intact End Point Boundary

At the intact or closed end of the pipeline, only the negative Mach line (C_-) and path line (C_0) characteristics are applicable and hence only two compatibility equations are valid. In this case one boundary condition must be supplied in order to determine the pertinent flow variables *P*, *h* and *u*. Figure **Error! Reference source not found.** shows the grid scheme at the intact end point.

The first order finite difference approximation (equation **Error! Reference source not found.**) of the negative characteristic equation, C_-, can be written as:

$$P_j = K_2 + (\rho a)_n(u_j - u_n) + P_n \qquad \textbf{(4.14)}$$

Where, K_2 is given by:

$$K_2 = \left(\frac{\varphi\psi}{\rho T} - a\alpha\right)_n \Delta t \qquad \textbf{(4.15)}$$

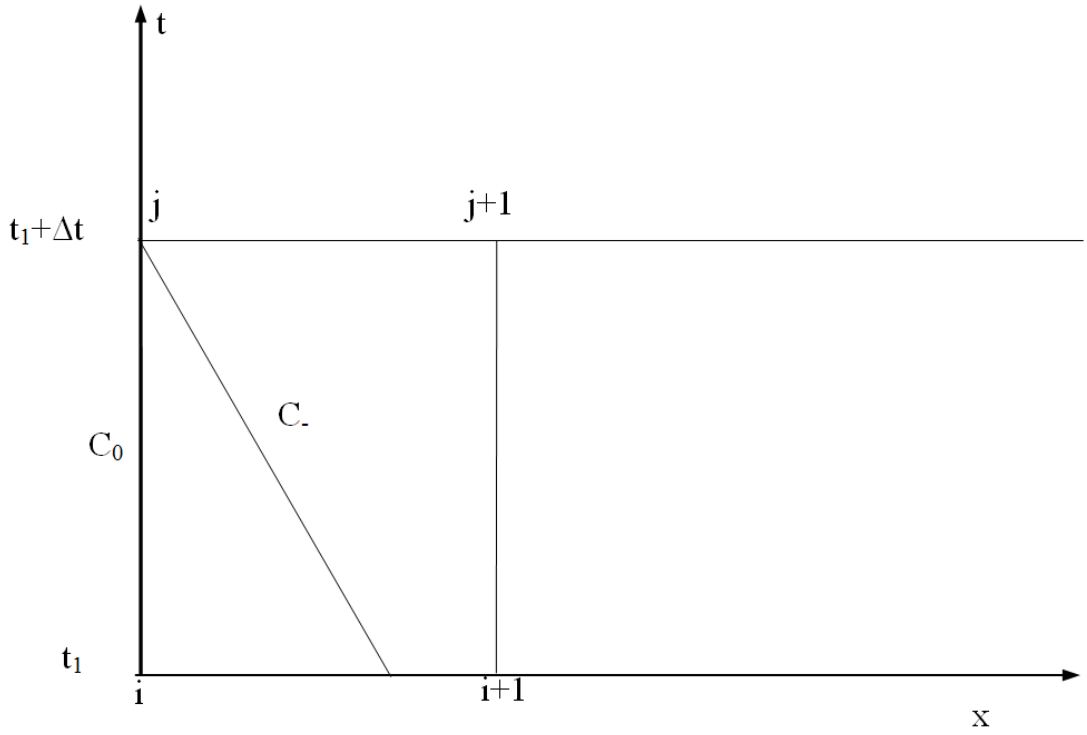

Figure 4.4: Grid scheme showing the active characteristic lines (C_0 and C-) at the inlet intact end point.

Applying the boundary condition that the velocity at the closed end is equal to zero gives:

$$P_j = K_2 + (\rho a u)_n + P_n \qquad \textbf{(4.16)}$$

The upstream enthalpy may then be calculated using the path line characteristic (equation **Error! Reference source not found.**):

$$h_j = \frac{\psi_0 \Delta t + (P_j - P_0) + \rho_0 h_0}{\rho_0} \qquad \textbf{(4.17)}$$

The corrector step as described in section **Error! Reference source not found.** is then subsequently employed to yield the flow variables at the intact end.

4.3.2 Centrifugal Pump at the Pipeline Inlet

To account for the possibility of the failure of an un-isolated pipeline where pumping continues despite pipeline failure Denton (2009) developed a boundary condition for a centrifugal pump at the pipeline inlet. This model utilises the steady state pump head-

discharge curve (Al-Khomairi, 2003) to predict the pump head and is summarised below.

The equation for a centrifugal pump given by Wylie and Streeter (1993) is employed to describe the behaviour of the pump discharge pressure as a function of its discharge rate or velocity:

$$P_j = P_{sh} + K_{P1}u_j + K_{P2}u_j^2 \quad \textbf{(4.18)}$$

Where, P_j and u_j are the pump discharge pressure and discharge velocity respectively. P_{sh} is the pump shut-off head and represents the maximum discharge pressure of the pump. K_{P1} and K_{P2} are constants which are dependent on the type of pump used. The values of P_{sh}, K_{P1} and K_{P2} are obtained by fitting equation **Error! Reference source not found.** to the steady state pump head-discharge curve given for the pump (Denton, 2009).

As with the intact end boundary condition (section **Error! Reference source not found.**), only the path and negative Mach line compatibility equations are active at the pump boundary. Rearranging equation **Error! Reference source not found.** to make u_j the subject of the equation gives:

$$u_j = \frac{P_j}{(\rho a)_n} - \frac{P_n}{(\rho a)_n} - \frac{K_2}{(\rho a)_n} + u_n \quad \textbf{(4.19)}$$

Simplifying equation **Error! Reference source not found.** gives:

$$u_j = K_{nu1}P_j - K_{nu2} \quad \textbf{(4.20)}$$

Where,

$$K_{nu1} = \frac{1}{(\rho a)_n} \quad \textbf{(4.21)}$$

$$K_{nu2} = \frac{P_n + K_2}{(\rho a)_n} - u_n \quad \textbf{(4.22)}$$

Substituting equation **Error! Reference source not found.** into equation **Error! Reference source not found.** gives:

$$K_{nu1}K_{P2}u_j^2 + (K_{nu1}K_{P1} - 1)u_j + K_{nu1}P_{sh} - K_{nu2} = 0 \quad \textbf{(4.23)}$$

The positive root of equation **Error! Reference source not found.** corresponds to u_j. Therefore, substituting this value into equation **Error! Reference source not found.** gives the corresponding value of P_j.

4.3.3 Full Bore Rupture and Puncture at the Downstream End

Two distinct types of flow are assumed to occur at the release plane during pipeline failure, namely:

1. Critical/choked flow
2. Non-choked flow.

During choked flow where the release flow rate is at a maximum and the fluid is assumed to undergo an isentropic expansion, discharging at a pressure above the ambient. In the case of single-phase flow the release velocity corresponds to the sonic velocity at the prevailing pressure. Consequently, disturbances downstream of the release plane cannot propagate upstream.

Once the pressure at the release plane has reached the ambient pressure the flow is no longer choked. The release velocity in this case is subsonic and the discharge is driven only by the momentum of the remaining fluid inventory.

At the rupture plane both the C_+ and C_0 characteristics lie within the computational domain. In the absence of a simple analytical relationship expressing the expansion process across the release plane, a 'ghost' cell adjacent to the boundary cell, as depicted in figure **Error! Reference source not found.**, is used to apply suitable conditions to the C- characteristic. The ghost cell is a fictitious node (*i+1*) lying at the same position as node *i* as illustrated in figure **Error! Reference source not found.**.

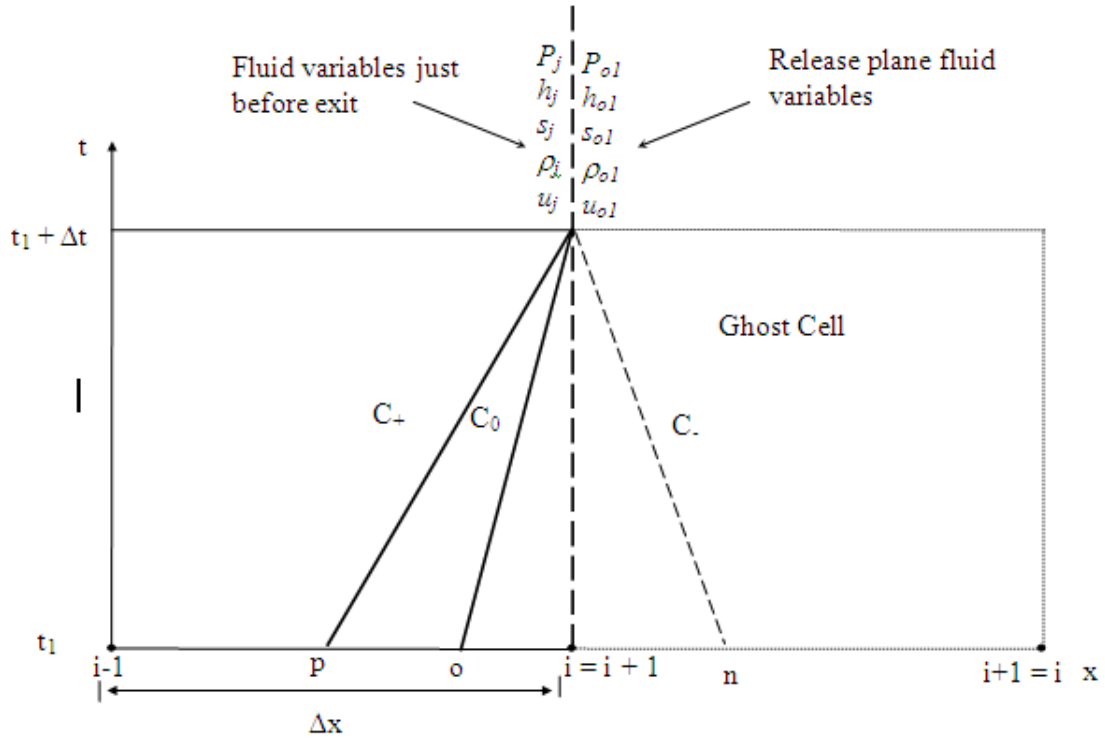

Figure 4.5: Diagram illustrating characteristic lines at the rupture plane based on the concept of a ghost cell.

The introduction of this extra node allows the solution along the negative characteristic. The flow properties at point *j* are then obtained just as for interior points using equations **Error! Reference source not found.**, **Error! Reference source not found.** and **Error! Reference source not found.**. In this case however interpolation is not required within the ghost cell as all the properties within it are spatially invariant.

The flow variables P_{o1}, h_{o1} and u_{o1} (see figures **Error! Reference source not found.**) at the release plane are calculated using the method described in the next section.

Across the release plane the mass flow rate is conserved. While the expansion process at the release plane is assumed to be isentropic, non-isentropic effects may occur during puncture due to the hydraulic resistance posed by the release orifice. Hence, the actual flow rate of the exiting fluid may be smaller than the assumed isentropic flow rate with the ratio between the two being equal to the discharge coefficient, C_d.

Therefore, the mass flow rate both approaching and leaving the release plane can be expressed as:

$$u_j \rho_j A_{pipe} = C_d \rho_{o1} u_{o1} A_{o1} \quad \textbf{(4.24)}$$

Where A_{o1} and A_{pipe} are the orifice area and pipe areas respectively. ρ_{o1} and u_{o1} are the fluid density and fluid velocity respectively.

4.3.4 Discharge Rate Calculation Algorithm

As discussed in the previous section, while the discharge pressure is above the downstream pressure the flow is choked. Under these conditions, the mass flow rate at the release plane is at a maximum. When the pressure at the release plane drops to the downstream pressure, the flow is no longer choked and the release rate is calculated accordingly.

Figure **Error! Reference source not found.** shows the relevant pressures at the release plane that govern the discharge process. P_j, P_{o1} and P_d represent the pressure of the fluid approaching the release plane, the discharge pressure and the downstream or ambient pressure respectively.

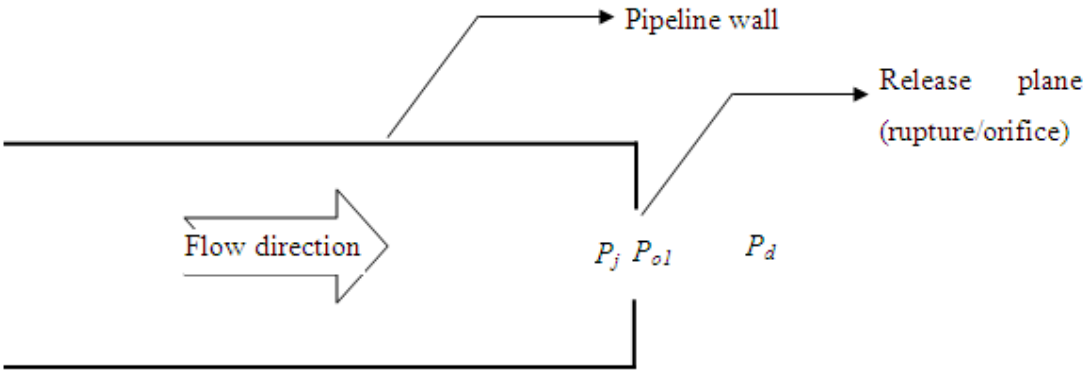

Figure 4.6: A schematic representation of pertinent pressures at the failure plane governing the discharge rate.

The choked and non-choked discharge rates are calculated by applying an energy balance across the release plane. As mentioned previously, the expansion process is assumed to be isentropic. Any additional non-isentropic effects are accounted for by introducing a discharge coefficient (C_d; equation **Error! Reference source not found.**).

The energy balance across the release plane, ignoring changes in potential energy between the flow approaching and exiting the failure plane is given by:

$$h_j + \frac{1}{2}u_j^2 = h_{o1} + \frac{1}{2}u_{o1}^2 \qquad \textbf{(4.25)}$$

Where, the subscripts j and $o1$ represent upstream and the release plane conditions respectively.

In the case of choked/critical flow the velocity, u_{o1}, is replaced by the local single/two-phase speed of sound, a_{o1}. The release pressure (P_{o1}) is then obtain by solving equation **Error! Reference source not found.** using Brent's (2002) algorithm. The iterative solution of equation **Error! Reference source not found.** involves guessing and updating the discharge pressure, P_{o1}, in conjunction with pressure-entropy (isentropic) flash calculations until equation **Error! Reference source not found.** is satisfied. Once a solution is obtained, other flow variables at the release plane ρ_{o1}, T_{o1} and h_{o1} are determined from a corresponding pressure-entropy (P_{o1}-s_j) flash calculation.

For non-critical flow the release pressure, P_{o1}, is equal to the ambient pressure, P_d. The remaining outflow variables such as ρ_{o1}, T_{o1} and h_{o1} may be calculated using a pressure-entropy (P_{o1}-s_j) flash calculation. The release velocity, u_{o1} may then be obtained from equation **Error! Reference source not found.**.

Once the release plane flow conditions are determined, u_j is updated using equation **Error! Reference source not found.** and employed in the corrector steps (see section **Error! Reference source not found.**) until convergence is observed. The corresponding calculation flow logic diagram for determining the discharge rate is shown in figure **Error! Reference source not found.**.

4.3.5 Puncture on Pipe Wall

The pipeline puncture model proposed by Atti (2006) is used in this study to predict outflow. A summary of its main features by reference to the flow parameters given in figure **Error! Reference source not found.** follows. As depicted, the puncture is assumed to split the pipeline into two sections:

- Upstream pipe section
- Downstream pipe section.

The control volume around the puncture region (see figure **Error! Reference source not found.**) acts as a boundary to both pipeline sections 1 and 2. These are denoted by B_1 and B_2 respectively. The third boundary of the control volume, denoted by B_3, represents the puncture plane. As depicted in figure **Error! Reference source not found.**, for the upstream pipeline section only the positive Mach line and the path line lie within the computational domain at the boundary, B_1. Similarly at B_2 only the negative Mach line and the path line lie within this domain.

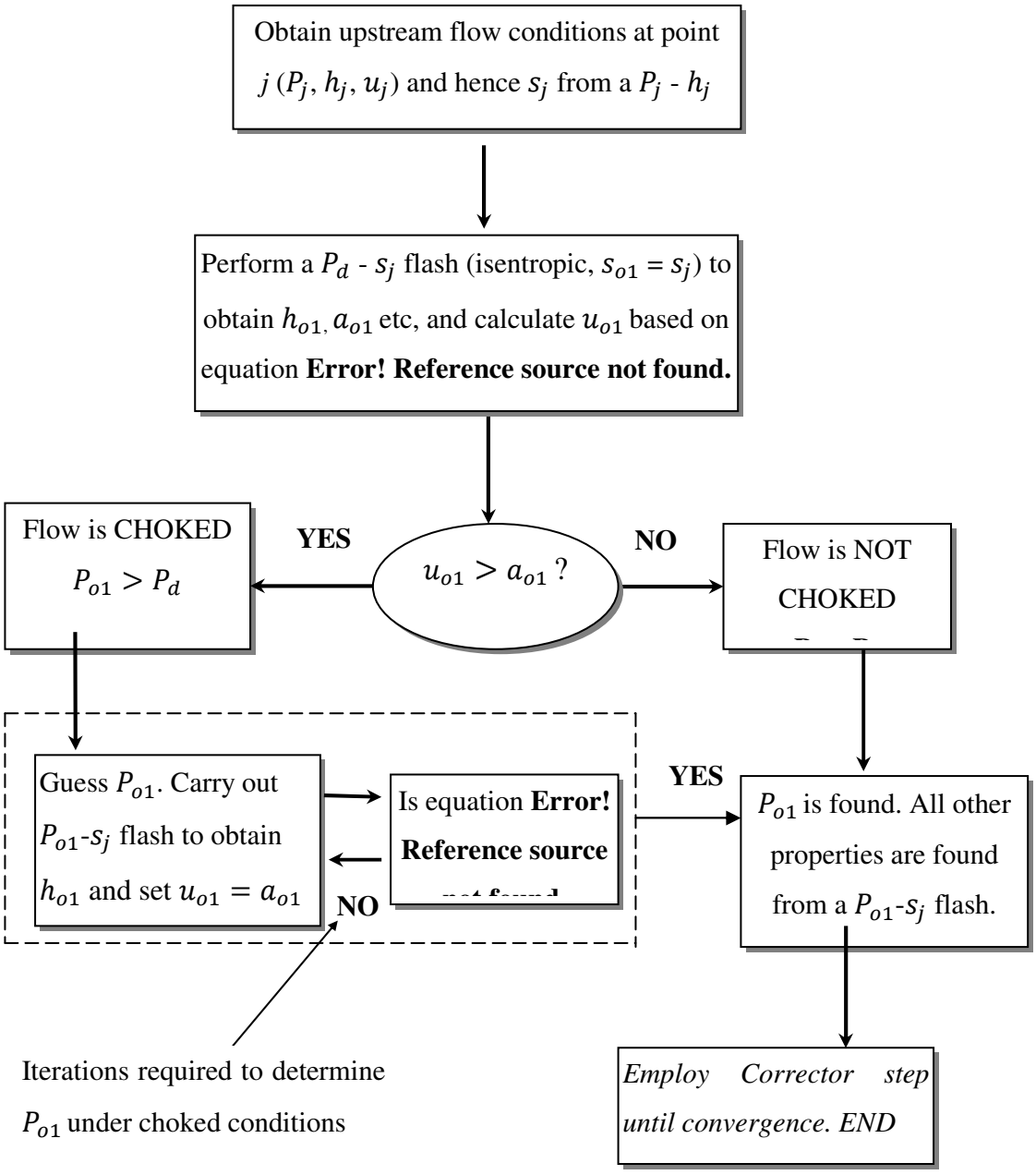

Figure 4.7: Calculation algorithm for obtaining flow variables at the discharge plane.

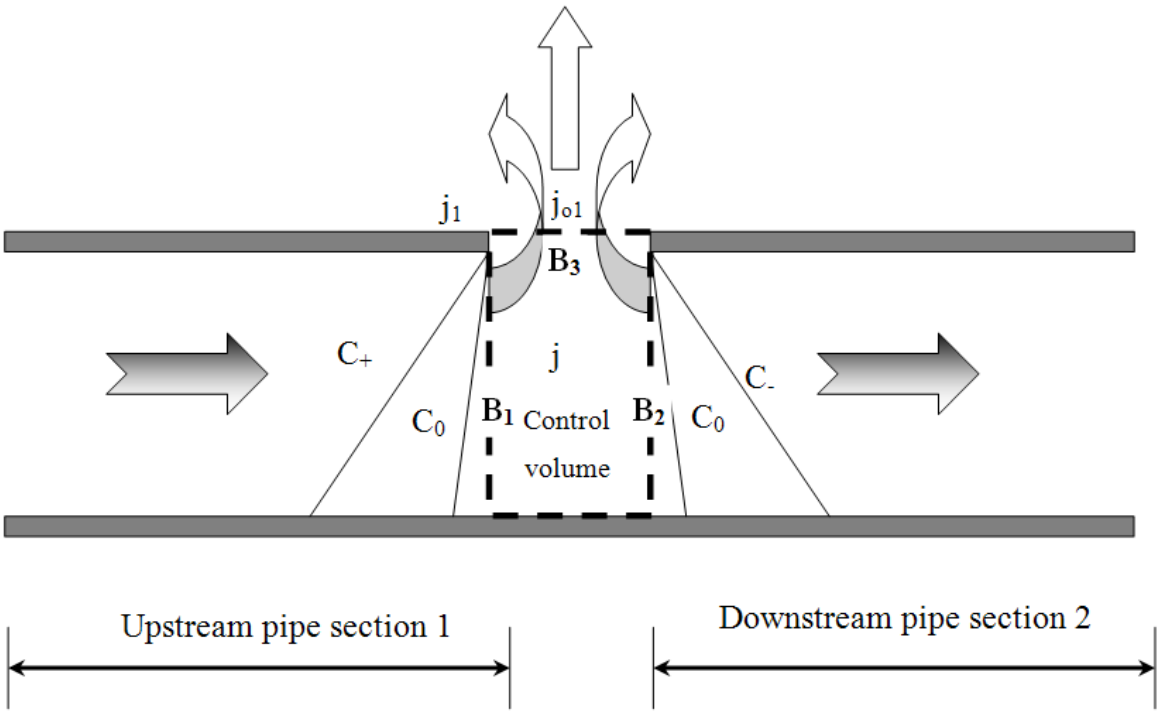

Figure 4.8: Schematic representation of fluid flow analysis following pipeline puncture.

To resolve the fluid flow phenomena, appropriate conditions must be applied at the flow boundaries and orifice, B_1, B_2 and B_3 (denoted by j_1, j_2 and j_{o1} respectively). The required conditions are derived by assuming that the pressure in the control volume is constant at the current time step:

$$P_{j1} = P_{j2} = P_j \quad \textbf{(4.26)}$$

Where, P_{j1}, P_{j2} and P_j are the pressures at j_1, j_2 and within the control volume respectively. The properties in the control volume are defined at the cell centre such that:

$$s_j = \frac{s_{j1} + s_{j2}}{2} \quad \textbf{(4.27)}$$

The flow through the orifice (B_3) is assumed to be isentropic, hence:

$$s_{o1} = s_j \quad \textbf{(4.28)}$$

Assuming that the flow at the puncture region is two-dimensional, the conservation of mass applied over the control volume is given by:

$$V\frac{d\rho}{dt} + A_{pipe}\partial(\rho u) + A_{o1}\partial(\rho v) = 0 \quad \textbf{(4.29)}$$

Where, V and v are the volume of the control volume and the fluid velocity normal to the axial direction respectively. Integrating equation **Error! Reference source not found.** with respect to t over the interval $[t_2, t_1]$ where $\Delta t = t_2 - t_1$ gives:

$$V\left(\rho_{j_{|t=t_2}} - \rho_{j_{|t=t_2}}\right) + A_{pipe}\int_{t_1}^{t_2}\left[(\rho u)_{x_2} - (\rho u)_{x_1}\right]dt + A_{o1}\int_{t_1}^{t_2}\left[(\rho v)_{y_2} - (\rho v)_{y_1}\right]dt = 0 \quad \textbf{(4.30)}$$

Evaluating the integrals numerically and applying the condition that $(\rho v)_{y_1}$ is zero gives:

$$V\left(\rho_{j_{|t=t_2}} - \rho_{j_{|t=t_2}}\right) + \left\{A_{pipe}\left[(\rho u)_{j_{|x=x_2}} - (\rho u)_{j_{|x=x_1}}\right] + A_{o1}\left((\rho v)_{j_{|y=y_2}}\right)_{ave}\right\}\Delta t = 0 \quad \textbf{(4.31)}$$

Where the subscript *ave* represents the average of the value in the brackets in the interval $[t_2, t_1]$ while x_2 and x_1 represent the upper (B_2) and lower bounds (B_1) along the *x*-axis of the control volume V.

Introducing the discharge coefficient equation **Error! Reference source not found.** becomes:

$$V\left(\rho_{j_{|t=t_2}} - \rho_{j_{|t=t_2}}\right) + \left\{A_{pipe}\left[(\rho u)_{j_{|x=x_2}} - (\rho u)_{j_{|x=x_1}}\right] + C_d A_{o1}\left((\rho v)_{j_{|y=y_2}}\right)_{ave}\right\}\Delta t = 0 \quad \textbf{(4.32)}$$

Equation **Error! Reference source not found.** represents the boundary equation based on the 2D mass conservation which couples the flow behaviour at planes B_2 and B_1. Hence, the solution at the common junction must satisfy equation **Error! Reference source not found.**.

The solution algorithm employed involves the iterative solution of equation **Error! Reference source not found.** using the Brent iteration method (Brent, 2002)coupled with the Euler predictor-corrector method applied to obtain u_{j_1} and h_{j_1} from the compatibility equations **Error! Reference source not found.** and **Error! Reference source not found.** at the B_1 boundary. The fluid entropy, s_{j_1}, at j_1 is then determined from a P_{j_1}-h_{j_1} flash calculation. Similarly at B_2, u_{j_2} and h_{j_2} are found from equations **Error! Reference source not found.** and **Error! Reference source not found.**, after which a P_{j_2}-h_{j_2} flash is used to calculate s_{j_2}.

The discharge rate algorithm described in section **Error! Reference source not found.** is employed to determine the conditions at the failure plane. The flow properties obtained from the solution of characteristic/boundary equations at planes B_1, B_2 and B_3 are substituted into equation **Error! Reference source not found.**.

4.3.6 Junction of Two Pipelines in a Multi-Segment Pipeline Network

Denton's (2009) model for the effect of pressure losses between segments in pipeline networks is applied in this study and outlined below. Figure **Error! Reference source not found.** is a schematic representation of the characteristic lines at a typical bend or connector. B_1 and B_2 refer to the flow boundaries at the common junction associated with pipeline 1 and 2 respectively.

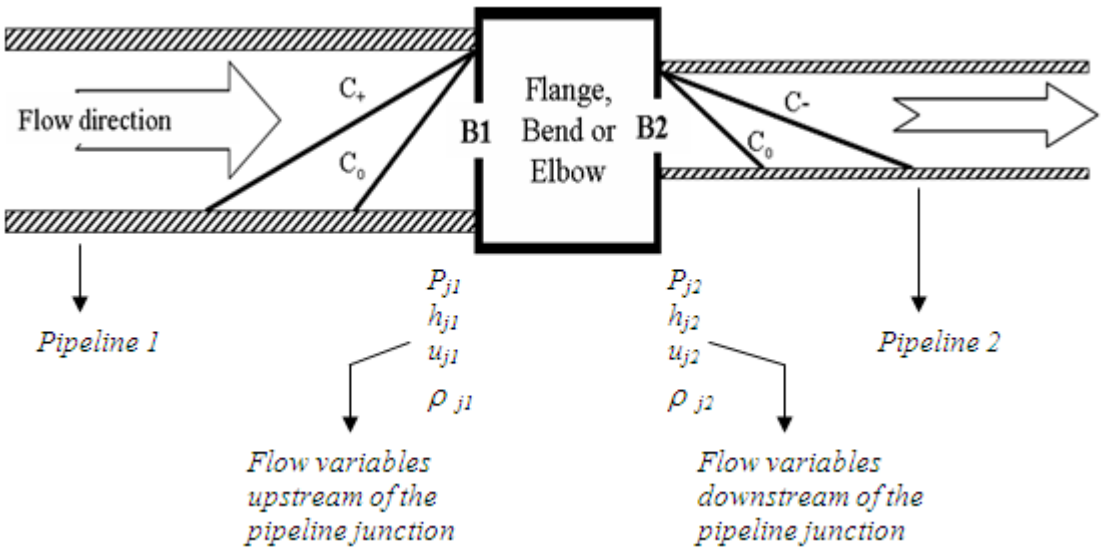

Figure 4.9: Schematic representation of characteristic lines upstream and downstream of a 2-way junction.

At the boundary B_1, only the positive Mach line (C_+) and path line (C_0) characteristics lie within the computational domain. Similarly, at B_2 only the negative Mach line (C_-) and the path line (C_0) are applicable. The solution at points B_1 and B_2 are denoted by j_1 and j_2 respectively. K_{loss} coefficients are used to account for pressure losses due to friction or changes in flow direction across the fitting (Perry and Green, 1997). These coefficients are determined empirically for different types of fittings, and are employed in calculating the pressure drop resulting from flow across a given fitting (Perry and Green, 1997).

The pressure drop at the pipeline junction is given by:

$$P_{j2} = P_{j1} + K_{pl} \quad \textbf{(4.33)}$$

Where,

$$K_{pl} = 0.5\left(\rho_{j1}u_{j1}\left|u_{j1}\right| - \rho_{j2}(1 + K_{loss})u_{j2}\left|u_{j2}\right|\right) \quad \textbf{(4.34)}$$

And ρ_j, u_j and P_j are the density, velocity and pressure at junction j.

The coefficient K_{loss} accounts for the pressure drop resulting from the losses described above. Its values are obtained from the literature (Perry and Green, 1997). These loss coefficients are relatively insensitive to the Reynolds number for $Re \geq 500$ (Perry and Green, 1997). As flow conditions where $Re \geq 20{,}000$ are likely to be prevalent at pipeline junctions during the depressurisation process, constant loss coefficients are utilised in this study. These are summarised in table **Error! Reference source not found.**.

Table 4.1: K_{loss} for turbulent flow through fittings and valves (Perry and Green, 1997).

Type of fitting or valve	K_{loss}
45^o elbow (standard)	0.35

90^o elbow (standard)	0.75
Coupling/Union	0.04
Tee (standard, branch blanked off)	0.40
Gate valve (open)	0.17
Angle valve (open)	2

Taking the junction as a control volume, assuming no mass accumulation and considering flow into the junction as positive, applying a continuity equation gives:

$$\rho_{j1} u_{j1} A_{j1} + \rho_{j2} u_{j2} A_{j2} = 0 \quad \textbf{(4.35)}$$

Where, A_j is the cross-sectional area of the pipeline.

If continuity is satisfied across the boundaries, the flow transport properties obtained are adopted as the required solution.

4.4 Concluding Remarks

In this chapter, the formulation of the MOC based on the Method of Specified Time intervals (MST) was presented. The governing conservation equations were resolved into compatibility equations which were in turn discretised using the Euler predictor-corrector technique. By assuming that the fluid properties varied linearly with distance, algebraic expressions for the fluid variables at the next time step along the pipeline length were obtained.

These compatibility equations were combined with appropriate boundary conditions to model the fluid dynamics following the failure of multi-segment pipeline networks. The frictional losses due to valves, fittings, changes in pipeline diameter and changes in elevation were accounted for by the introduction of a loss coefficient, K_{loss}.

Chapter 5 will present a Finite Volume Method as an alternative technique to the MOC for the resolution of the conservation equations. The results relating to the testing and where possible validation of this technique will also be presented.

Chapter 5: Development of a Finite Volume Model for Outflow Following Pipeline Failure

5.1 Introduction

In the proceeding chapter, an MOC based model for simulating the transient flow following pressurised pipeline failure was presented. Although the MOC has been shown to successfully predict experimental data (see for example, Mahgerefteh et al., 1999; Oke et al., 2003) it is often criticised for the high computational cost of each simulation. Despite the considerable effort and progress in developing new techniques to address this issue (Mahgerefteh et al., 1999; Oke et al., 2003), there still remains a significant CPU runtime overhead associated with the use of the MOC.

The majority of the work in reducing the CPU runtime thus far has focussed on the reduction of the computational cost of the thermo-physical property calculations. However, as highlighted by Atti (2006), the large number of iterations required in the corrector step (see section 4.2.3) of the MOC inevitably leads to longer CPU runtimes. Hence a non-iterative numerical technique may significantly increase the efficiency of the model. Finite Volume (FV) Methods provide an alternative in which only a small, fixed number of calculations are required, while retaining numerical accuracy.

The PHU (Oke et al., 2003) formulation of the conservation equations is said to be in non-conservative form as it is in terms of 'primitive' variables (Toro, 2009), rather than the conserved variables (i.e. density, momentum and energy). FV schemes for non-conservative hyperbolic equations may be categorised into upwind and centred methods. Upwind techniques normally require the solution of the local Riemann problem, either exact or approximate (Karni, 1994; Toro, 1991), to capture wave propagation information. No explicit knowledge of the Riemann problem or wave information is required for centred schemes, where only the eigenvalues of the system

are needed for the enforcement of the CFL criterion (Toro and Siviglia, 2003). Hence, centred methods provide an accurate, robust alternative numerical technique without requiring time consuming characteristic decomposition.

In this chapter, the development of an appropriate FV method which when coupled with the numerical boundary conditions developed in chapter 4, provides an alternative to the MOC presented previously. This is then followed by comparison of the performance of the two methods in terms of:

i) The degree of agreement of their predictions against real pipeline rupture data

ii) Computational runtimes expended based on simulations involving the rupture of hypothetical pipelines containing different phase fluid mixtures.

5.2 Mathematical formulation of the Finite Volume

Using simple algebra the PHU formulation of the governing conservation equations (equations (3.1) to (3.3)) presented in chapter 3 may be written in matrix form as:

$$\partial_t \boldsymbol{Q} + \boldsymbol{A}(\boldsymbol{Q})\partial_x \boldsymbol{Q} = \boldsymbol{H}(\boldsymbol{Q}) \quad \textbf{(5.1)}$$

Where:

$$\boldsymbol{Q} = \begin{pmatrix} h \\ u \\ P \end{pmatrix} \quad \textbf{(5.2)}$$

$$\boldsymbol{A}(\boldsymbol{Q}) = \begin{pmatrix} u & a^2 & 0 \\ 0 & u & \frac{1}{\rho} \\ 0 & \rho a^2 & u \end{pmatrix} \quad \textbf{(5.3)}$$

$$\boldsymbol{H}(\boldsymbol{Q}) = \begin{pmatrix} \dfrac{(\rho T + \varphi)\psi}{\rho^2 T} \\ \dfrac{\alpha}{\rho} \\ \dfrac{\varphi\psi}{\rho T} \end{pmatrix} \tag{5.4}$$

Where, all symbols are as defined in chapter 3. The functions α, ψ and φ are given by equations (3.51), (3.52) and (3.10) respectively.

In order to apply FV schemes designed for hyperbolic systems of equations, the right-hand terms (referred to as 'source terms') are initially neglected. These are then solved separately with an explicit Euler method using operator splitting (Leveque, 2002). The remaining left hand terms are given by:

$$\partial_t \boldsymbol{Q} + \boldsymbol{A}(\boldsymbol{Q})\partial_x \boldsymbol{Q} = \boldsymbol{0} \tag{5.5}$$

Given the non-conservative form of these equations, the primitive centred PRICE-T scheme of Toro and Siviglia (2003) is selected. In this method the staggered grid Random Choice Method (RCM) of Gottlieb (1988) is reformulated in terms of averages rather than stochastic sampling. The basis of this method is the integration of equation (5.5) over a control volume $V = [x_1, x_2] \times [t_1, t_2]$ in $x - t$ space:

$$\int_{x_1}^{x_2} \int_{t_2}^{t_2} [\partial_t \boldsymbol{Q} + \boldsymbol{A}(\boldsymbol{Q})\partial_x \boldsymbol{Q}]\, dt\, dx = 0 \tag{5.6}$$

Assuming a local linearisation of (5.6) and a constant matrix $\widehat{\boldsymbol{A}}_i$ within the control volume, the integration gives:

$$\int_{x_1}^{x_2} \boldsymbol{Q}(x, t_2)dx = \int_{x_1}^{x_2} \boldsymbol{Q}(x, t_1)dx - \widehat{\boldsymbol{A}}_i \left[\int_{t_1}^{t_2} \boldsymbol{Q}(x_2, t)dt - \int_{t_1}^{t_2} \boldsymbol{Q}(x_1, t)dt \right] \tag{5.7}$$

Figure 5.1 shows a schematic representation of the discretisation used in the space (x) – time (t) plane. The flow variables are assumed to be known at positions $i-1$, i and $i+1$ at time step n ($\boldsymbol{Q}_{i-1}^{n}$, $\boldsymbol{Q}_{i}^{n}$ and $\boldsymbol{Q}_{i+1}^{n}$ respectively). The staggered grid RCM updates the flow variables $\boldsymbol{Q}_{i}^{n}$ at time t to the new value of $\boldsymbol{Q}_{i}^{n+1}$ at time $t+\Delta t$ in two steps.

The first step in the application of the RCM is the solution of the Riemann problems at $i-\frac{1}{2}$ and $i+\frac{1}{2}$ (denoted by $RP(\boldsymbol{Q}_{i-1}^{n}, \boldsymbol{Q}_{i}^{n})$ and $RP(\boldsymbol{Q}_{i}^{n}, \boldsymbol{Q}_{i+1}^{n})$ (Toro and Siviglia, 2003)) to find the solutions $\widehat{\boldsymbol{Q}}_{i-\frac{1}{2}}^{n+\frac{1}{2}}(x,t)$ and $\widehat{\boldsymbol{Q}}_{i+\frac{1}{2}}^{n+\frac{1}{2}}(x,t)$ respectively. These solutions are then randomly sampled at time $\frac{1}{2}\Delta t$ as indicated in figure 5.1. This is done by taking a random number θ^n in the interval $\left[-\frac{1}{2},\frac{1}{2}\right]$ and taking the intermediate values of the flow variables as:

$$\boldsymbol{Q}_{i-\frac{1}{2}}^{n+\frac{1}{2}} = \widehat{\boldsymbol{Q}}_{i-\frac{1}{2}}^{n+\frac{1}{2}}\left(\theta^n \Delta x, \frac{1}{2}\Delta t\right), \qquad \boldsymbol{Q}_{i+\frac{1}{2}}^{n+\frac{1}{2}} = \widehat{\boldsymbol{Q}}_{i+\frac{1}{2}}^{n+\frac{1}{2}}\left(\theta^n \Delta x, \frac{1}{2}\Delta t\right) \tag{5.8}$$

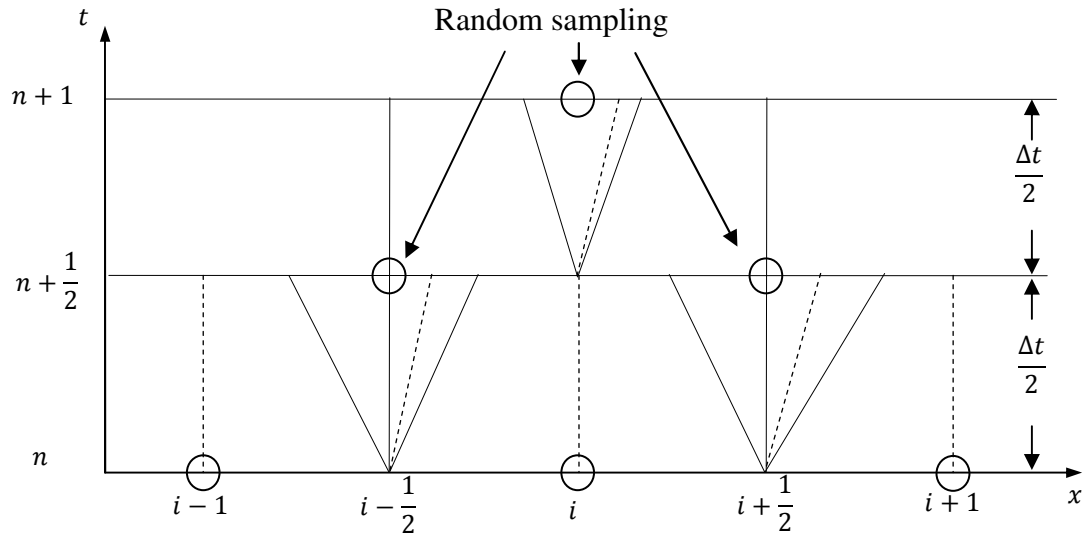

Figure 5.1: Schematic representation of the RCM for a grid point (i) along the time (t) and space (x) axes on a staggered grid.

Once the flow variables have been obtained at time level $n+\frac{1}{2}$, the Riemann problem $RP\left(\boldsymbol{Q}_{i-\frac{1}{2}}^{n+\frac{1}{2}}, \boldsymbol{Q}_{i+\frac{1}{2}}^{n+\frac{1}{2}}\right)$ is solved to give $\widehat{\boldsymbol{Q}}_i^{n+1}(x,t)$. This is then randomly sampled, as described above, at a stable time Δt to obtain:

$$\boldsymbol{Q}_i^{n+1} = \widehat{\boldsymbol{Q}}_i^{n+1}(\theta^{n+1}\Delta x, \Delta t) \qquad \textbf{(5.9)}$$

The PRICE-T is obtained by replacing the stochastic steps equations (5.8) and (5.9) with integral averages of the Riemann problem solutions. Figure 5.2 shows a schematic illustration of the PRICE-T method.

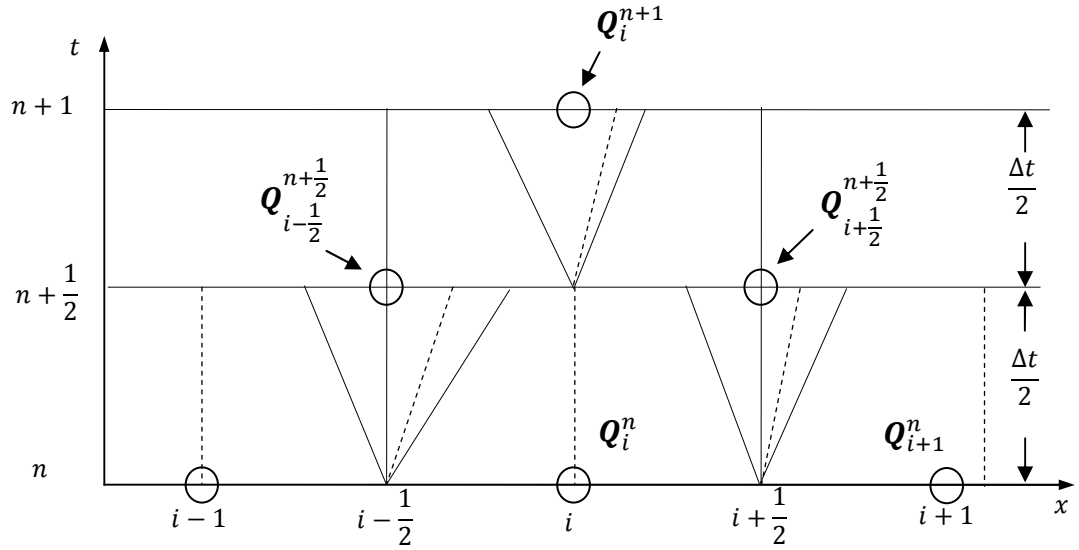

Figure 5.2: Schematic representation of the PRICE-T for a grid point (i) along the time (t) and space (x) axes on a staggered grid.

The development of PRICE-T first requires the replacement of the stochastic approximations in equation (5.8) with the following integral averages:

$$\boldsymbol{Q}_{i-\frac{1}{2}}^{n+\frac{1}{2}} = \int_{-\frac{1}{2}\Delta x}^{\frac{1}{2}\Delta x} \widehat{\boldsymbol{Q}}_{i-\frac{1}{2}}^{n+\frac{1}{2}}\left(x, \frac{1}{2}\Delta t\right) dx \qquad \textbf{(5.10)}$$

$$\boldsymbol{Q}_{i+\frac{1}{2}}^{n+\frac{1}{2}} = \int_{-\frac{1}{2}\Delta x}^{\frac{1}{2}\Delta x} \widehat{\boldsymbol{Q}}_{i+\frac{1}{2}}^{n+\frac{1}{2}}\left(x, \frac{1}{2}\Delta t\right) dx \tag{5.11}$$

These estimates may then be used in equation (5.7) for the control volume $V_i = \left[x - \frac{1}{2}\Delta x, x + \frac{1}{2}\Delta x\right] \times \left[0, \frac{1}{2}\Delta t\right]$, for equation (5.11) we take $x = x_{i+\frac{1}{2}}$ which results in:

$$\boldsymbol{Q}_{i+\frac{1}{2}}^{n+\frac{1}{2}} = \frac{1}{2}(\boldsymbol{Q}_i^n + \boldsymbol{Q}_{i+1}^n) - \frac{1}{2}\frac{\Delta t}{\Delta x}\widehat{\boldsymbol{A}}_{i+\frac{1}{2}}[\boldsymbol{Q}_{i+1}^n - \boldsymbol{Q}_i^n] \tag{5.12}$$

Similarly, for equation (5.10) around $x = x_{i-\frac{1}{2}}$:

$$\boldsymbol{Q}_{i-\frac{1}{2}}^{n+\frac{1}{2}} = \frac{1}{2}(\boldsymbol{Q}_{i-1}^n + \boldsymbol{Q}_i^n) - \frac{1}{2}\frac{\Delta t}{\Delta x}\widehat{\boldsymbol{A}}_{i-\frac{1}{2}}[\boldsymbol{Q}_i^n - \boldsymbol{Q}_{i-1}^n] \tag{5.13}$$

Replicating the above procedure for second step of the RCM, the Riemann problem $RP\left(\boldsymbol{Q}_{i-\frac{1}{2}}^{n+\frac{1}{2}}, \boldsymbol{Q}_{i+\frac{1}{2}}^{n+\frac{1}{2}}\right)$ may be solved to give $\widehat{\boldsymbol{Q}}_i^{n+1}(x,t)$. An integral average is then substituted for the stochastic sampling process at the complete time step Δt in terms of $\widehat{\boldsymbol{Q}}_i$ at $t = \frac{1}{2}\Delta t$:

$$\boldsymbol{Q}_i^{n+1} = \int_{-\frac{1}{2}x}^{\frac{1}{2}x} \widehat{\boldsymbol{Q}}_i\left(x, \frac{1}{2}\Delta t\right) dx \tag{5.14}$$

Substitution of this into equation (5.7) gives:

$$\boldsymbol{Q}_i^{n+1} = \frac{1}{2}\left(\boldsymbol{Q}_{i+\frac{1}{2}}^{n+\frac{1}{2}} + \boldsymbol{Q}_{i-\frac{1}{2}}^{n+\frac{1}{2}}\right) - \frac{1}{2}\frac{\Delta t}{\Delta x}\widehat{\boldsymbol{A}}_i\left[\boldsymbol{Q}_{i+\frac{1}{2}}^{n+\frac{1}{2}} - \boldsymbol{Q}_{i-\frac{1}{2}}^{n+\frac{1}{2}}\right] \tag{5.15}$$

Where, following Toro and Siviglia (2003), we take:

$$\widehat{\boldsymbol{A}}_i = \boldsymbol{A}\left(\frac{1}{2}\left(\boldsymbol{Q}_{i+\frac{1}{2}}^{n+\frac{1}{2}} + \boldsymbol{Q}_{i-\frac{1}{2}}^{n+\frac{1}{2}}\right)\right) \tag{5.16}$$

and

$$\widehat{\boldsymbol{A}}_{i+\frac{1}{2}} = \boldsymbol{A}\left(\frac{1}{2}(\boldsymbol{Q}_i^n + \boldsymbol{Q}_{i+1}^n)\right) \tag{5.17}$$

The PRICE-T method therefore comprises the numerical scheme given by equation (5.15) coupled with the intermediate states given respectively by equations (5.12) and (5.13). It has been shown (Toro and Siviglia, 2003) that this numerical technique is monotonic and requires that the time step obeys the CFL criterion to ensure stability (see section 4.2.2).

The above method is first-order accurate. In order to extend the scheme to second-order accuracy additional steps are required. The method applied is the MUSCL-Hancock originally developed for conservative methods, but later adapted for use with non-conservative methods by Toro (1998). The strategy in this method is to gain accuracy by better describing the state at time t using a higher order polynomial reconstruction. In order to avoid oscillations near discontinuities a slope limiter (see for example Toro, 2009) is used to reduce this reconstruction to first-order. This is necessary due to the theorem of Godunov (1959) which states that only first-order monotonic schemes may capture these correctly.

For the scheme developed above the MUSCL-Hancock approach initially requires MUSCL reconstruction:

$$\boldsymbol{Q}_i^L = \boldsymbol{Q}_i^n - \frac{1}{2}\bar{\Delta}_i, \qquad \boldsymbol{Q}_i^{\mathrm{R}} = \boldsymbol{Q}_i^n + \frac{1}{2}\bar{\Delta}_i \tag{5.18}$$

Where, $\bar{\Delta}_i$ is a limited slope given by

$$\bar{\Delta}_i = \phi(r)(\boldsymbol{Q}_{i+1}^n - \boldsymbol{Q}_i^n) \tag{5.19}$$

The function ϕ is a slope limiter with argument:

$$\boldsymbol{r} = \frac{\boldsymbol{Q}_i^n - \boldsymbol{Q}_{i-1}^n}{\boldsymbol{Q}_{i+1}^n - \boldsymbol{Q}_i^n} \tag{5.20}$$

And is defined as

$$\phi(r) = \begin{cases} 0 & \text{if } r \leq 0 \\ min\left\{\frac{2r}{1+r}, r\right\} & \text{if } r \geq 0 \end{cases} \quad \textbf{(5.21)}$$

The reconstructed states are then evolved by a time of increment $\frac{1}{2}\Delta t$ as follows:

$$\overline{\boldsymbol{Q}}_i^{L,R} = \boldsymbol{Q}_i^{L,R} - \frac{1}{2}\frac{\Delta t}{\Delta x}\widehat{\boldsymbol{A}}_i[\boldsymbol{Q}_i^R - \boldsymbol{Q}_i^L] \quad \textbf{(5.22)}$$

Computation of the intermediate states (for example $\boldsymbol{Q}_{i+\frac{1}{2}}$) using the PRICE-T scheme is then given by:

$$\boldsymbol{Q}_{i+\frac{1}{2}}^{n+\frac{1}{2}} = \frac{1}{2}(\overline{\boldsymbol{Q}}_i^R + \overline{\boldsymbol{Q}}_{i+1}^L) - \frac{1}{2}\frac{\Delta t}{\Delta x}\widehat{\boldsymbol{A}}_{i+\frac{1}{2}}[\overline{\boldsymbol{Q}}_{i+1}^n - \overline{\boldsymbol{Q}}_i^n] \quad \textbf{(5.23)}$$

5.3 Validation

The full description of the FV PRICE-T scheme applied to the PHU formulation of Atti's (2006) model was presented above. In this section, the performance of both first and second order PRICE-T schemes (PRICE-1 and PRICE-2 resp.) is assessed by comparison of their predictions against three sets of field data appropriate for the modelling of the failure of long pipelines (> 100 m). These are the intact end pressure data from the Piper Alpha disaster, the release rate measurements from the TransCanada accident and the series of experiments carried out by Shell and BP on the Isle of Grain (Chen, 1993; Richardson and Saville, 1996). The validations have been grouped according to the type of failure including the more catastrophic full bore rupture (FBR) and pipeline puncture. All simulations presented in this work are conducted on a Dell 3.2 GHz Intel Xeon PC.

5.3.1 Full Bore Rupture

The TransCanada pipeline accident (HSE, 2004) involved the FBR of a 76 km, 894.4 mm i.d. pipeline containing 100 % methane at 61 bara. The rupture location was 38 km along the isolated pipeline length. The Piper Alpha investigation on the other hand is based on the pressure-time data recorded (Cullen, 1990) during the night of the Piper Alpha tragedy involving the full bore rupture of the main 54 km natural gas riser connecting the Piper Alpha to the MCP01 platform. Table 5.1 shows the prevailing conditions used to simulate both pipeline ruptures.

Figure 5.3 shows the comparison of the discharge rate with time following the rupture of the TransCanada pipeline. Curve A represents the measured data, while curves B, C and D are the predicted results obtained using the Method of Characteristics (MOC), PRICE-1 and PRICE-2 respectively. As no data were recorded during the first 10 s following pipeline rupture, it is impossible to compare the performance of the numerical techniques in this highly transient region. However, subsequent to this period a reasonably good degree of agreement between theory and measurements is observed in all cases with MOC being in best accord. A possible explanation for the finite discrepancies between experiment and theory could be due to the assumption of the pipeline inventory being 100 % methane. In practice heavier molecular weight hydrocarbons may have been present.

The differences between the theoretical predictions on the other hand are likely due to the numerical diffusion effects associated with the discretisation. The computational runtimes for the MOC and the PRICE-1 and PRICE-2 schemes are 627, 414 and 725 s respectively. As the focus of this study is the reduction in the CPU runtime and there is no appreciable difference between the PRICE-2 and PRICE-1 predictions, the latter scheme is used as the numerical solution technique for comparison with MOC in the proceeding investigations. For simplicity all subsequent simulations employing the PRICE-1 scheme are hereby referred to as FVM.

Figure 5.4 shows the variation of the intact end pressure with time data recorded following the full bore rupture of the MCP01 during the night of the Piper Alpha. Curve

A is the measured field data while curves B and C are the MOC and FVM simulation results respectively.

As it may be observed, there is good agreement between the simulation and the measured data throughout with the predictions showing no discernable differences. The corresponding CPU times for MOC and FVM are 20685 and 11762 s respectively representing a ca. 43 % reduction.

Table 5.1: Pipeline characteristic for the simulations of the Piper Alpha (Cullen, 1990) and TransCanada (HSE, 2004) pipeline ruptures.

Input		Piper Alpha	TransCanada
Inlet Parameters	Number of components	9	1
	Feed composition (mole %)	methane - 73.6 ethane - 13.4 propane - 7.4 i-butane - 0.4 n-butane - 1.0 i-pentane - 0.08 n-pentane -0.07 hexane - 0.02 nitrogen - 4.03	methane - 100
	Feed inlet temperature (K)	283	283
	Feed inlet pressure (bara)	117	61
	Ambient temperature (K)	283	283
	Ambient pressure (bara)	1.01	1.01
Pipeline Characteristics	Length (m)	54000	76000
	External diameter (mm)	457	914.4
	Wall thickness (mm)	19	10
	Roughness (mm)	0.026	0.05
	Orientation to the horizontal plane (deg)	0	0
Rupture Conditions	Failure mode	FBR	FBR
	Failure location relative to high pressure end (m)	54000	38000
	Rupture diameter (mm)	419	894.4
	Discharge coefficient	1	1
Other Parameters	Feed flow rate prior to rupture (m^3/s)	0	0
	Pumping cessation time following pipeline failure (s)	0	0
	Pump shut-off head (bara)	110	110
	Grid system used	Nested	Simple
	Number of grid points specified	108	3000
	Equation of State	PR	PR
	Friction factor correlation	Chen	Chen
	Heat transfer coefficient (W/m^2K)	1.136	5
	Total depressurisation time (s)	20000	60

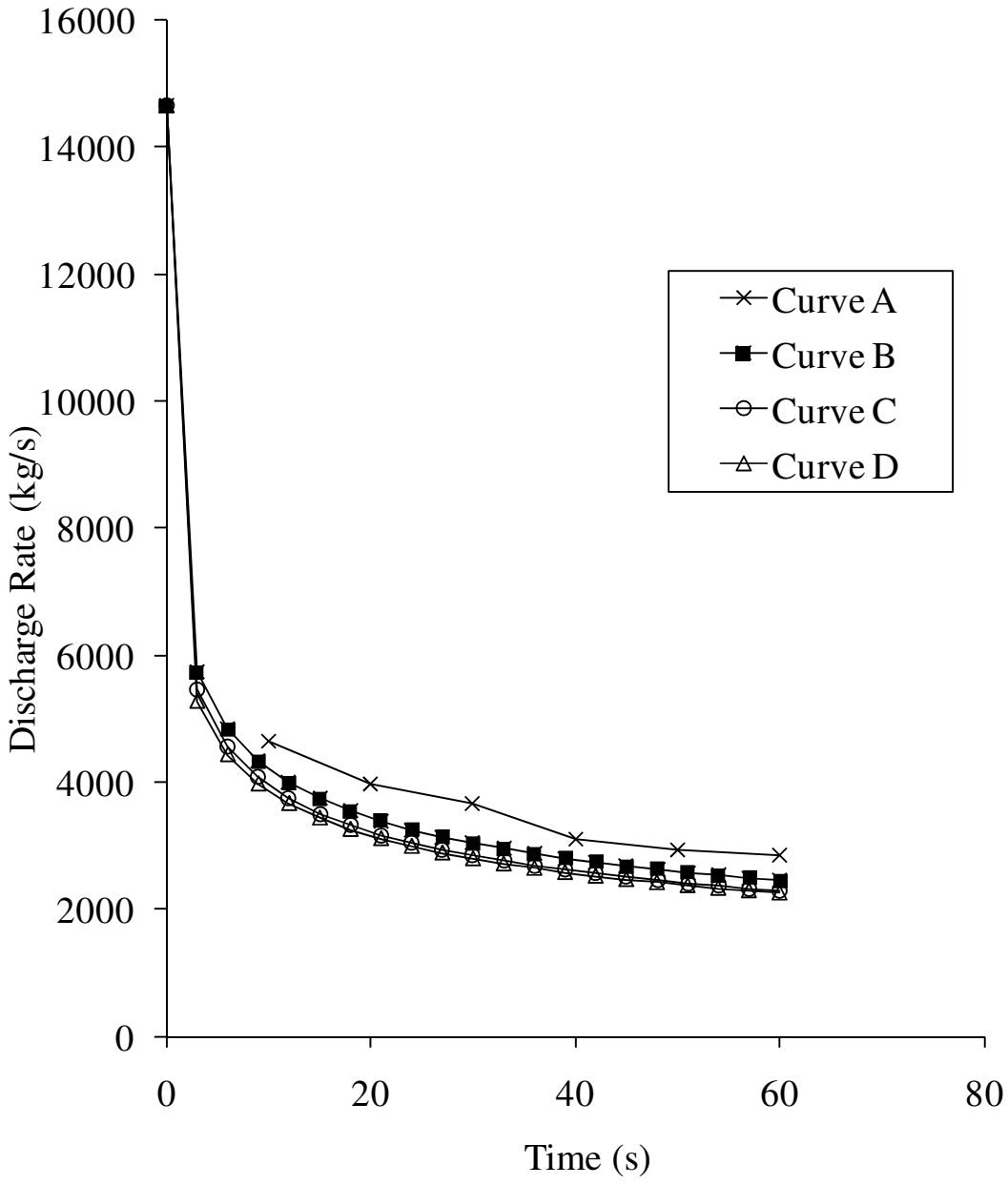

Figure 5.3: Comparison of variation of release rate with time following the FBR TransCanada pipeline.

Curve A: Experimental data (HSE, 2004)

Curve B: MOC, CPU runtime = 627 s

Curve C: PRICE-1 method, CPU runtime = 414 s

Curve D: PRICE-2 method, CPU runtime = 725 s

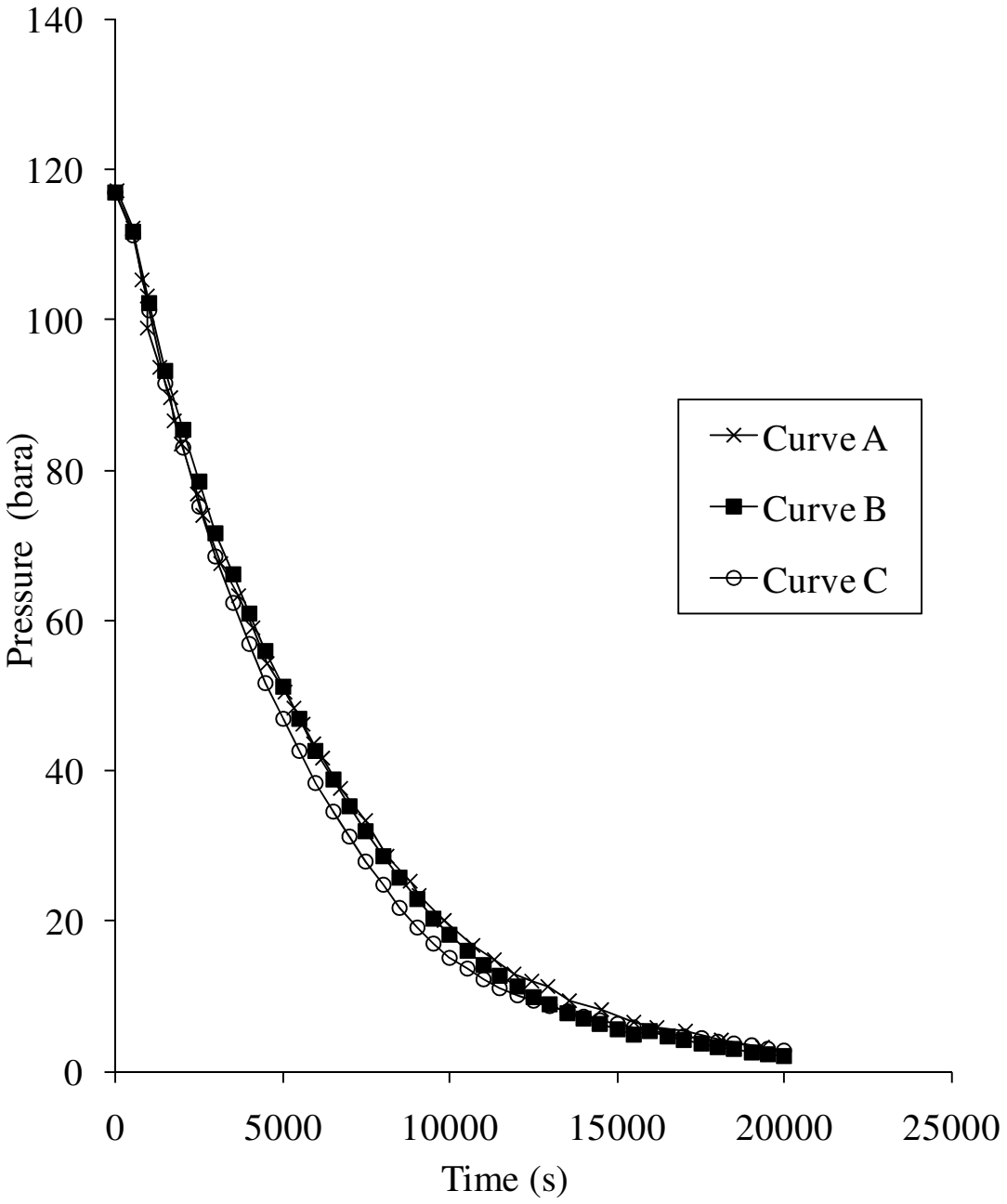

Figure 5.4: Comparison of the variation of closed end pressure with time data following the FBR of the MCP01 pipeline during the Piper Alpha disaster.

Curve A: Field data (Cullen, 1990)

Curve B: MOC, CPU runtime = 20685 s

Curve C: FVM, CPU runtime = 11762 s

Similar comparisons were attempted for the Isle of Grain FBR tests P40 and P42 (Chen, 1993; Richardson and Saville, 1996). As discussed in chapter 2, the inventory for these tests was a mixture of 95 % propane 5 % n-butane which was initially liquid but became two-phase upon depressurisation. However for both tests P40 and P42 the FV scheme was found to be unstable at the initial time step. This was due to large oscillations resulting in a negative pressure, induced by the rapid discontinuity in the fluid properties. Upon further investigation, this behaviour was observed in all FBR scenarios where the fluid was initially in the liquid phase.

5.3.2 Punctures

In this section the validation of the PRICE-1 method against the Isle of Grain tests P45 and P47 (Chen, 1993; Richardson and Saville, 1996) is presented. A discharge coefficient of 0.8 and the nominal diameters are applied following Richardson and Saville (1996). The pipeline characteristics, inventory and prevailing conditions are given in table 5.2.

Figures 5.5 and 5.6 respectively show the variation of release pressure and temperature with time for the Isle of Grain Test P45. Figures 5.7 and 5.8 on the other hand show the corresponding data for Test P47. Curves A shows the measured data, while curves B and C are the simulated data obtained from the MOC and FVM schemes respectively.

Table 5.2: Simulation Input Data for Isle of Grain P45 and P47.

Inputs		Isle of Grain P45	Isle of Grain P47
Inlet Parameters	Number of components	2	2
	Feed Composition (mole %)	propane – 95	propane – 95
		n-butane - 5	n-butane – 5
	Feed Inlet Temperature (K)	290.45	288.75
	Feed Inlet Pressure (bara)	11.4	21.6
	Ambient Temperature (K)	292.25	291.75
	Ambient Pressure (bara)	1.01	1.01
Pipeline Characteristics	Pipeline Length (m)	100	100
	Pipe External Diameter (mm)	168.6	168.6
	Pipe Wall Thickness (mm)	7.3	7.3
	Pipeline Roughness (mm)	0.05	0.05
	Pipe Orientation to the Horizontal Plane (deg)	0	0
Rupture Conditions	Failure Mode	Puncture	Puncture
	Failure Location Relative to High Pressure end (m)	-	-
	Orifice/Rupture Diameter (mm)	95	70
	Discharge Coefficient	0.8	0.8
Other Parameters	Feed Flow Rate prior to Rupture (m^3/sec)	0	0
	Pumping Cessation Time Following Pipeline Failure (s)	0	0
	Pump Shut-off Head (bara)	110	110
	Grid System Used	Simple	Simple
	Number of Grid Points Specified	50	50
	Equation of State	Peng-Robinson	Peng-Robinson
	Friction Factor Correlation	Chen	Chen
	Heat Transfer Coefficient	Automatically Determined	Automatically Determined
	Total Depressurisation Time (s)	65	150

Returning to figure 5.5, an instantaneous drop in the pressure is observed upon onset of the blowdown corresponding to the transition from the liquid to the two-phase state. The FVM (curve C) shows a slightly greater drop than the MOC (curve B), before recovering to a similar pressure after 2 s. Both models then predict a slow decline to the ambient conditions, both sets of results indicating complete depressurisation at roughly the same time. The MOC produces marginally better agreement with the measured data for the latter stages of the depressurisation as compared to the FVM. The deviation between the two models most likely a result of numerical diffusion due to phase

transition. The discrepancy between both models and the experimental data at the tail end of blowdown (> 50 s) could be due to non-homogeneous effects highlighted by Richardson et al. (2006).

As it may be observed from figure 5.6, the release temperatures predicted by both methods are in relatively good agreement with the measured data up to ca. 40 s following puncture. Following this both the MOC and the FVM (curves B and C resp.) show a marked drop in the temperature before recovering towards the ambient temperature of 292.25 K. This increase in temperature is more marked in the case of the FVM. The latter case recovery in the temperature, not seen in the case of the measured data may be expected due to the warming of the pipe wall by the surrounding ambient. The corresponding respective CPU runtimes of 1027 s for the MOC and 694 s for FVM are given in the figure captions.

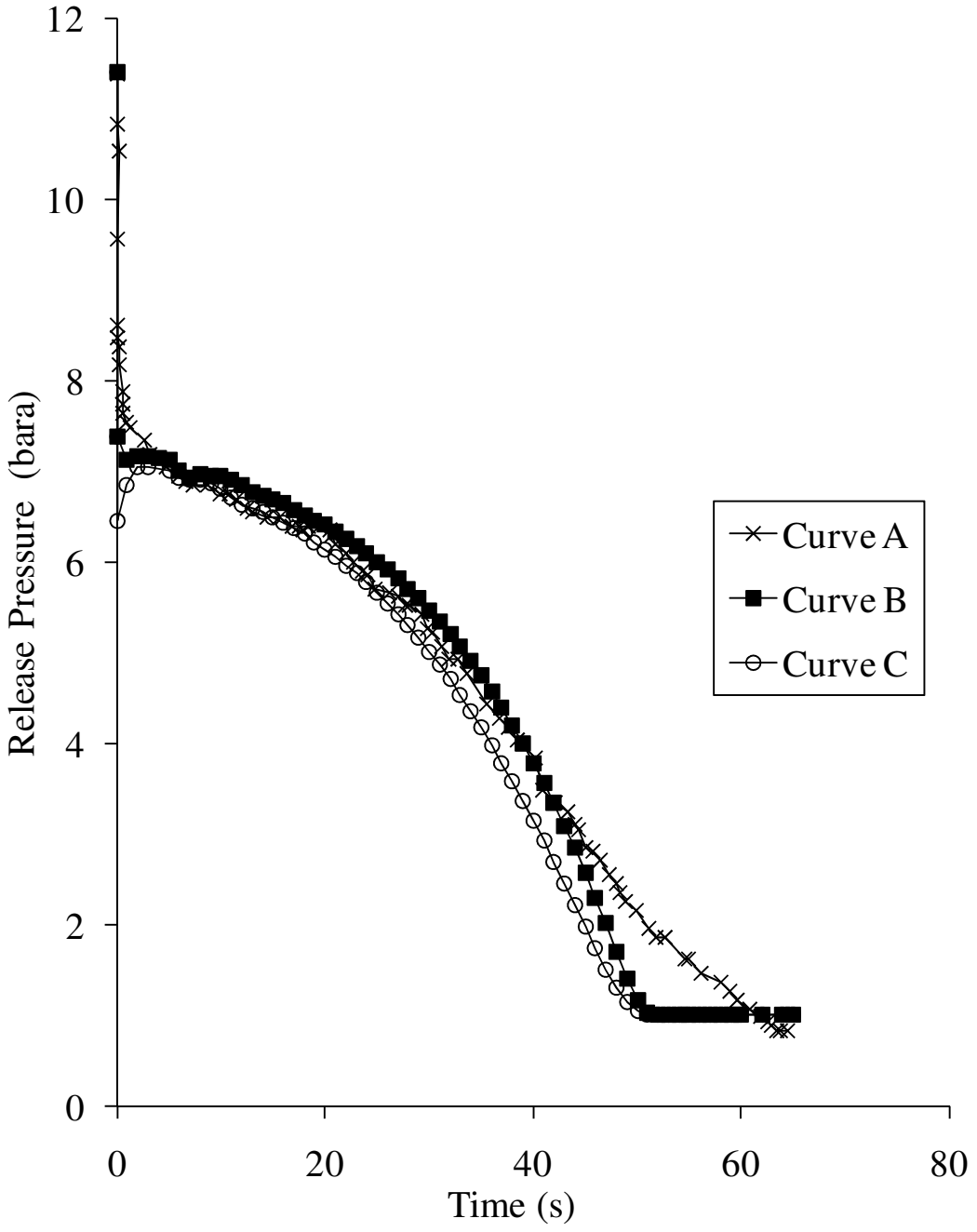

Figure 5.5: Variation of open end pressure with time following a 95 mm diameter axisymmetric puncture for test P45.

Curve A: Experimental (Richardson and Saville, 1996)

Curve B: MOC, CPU runtime = 1027 s

Curve C: FVM, CPU runtime = 694 s

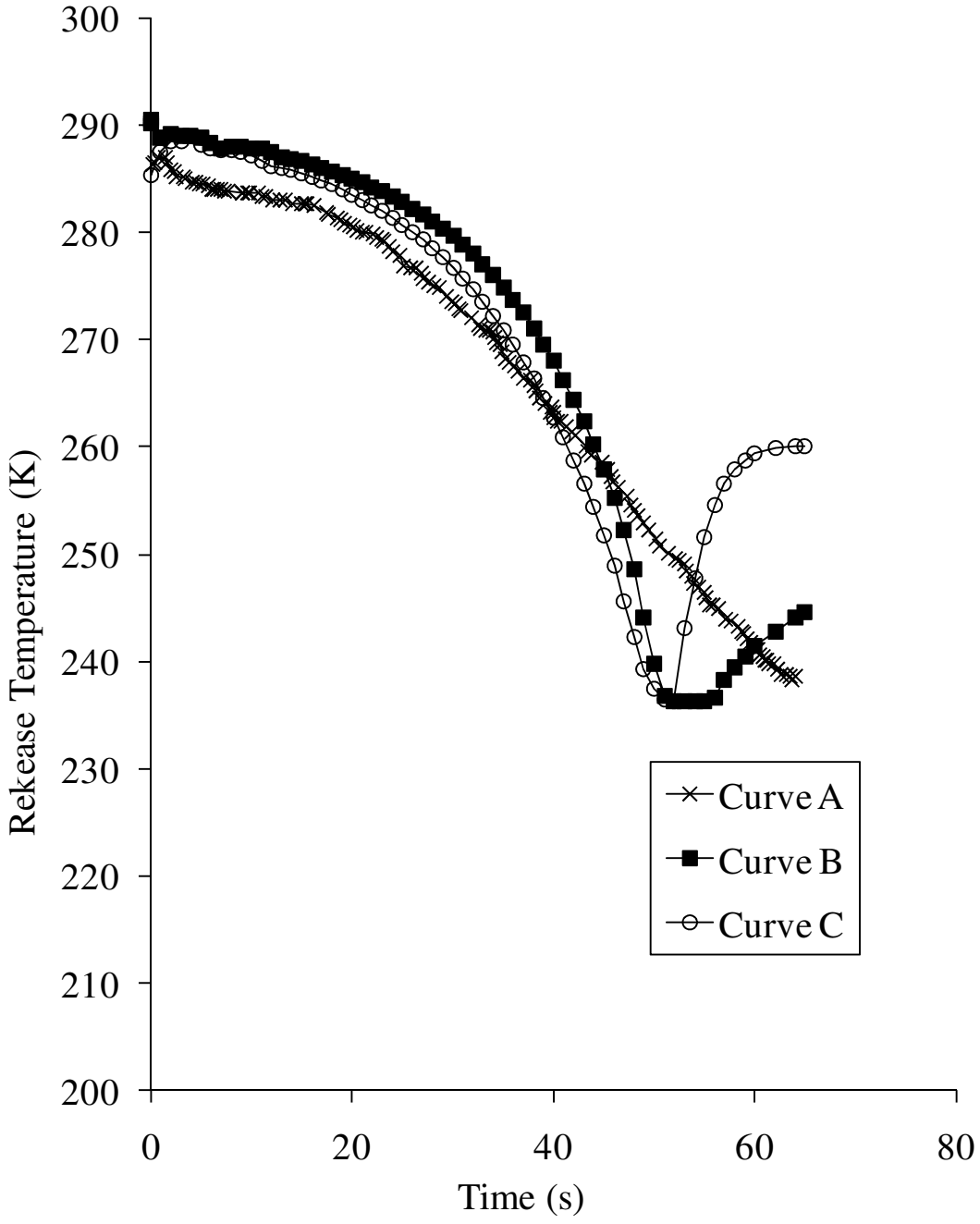

Figure 5.6: Variation of open end temperature with time following a 95 mm diameter axisymmetric puncture for test P45.

Curve A: Experimental (Richardson and Saville, 1996)

Curve B: MOC, CPU runtime = 1027 s

Curve C: FVM, CPU runtime = 694 s

The data presented in figures 5.7 and 5.8 for Test P47 (70 mm puncture diameter) show similar trends to those for P45 (90 mm diameter). However, the initial pressure recovery observed in the corresponding FVM data (curve C) for P45 is not seen in this case. Both models then predict a slow depressurisation to the ambient pressure. The FVM produces marginally better agreement with the experimental data as compared to the MOC.

The rupture plane temperature data shown in figure 5.8 exhibits similar trends to the above. Corresponding to the time at which depressurisation occurs (see figure 5.7) the MOC (curve B) predicts a temperature recovery similar to that observed in the measured data. In contrast, the FVM (curve C) remains constant from this point. The reason for this disagreement is not clear given the post-depressurisation temperature recovery observed for Test P45.

The corresponding respective CPU runtimes of 2351 s for the MOC and 1625 s for the FVM are given in the figure captions. Based on the above, the FVM requires ca. 31 % less computational runtime as compared to the MOC.

Given the degree of uncertainty over the precise composition of the pipeline inventory pipeline (Atti, 2006), the inaccuracies associated with the vapour-liquid equilibrium (VLE) calculations, and the significantly shorter computational runtime, the predictions given by the FVM present an acceptable alternative to those provided by the MOC.

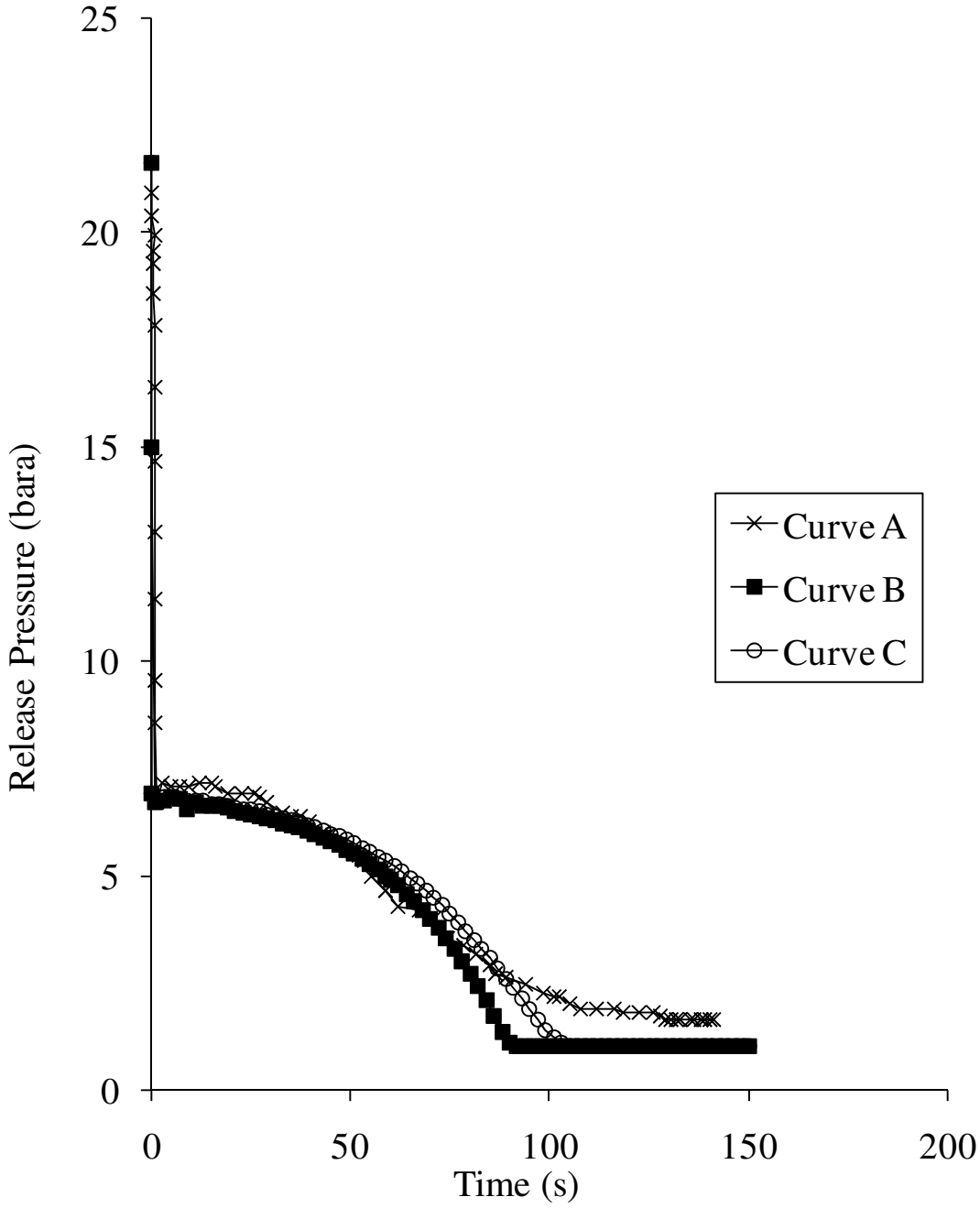

Figure 5.7: Variation of open end pressure with time following a 70 mm diameter axisymmetric puncture for test P47.

Curve A: Experimental (Richardson and Saville, 1996)

Curve B: MOC, CPU runtime = 2351 s

Curve C: FVM, CPU runtime = 1625 s

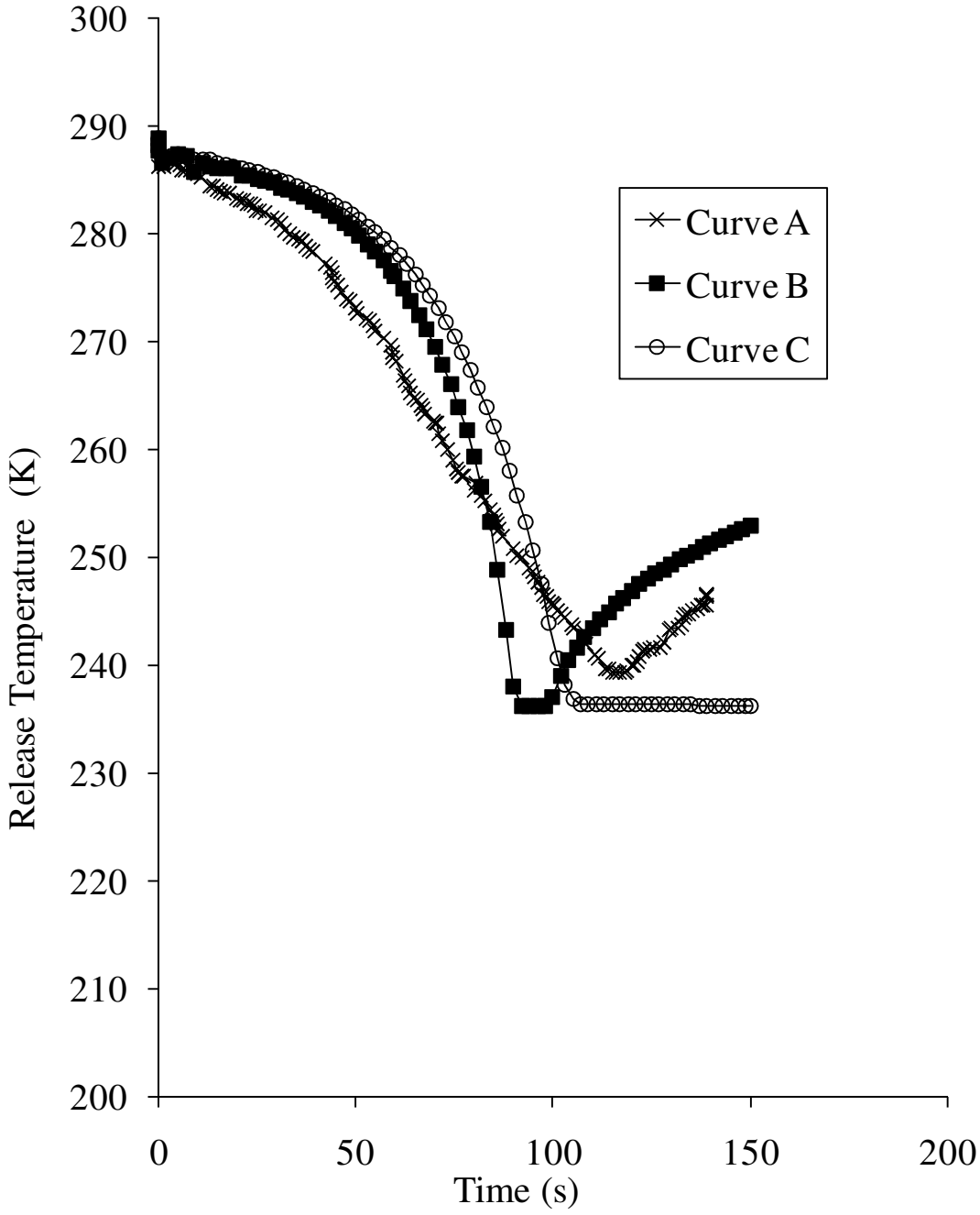

Figure 5.8: Variation of open end temperature with time following a 70 mm diameter axisymmetric puncture for test P47.

Curve A: Experimental (Richardson and Saville, 1996)

Curve B: MOC, CPU runtime = 2351 s

Curve C: FVM, CPU runtime = 1625 s

5.4 Case Study

In the previous section the FVM (PRICE-1) was validated against experimental and field data sets for full bore rupture and punctures. In order to further evaluate the efficacy of the FVM in comparison with the predictions of the MOC, the following presents and discusses the results of a series of simulations based on the failure of an hypothetical 1 km pipeline at 60 bara and 293.15 K. Different classes of inventories including a permanent gas, a two-phase mixture and a permanent liquid are investigated for both full bore rupture and puncture failure scenarios.

Table 5.3 gives the corresponding detailed pipeline characteristics, prevailing conditions and respective mixtures used for the simulations. In the case of full bore rupture, failure is assumed to occur at the end of the 1 km long, 154 mm i.d. pipeline. For the puncture case on the other hand a 50 mm dia. failure is assumed to take place half way along the pipeline.

5.4.1 Permanent Gas

Figures 5.9, 5.10 and 5.11 respectively show the variations of rupture plane pressure, discharge rate and rupture plane temperature with time following the full bore rupture of an hypothetical pipeline containing 95 % methane and 5 % ethane. For the conditions tested, the inventory remains in the gaseous phase throughout the depressurisation process. Curve A represents the results predicted using the MOC while curve B shows those obtained from the FVM. The corresponding data relating to the puncture scenario are given in figures 5.12, 5.13 and 5.14 respectively.

As may be observed from figure 5.9, with the exception of the slightly faster depressurisation rate in the case of FVM immediately following the almost instantaneous pressure drop the two sets of predictions are in excellent accord. The discharge rate data shown in figure 5.10 exhibits exactly the same trend.

In the case of the rupture plane temperature (figure 5.11), both the FVM and MOC exhibit the large initial temperature drop and subsequent recovery. However, the temperature recovery predicted by the FVM is ca. 4 K greater than that by the MOC. Following this both profiles show:

1. A further small temperature drop
2. A period of almost constant temperature
3. A temperature recovery starting at ca. 40 s.

For this period the FVM continues to predict temperatures of approximately 4 K above those predicted by the MOC. Initially this discrepancy was thought to originate from numerical diffusion associated with the spatial discretisation, however upon further study this was found not to be the case. The reason for this disagreement is therefore unknown, importantly however it is not observed in any other comparisons in this case study.

The corresponding CPU runtimes for the MOC and FVM are 901 and 366 s respectively are given in the figure captions. Hence, the use of the FVM leads to a ca. 59 % reduction in the CPU runtime as compared to MOC.

Returning to the puncture data (figures 5.12 to 5.14) as was seen in the case of FBR (figures 5.9 to 5.11), the simulation results show a good degree of agreement. However, interestingly in contrast to FBR, better agreement between the two sets of simulations is obtained during the early part of the depressurisation process as compared to the latter stages where the FVM indicates marginally slower discharge and depressurisation rates as compared to the MOC.

Table 5.3: Simulation Input Data for comparative case study.

Inputs		Full Bore Rupture	Puncture
Inlet Parameters	Feed Inlet Temperature (K)	293.15	293.15
	Feed Inlet Pressure (bara)	60	60
	Ambient Temperature (K)	293.15	293.15
	Ambient Pressure (bara)	1.01	1.01
Pipeline Characteristics	Pipeline Length (m)	1000	1000
	Pipe External Diameter (mm)	168.6	168.6
	Pipe Wall Thickness (mm)	7.3	7.3
	Pipeline Roughness (mm)	0.05	0.05
	Pipe Orientation to the Horizontal Plane (deg)	0	0
Rupture Conditions	Failure Mode	Full Bore Rupture	Puncture Along the Pipeline length
	Failure Location Relative to High Pressure end (m)	1000	500
	Orifice/Rupture Diameter (mm)	154	50
	Discharge Coefficient	1	1
Other Parameters	Feed Flow Rate prior to Rupture (m^3/sec)	0	0
	Pumping Cessation Time Following Pipeline Failure (s)	0	0
	Pump Shut-off Head (bara)	110	110
	Grid System Used	Simple	Simple
	Number of Grid Points Specified	250	250
	Equation of State	Peng-Robinson	Peng-Robinson
	Friction Factor Correlation	Chen	Chen
	Heat Transfer Coefficient	Automatically Determined	Automatically Determined
	Total Depressurisation Time (s)	60	60

The corresponding CPU times for the MOC and FVM are 1631 and 1255 s respectively are given in the figure captions. Hence, the use of the FVM leads to a ca. 23 % reduction in the CPU runtime as compared to the MOC.

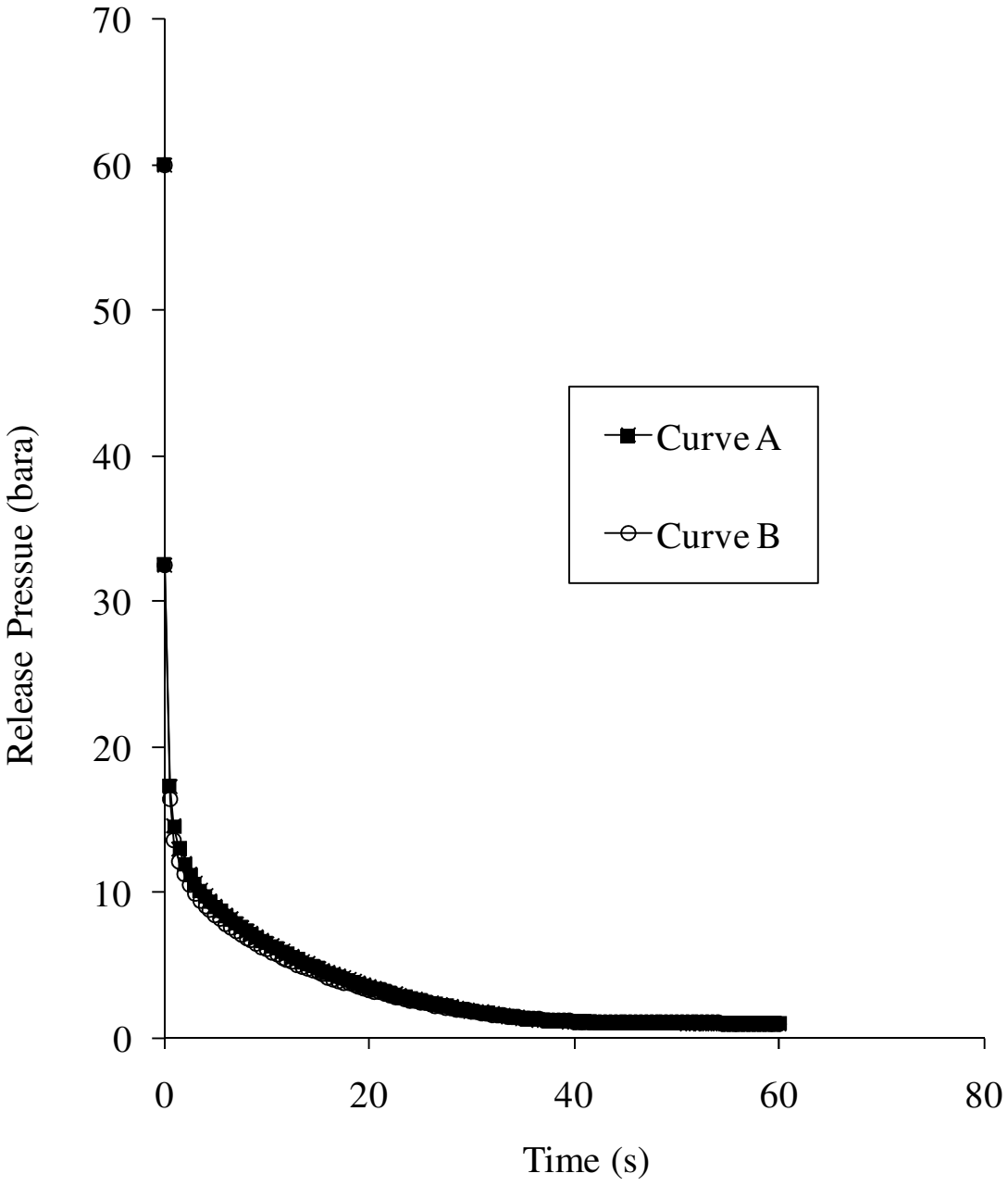

Figure 5.9: Variation of release pressure with time for the permanent gas inventory following FBR.

Curve A: MOC, CPU runtime = 901 s

Curve B: FVM, CPU runtime = 366 s

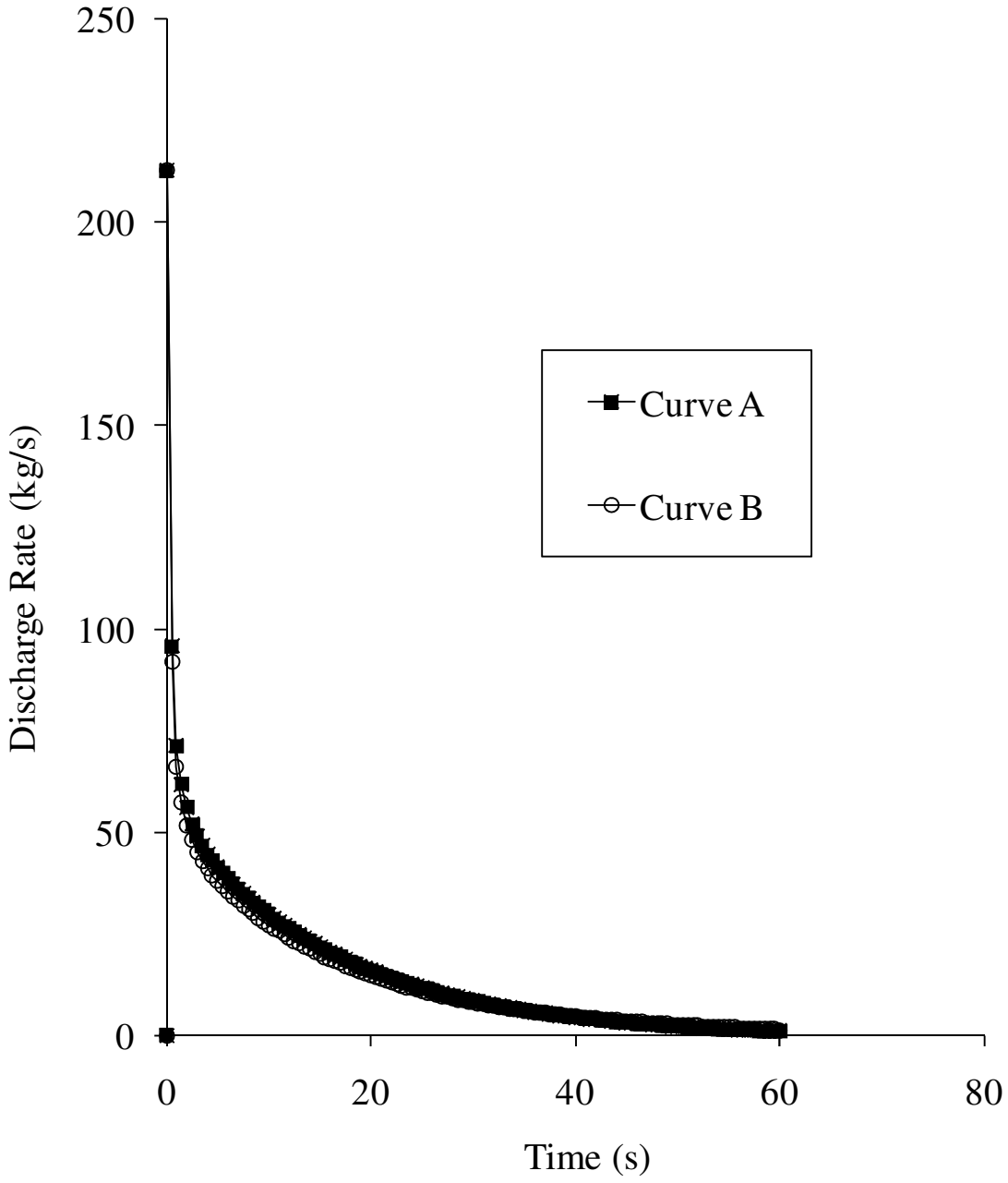

Figure 5.10: Variation of discharge rate with time for the permanent gas inventory following FBR.

Curve A: MOC, CPU runtime = 901 s

Curve B: FVM, CPU runtime = 366 s

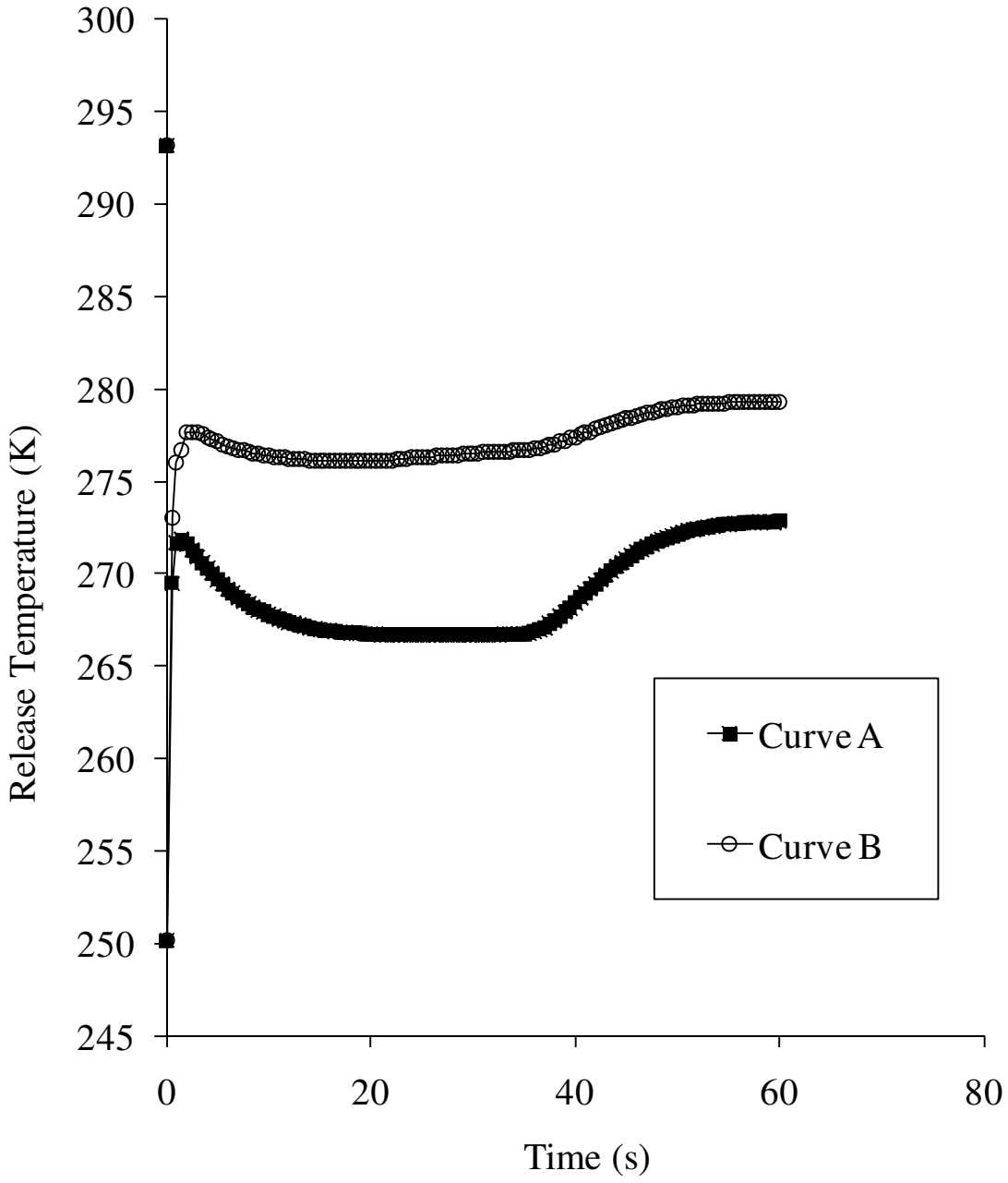

Figure 5.11: Variation of release temperature with time for the permanent gas inventory following FBR.

Curve A: MOC, CPU runtime = 901 s

Curve B: FVM, CPU runtime = 366 s

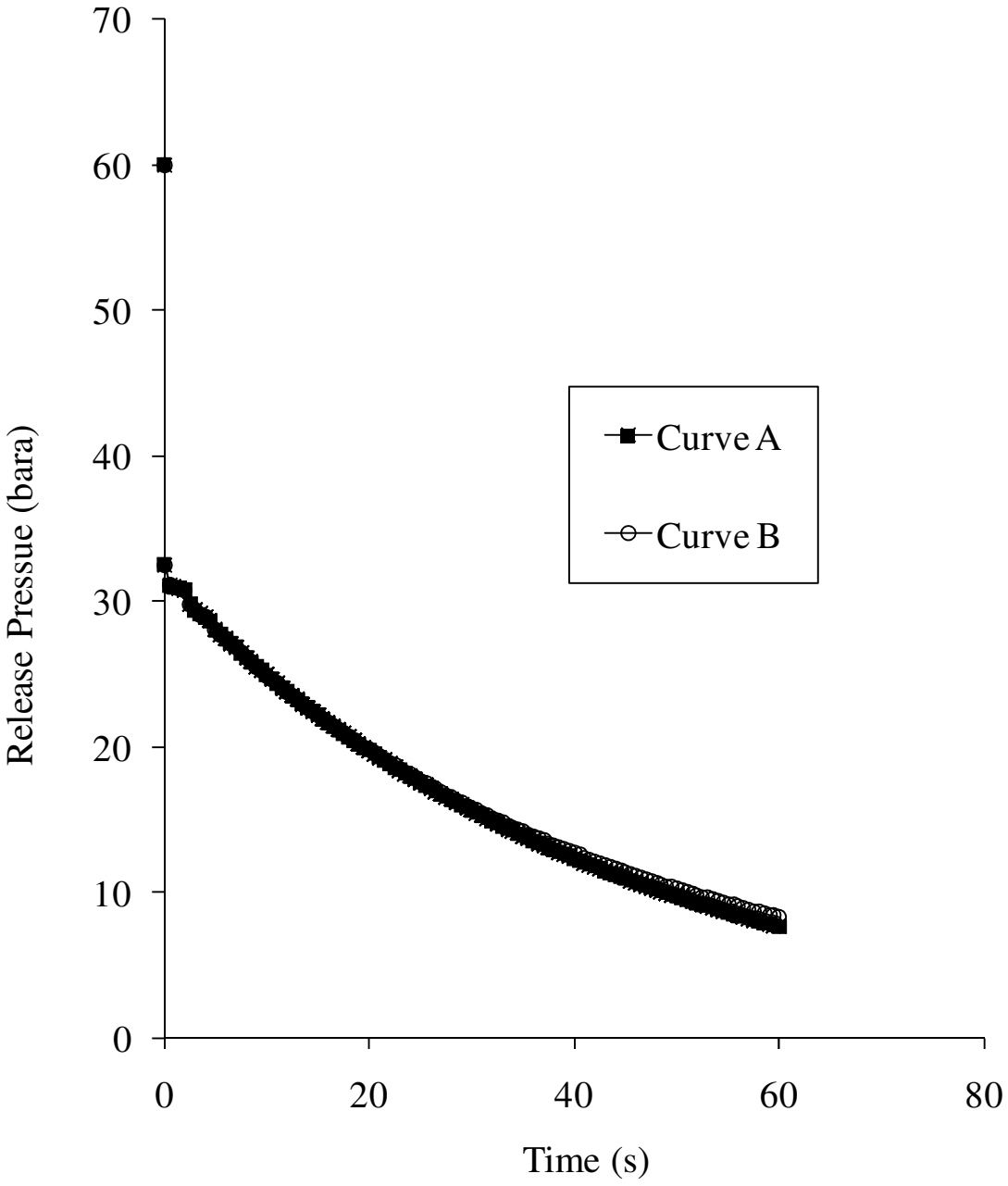

Figure 5.12: Variation of release pressure with time for the permanent gas inventory following puncture.

Curve A: MOC, CPU runtime = 1631 s

Curve B: FVM, CPU runtime = 1255 s

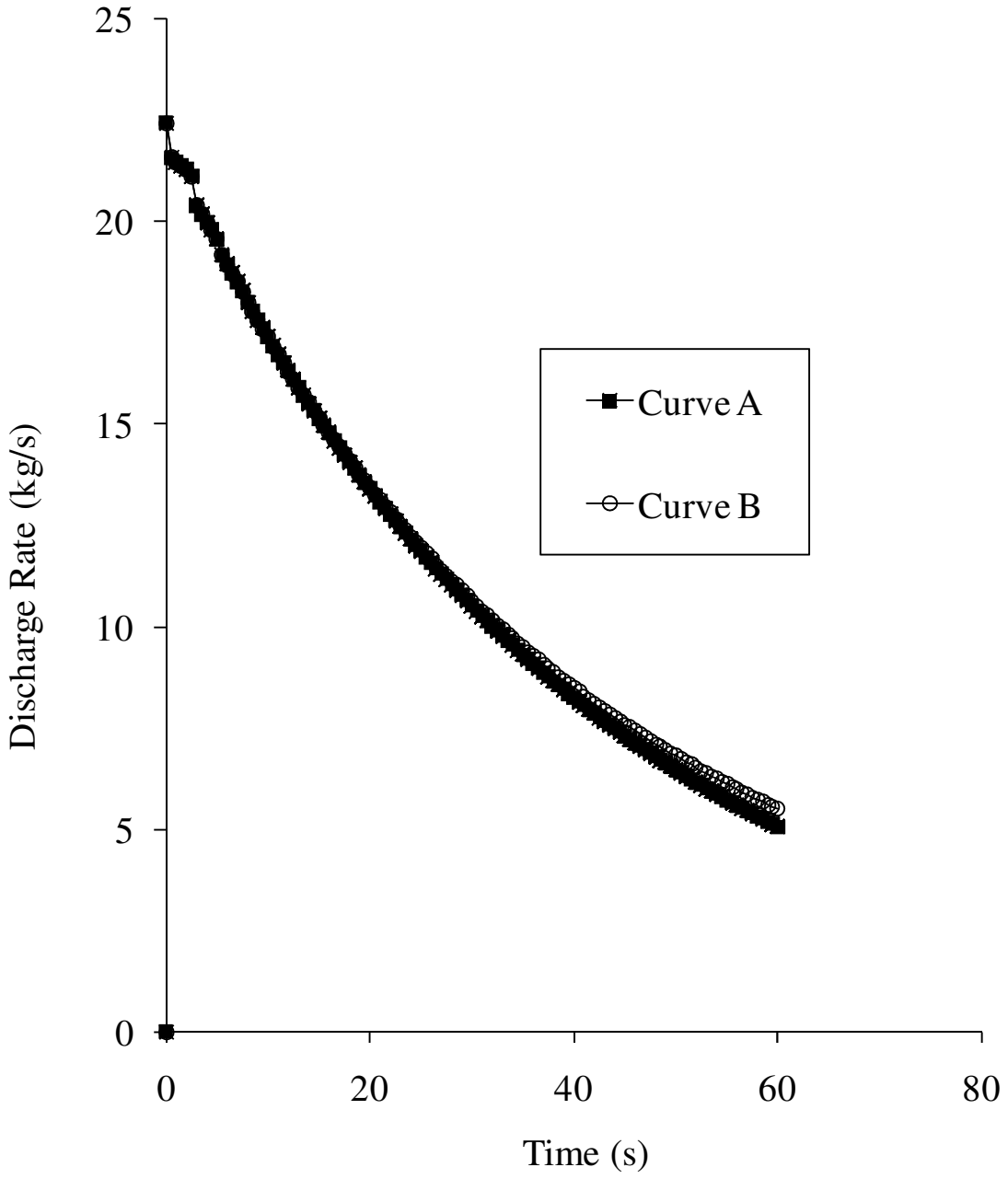

Figure 5.13: Variation of discharge rate with time for the permanent gas inventory following puncture.

Curve A: MOC, CPU runtime = 1631 s

Curve B: FVM, CPU runtime = 1255 s

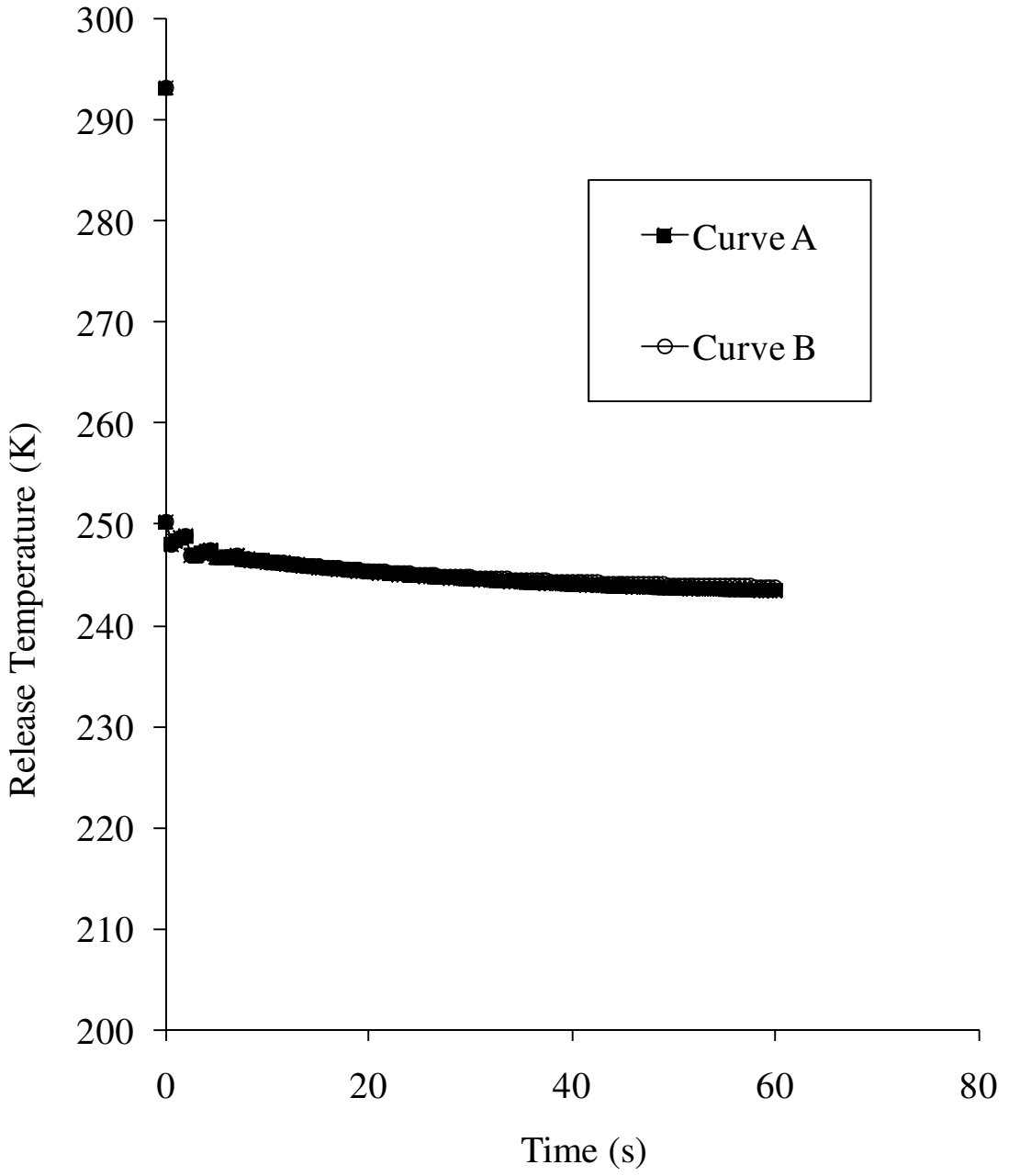

Figure 5.14: Variation of release temperature with time for the permanent gas inventory following puncture.

Curve A: MOC, CPU runtime = 1631 s

Curve B: FVM, CPU runtime = 1255 s

5.4.2 Two-phase Mixture

Figures 5.15, 5.16 and 5.17 respectively show the variations of rupture plane pressure, discharge rate and rupture plane temperature with time following the full bore rupture for a pipeline carrying 50 % methane and 50 % n-butane. The inventory remains a two-phase mixture throughout the depressurisation process. Figures 5.18, 5.19 and 5.20 show the corresponding comparisons for the puncture scenario.

As it may be observed from figure 5.15, despite the slightly faster depressurisation rate exhibited by the FVM immediately following the almost instantaneous pressure drop the two sets of predictions are in excellent agreement.

The discharge rate and rupture plane temperature data shown in figures 5.16 and 5.17 respectively exhibit exactly the same trends as above. The corresponding CPU times for the MOC and FVM are 1233 and 274 s respectively corresponding to a ca. 78 % reduction.

Returning to the puncture data (figures 5.18 to 5.20) in contrast to the case of FBR (figures 5.15 to 5.17) the puncture simulation results are identical throughout the depressurisation process. The CPU runtimes for the MOC and FVM are 1283 and 874 s respectively corresponding to a ca. 32 % reduction.

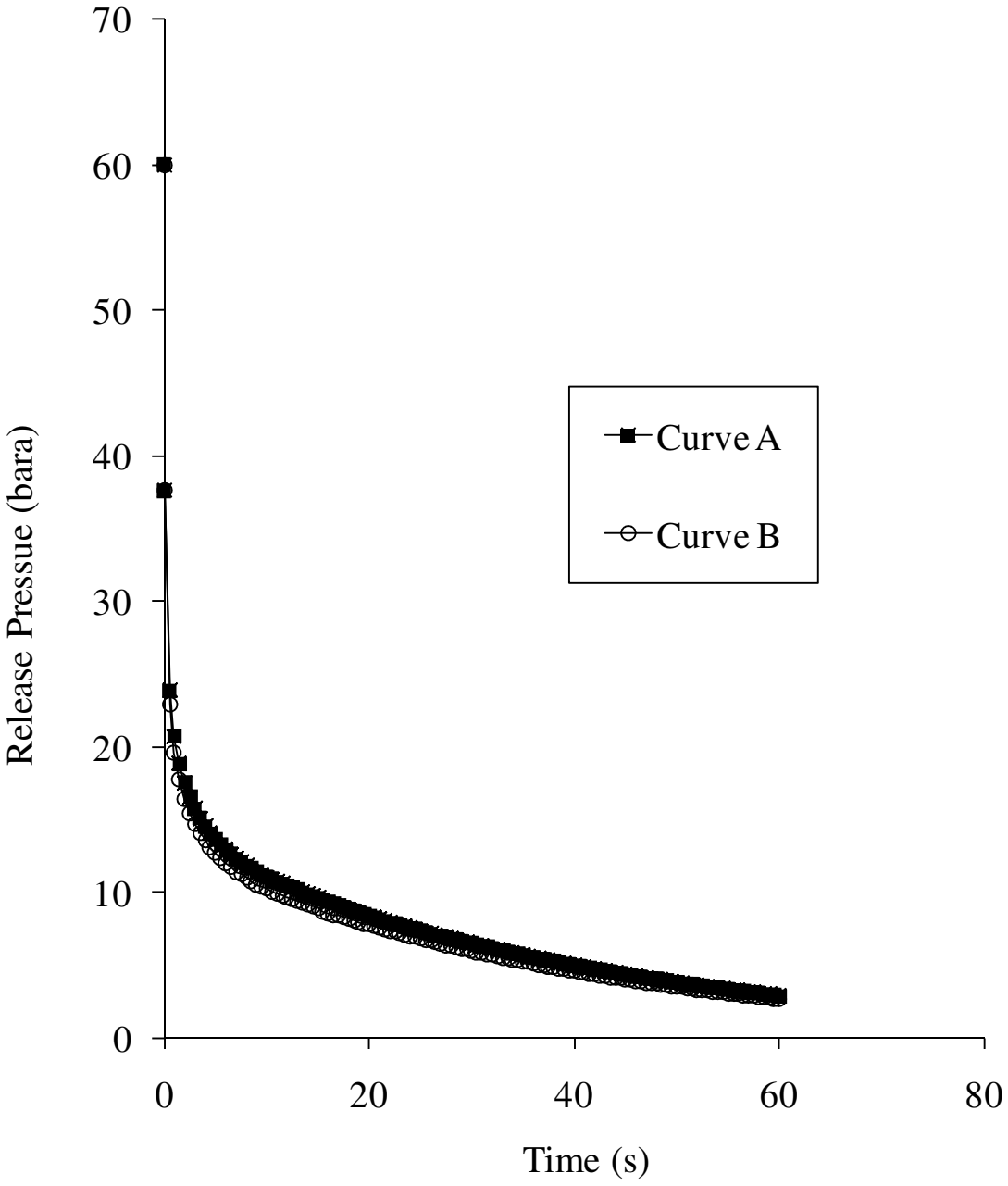

Figure 5.15: Variation of release pressure with time for the two-phase inventory following FBR.

Curve A: MOC, CPU runtime = 1233 s

Curve B: FVM, CPU runtime = 274 s

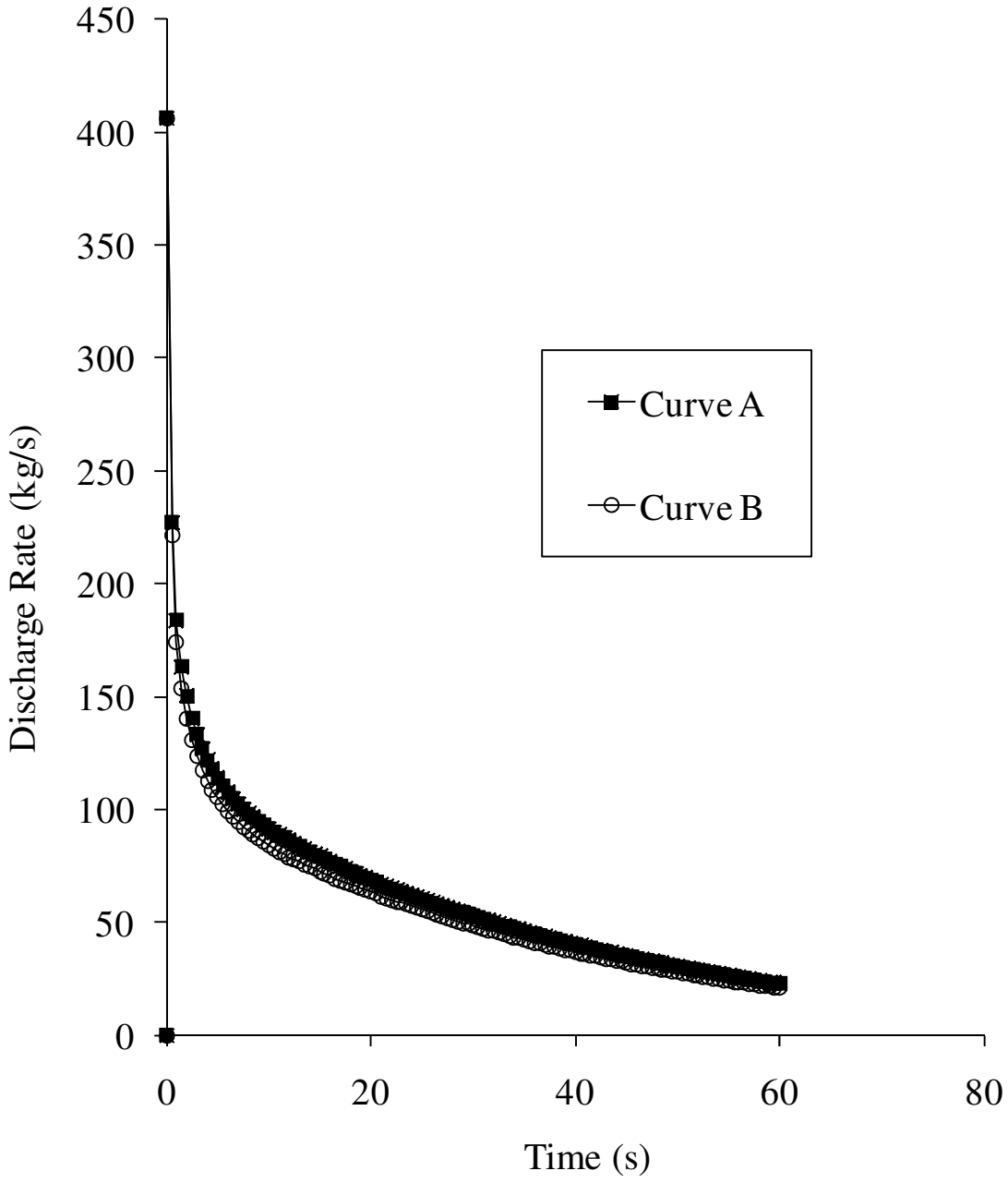

Figure 5.16: Variation of discharge rate with time for the two-phase inventory following FBR.

Curve A: MOC, CPU runtime = 1233 s

Curve B: FVM, CPU runtime = 274 s

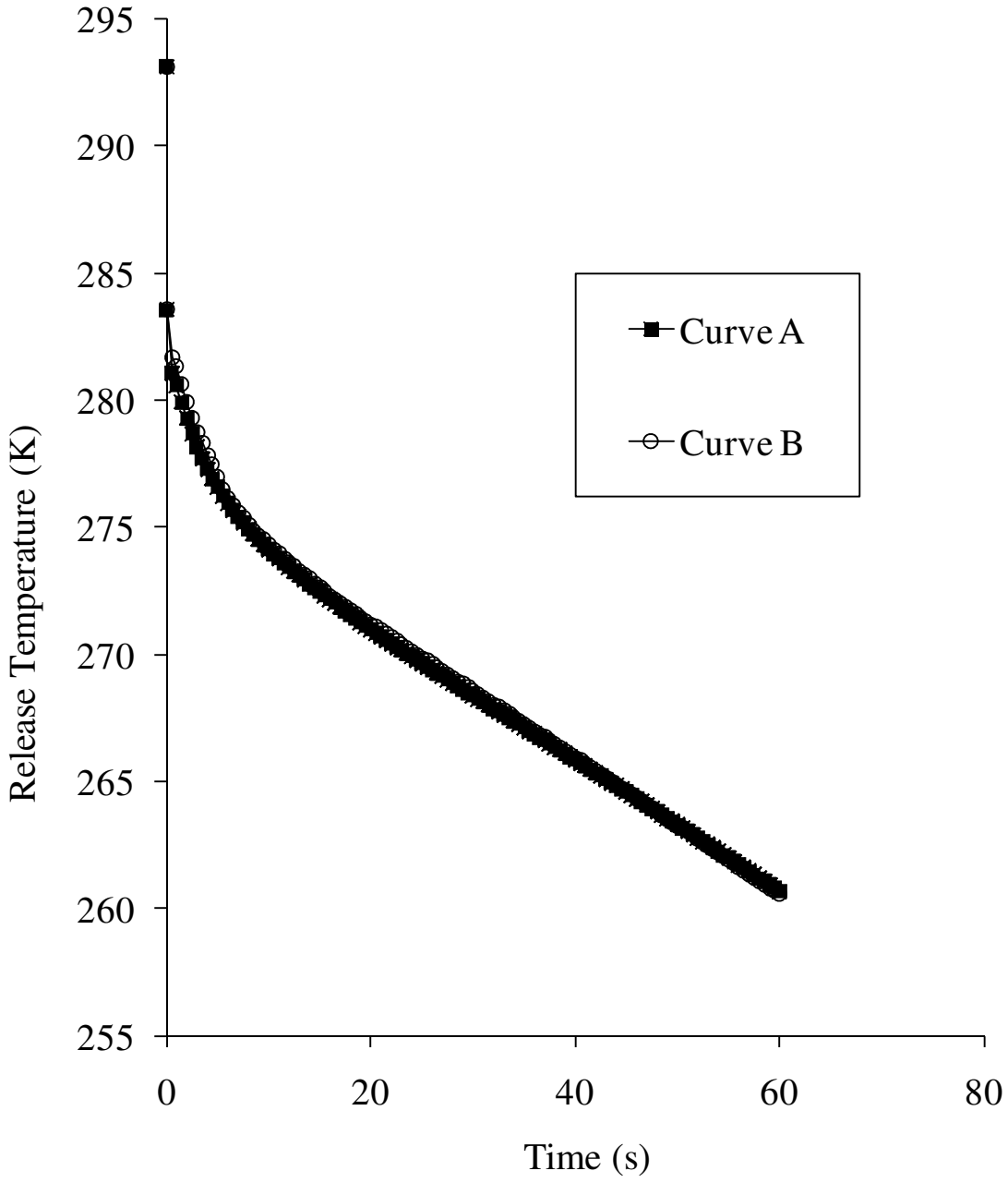

Figure 5.17: Variation of release temperature with time for the two-phase inventory following FBR.

Curve A: MOC, CPU runtime = 1233 s

Curve B: FVM, CPU runtime = 274 s

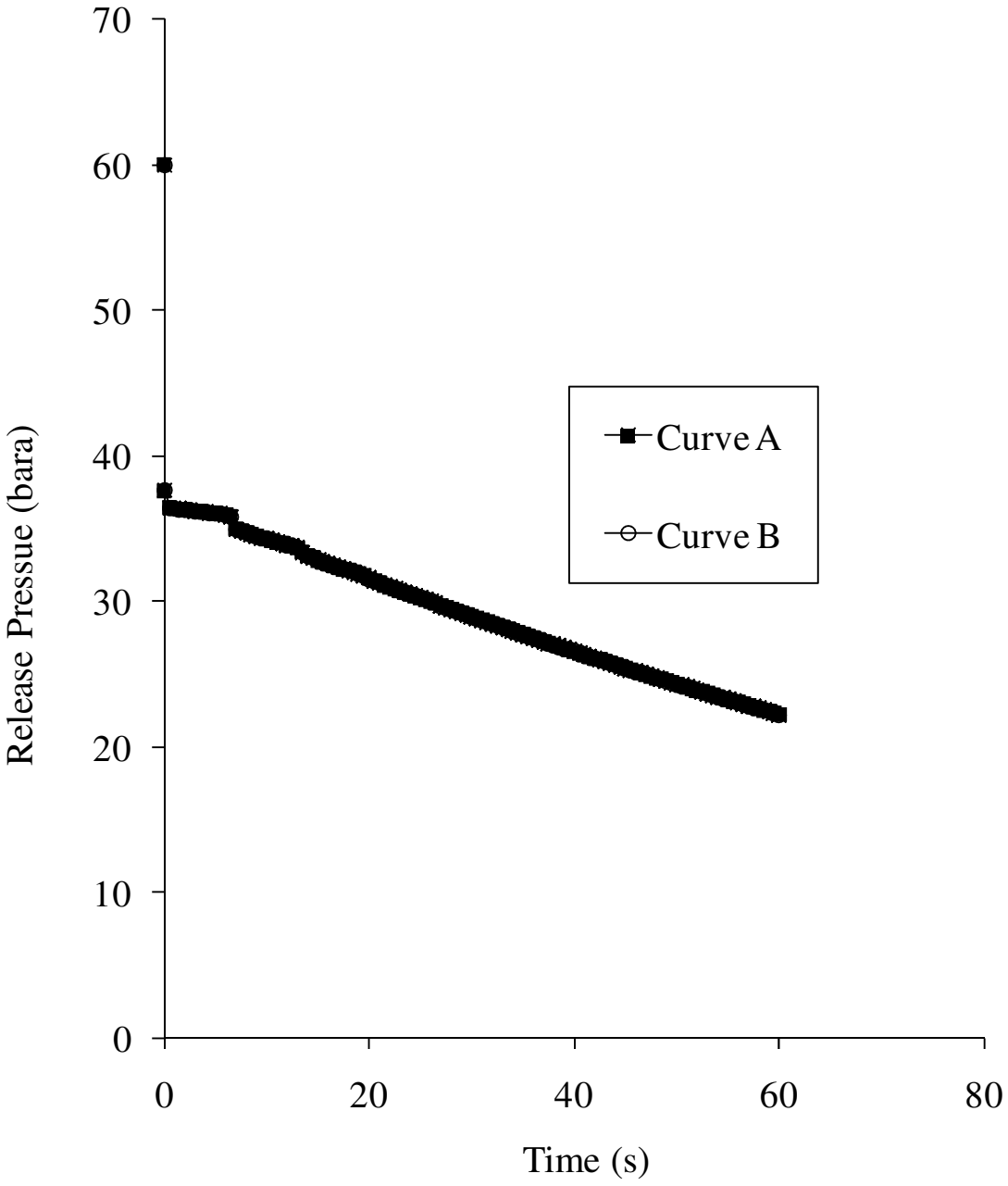

Figure 5.18: Variation of release pressure with time for the two-phase inventory following puncture.

Curve A: MOC, CPU runtime = 1283 s

Curve B: FVM, CPU runtime = 874 s

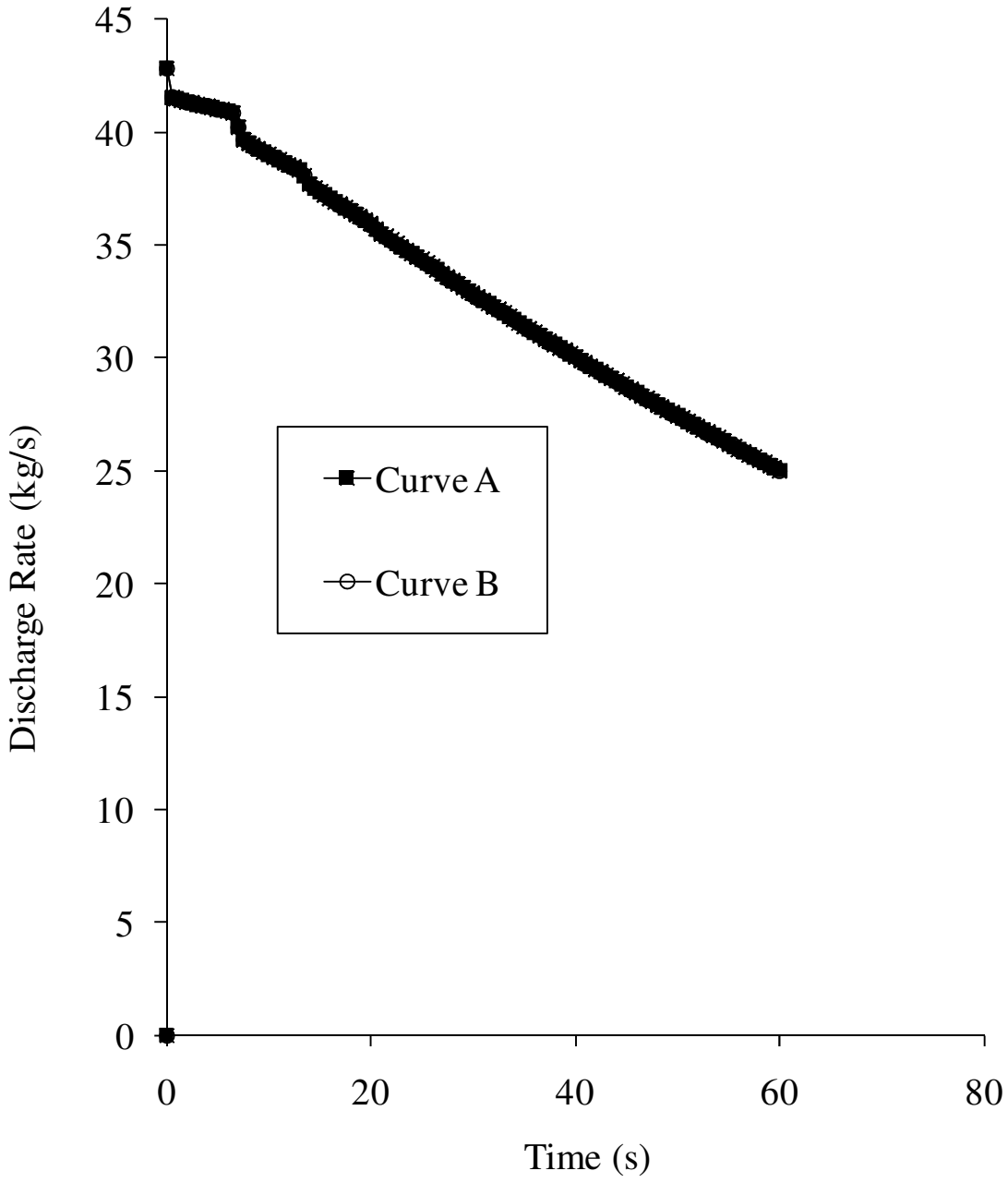

Figure 5.19: Variation of discharge rate with time for the two-phase inventory following puncture.

Curve A: MOC, CPU runtime = 1283 s

Curve B: FVM, CPU runtime = 874 s

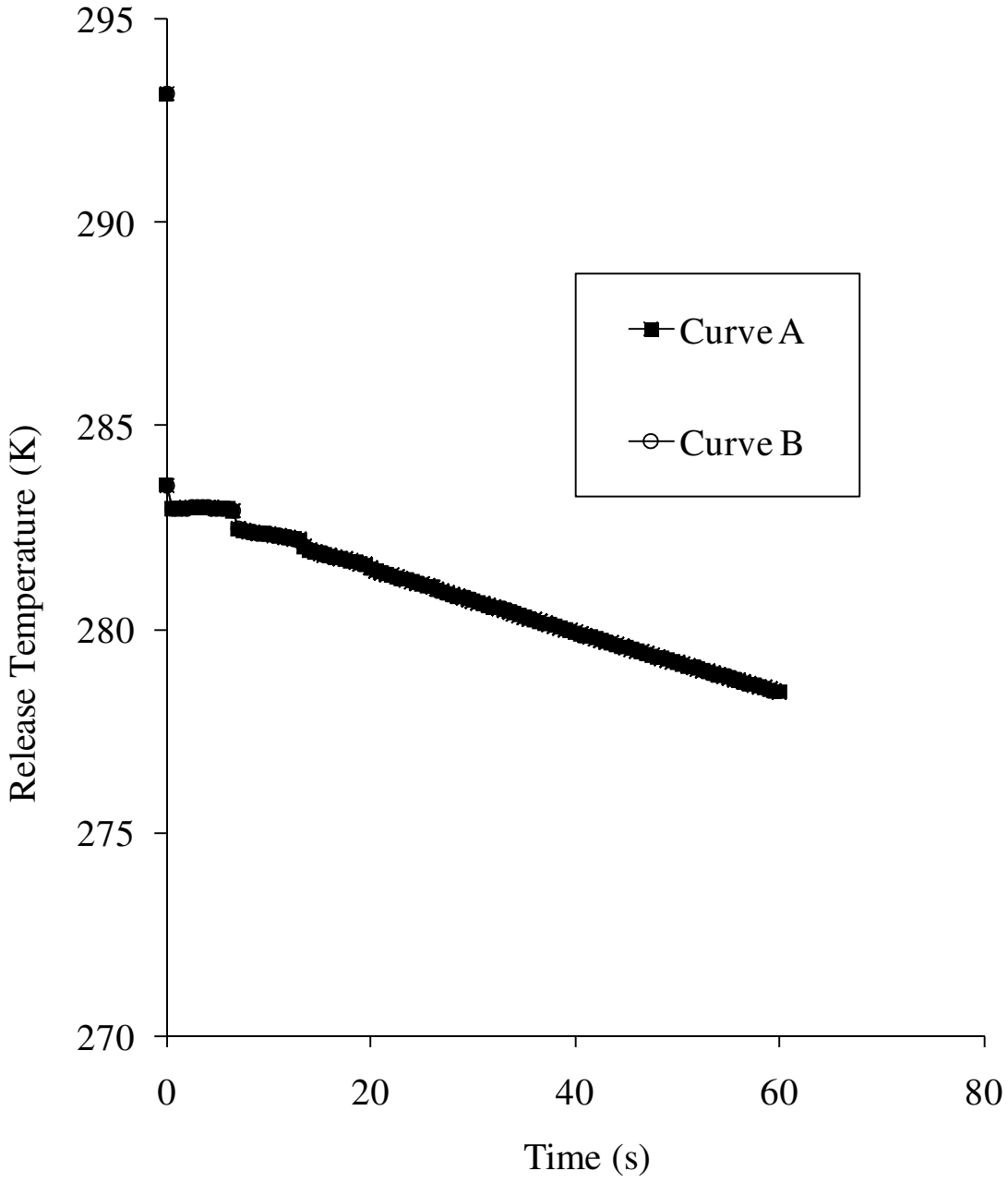

Figure 5.20: Variation of release temperature with time for the two-phase inventory following puncture.

Curve A: MOC, CPU runtime = 1283 s

Curve B: FVM, CPU runtime = 874 s

5.4.3 Liquid

As pointed out in section 5.3.1, in the case of full bore rupture for the flashing liquid inventories, the FVM becomes unstable. This behaviour is due to the inability of FVM in handling the large discontinuities occurring in the flow variables during the almost instantaneous fluid expansion and is synonymous with systems of equations which are in non-conservative form.

Notwithstanding this, the variations of the rupture plane pressure, discharge rate and rupture plane temperature with time for the puncture scenario are given in figures 5.21, 5.22 and 5.23 respectively. As before, curves A and B represent the results obtained using the MOC and FVM models respectively. From figure 5.21 both the MOC (curve A) and the FVM (curve B) predict an instantaneous depressurisation at the release plane due to the finite compressibility of the liquid inventory.

However, in the case of the discharge rate data (figure 5.22) while the two methods are in agreement during the early part of the depressurisation the MOC (curve A) indicates a period of hyperbolic decline before falling to zero while the FVM predicts zero flow rate. This could be due to the same behaviour described above for the FBR case. It is postulated that due to the slower decompression induced by the smaller orifice, the error is not of sufficient size to cause the simulation to fail. This is supported by the corresponding CPU runtimes of 3135 and 31048 s for the MOC and FVM respectively. The oscillation produced in the FVM predictions causes the interpolation of the thermo-physical properties to fail, as a result these must be found iteratively, leading to the increase in magnitude of the CPU runtime.

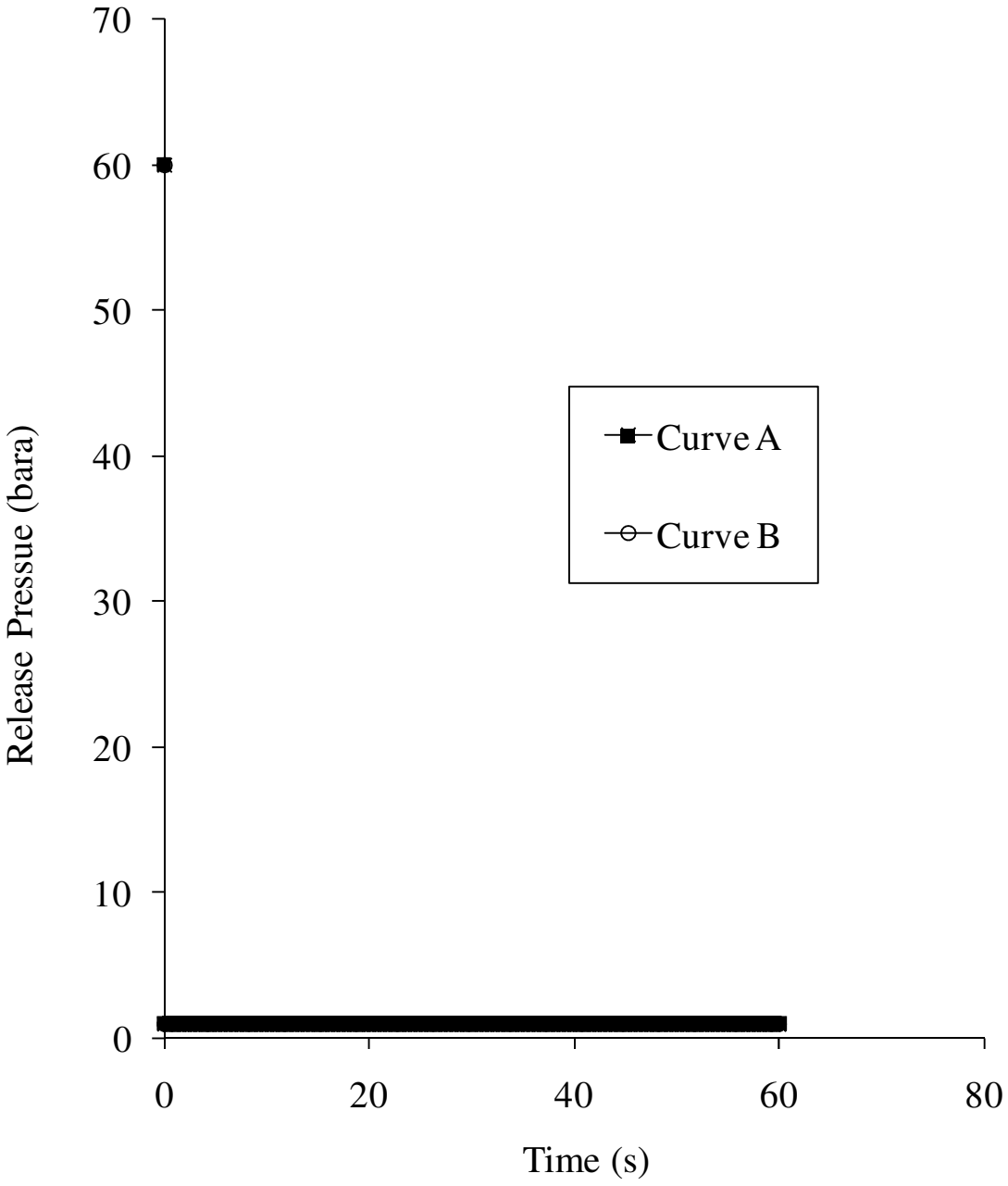

Figure 5.21: Variation of release pressure with time for the liquid inventory following puncture.

Curve A: MOC, CPU runtime = 3135 s

Curve B: FVM, CPU runtime = 31048 s

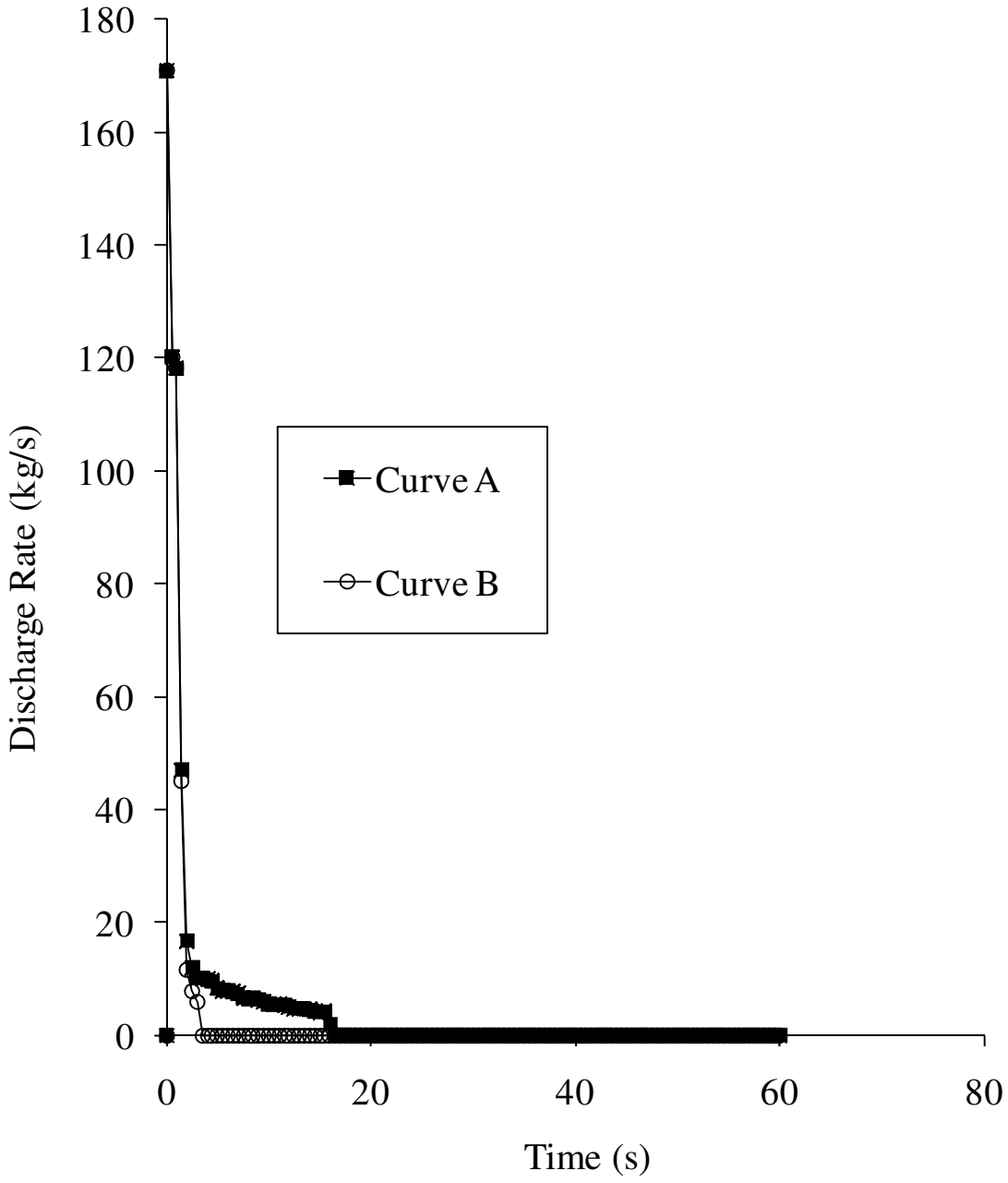

Figure 5.22: Variation of discharge rate with time for the liquid inventory following puncture.

Curve A: MOC, CPU runtime = 3135 s

Curve B: FVM, CPU runtime = 31048 s

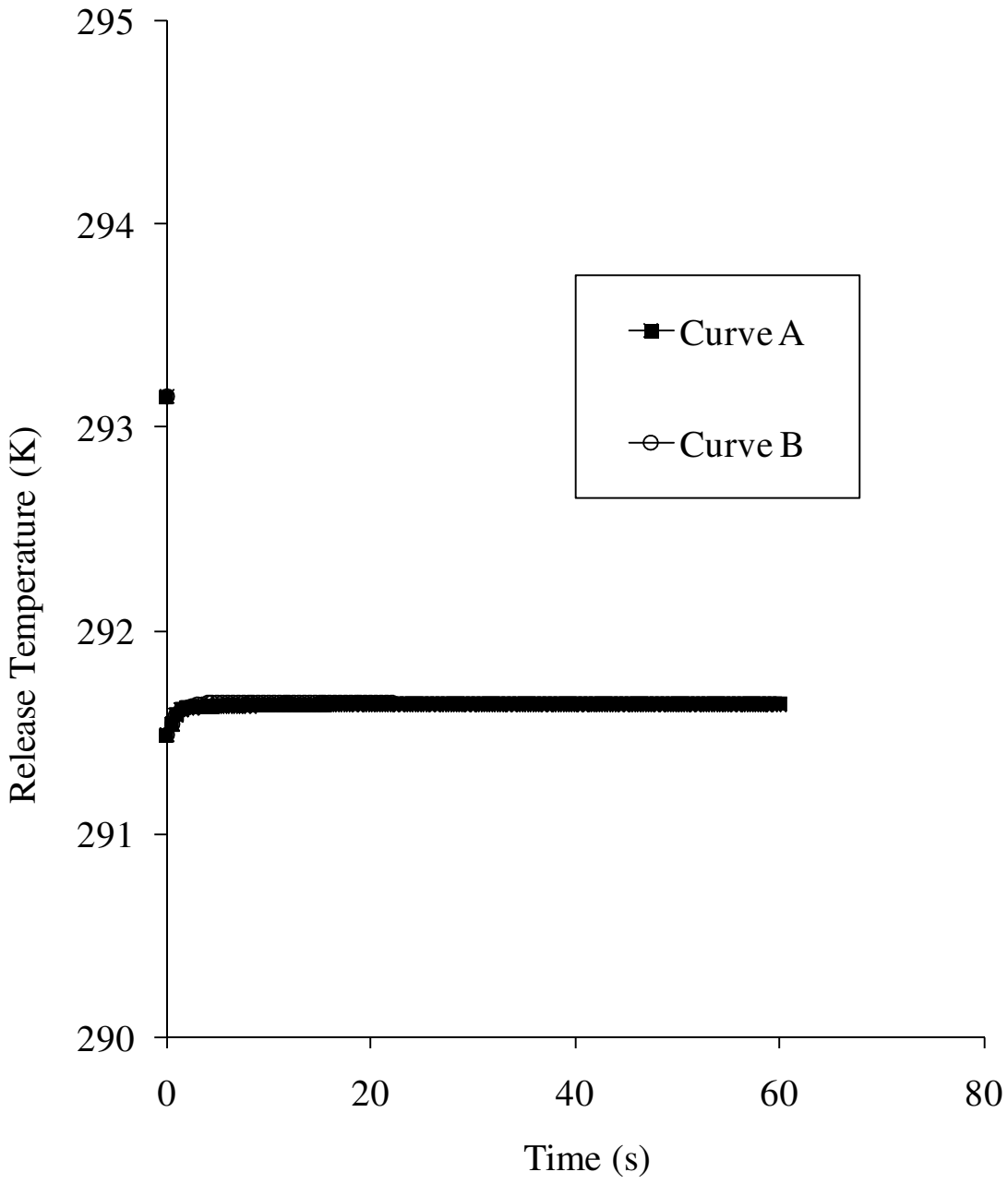

Figure 5.23: Variation of release temperature with time for the liquid inventory following puncture.

Curve A: MOC, CPU runtime = 3135 s

Curve B: FVM, CPU runtime = 31048 s

5.5 Conclusions

This chapter presented a Finite Volume Method as an alternative resolution technique for the system of conservation equations with the aim of further reducing the CPU runtime. The particular FVM used was based on the PRICE-T scheme (Toro and Siviglia, 2003) which is a deterministic re-formulation of the staggered grid RCM of (Gottlieb, 1988) developed specifically for the non-conservative form of the equations.

The performance of the model was tested by comparison of its predictions against available experimental data as well as the hypothetical rupture of a realistic pipeline containing a full range of pressurised inventories including gas, two-phase and liquid hydrocarbons. In all cases the FVM predictions were also compared against those obtained using the MOC. It was found that, in general, the FVM performed well. However, it was found that the model was unable to simulate the full bore rupture of pipelines where the inventory was initially in the liquid state. In this case large discontinuities in the fluid properties resulted in numerical instabilities.

Importantly though, in the cases examined significant reductions in the CPU runtimes (compiled in table 5.4) were observed using the FVM as compared to the MOC.

Table 5.4: Comparison of CPU runtimes for the MOC and FVM for all simulations presented.

	CPU runtime (s)		% CPU runtime reduction
	MOC	FVM	
Experimental tests			
TransCanada	627	414	33.97
Piper Alpha	20685	11762	43.14
P45	1027	694	32.42
P47	2351	1625	30.88
Case Study			
Full Bore Rupture			
Permanent Gas	901	366	59.38
Two-phase Mixture	1233	274	77.78
Puncture			
Permanent Gas	1631	1255	23.05
Two-phase Mixture	1283	874	46.80
Liquid	3135	31048	-890.37

Chapter 6: A Dynamic Boundary Ductile Fracture Propagation Model for CO_2 Pipelines

6.1 Introduction

Propagating factures are considered as by far the most catastrophic type of pipeline failure. Such failures involve the rapid axial splitting or tearing of the pipeline, sometimes running over distances of several hundred metres resulting in massive loss of inventory in a very short period of time. Deservedly, understanding and modelling of the mechanisms responsible for such failures has led to a large number of studies (see for example Leis et al., 2005; Maxey, 1974). Such interest has intensified recently (Mahgerefteh et al., 2008; Cosham and Eiber, 2008; Bilio et al., 2009) given the prospect of using pressurised pipelines for transporting captured CO_2 from fossil plants for subsequent storage. Given that CO_2 at concentration of >10% v/v is likely to be instantly fatal (Kruse and Tekiela, 1996), the rupture of a CO_2 pipeline near a populated area can lead to catastrophic consequences.

Fractures can initiate from defects introduced into the pipe by outside forces such as mechanical damage, soil movement, corrosion, material defects or adverse operating conditions. The crack will propagate when the stresses acting on the defect overcome the fracture tolerance of the pipe, reaching a critical size based on the pipeline material properties and operating condition. At the onset of such a failure a series of expansion waves propagate from the rupture plane towards the intact end of the pipeline at the speed of sound (Picard and Bishnoi, 1988). As the main driving force for crack propagation is the crack tip pressure (Fearnehough, 1974), the precise tracking of these expansion waves, and their effect on the pressure profile along the pipeline is essential for the proper modelling of fracture propagation.

The so called Battelle Two Curve (BTC) approach by Maxey (1974) was the first method used to express the criterion for the propagation of a ductile fracture in terms of the relation between the fluid decompression wave velocity and the crack propagation velocity. If the fluid decompression wave velocity is greater than the crack velocity, the crack tip stress will decrease, eventually dropping below the arrest stress causing the crack to arrest. Conversely, if the decompression wave velocity remains smaller than the crack velocity, the crack tip pressure will remain constant resulting in indefinite propagation.

A number of studies have since been conducted for modelling ductile fractures in pressurised pipelines. Some employ sophisticated finite element methods for simulating material deformation but use over-simplistic transient fluid flow models for predicting the rupture plane pressure and hence the crack driving force (see for example O'Donoghue et al., 1997; O'Donoghue and Zhang, 1999). Others based on the BTC approach (see for example Leis, 1997; Makino et al., 2008), account for the transient depressurisation profile within the pipeline, but do not deal with the impact of pipe wall heat transfer and friction effects on the fluid decompression behaviour (see for example Makino et al., 2001; Terenzi, 2005). As described in chapter 2, Botros et al. (2010b) have recently shown that ignoring pipe friction may result in underestimating the decompression wave velocity with the effect becoming more significant with increasing line pressure and reducing pipe diameter. This is important since an under-prediction of decompression wave velocity results in underestimating the pipe toughness that would be required in order to arrest fracture.

Additionally a reliable decompression model must also incorporate a suitable Equation of State. This is especially important in the case of CO_2 pipelines given the unique depressurisation thermodynamic trajectory of CO_2 (Bilio et al., 2009).

Crucially, given that the decompression and the fracture velocity curves are not coupled means that the BTC method is primarily indicative as to whether or not a fracture will propagate for a given pipe toughness. Important information such as the variation of the crack length with crack propagation velocity and ultimately the crack arrest length cannot be produced using this approach.

In this chapter, the development and validation of a rigorous dynamic boundary ductile fracture propagation model is presented. This model accounts for all of the important transient fluid/structure interactions governing the fracture process. The performance of the model in terms of predicting the crack propagation velocity and arrest length is tested by comparison against real data. These full scale burst tests conducted by the High-Strength Line Pipe Committee (Inoue et al., 2003), ECSC X100 (Takeuchi et al., 2006) and Alliance (Johnson et al., 2000) for pipes containing either air or rich gas mixtures.

The validated model is next used to test the propensity of an hypothetical but realistic pressurised CO_2 pipeline to ductile fracture propagation failure as a function of various parameters. These include the starting line temperature, pressure and the different types and levels of the likely impurities in the CO_2 stream. The compositions of the impurities assumed are those based on the various capture technologies, including pre-combustion, post-combustion and oxy-fuel as suggested by ICF International (2010). In each case, the variation of fracture velocity versus fracture length is reported for an hypothetical CO_2 pipeline with a realistic fracture toughness. The study of the impact of the line temperature and pressure on ductile fracture propagation is important given the likely extensive variations in the geographical locations of the next generation CO_2 pipelines.

6.1.1 Model Formulation

The key step in the BTC method is the derivation of two sets of curves; one set describing the crack velocity and the other the velocity of the fluid decompression wave. The resistance to crack propagation is indicated by the Charpy V-Notch (C_v) energy (Maxey, 1974). However, in the full scale pipe burst tests conducted by the High-Strength Line Pipe Committee (HLP) (Makino et al., 2001), the BTC theory is used in conjunction with the Drop Weight Tear Test (DWTT) energy. This was shown to provide a more accurate indication of the pipeline resistance to fracture. Consequently this is the model applied in this work.

The two curve model for the crack propagation velocity, v_c and crack arrest pressure, P_a are respectively given by (Makino et al., 2001):

$$v_c = 0.67 \frac{\sigma_{flow}}{\sqrt{\frac{D_p}{A_p}}} \left(\frac{P_t}{P_a} - 1\right)^{0.393} \quad \textbf{(6.1)}$$

$$P_a = 0.382 \frac{t_w}{D} \sigma_{flow} cos^{-1} exp\left(\frac{-3.81 \times 10^7 \frac{D_p}{A_p}}{\sqrt{Dt}\sigma_{flow}}\right) \quad \textbf{(6.2)}$$

Where, σ_{flow}, D_p and A_p are respectively the flow stress (the mean value of the tensile and yield stresses), pre-cracked DWTT energy and ligament area of a pre-cracked DWTT specimen. On the other hand P_t and t_w are the crack tip pressure and pipe wall thickness respectively. The crack tip pressure P_t is taken to be the choked pressure at the pipeline release plane.

6.1.2 The Coupled Decompression and Fracture Model

The calculation algorithm coupling the decompression and fracture models for simulating the fracture behaviour is given in figure 6.1. The first step involves the use of the MOC based decompression model to calculate the crack tip pressure, P_t, based on the given pipeline characteristics and the prevailing conditions. The crack velocity, v_c, is then calculated by substituting P_t and P_a (in turn determined from equation (6.2)) into equation (6.1).

A negative or zero crack velocity, v_c means that the crack will not extend and the calculations are terminated. A positive value on the other hand means that the crack will extend. The crack length is determined after an arbitrary small time interval, Δt (=0.01 s), during which v_c is assumed to remain constant. A calculated crack length greater than or equal to the remaining pipe length means catastrophic pipeline failure and the calculations are ended. Otherwise, the new effective pipeline length is used to calculate the crack tip pressure, P_t. The calculations continue until $v_c \leq 0$.

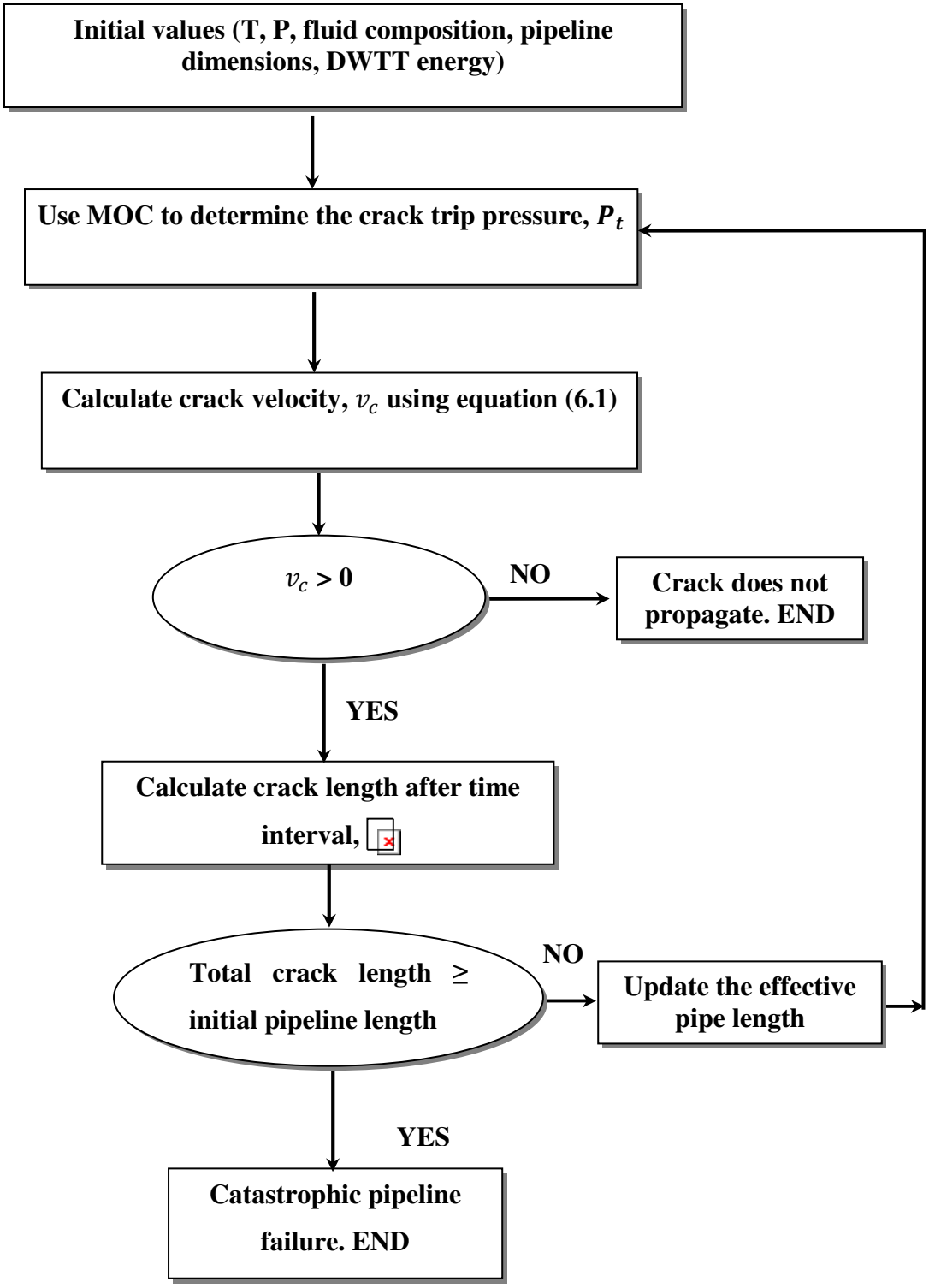

Figure 6.1: Crack propagation calculation flow algorithm.

6.2 Results and Discussion

6.2.1 Dynamic Boundary Ductile Fracture Model (DBFM) Validation

The following presents the results relating to the validation of the Dynamic Boundary Ductile Fracture Model (DBFM) presented above by comparison of its predictions against the following published experimental data:

- HLP full scale burst test (Inoue et al., 2003)
- ECSC X100 pipe full scale burst test (Takeuchi et al., 2006)
- Alliance full scale burst tests (Johnson et al., 2000).

Table 6.1 shows the pertinent conditions relating to each test. Table 6.2 on the other hand shows the rich gas feed compositions for the HLP C2 and Alliance tests.

Table 6.1: Pipeline characteristics and prevailing conditions utilised for the full scale burst tests.

Parameter	HLP			ECSC	Alliance
	A1	B1	C2		
Inventory	Air	Air	Rich Gas (see table 6.2)	Air	Rich Gas (see table 6.2)
Internal diameter (m)	1.182	1.182	1.182	1.4223	0.8856
Pipe thickness (m)	0.0183	0.0183	0.0183	0.0191	0.0142
Initial pressure (bara)	116	116	104	126	120.2
Initial temperature (^{o}C)	12	6	-5	20	23.9
Ambient pressure (bara)	1.01	1.01	1.01	1.01	1.01
Ambient temperature (^{o}C)	20	20	20	20	20
Pipe length (m)	35	35	35	35	100
Tensile stress (MPa)	505	505	505	807	505
Yield stress (MPa)	482	482	482	728	482
Pipe grade	X70	X70	X70	X100	X70

Table 6.2: Rich gas feed % compositions.

Component	HLP C2	Alliance Test 1
CH_4	89.57	80.665
C_2H_6	4.7	15.409
C_3H_8	3.47	3.090
iC_4H_{10}	0.24	0.232
nC_4H_{10}	0.56	0.527
iC_5H_{12}	0.106	0.021
nC_5H_{12}	0.075	0.014
nC_6H_{14}	0.033	0.003
nC_7H_{16}	0.017	0
nC_8H_{18}	0.008	0
nC_9H_{20}	0.001	0
N_2	0.5	0.039
CO_2	0.72	0

The full burst test pipelines used comprised several sections of differing toughness for which the corresponding DWTT energy may be calculated. In all simulations, the pipe wall roughness and heat transfer coefficient are taken as 0.05 mm and 5 W/(m^2 K) respectively. The latter corresponds to the un-insulated pipeline exposed to still air in all simulations.

The Peng-Robinson Equation of State (Peng and Robinson, 1976) (PR EoS) is used for the prediction of the pertinent fluid phase equilibrium data for both air and rich gas mixtures. In the case of CO_2, the Modified Peng-Robinson (Wu and Chen, 1997) EoS is used. An equi-distant grid system comprising 100 nodal points is employed for the MOC based fluid dynamic simulations. The corresponding discretisation time element is determined using 90% of the CFL value (Mahgerefteh et al., 2009).

The HLP full scale experiments involved three series of burst tests, referred to as test series A, B and C using X70 API grade pipelines containing air and a rich gas mixture. Pipeline fracture was initiated using an explosive charge. Figure 6.2 shows a schematic representation of the pipe setup.

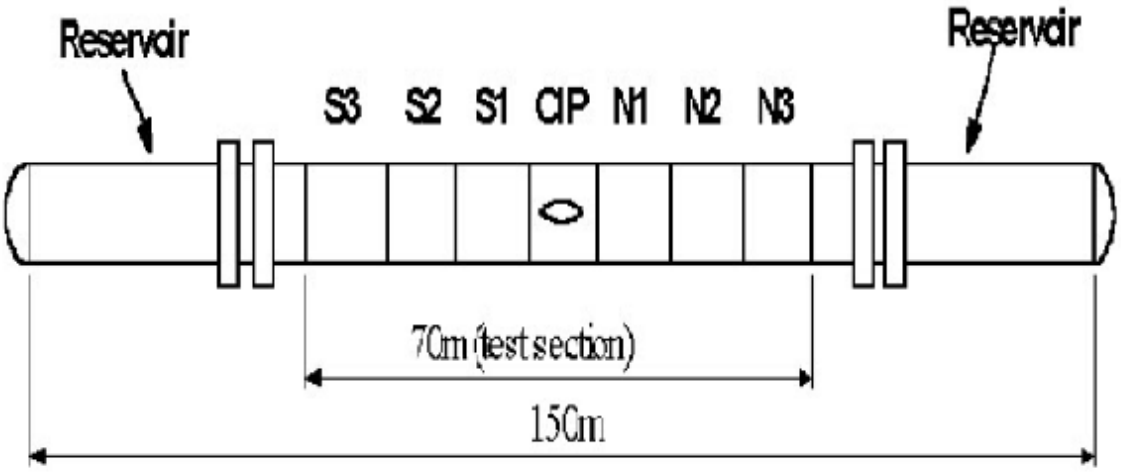

Figure 6.2: Schematic representation of the experimental setup used in the HLP full scale pipe burst tests (Inoue et al., 2003).

Figures 6.3 to 6.5 show the variation of the crack velocity with crack length for the south running A1, B1 and C2 tests respectively for the HLP full scale experiments. Curves A show the measured crack length, curves B on the other hand are the simulation predictions. In all cases, the corresponding Charpy Energy, C_v, for each pipe section is given in the figures.

Figures 6.6 and 6.7 show the corresponding data for ECSC X100 (Takeuchi et al., 2006) and Alliance full scale burst tests (Johnson et al., 2000) respectively.

According to figures 6.3 to 6.5, as it may be observed, the crack velocity rapidly decreases with increase in crack length. This is due to the rapid decrease in the crack tip pressure as the pipeline depressurises. As an example, such behaviour expressed in terms of the variation of the crack tip pressure with time is shown in figure 6.8 for the HLP A1 south running crack.

Also, returning to figures 6.3 to 6.5, as expected the crack velocity decreases as the crack propagates into the pipeline section with the higher toughness, eventually coming to rest in all cases. As expected, the data in figure 6.5 shows the smallest crack length as compared to the other tests due to the combination of the much higher fracture toughness pipe material employed together with the lowest initial pressure.

The initial rapid increase in the crack velocity observed in many of the test data (e.g. figures 6.3, 6.4 and 6.6) is postulated to be due to the finite time taken for the initial notch to fully develop into an open flap following detonation. This time domain, which is most pronounced for Alliance Test 1 (rich gas mixture, figure 6.7), is not accounted for in the present simulations.

Despite the uncertainties in the experimental data, all the DBFM predictions (figures 6.3 to 6.7; curves A) are in reasonably good agreement with the test data.

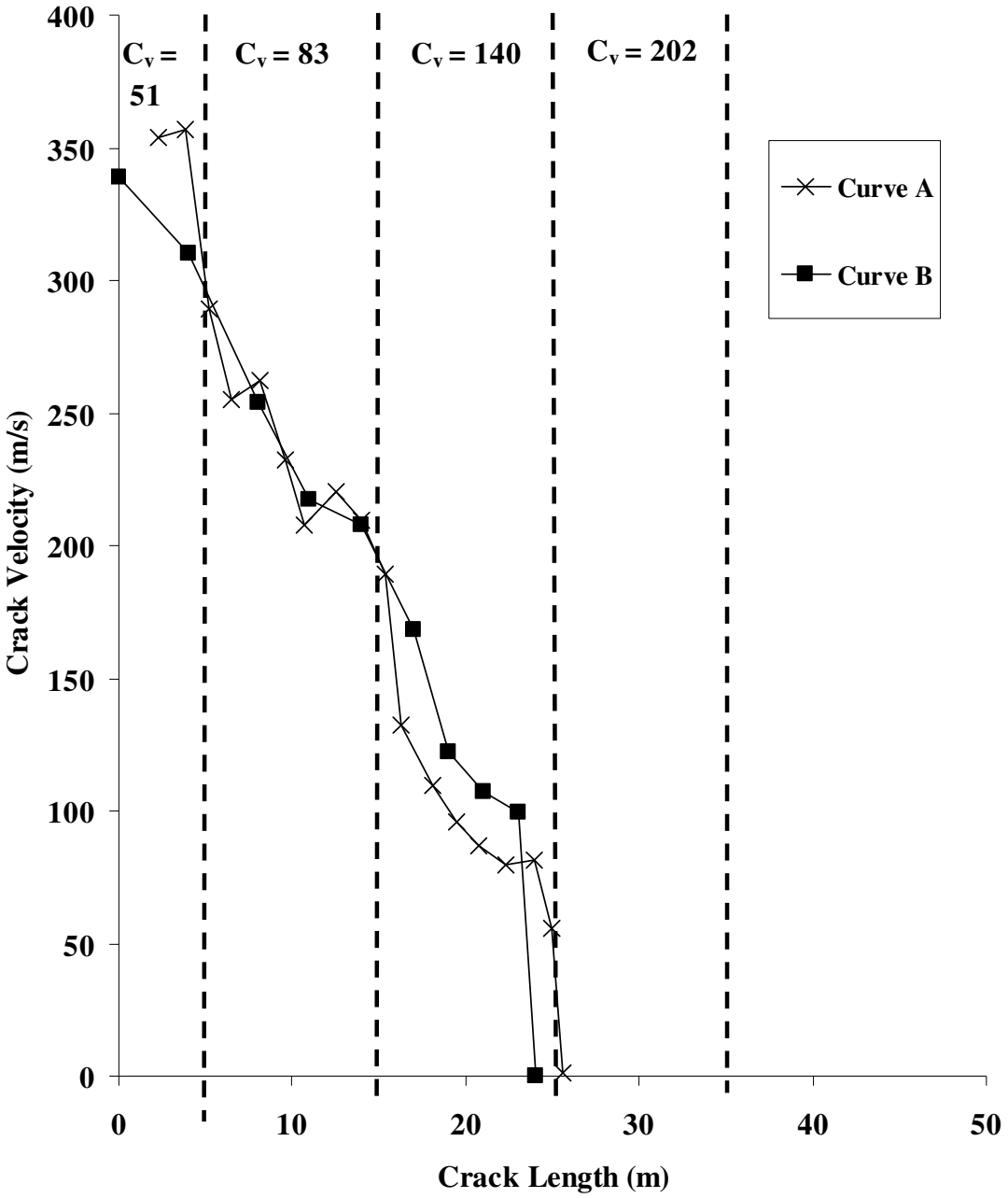

Figure 6.3: Variation of crack velocity with crack length for test A1 south running crack. Inventory: Air, Initial pressure = 116 bara, Initial temperature = 12 ^{o}C.

Curve A: Experimental data (Inoue et al., 2003)

Curve B: DBFM prediction

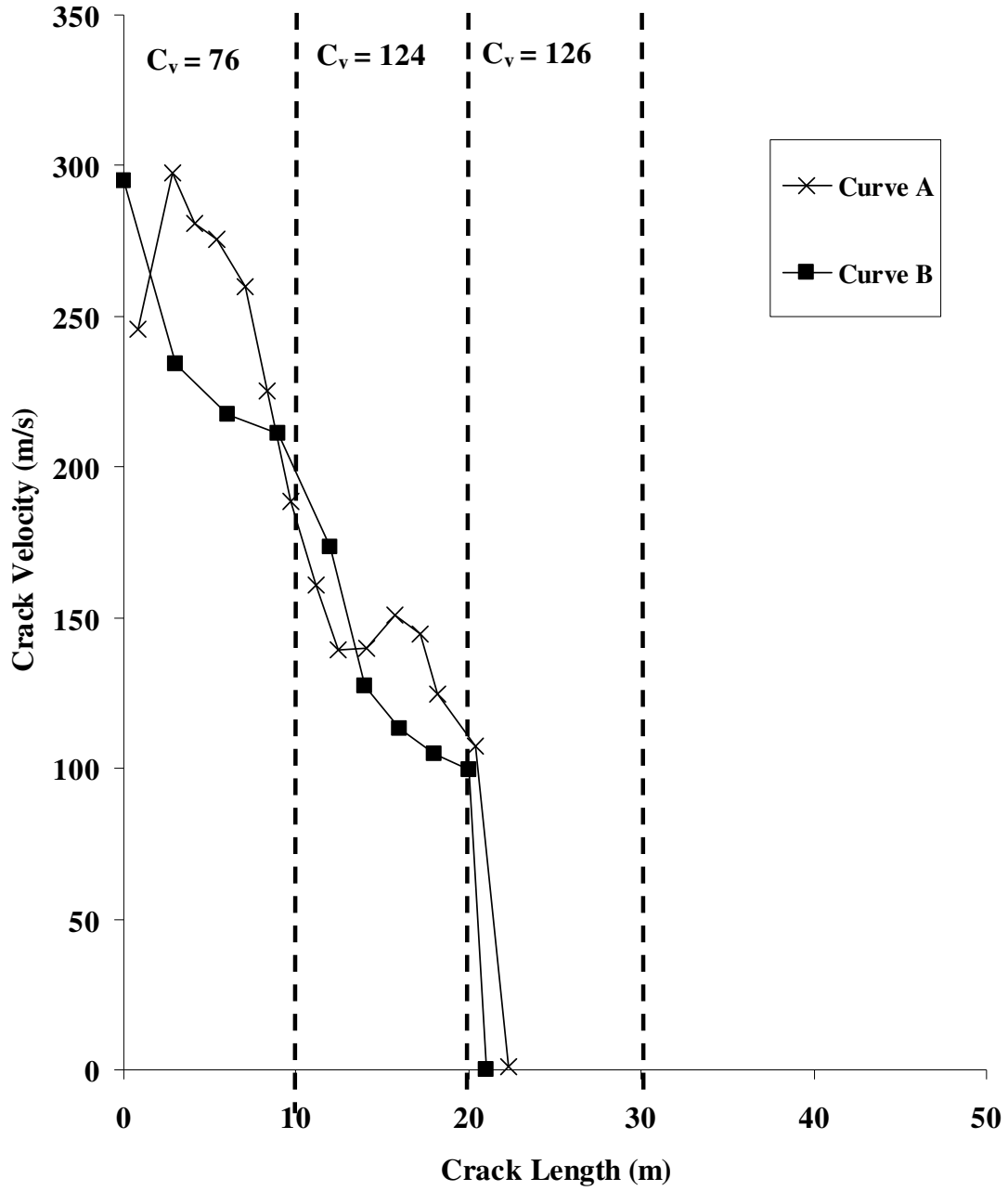

Figure 6.4: Variation of crack velocity with crack length for test B1 south running crack. Inventory: Air, Initial pressure = 116 bara, Initial temperature = 6 ^{o}C.

Curve A: Experimental data (Inoue et al., 2003)

Curve B: DBFM prediction

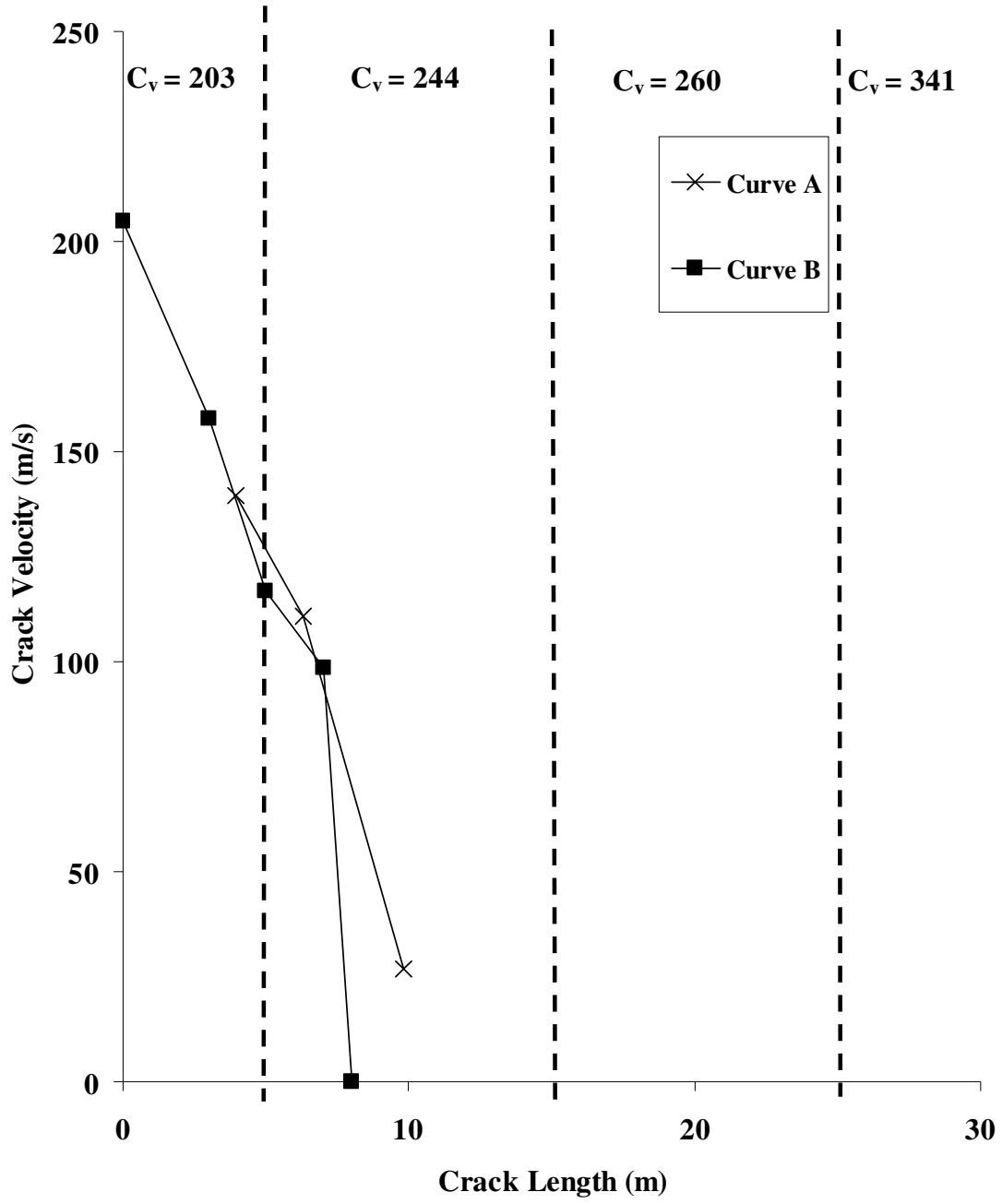

Figure 6.5: Variation of crack velocity with crack length for test C2 south running crack. Inventory: Rich Gas (table 6.2), Initial pressure = 104 bara, Initial temperature = -5 ^{o}C.

Curve A: Experimental data (Inoue et al., 2003)

Curve B: DBFM prediction

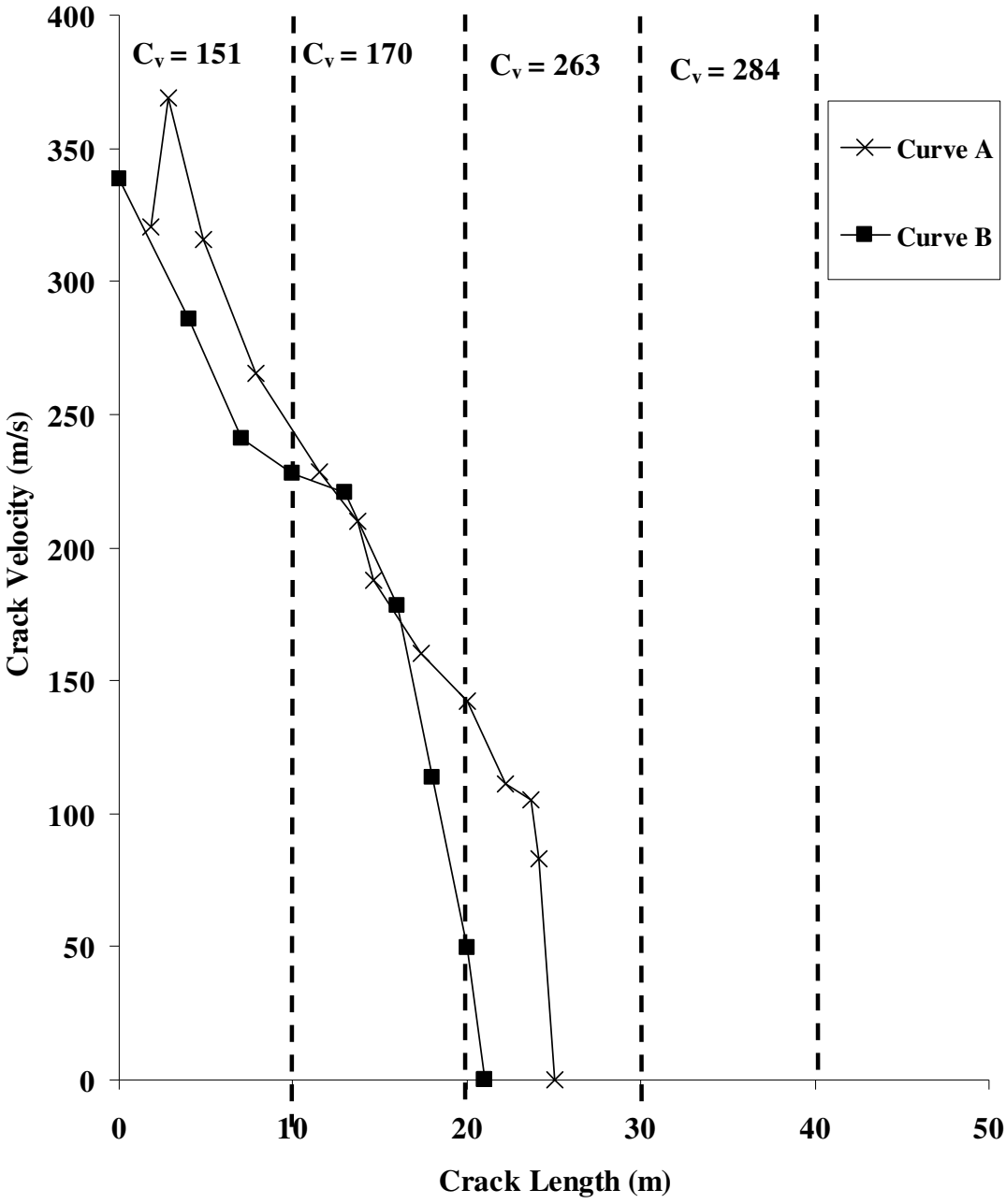

Figure 6.6: Variation of crack velocity with crack length for test ECSC X100 south running crack. Inventory: Air, Initial pressure = 126 bara, Initial temperature = 20 ^{o}C.

Curve A: Experimental data (Makino et al., 2008)

Curve B: DBFM prediction

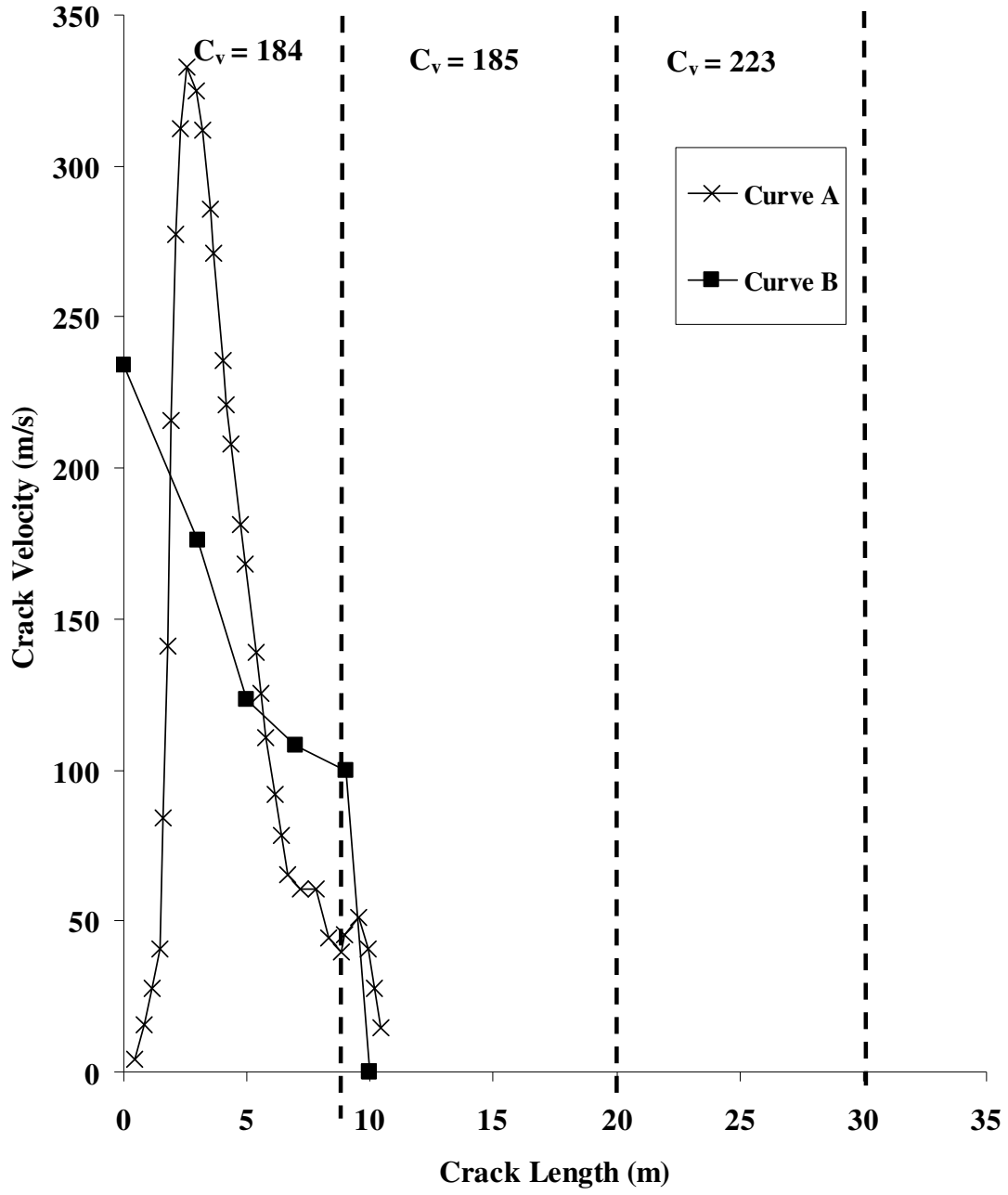

Figure 6.7: Variation of crack velocity with crack length for test Alliance Test 1. Inventory: Rich Gas (table 6.2), Initial pressure = 120.2 bara, Initial temperature = 23.9 ^{o}C.

Curve A: Experimental data (Johnson et al., 2000)

Curve B: DBFM prediction

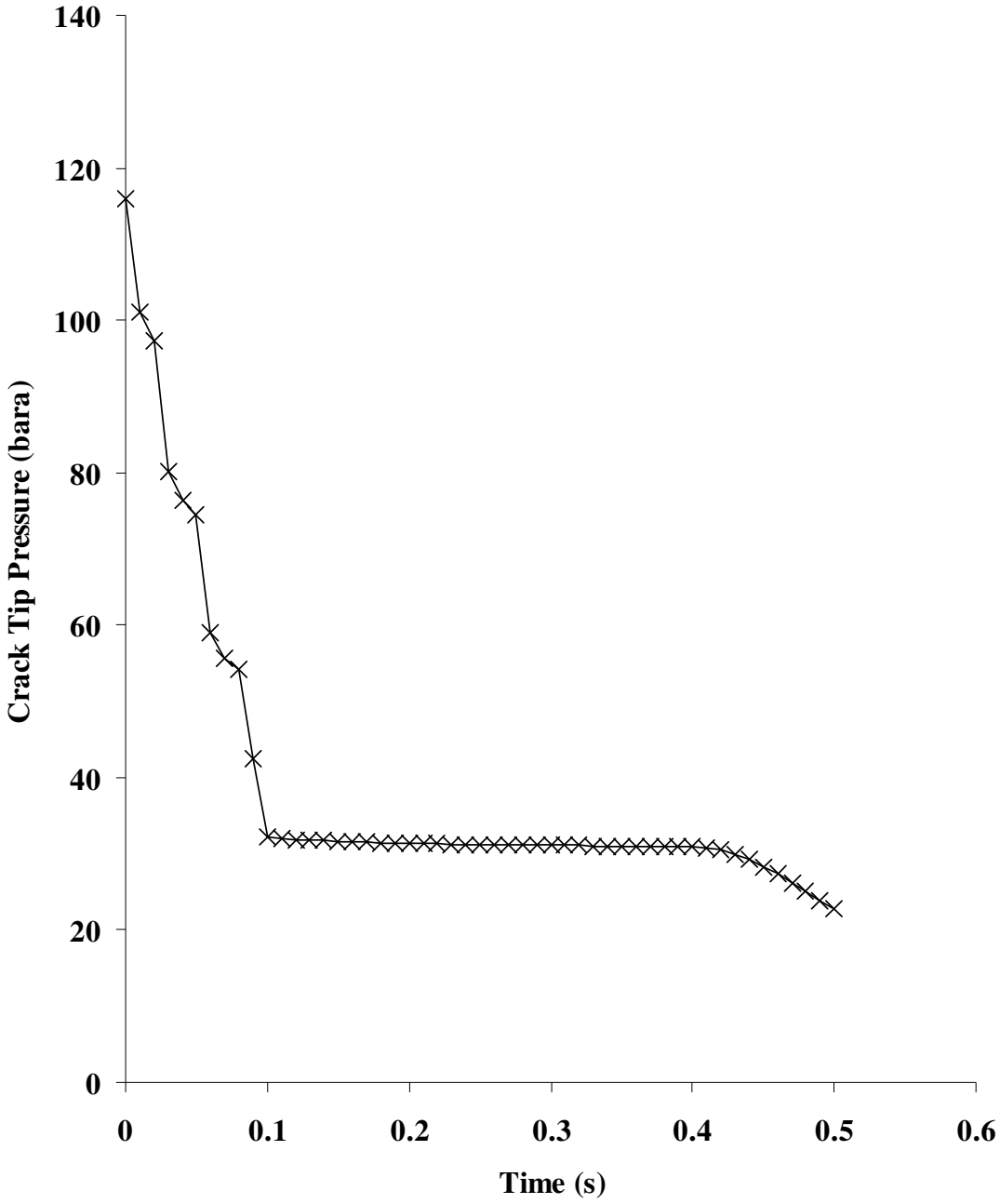

Figure 6.8: Simulated variation of crack tip pressure versus time for test HLP A1 south running crack.

In figure 6.9, curve A shows the predicted variation of the crack velocity versus crack length for a CO_2 pipeline. For the sake of comparison, the analogous data for methane (curve B) and natural gas (85 % methane-15 % ethane; curve C) inventories are also presented. Table 6.3 shows the prevailing conditions and the pipeline characteristics selected to generate the simulations. To ensure practical relevance, the respective pipeline internal diameter and wall thickness of 590.5 mm and 9.45 mm are employed in the simulations. Cosham and Eiber (2008) suggest that such dimensions are the most likely for CO_2 pipelines to be employed in CCS. The same authors also propose that a C_v (Charpy V-Notch energy) of 50 J would be sufficient to arrest a fracture for typical operating conditions of 100 barg and 10 ^oC. The same pipeline operating conditions are chosen in the proceeding simulations.

As it may be observed following an initial drop, the natural gas pipeline (curve C) exhibits a relatively constant high velocity crack which propagates through almost the entire length of the pipeline before coming to rest at approximately 89 m. Similar trends in behaviour but of a smaller magnitudes are observed in the case of the methane pipeline (curve B) where the fracture comes to rest at a distance of approximately 18 m. Of the three cases examined, the CO_2 pipeline (curve A) offers the best resistance to ductile fracture. Here the fracture almost instantaneously comes to rest after a distance of only 6 m.

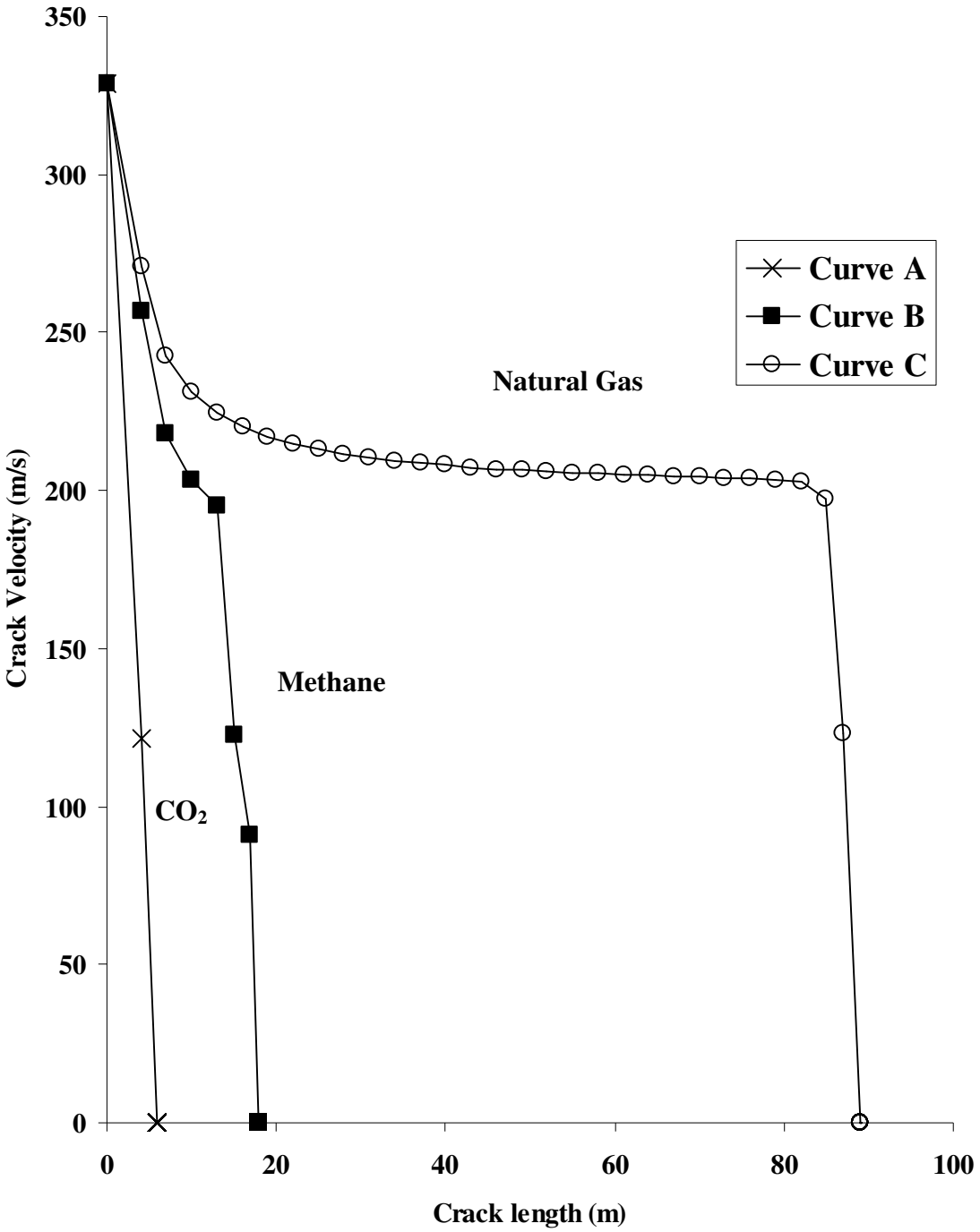

Figure 6.9: Variation of crack velocity with crack length for a 100 m long pipe at 100 barg and 10 ^{o}C containing various inventories.

Table 6.3: Pipeline characteristics and prevailing conditions utilised for the fracture propagation simulations.

Parameter	Value
Internal diameter (m)	0.5905
Wall thickness (mm)	9.45
Line pressure (barg)	100
Ambient pressure (bara)	1.01
Ambient temperature (^oC)	20
Feed temperature (^oC)	10
Pipe length (m)	100
Tensile stress (MPa)	531
Yield stress (MPa)	448
Pipe wall roughness (mm)	0.05
Heat transfer coefficient (W/m^2K)	5
Wind speed (m/s)	0
Pipe grade	X65
Fracture toughness (J)	50

6.2.2 Impact of line temperature and impurities

The study of the impact of different types of impurities on ductile fracture propagation behaviour of CO_2 pipelines is receiving increasing attention (see for example de Visser et al., 2008, Heggum et al., 2005). Recent studies using various Equations of State have shown that even small amounts of the likely impurities in the CO_2 stream will increase the saturation pressure significantly (see for example Oosterkamp and Ramsen, 2008; Li and Yan, 2006). It will be shown later that this will in turn increase the pipeline's propensity to fracture propagation.

As mentioned previously, the type of the impurities in the CO_2 stream will depend on the fuel, capture method (i.e. pre-combustion, post-combustion or oxy-fuel) and the post-capture processing (ICF International, 2010; Oosterkamp and Ramsen, 2008). The percentage composition of the transported stream on the other hand, although being overwhelmingly CO_2, will have to comply with the prevailing legislative emission limits (de Visser et al., 2008; ICF International, 2010).

So far most of the studies reported investigate the impact of impurities on the CO_2 phase equilibrium behaviour using various Equations of State (Brown and Mahgerefteh, 2009; Li and Yan, 2009) and the resulting CO_2 decompression behaviour (Cosham and Eiber, 2008). In the latter case, a comparison of the resulting decompression and crack propagation velocity curves against pressure based on the BTC methodology (Maxey, 1974) is in turn used to infer the pipe toughness that would be required in order to arrest a fracture (see for example King and Kumar (2010)).

The following presents the results of an investigation into the impact of the various impurities on the fracture propagation behaviour of dense phase CO_2 pipelines. The compositions of the impurities assumed are those based on the various capture technologies, including pre-combustion, post-combustion and oxy-fuel as suggested by ICF International (2010). In each case, the variation of fracture velocity versus fracture length is reported for a hypothetical CO_2 pipeline with a realistic fracture toughness. Given the likely extensive variations in the geographical locations of the next generation CO_2 pipelines, the study also investigates the impact of the line temperature, in the range 0 to 30 ^oC, on the pipeline's propensity to fracture propagation.

The pipeline characteristics and the prevailing conditions assumed in the following investigations are the same as those given in table 6.3. However, in order to ensure the capture of all salient features in the data, the pipeline length is increased to 500 m. Table 6.4 shows the corresponding CO_2 mixture compositions assumed based on the various capture technologies as proposed by ICF International (2010). An equi-distant grid system comprising 500 nodal points is employed for the fluid dynamic simulations.

Table 6.4: CO_2 stream % compositions based on the various capture technologies (ICF International, 2010).

Species	Post-combustion	Pre-combustion	Oxy-fuel
CO_2	99.82	95.6	88.4
Ar	0	0	3.7
CO	0	0.4	0
N_2	0.17	0.6	2.8
H_2S	0	3.4	0
Cl	0	0	0.14
H_2	0	0	0
O_2	0.01	0	3.6
SO_2	0	0	1.36
H_2O	0	0	0
NO_2	0	0	0

Figures 6.10 to 6.13 respectively show the impact of the line temperature in the range 0 to 30 ^oC on the variation of the crack velocity with crack length for the pure CO_2, post-combustion, pre-combustion and oxy-fuel mixtures.

The following pertinent observations may be made based on the data presented in the figures:

- Referring to figure 6.10 for pure CO_2, in the temperature range 0 to 20 ^oC (curves A to C), an increase in the line temperature results in a modest increase in the crack arrest length and fracture velocity. The maximum crack length is limited to a distance of 13 m. However, remarkably only a 10 ^oC rise in the line temperature to 30 ^oC (curve D) results in a fast running fracture travelling through the entire length of the 500 m pipeline

- Based on the data presented in figure 6.11 for the post-combustion CO_2 stream, the fracture behaviour is substantially the same as that for the pure CO_2 (figure 6.10). Once again the rise in the line temperature to 30 ^oC results in fracture propagating through the entire pipeline length

- In the case of the pre-combustion CO_2 stream; figure 6.12, the transition to a long running facture commences at a lower temperature of 20 ^{o}C as compared to the pure (figure 6.10) and post-combustion (figure 6.11) CO_2 streams

- According to figure 6.13, the oxy-fuel composition demonstrates the worst case scenario. Here long running fractures are obtained at all the temperatures tested.

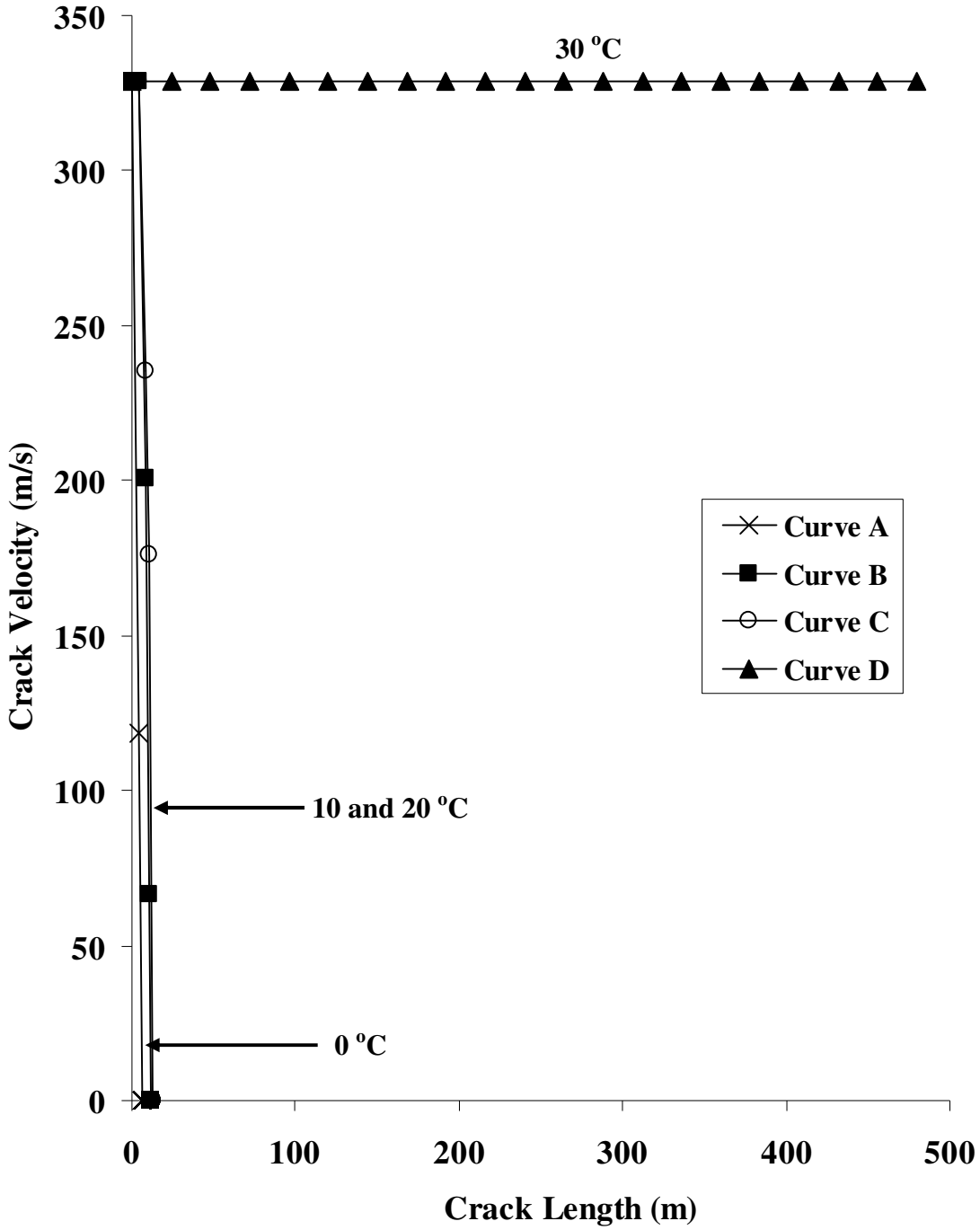

Figure 6.10: The impact of the line temperature on the variation of crack velocity with crack length for pure CO_2 pipeline at 100 barg.

Curve A: 0 °C

Curve B: 10 °C

Curve C: 20 °C

Curve D: 30 °C

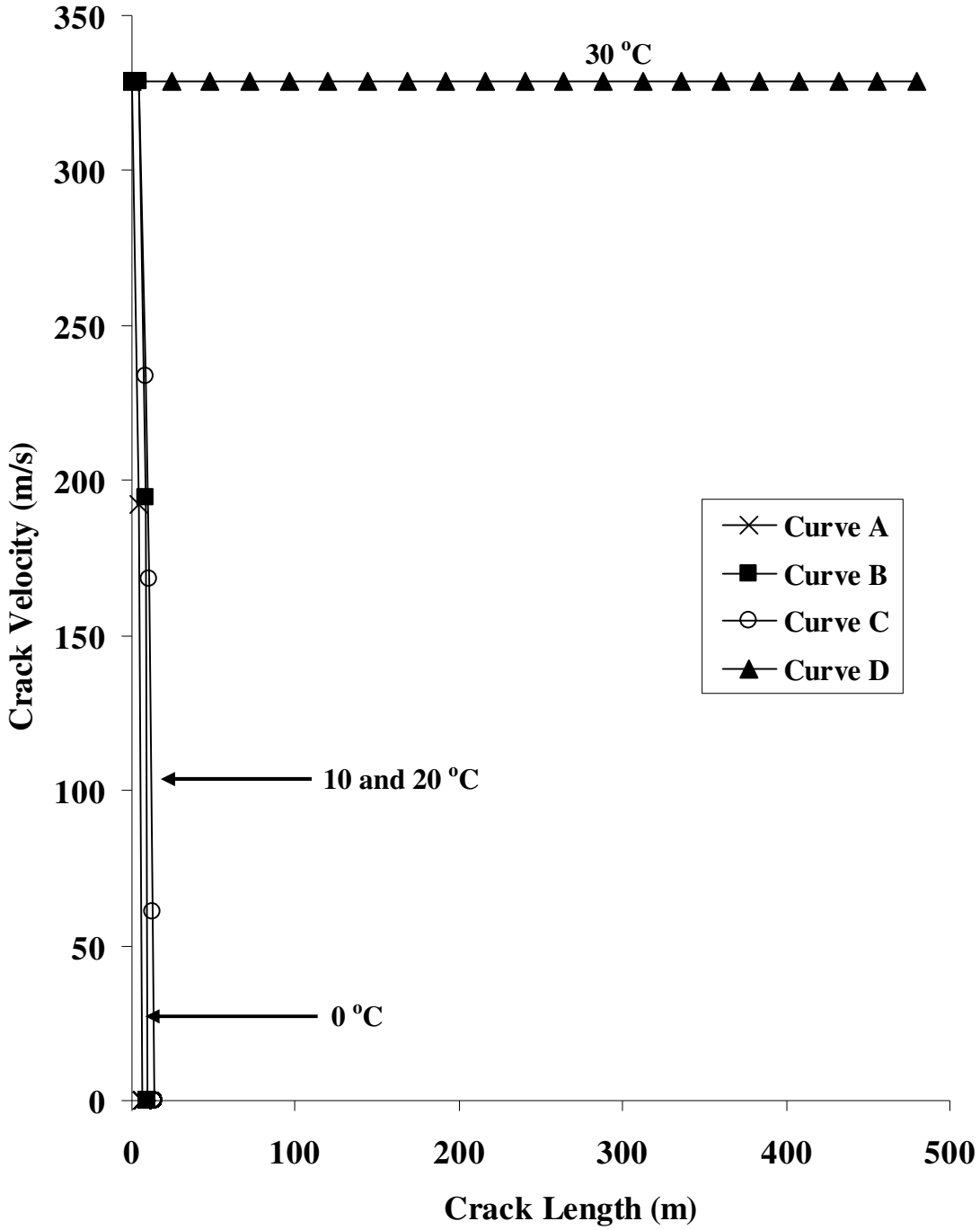

Figure 6.11: The impact of the line temperature on the variation of crack velocity with crack length for post-combustion CO_2 pipeline at 100 barg.

Curve A: 0 °C

Curve B: 10 °C

Curve C: 20 °C

Curve D: 30 °C

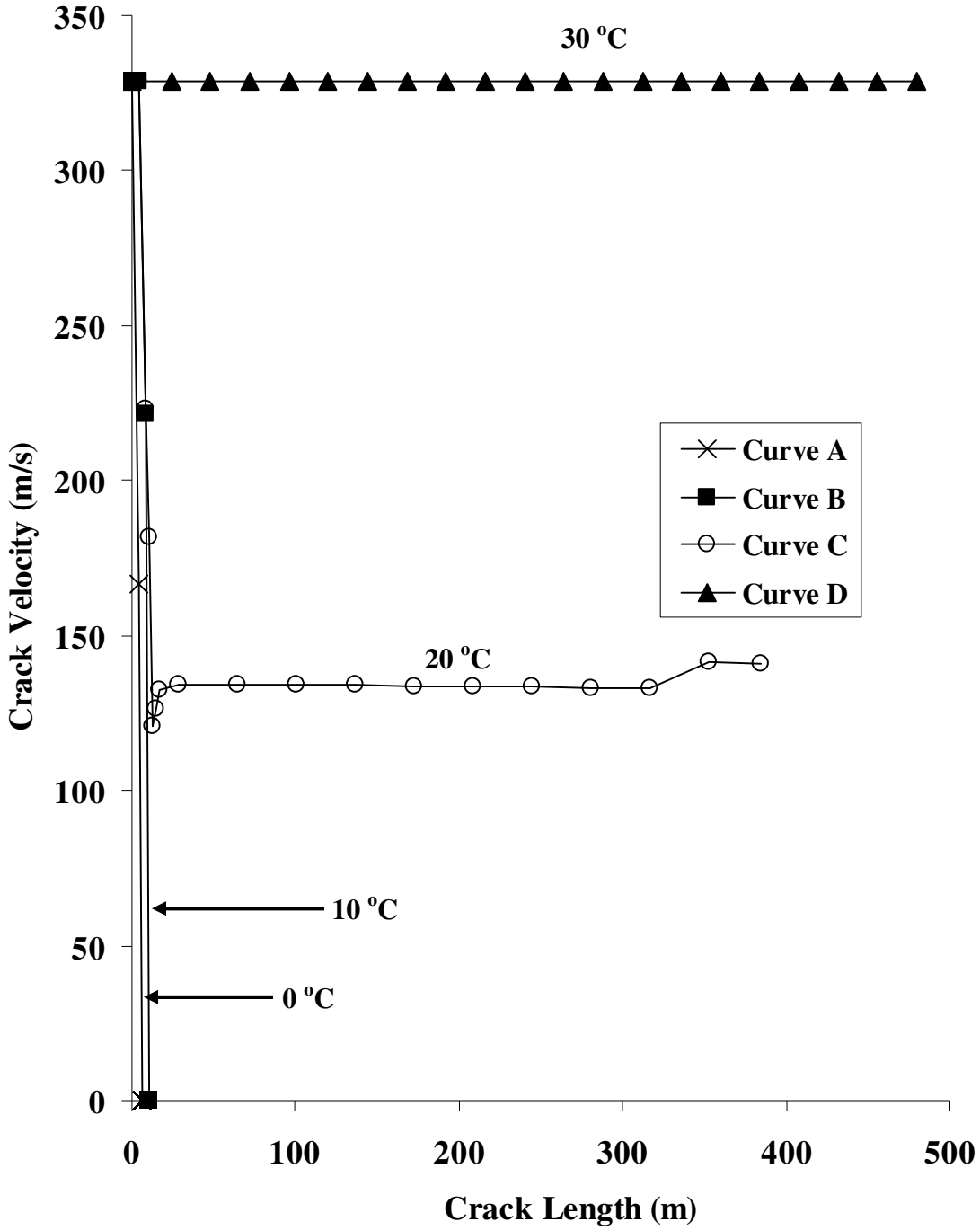

Figure 6.12: The impact of the line temperature on the variation of crack velocity with crack length for pre-combustion CO_2 pipeline at 100 barg.

Curve A: 0 °C

Curve B: 10 °C

Curve C: 20 °C

Curve D: 30 °C

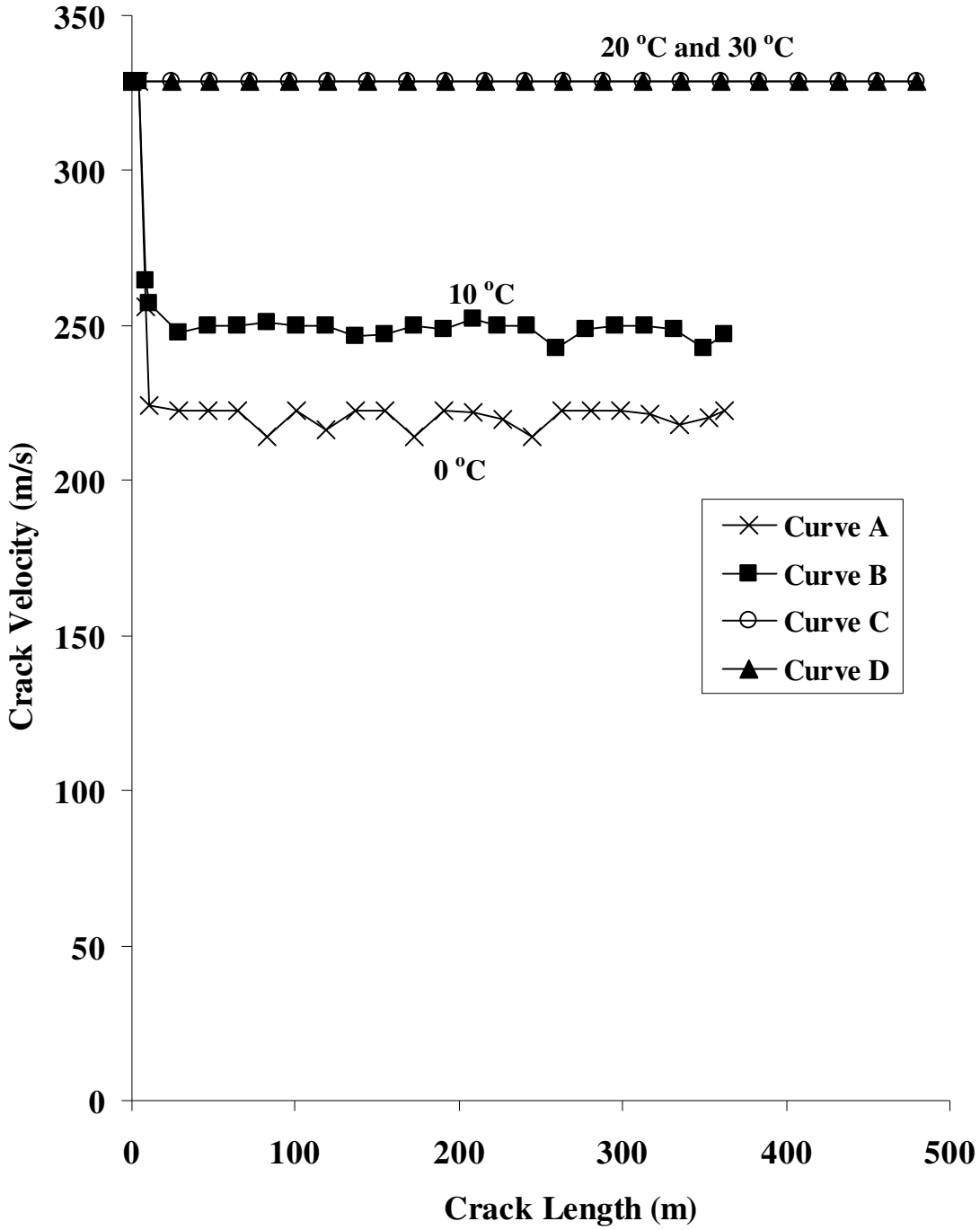

Figure 6.13: The impact of the line temperature on the variation of crack velocity with crack length for oxy-fuel combustion CO_2 pipeline at 100 barg.

Curve A: 0 °C

Curve B: 10 °C

Curve C: 20 °C

Curve D: 30 °C

Table 6.5 shows a summary of the data presented in figures 6.10 to 6.13 expressed in terms of the variation of ratio of crack length to pipeline length for the various capture technologies. A crack ratio of unity corresponds to a fracture running through the length of the pipeline.

Table 6.5: Ratio of crack to pipeline length for the various capture technologies in the temperature range 0 to 30 ^{o}C at the line pressure of 100 barg.

Capture technology	Temperature (^{o}C)	Ratio of crack to pipeline length
100% CO_2	0	0.012
	10	0.024
	20	0.026
	30	1
Post-combustion	0	0.0012
	10	0.02
	20	0.028
	30	1
Pre-combustion	0	0.012
	10	0.022
	20	1
	30	1
Oxy-fuel	0	1
	10	1
	20	1
	30	1

To explain the above behaviour, figure 6.14 shows the fluid depressurisation trajectories expressed in terms of the variation of crack tip pressure with the fluid crack tip temperature at different starting line temperatures of 0 ^{o}C (curve A), 10 ^{o}C (curve B), 20 ^{o}C (curve C) and 30 ^{o}C (curve D) for the CO_2 pipeline. The vapour/liquid saturation curve generated using REFPROP (Lemmon et al., 2007) is also shown. The crack arrest pressure of 43.65 barg calculated from equations (6.1) and (6.2) is also shown for comparison. The corresponding data for the post-combustion, pre-combustion and oxy-fuel mixtures are given in figures 6.15 to 6.17 respectively. The appearance and the subsequent broadening of the phase transition

envelop in moving from the pre-combustion to the oxy-fuel compositions is due to the presence of increasing amounts of impurities in the CO_2 stream.

Returning to figure 6.14, as it may be observed for pure CO_2 in the 0 to 20 ^oC range, the onset of fracture results in a rapid drop in the crack tip pressure from the dense phase to the saturated state. The accompanying significant drop in the fluid temperature is due to its near adiabatic expansion. The above is followed by the relatively slow decompression along the saturation curve where the liquid/vapour transition takes place.

Based on the data presented, it is important to note that the pressure at which the depressurisation trajectories intersect the saturation curve increases with increase in the starting line temperature. Given that the crack will propagate until such time that the crack tip pressure is equal to the crack arrest pressure, it is to be expected that the crack length must increase with increase in the line temperature. This is consistent with the data shown in figure 6.10 presenting the variation of the crack velocity versus crack length. In the case of the pure CO_2 stream at 30 ^oC (figure 6.14, curve D), the crack tip pressure remains well above the crack arrest pressure of 43.65 barg throughout the depressurisation. Hence the crack will propagate through the entire pipeline length as indicated in figure 6.10 (curve D).

Exactly the same arguments apply in explaining the trends observed in figures 6.15 to 6.17. Given the relatively low level of impurities, the post-combustion pipeline exhibits (figure 6.15) a very similar propensity to fracture propagation to the CO_2 pipeline (figure 6.14) where propagating crack occurs only when the line temperature reaches 30 ^oC.

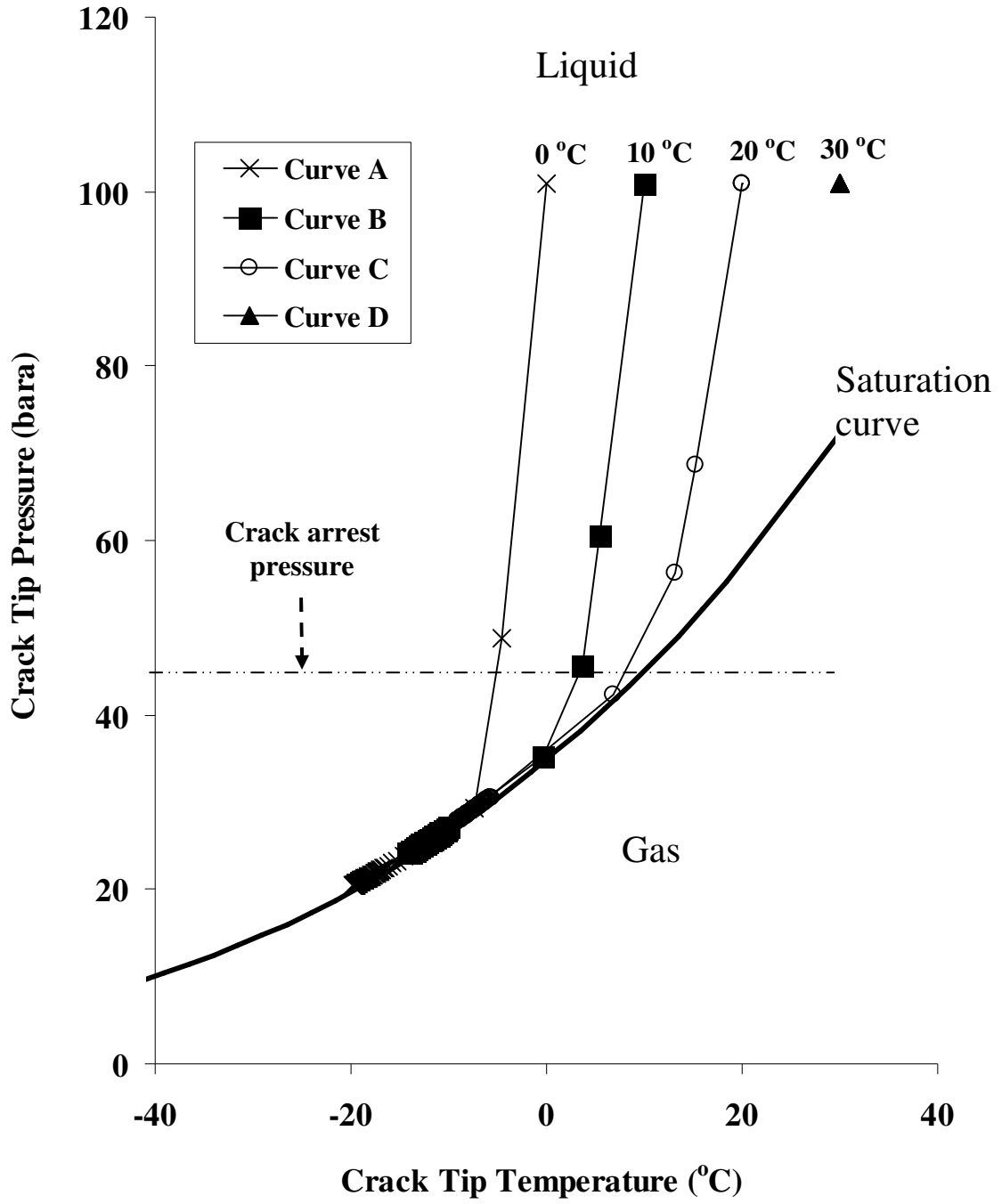

Figure 6.14: The variation of crack tip pressure with temperature for the 500 m long, 100 barg CO_2 pipeline at different starting line temperatures.

Curve A: 0 °C

Curve B: 10 °C

Curve C: 20 °C

Curve D: 30 °C

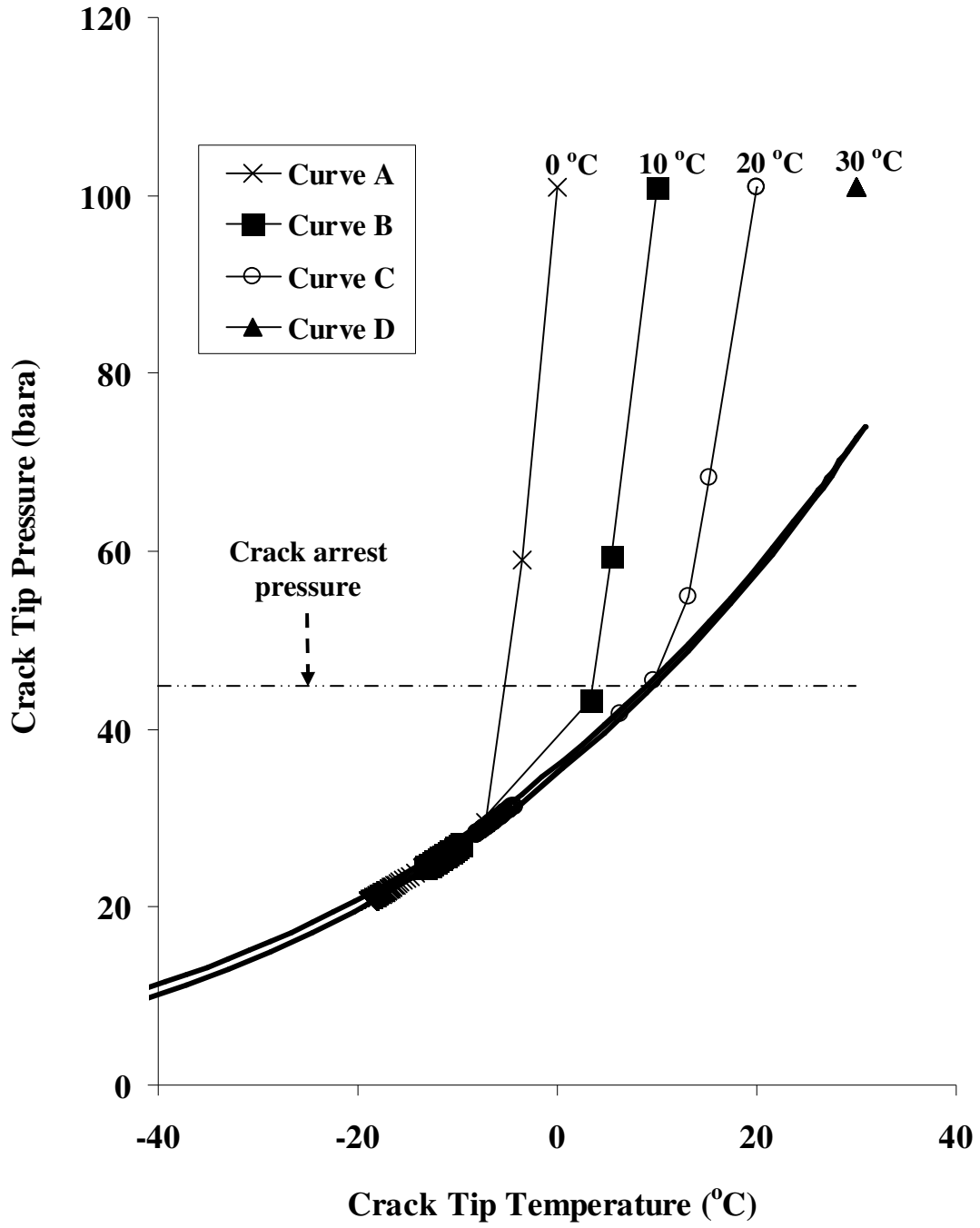

Figure 6.15: The variation of crack tip pressure with temperature for the 500 m long, 100 barg post-combustion pipeline at different starting line temperatures.

Curve A: 0 °C

Curve B: 10 °C

Curve C: 20 °C

Curve D: 30 °C

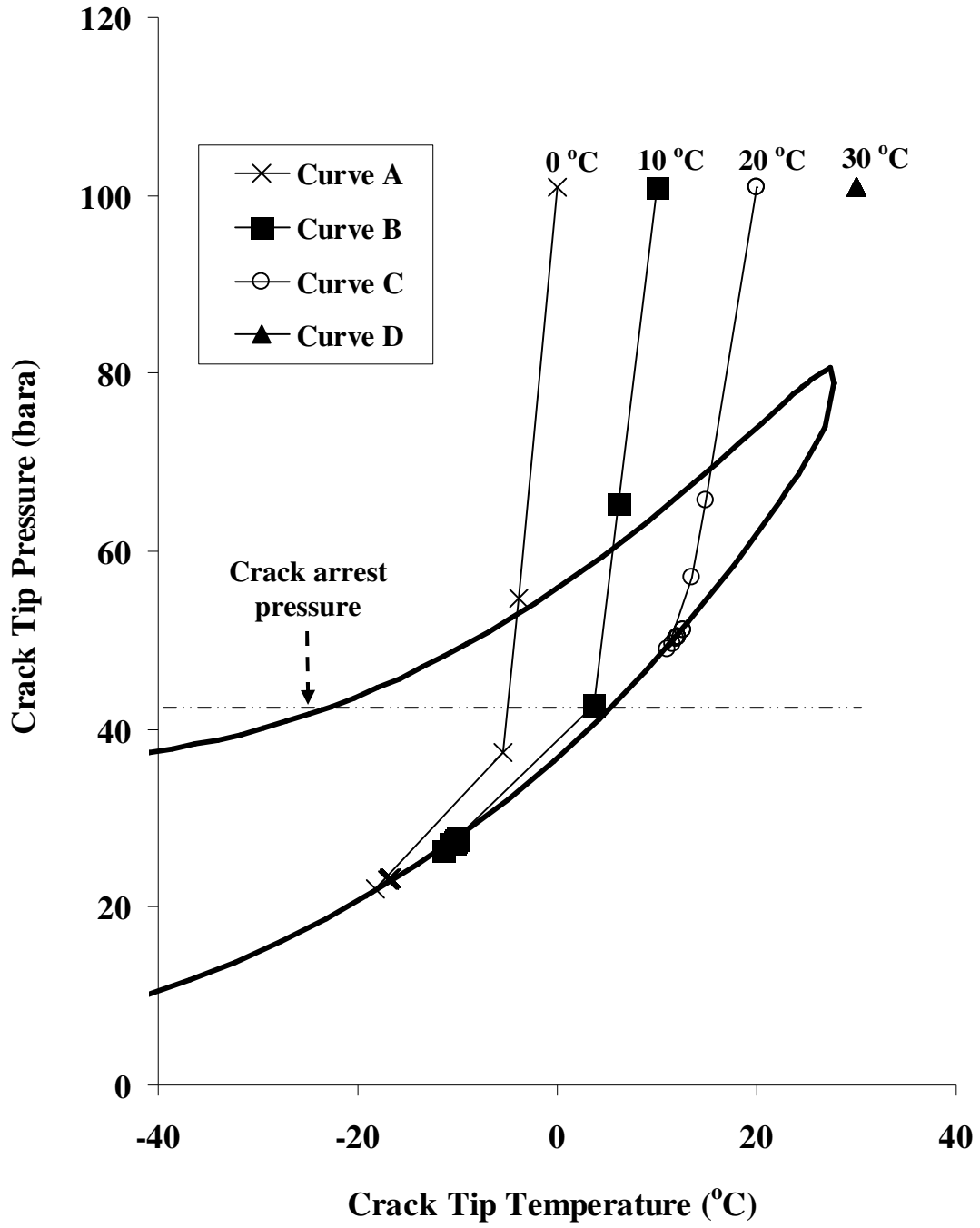

Figure 6.16: The variation of crack tip pressure with temperature for the 500 m long, 100 barg pre-Combustion pipeline at different starting line temperatures.

Curve A: 0 °C

Curve B: 10 °C

Curve C: 20 °C

Curve D: 30 °C

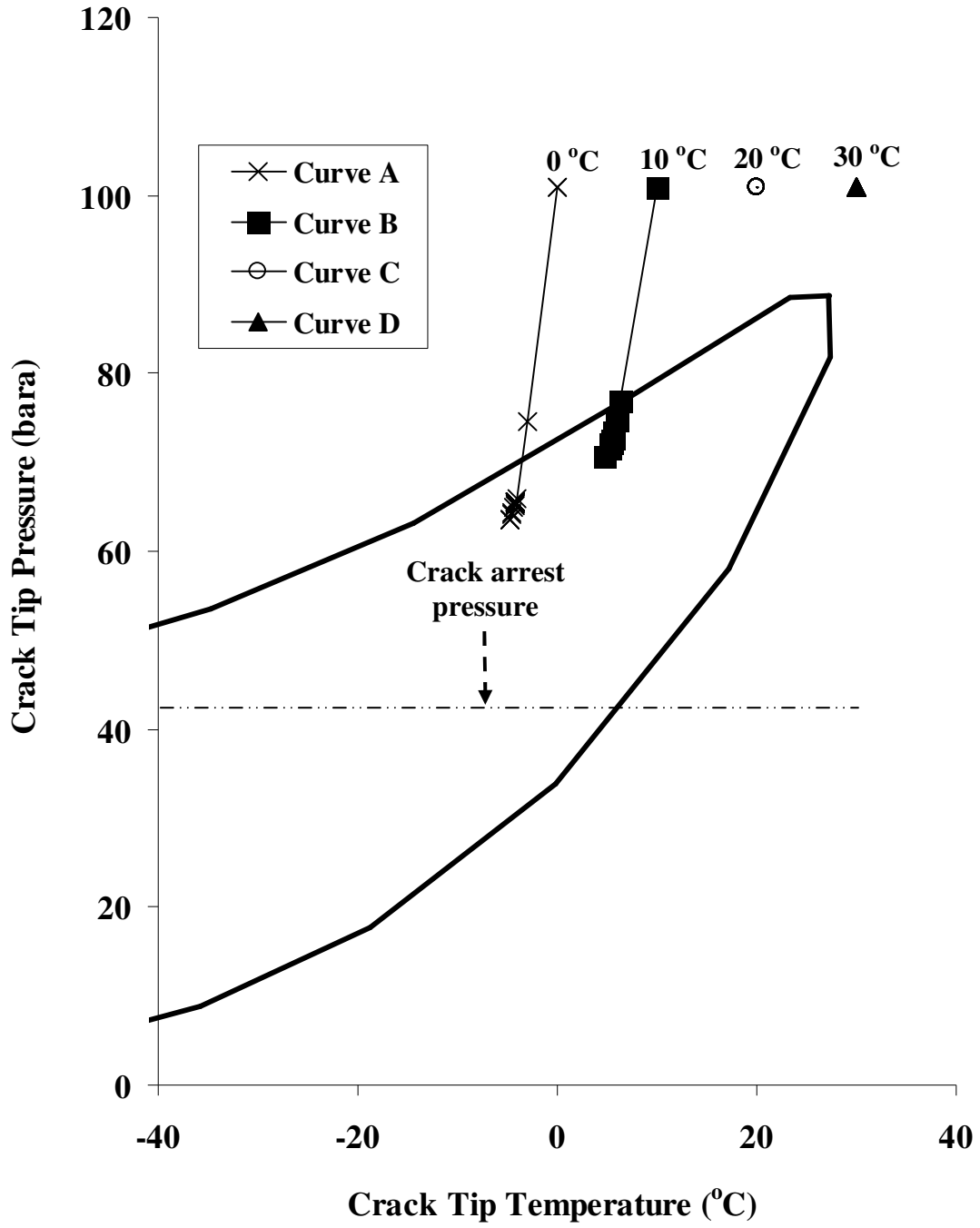

Figure 6.17: The variation of crack tip pressure with temperature for the 500 m long, 100 barg oxy-fuel pipeline at different starting line temperatures.

Curve A: 0 °C

Curve B: 10 °C

Curve C: 20 °C

Curve D: 30 °C

6.2.3 Impact of the Line Pressure

Figures 6.18 to 6.21 show the pipeline fracture propagation data for the various CO_2 compositions simulated at the higher line pressure of 180 barg.

Table 6.6 shows a summary of the data presented in figures 6.18 to 6.21 expressed in terms of the variation of ratio of crack length to pipeline length for the various capture technologies. Once again a crack ratio of unity corresponds to a fracture running through the entire length of the pipeline. The corresponding data for the 100 barg pipeline as previously presented in table 6.5 is reproduced in the same table for comparison.

As it may be observed, despite the significant increase in the line pressure, with the exception of the increase in the crack length, the fracture behaviour in the case of the pure CO_2 (figure 6.18), post-combustion (figure 6.19) and oxy-fuel (figure 6.21) mixtures remain relatively unchanged. In the former two cases, for the temperature range 0 to 20 ^{o}C, the fracture lengths are limited to only a few meters. The rise in the temperature to 30 ^{o}C once again results is a long running facture in both cases. For the oxy-fuel mixture, long running fractures are expected at all the temperatures and pressures under consideration.

However, surprisingly and somewhat counter-intuitively, in the case of the pre-combustion mixture at 20 ^{o}C, the increase in the line pressure results in a finite crack length as opposed to a running fracture. The pipeline's propensity to fracture propagation is reduced as a result of an increase in pressure.

Table 6.6: Ratio of crack to pipeline length for the various capture technologies in the temperature range 0 to 30 ^{o}C at 100 barg and 180 barg.

Capture technology	Temperature (^{o}C)	Ratio of crack to pipeline length (100 barg)	Ratio of crack to pipeline length (180 barg)
100% CO_2	0	0.012	0.32
	10	0.024	0.032
	20	0.026	0.036
	30	1	1
Post-combustion	0	0.012	0.032
	10	0.02	0.0232
	20	0.028	0.036
	30	1	1
Pre-combustion	0	0.012	0.026
	10	0.022	0.034
	20	1	0.036
	30	1	1
Oxy-fuel	0	1	1
	10	1	1
	20	1	1
	30	1	1

Much the same phenomena as those described previously when explaining the impact of the line temperature are responsible for the observed effect of the increase in the line pressure on the fracture behaviour.

Figures 6.22 to 6.25 show the comparisons of the fluid depressurisation trajectories at the two starting line pressures of 180 barg (curve A) and 100 barg (curve B) based on the various CO_2 compositions. The data are presented for a line temperature of 20 ^{o}C chosen as an example. The vapour/liquid saturation curve and the crack arrest pressure of 43.65 barg are plotted in the same figures for reference.

As it may be observed, in all cases the pressure at which the depressurisation trajectories cross the saturation curves decrease with increase in the line pressure. This is due to the

greater degree of the expansion induced cooling obtained when starting at the higher line pressure.

Referring to figure 6.24 in particular, the depressurisation trajectory for the pre-combustion mixture shows the expected rapid drop to saturation conditions as observed previously. However for the 100 barg pipeline the pressure at which the high pressure depressurisation trajectory intersects the saturation curve is ca. 46 barg. The corresponding value for the 180 barg pipeline is at the significantly lower pressure of ca. 38 barg. Given that the crack arrest pressure is ca. 43 barg, it is to be expected that a long running fracture may not be expected in the case of the 180 barg pipeline at 20 ^{o}C. This is consistent with the data shown in figure 6.20; curve C.

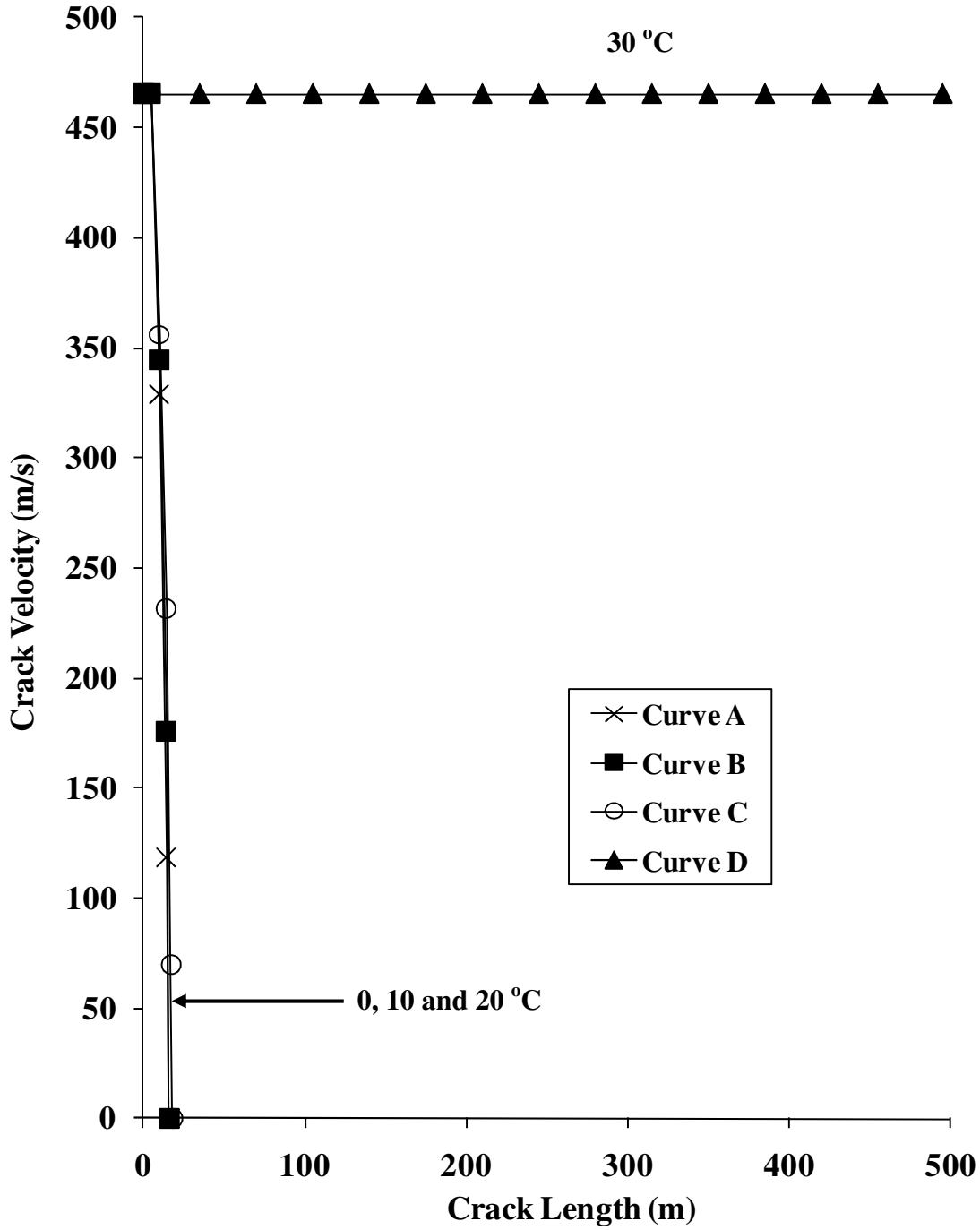

Figure 6.18: The impact of the line temperature on the variation of crack velocity with crack length for pure CO_2 pipeline at 180 barg.

Curve A: 0 °C

Curve B: 10 °C

Curve C: 20 °C

Curve D: 30 °C

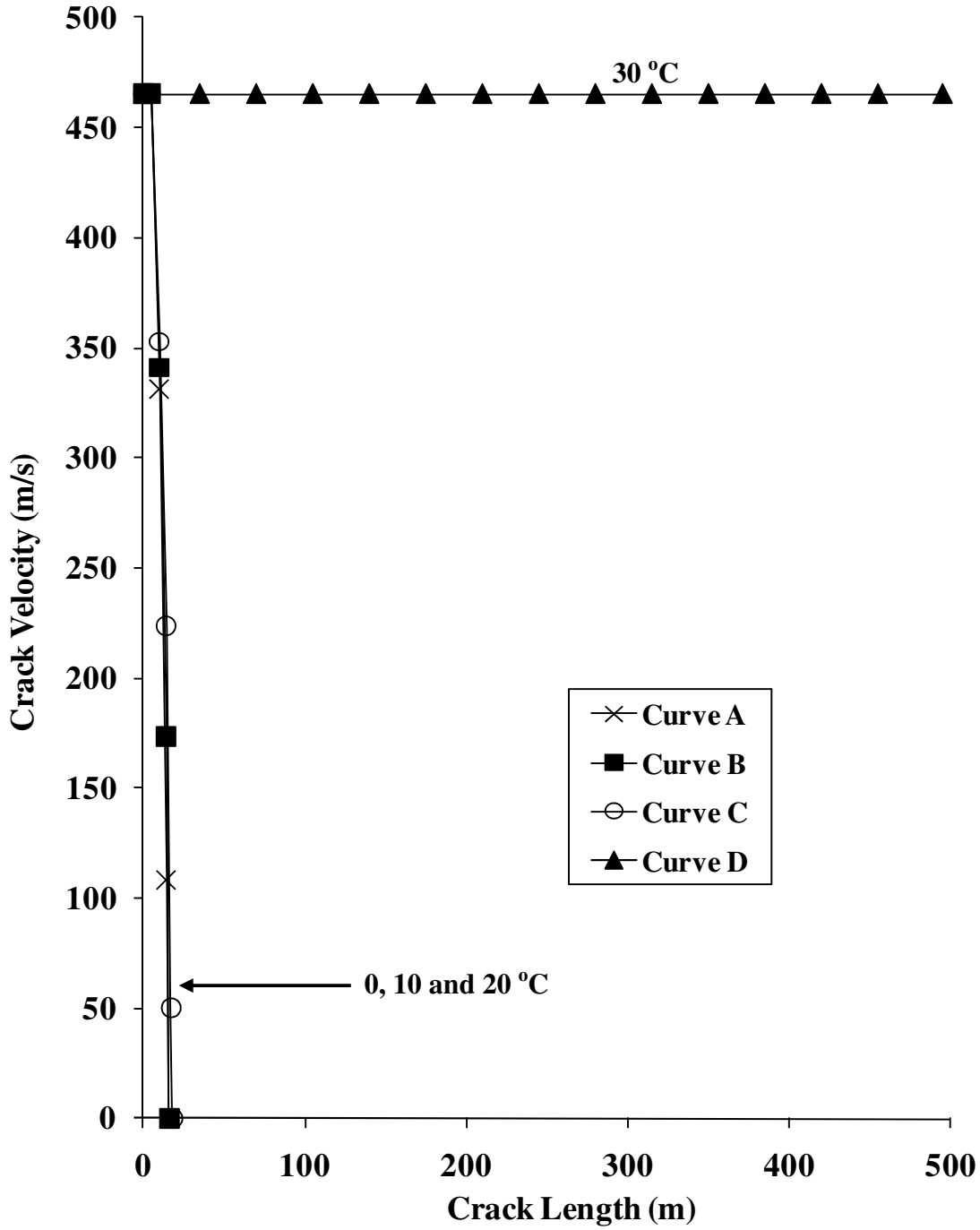

Figure 6.19: The impact of the line temperature on the variation of crack velocity with crack length for post-combustion CO_2 pipeline at 180 barg.

Curve A: 0 °C

Curve B: 10 °C

Curve C: 20 °C

Curve D: 30 °C

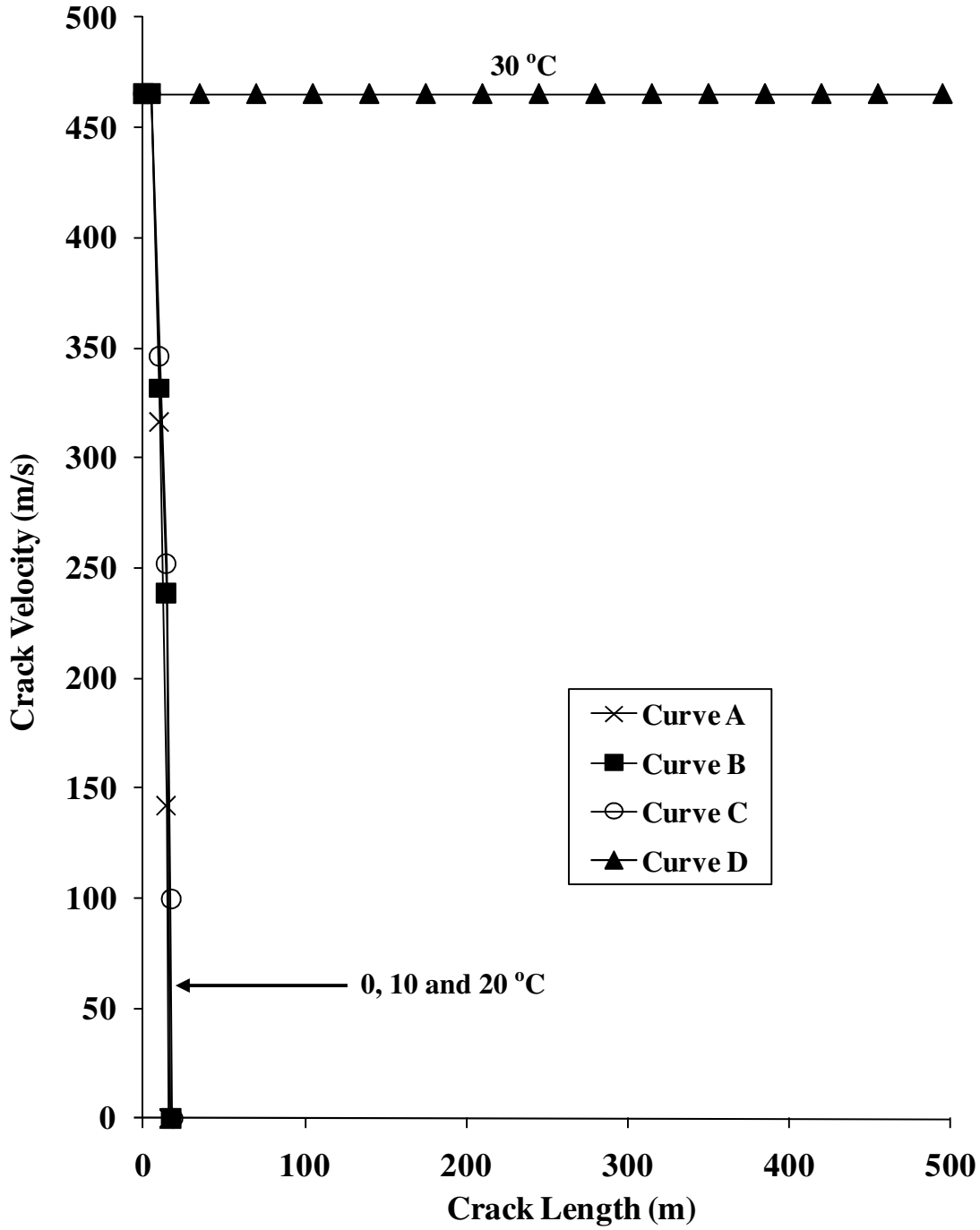

Figure 6.20: The impact of the line temperature on the variation of crack velocity with crack length for pre-combustion CO_2 pipeline at 180 barg.

Curve A: 0 °C

Curve B: 10 °C

Curve C: 20 °C

Curve D: 30 °C

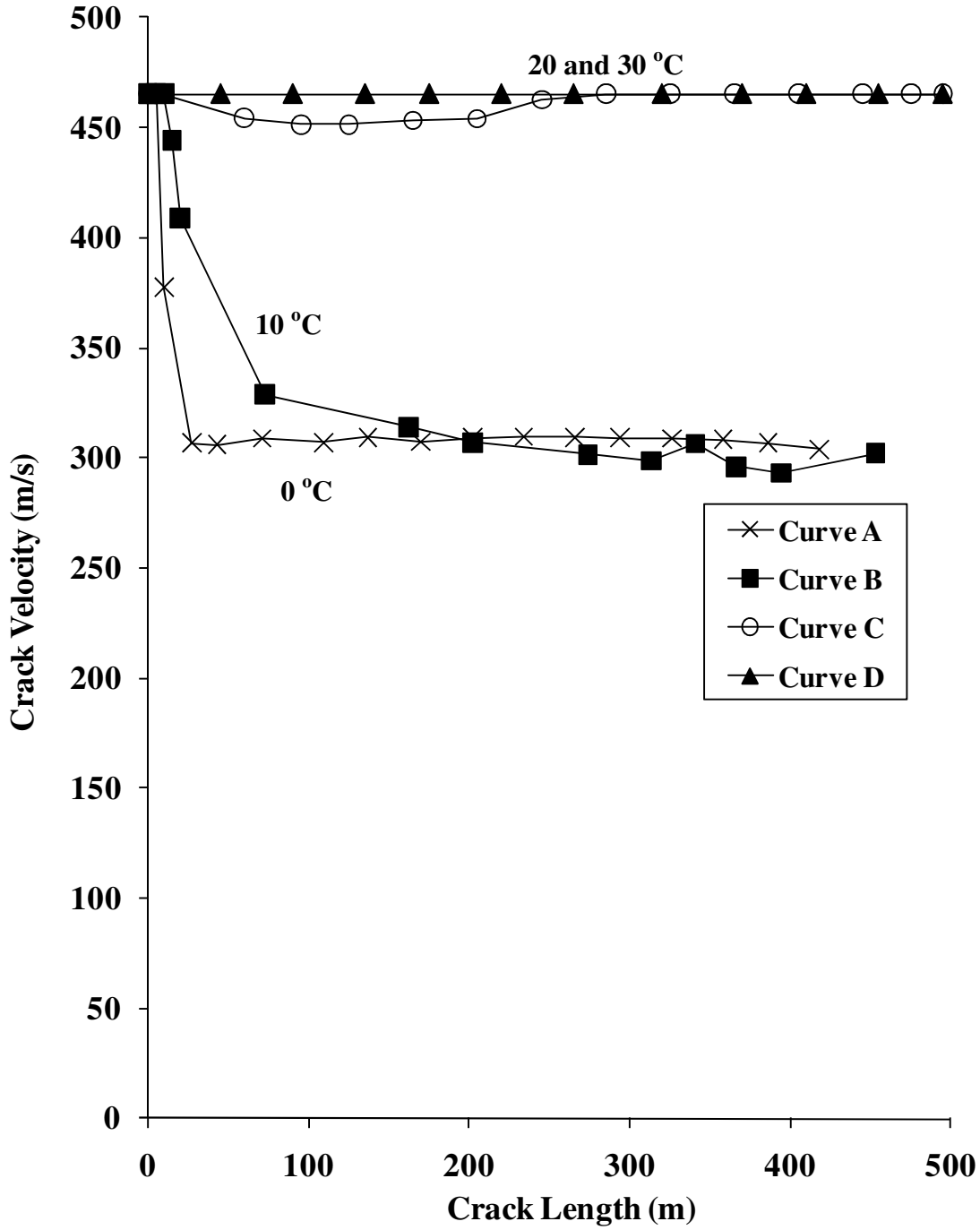

Figure 6.21: The impact of the line temperature on the variation of crack velocity with crack length for oxy-fuel combustion CO_2 pipeline at 180 barg.

Curve A: 0 °C

Curve B: 10 °C

Curve C: 20 °C

Curve D: 30 °C

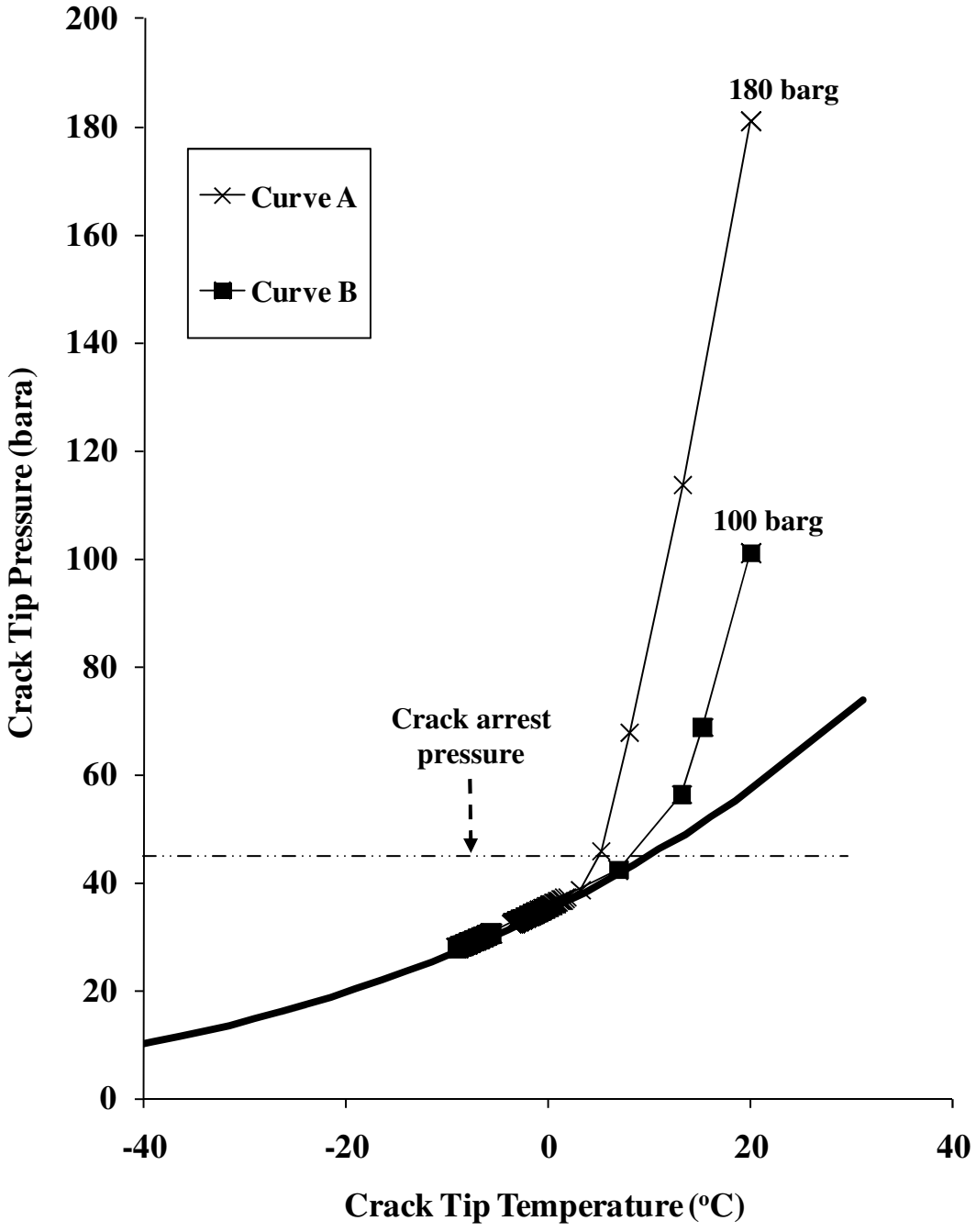

Figure 6.22: The variation of crack tip pressure with discharging fluid temperature for the pure CO_2 pipeline at different starting line pressures. Line temperature: 20 ^{o}C.

Curve A: 180 barg

Curve B: 100 barg

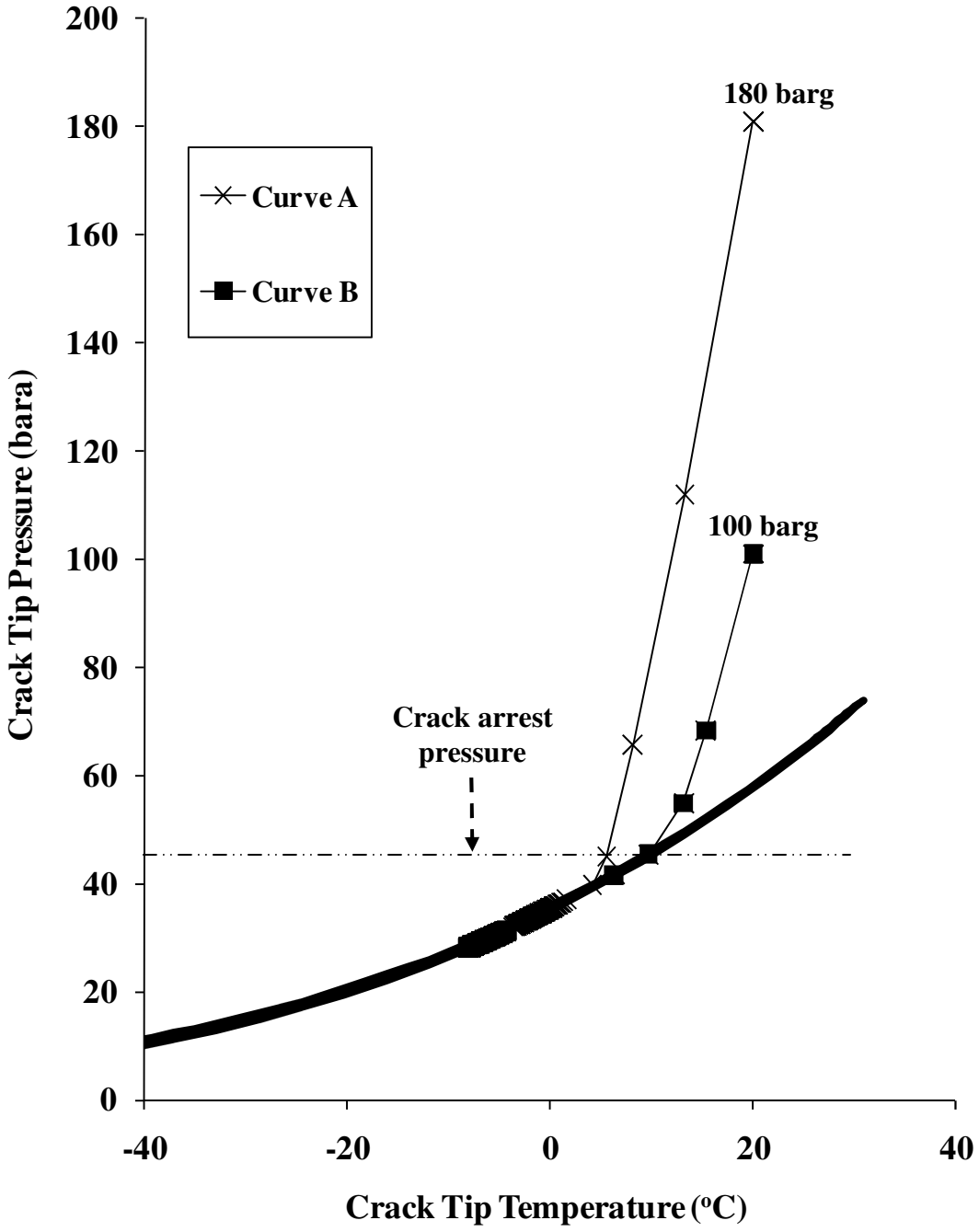

Figure 6.23: The variation of crack tip pressure with discharging fluid temperature for the post-combustion pipeline at different starting line pressures. Line temperature: 20 °C.

Curve A: 180 barg

Curve B: 100 barg

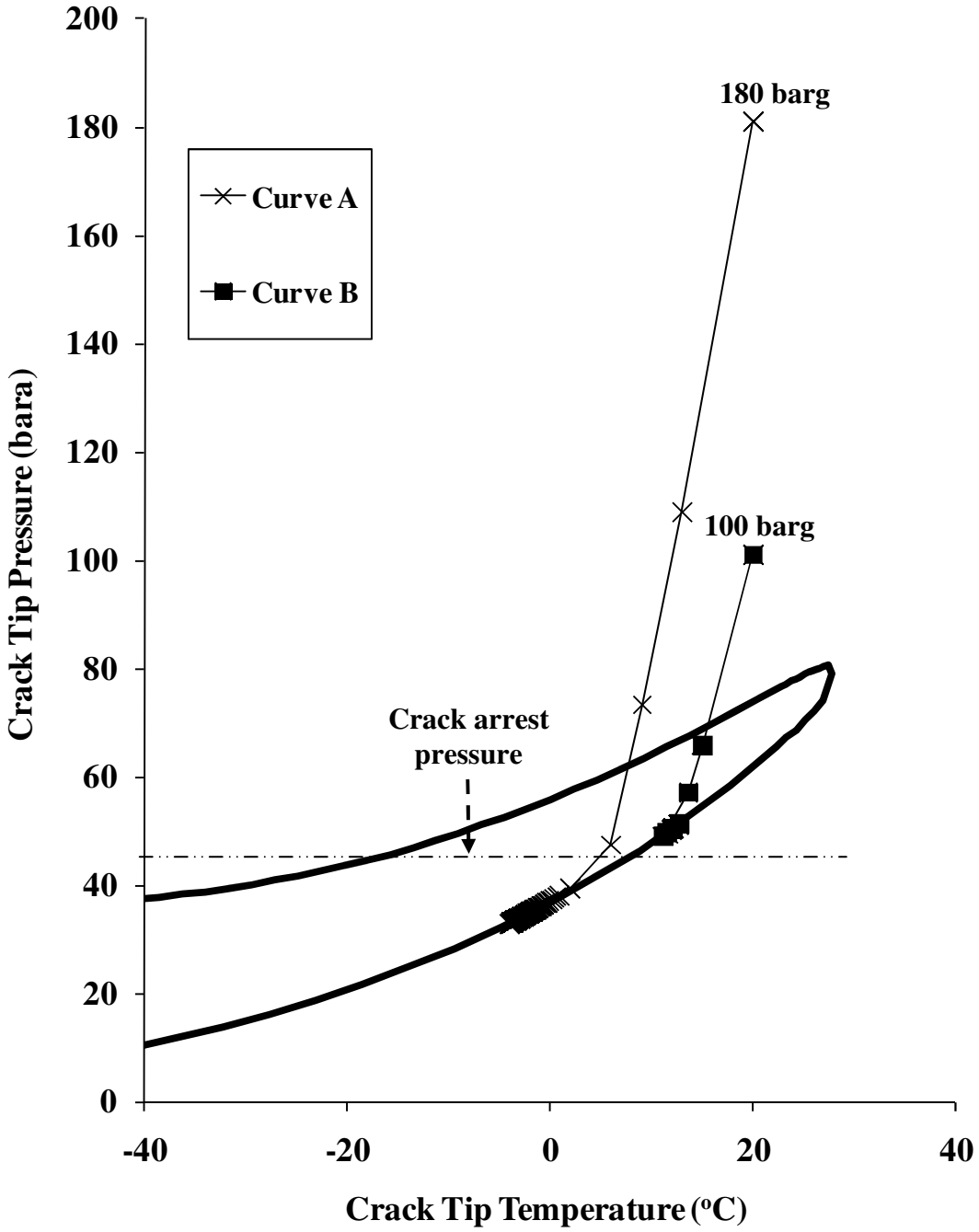

Figure 6.24: The variation of crack tip pressure with discharging fluid temperature for the pre-combustion pipeline at different starting line pressures. Line temperature: 20 °C.

Curve A: 180 barg

Curve B: 100 barg

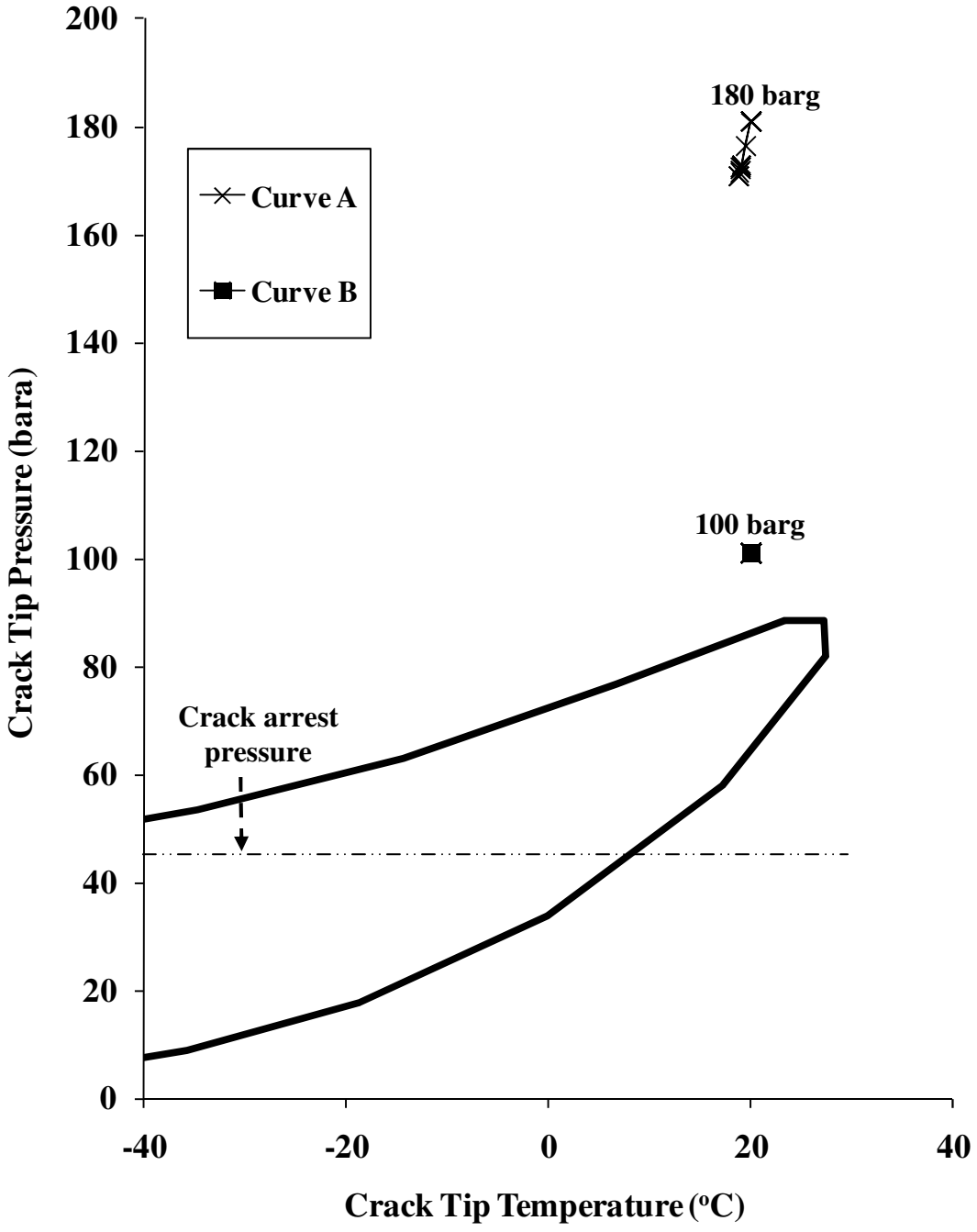

Figure 6.25: The variation of crack tip pressure with discharging fluid temperature for the oxy-fuel pipeline at different starting line pressures. Line temperature: 20 °C.

Curve A: 180 barg

Curve B: 100 barg

6.3 Conclusion

In this chapter the HEM based outflow model was coupled with a well-established Drop Weight Tear Test energy fracture technique (Makino et al., 2001) to simulate ductile fracture propagation in CO_2 pipelines. This study was prompted given the significant interest in and the associated safety concerns with the use of pressurised pipelines for transporting captured CO_2 from fossil fuel power plants as part of the Carbon Capture and Sequestration Chain.

Of all the possible modes of pipeline failure, long running ductile fractures are by far the most catastrophic. As such the development of reliable quantitative techniques for predicting such failures for CO_2 pipelines in the presence of the likely impurities is of significant value.

Based on the application of the model to a hypothetical 500 m pipeline with a realistic fracture toughness transporting dense phase pure CO_2 as well as those based on pre-combustion, post combustion and oxy-fuel capture technologies, the following general conclusions may be made:

1. In the case of pure CO_2, the starting line temperature has a profound effect on the fracture behaviour. Whereas in the temperature range 0 – 20 ^{o}C the fracture length is limited to very short distances, only a 10 ^{o}C rise in the temperature from 20 to 30 ^{o}C results in a fracture propagating through the entire pipeline length. Given the relatively small amounts of impurities present, the post-combustion pipeline behaves in much the same way. Clearly, the above finding has important implications for pipeline routes where the ambient temperatures may exceed 20 ^{o}C

2. The transition to a long running fracture in the case of pre-combustion CO_2 is at lower a lower temperature than that for the pure and post combustion CO_2. In this case, long running fractures is likely at any temperature above 10 ^{o}C

3. The oxy-fuel composition represents the worst case scenario. Here long running fractures would be expected under all the temperatures under consideration.

Remarkably, the increase in the line pressure from 100 to 180 barg reduced the pipeline's propensity to fracture propagation. All of the above findings were successfully explained by examining the CO_2 and its mixtures depressurisation trajectories during fracture propagation relative to the corresponding phase envelopes.

Chapter 7: Non-Isothermal Steady State Flow and Ultra High Pressure Pipeline Rupture Plane Modelling

7.1 Introduction

The accurate modelling of the highly transient flow following pipeline failure critically depends on the correct presentation of the fluid flow profile within the pipeline prior to the accidental discharge. The above is particularly relevant in the case of un-isolated flows involving pumping.

The steady state fluid flow model developed by Oke (2004) presented in chapter 3 (section 3.7; equations 3.37 and 3.39) was based on the assumption of a uniform temperature profile along the pipeline prior to its rupture. This ignored the following processes all of which to varying degrees invalidate this assumption:

- Pipe wall/ambient heat exchange due to any temperature difference between the feed and the surrounding ambient
- Flow induced frictional heating effects
- Expansion induced cooling effects due to the pressure drop along the pipe.

This chapter is divided into two independent but relevant parts in terms of modelling of pipeline failures. The development and validation of a more rigorous non-isothermal steady state flow model which accounts for the above processes is presented first. This is followed by the presentation and validation of a methodology for addressing the rupture plane instabilities encountered in Atti's (2006) outflow model in the case of ultra high pressure pipe failures.

7.2 Non-isothermal Steady State Model

The steady state continuity and momentum equations derived by Oke (2004) (see section 3.7) are recalled below (equations (3.37) and (3.39) respectively). Accounting for the non-isothermal effects due to frictional effects and heat transfer between the feed fluid and the surrounding ambient requires the addition of the energy conservation equation (equation (7.1) below) expressed in terms of entropy.

$$\frac{\partial \rho u}{\partial x} = 0 \qquad \textbf{(3.37)}$$

$$\frac{\partial \rho u^2 + P}{\partial x} = -\rho g \sin(\theta) - \beta \qquad \textbf{(3.39)}$$

$$\frac{\partial s}{\partial x} = \frac{Q_h - u\beta}{\rho u T} \qquad \textbf{(7.1)}$$

Where, ρ, u, s, T and P are the density, velocity, specific entropy, temperature and pressure of the homogeneous fluid as function of space, x, and θ is the angle of inclination to the horizontal. Q_h is the heat transferred between the pipe wall and the fluid calculated from equation (3.36). β is the friction force term given by:

$$\beta = -2\frac{f_w}{D}\rho u|u| \qquad \textbf{(3.4)}$$

Where, f_w is the Fanning friction factor, D the pipeline diameter.

Unlike Oke's (2004) isothermal flow model, no analytical solution for the system of equations (3.37), (3.39) and (7.1) is available. However, as these are ordinary differential equations (ODEs) the NAG sub-routine nag_ivp_ode_rk (Numerical Algorithms Group, 2000) is used to provide a numerical solution. This sub-routine solves the ODEs using a Runge-Kutta method based on the Brankin (1989) algorithm.

7.2.1 Validation

The following represents results based on the comparison of the isothermal and non-isothermal flow model predictions against the real pipeline flow data compiled by Uhl et al. (1965). Two tests groups; namely Test F1 and G1 each comprising different feed temperatures, flow rates and inlet pressures for two different pipelines are selected for this purpose. The pipelines characteristics as well as the number of grids employed for the numerical discretisation are given in table 7.1.

The ambient temperature is not supplied by the authors. Given this and the absence of any other suitable test measurements, the ambient temperature is assumed to be the same as the feed temperature. The wall/ambient heat transfer coefficient of 5 W/m^2K corresponding to an un-insulated pipeline exposed to still air (Mahgerefteh et al., 2006) is assumed as its value is also not given by the authors.

The pipeline feed compositions for both Tests F1 and G1 are given in table 7.2.

Table 7.1: Pipeline characteristics prior to failure of the pipeline for Tests F1 and G1 (Uhl et al., 1965).

	Test F1	Test G1
Length (m)	245255	101498
Pipe external diameter (mm)	513.7	513.7
Pipe wall thickness (mm)	10	10
Number of grids	5000	5000
Roughness (mm)	0.0163	0.0124
Pipeline inclination (^{o})	-0.0853	-0.0893

Table 7.2: Pipeline inventory for Tests F1 and G1 (Uhl et al., 1965).

Component	% Mole fraction
Methane	79.468
Ethane	9.357
Propane	6.322
I –butane	0.309
Butane	0.692
I –pentane	0.013
Pentane	0.002
Carbon –dioxide	1.886
Nitrogen	1.951

Tables 7.3 and 7.4 respectively show the comparison between the measured and predicted outlet pressures for Tests F1 and G1 based on a number of inlet feed conditions. Unless otherwise stated, the inlet conditions correspond to two-phase flow.

Referring to table 7.3 for the ca. 245.255 km pipeline, it may be observed that the non-isothermal model gives very good agreement with the field data. The average absolute error is 1.76 %. Notably, the increase in inlet flow rate and pressure results in an increase in the difference between model and test data, reaching a maximum value of ca. 4.5 % for Test 11.

The isothermal flow model on the other hand produces totally unrealistic results with the outlet pressure exceeding the inlet pressure. The average absolute error is 125.5 % with no discernable trend between the percentage error obtained and the inlet conditions.

Turning to table 7.4 for the shorter pipeline length of ca. 101.5 km, it may be observed that the non-isothermal again provides even better agreement with field data compared to the previous case for the longer pipeline (table 7.3). The average absolute error is 0.47 %. In contrast, Oke's (2004) model produces errors of up to ca. 129 % for runs 1 to 3 and 5 to 7. Simulation 4 failed due to non-convergence.

Notably, for tests 8 to 10 where, as indicated, the inventory at the inlet conditions is in the vapour phase, the isothermal model performs well, producing a similar level of accuracy as that based on the non-isothermal model.

Clearly the significant errors produced using the isothermal flow model are too large to be wholly attributed to the applicability of a uniform temperature profile assumption along the pipeline. Given that these errors are not encountered in the case of the gas phase inventory, they must have their origin in the two-phase flow formulation in Oke's (2004) flow model.

Table 7.3: Comparison of steady state models for Test F1 (Uhl et al., 1965).

Test number	Inlet conditions			Measured outlet pressure (bara)	Predicted outlet pressure (bara)		% difference between model and experiment	
	Flow rate (m^3/s)	Temperature (K)	Pressure (bara)		Non-isothermal	Isothermal (Oke, 2004)	Non-isothermal	Isothermal (Oke, 2004)
1	0.42	286.11	35.54	31.99	31.97	91.94	0.1	187.5
2	0.36	286.11	41.56	38.88	38.85	92.82	0.1	138.7
3	0.35	291.67	56.03	52.86	52.71	74.23	0.3	40.4
4	0.55	286.67	35.76	28.53	28.24	91.39	1.0	220.3
5	0.51	286.67	42.20	35.43	35.14	92.75	0.8	161.8
6	0.46	291.94	55.94	49.22	48.88	75.33	0.7	53.1
7	0.60	286.11	42.13	31.96	31.00	91.34	3.0	185.8
8	0.54	292.22	55.78	45.75	44.99	72.75	1.7	59.0
9	0.65	292.50	56.03	38.89	37.83	72.13	2.7	85.5
10	0.69	292.50	56.12	35.39	33.99	70.38	4.0	98.9
11	0.76	292.50	56.10	28.50	27.23	71.18	4.5	149.7
						% Absolute average error	1.7	125.5

Table 7.4: Comparison of steady state models for Test G1 (Uhl et al., 1965).

Test number	Inlet conditions			Measured outlet pressure (bara)	Predicted outlet pressure (bara)		% difference between model and experiment	
	Flow rate (m^3/s)	Temperature (K)	Pressure (bara)		Non-isothermal	Isothermal (Oke, 2004)	Non-isothermal	Isothermal (Oke, 2004)
1	0.43	290.44	35.54	34.18	34.16	78.10	0.1	128.5
2	0.37	290.72	41.56	40.51	40.49	78.85	0.1	94.6
3	0.36	293.33	56.03	54.81	54.78	67.51	0.1	23.2
4	0.56	290.17	35.76	33.16	32.98	failed	0.6	failed
5	0.52	290.56	42.20	39.74	39.56	79.37	0.5	99.7
6	0.46	294.44	55.94	53.42	53.28	59.43	0.3	11.3
7	0.61	290.28	42.13	38.54	38.11	78.61	1.1	104.0
8*	0.55	295.44	55.78	52.16	51.82	51.80	0.7	0.7
9*	0.66	295.56	56.03	50.05	49.72	49.66	0.7	0.8
10*	0.71	295.94	56.12	49.12	48.69	48.61	0.9	1.0
						% Absolute average error	0.5	51.5

* vapour

7.3 Ultra High Pressure Pipeline Rupture Modelling: Critical Discharge Algorithm (CDA)

As presented in chapter 4, the choked flow model presented by Atti (2006) is based on the assumption of sonic flow at the release plane following which the release pressure is found by solving an energy balance (chapter 4; equation (4.25)). In the following section it will be shown that at high pressures (> 400 bara), the model becomes unstable. An alternative rupture plane solution methodology termed the Critical Discharge Algorithm (CDA) addressing this shortcoming is presented in the following. Such capability is important given the current trend in operating pipelines at ultra high pressures (e.g. above 600 bara: Urbaniak et al., 2007) due to economic and extreme operational conditions.

7.3.1 Critical Discharge Algorithm (CDA)

Elias and Lellouche (1994) present an alternative formulation of the isentropic, HEM critical flow model to that employed by Atti (2006) (see section 4.3.4). In this model equation (4.25) recalled below is used to obtain the outflow rate, presented by equation (7.2):

$$h_j + \frac{1}{2}u_j^2 = h_{o1} + \frac{1}{2}u_{o1}^2 \qquad \textbf{(4.25)}$$

$$G = \sqrt{2\rho_j^2\left(h_{o1} + \frac{1}{2}u_{o1}^2 - h_j\right)} \qquad \textbf{(7.2)}$$

Where G is the outflow rate. The remaining notations in equation (7.2) were defined previously (section 4.3.4). The choked/critical discharge rate is then obtained by maximising the flow rate with respect to pressure (Elias and Lellouche, 1994) to yield the discharge pressure.

The CDA utilised in this study consists of the numerical maximisation of equation (7.2) using the method of Brent (2002). This involves the sampling of the pressure in order to

find the discharge pressure, P_{o1} in conjunction with isentropic flash calculations. Once the maximum discharge pressure has been obtained the remaining release plane flow variables ρ_{o1}, T_{o1} and h_{o1} are determined using a pressure-entropy (P_{o1}-s_j) flash calculation. The corresponding calculation flow logic diagram for determining the discharge rate is shown in figure 7.1.

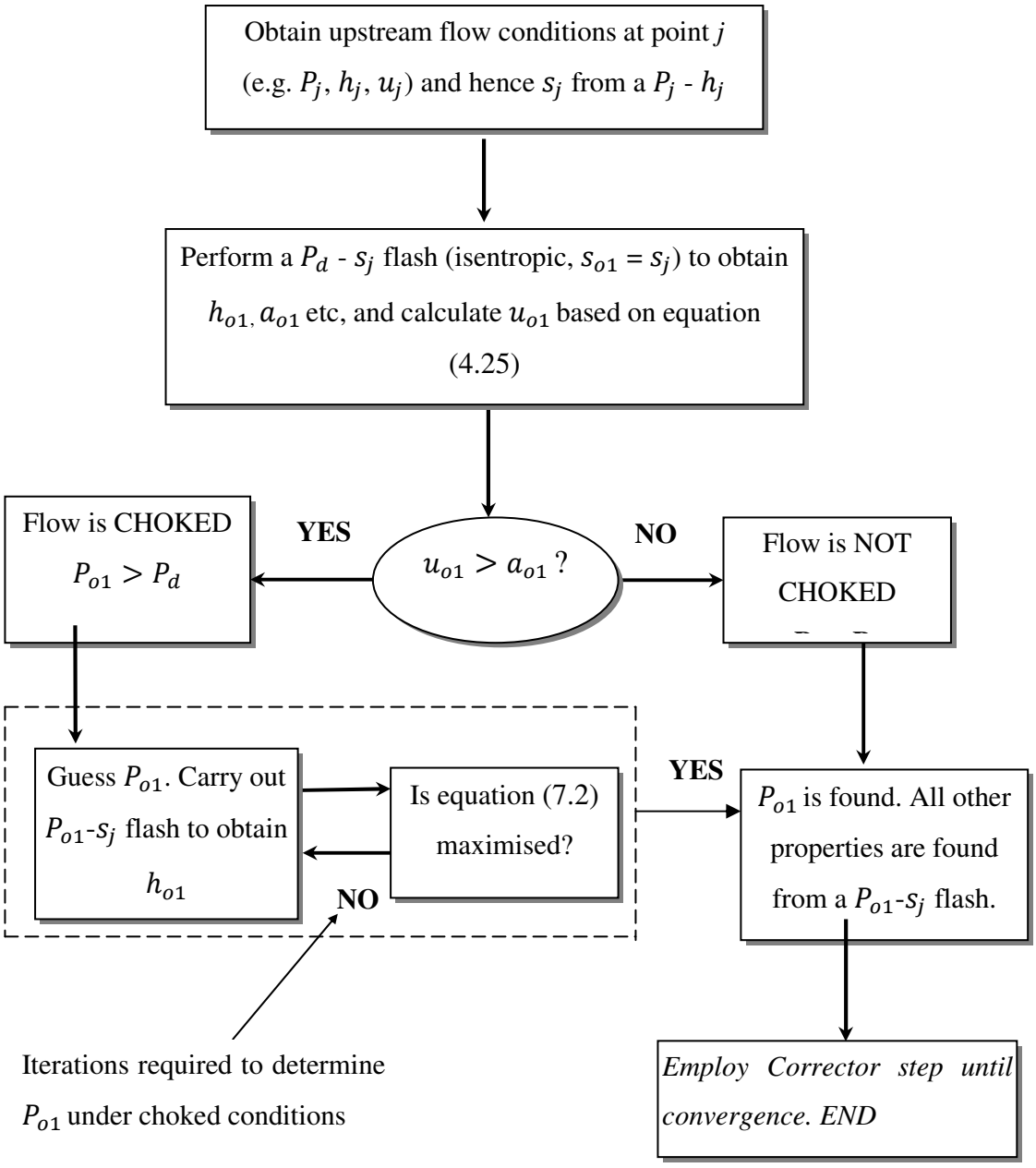

Figure 7.1: Flow diagram for the Critical Discharge Algorithm.

7.3.2 Validation of the Critical Discharge Algorithm (CDA)

Prior to the application of the CDA model to simulating ultra high pressure releases, its efficacy at moderate pressures is first examined by comparing its predictions against the Shell and BP on the Isle of Grain (Chen, 1993; Richardson and Saville, 1996) pipeline rupture tests.

Table 7.5 gives the pipeline characteristics, prevailing conditions and inventories used for the simulation of Isle of Grain P40 and P42 FBR tests. The corresponding data for pipeline puncture data Tests P45 and P47 were given previously (see section 5.3; table 5.2).

Figures 7.2 and 7.3 respectively show the variation of release pressure and temperature for Test P40. Curve A represents the measured data, while curves B and C are the predicted results obtained using the Atti's (2006) model and the CDA respectively. The corresponding data for Tests P42, P45 and P47 are given in figures 7.4 to 7.9 respectively.

Returning to figure 7.2, with the exception of the first 3 s where a slight discrepancy is observed the two predictions are essentially identical. The initial deviation appears to be a consequence of the fluids transition to two-phase, where the prediction of Atti's (2006) model is dependent on the accurate prediction of the speed of sound. Exactly the same trends are observed in figures 7.3 to 7.5.

Similar behaviour is observed in figures 7.6 to 7.9, however in these cases the deviations between measured and predicted data are seen in the latter stages of the depressurisation. In all cases the CDA (curves C) predicts a slightly faster pressure/temperature drop, this is most notable in figure 7.9. However, this effect has only a very small impact on the degree of agreement with the experimental data (curves A).

Table 7.5: Simulation input data for Isle of Grain P40 and P42.

Input		Test P40	Test P42
Inlet Parameters	Number of components	2	2
	Feed composition (mole %)	Propane - 95	Propane - 95
		n-Butane - 5	n-Butane - 5
	Feed inlet temperature (K)	293.15	293.15
	Feed inlet pressure (bara)	21.6	11.3
	Ambient temperature (K)	292.25	291.75
	Ambient pressure (bara)	1.01	1.01
Pipeline Characteristics	Length (m)	100	100
	External diameter (mm)	168.6	168.6
	Wall thickness (mm)	7.3	7.3
	Roughness (mm)	0.05	0.05
	Orientation to the horizontal plane (deg)	0	0
Rupture Conditions	Failure mode	FBR	FBR
	Failure location relative to the high pressure end (m)	100	100
	Rupture diameter (mm)	154	154
	Discharge coefficient	1	1
Other Parameters	Feed flow rate prior to rupture (m3/sec)	0	0
	Pumping cessation time following pipeline failure (s)	0	0
	Pump shut-off head (bara)	110	110
	Grid system used	Simple	Simple
	Number of grid points specified	50	50
	Equation of State	PR	PR
	Friction factor correlation	Chen	Chen
	Heat transfer coefficient (W/m^2K)	Automatically determined (Un-insulated pipeline exposed to still air)	Automatically determined (Un-insulated pipeline exposed to still air)
	Total depressurisation time (s)	25	25

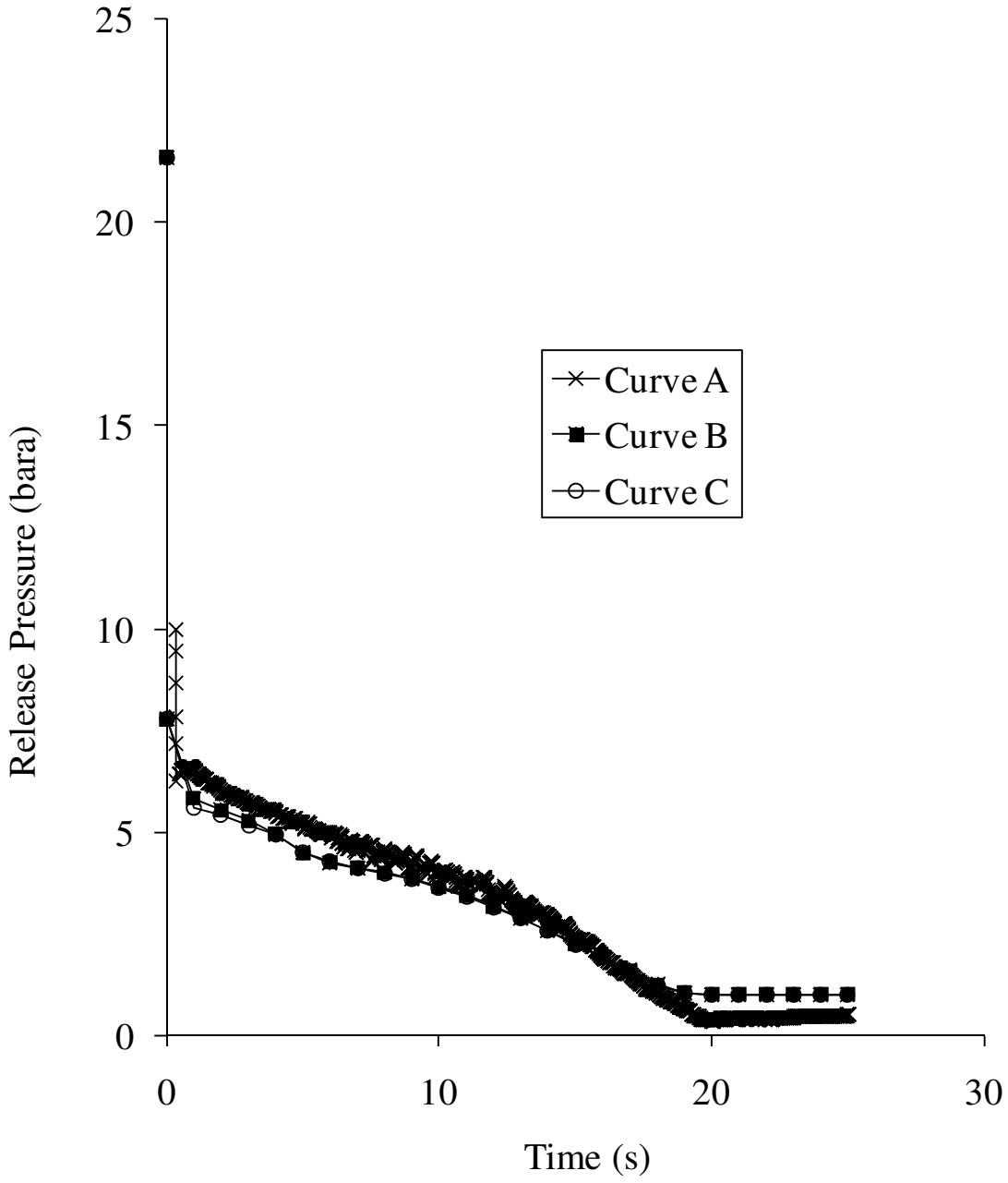

Figure 7.2: Variation of release pressure with time following a FBR for Test P40.

Curve A: Experimental data (Richardson and Saville, 1996)

Curve B: Atti's (2006)

Curve C: CDA

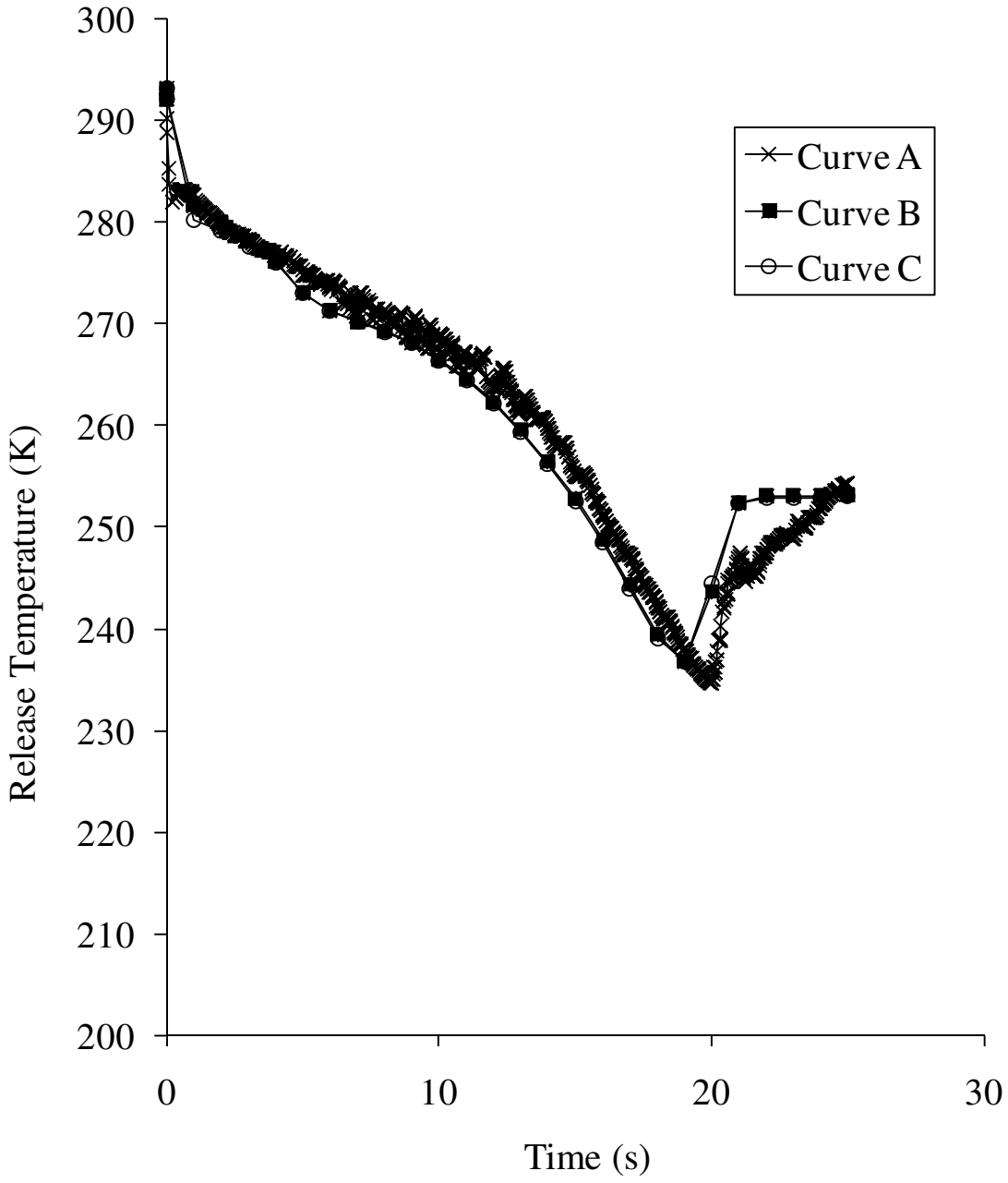

Figure 7.3: Variation of release temperature with time following a FBR for Test P40.

Curve A: Experimental data (Richardson and Saville, 1996)

Curve B: Atti's (2006)

Curve C: CDA

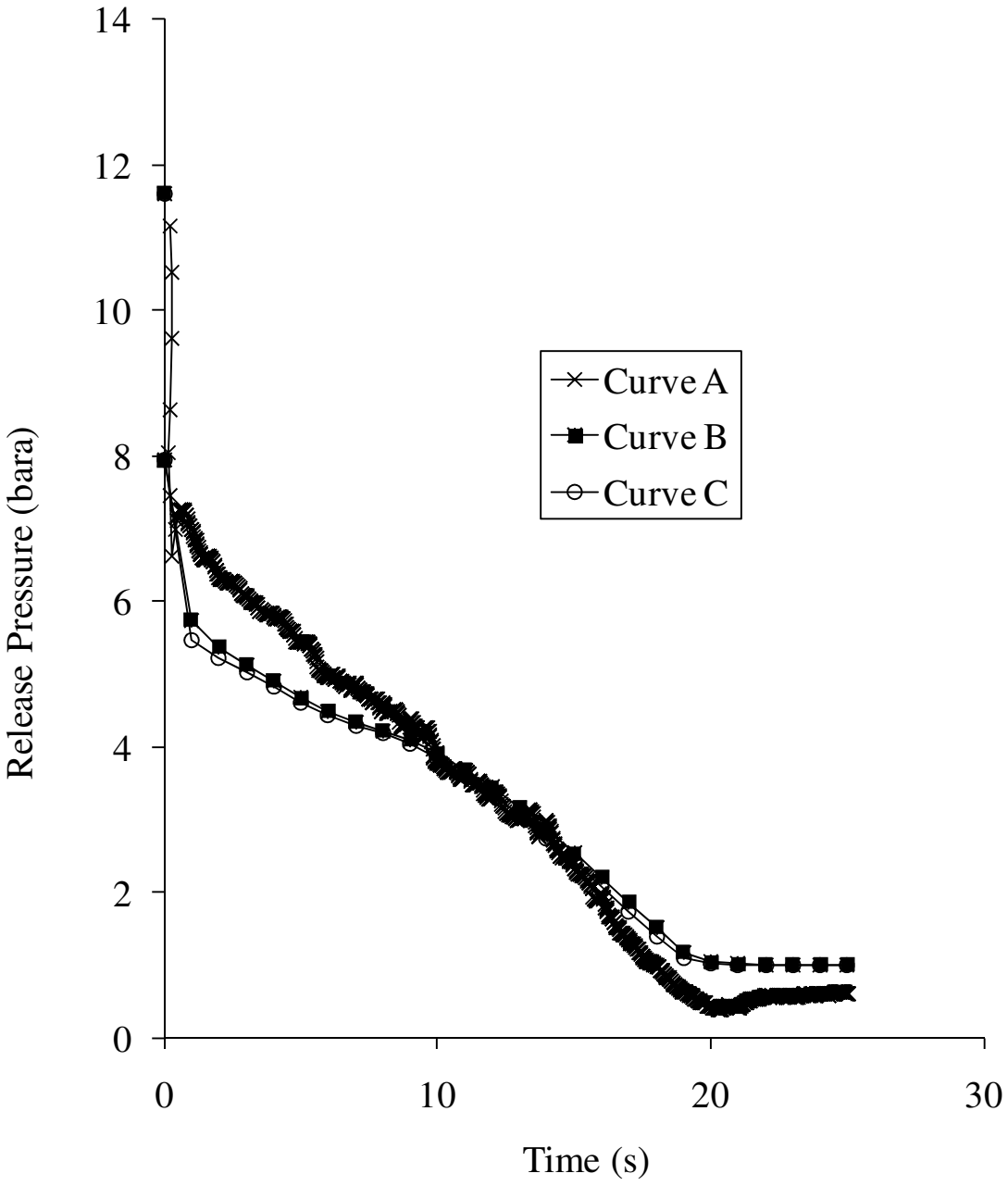

Figure 7.4: Variation of release pressure with time following a FBR for Test P42.

Curve A: Experimental data (Richardson and Saville, 1996)

Curve B: Atti's (2006)

Curve C: CDA

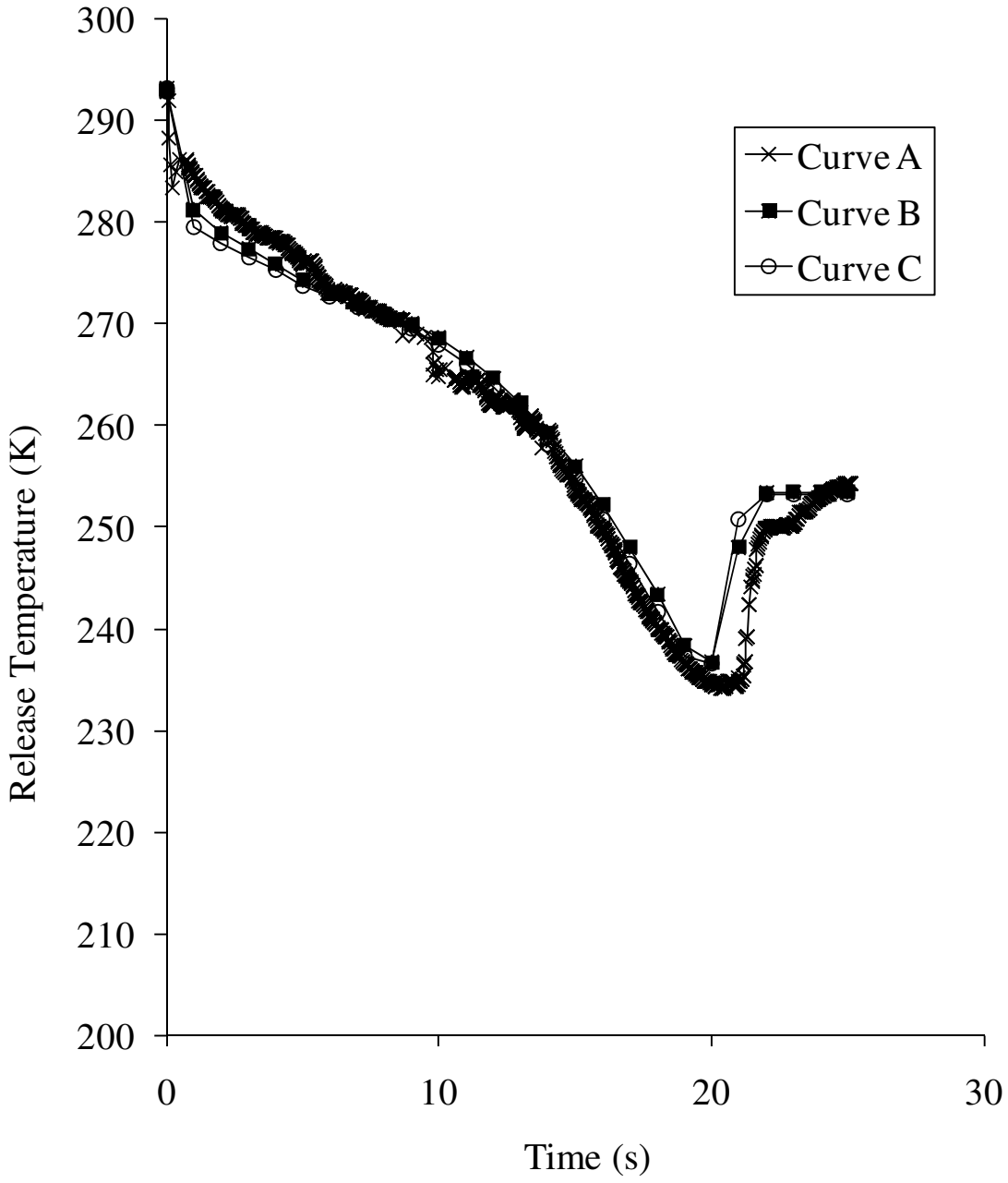

Figure 7.5: Variation of release temperature with time following a FBR for Test P42.

Curve A: Experimental data (Richardson and Saville, 1996)

Curve B: Atti's (2006)

Curve C: CDA

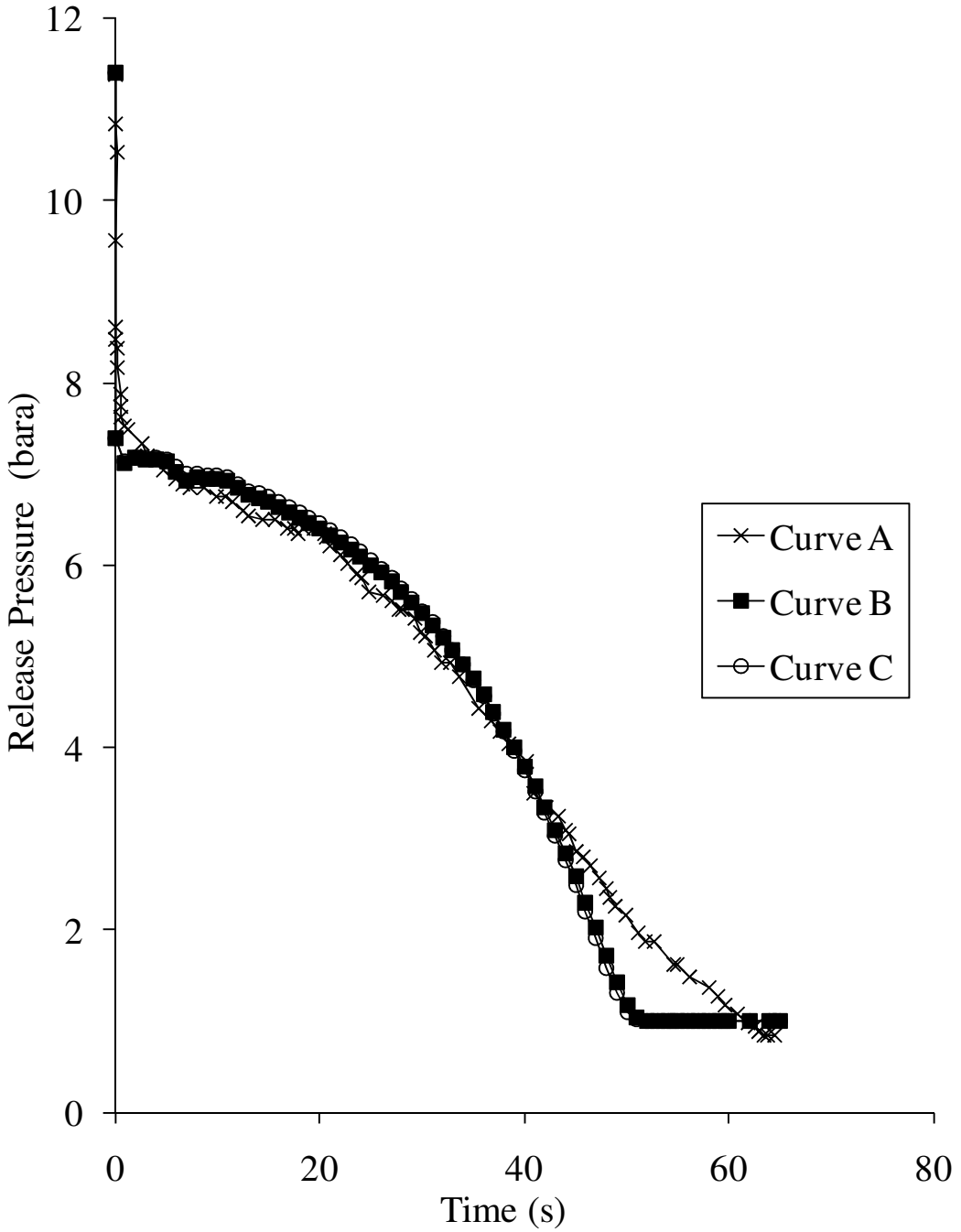

Figure 7.6: Variation of open end pressure with time following a 95 mm diameter axisymmetric puncture for test P45.

Curve A: Experimental data (Richardson and Saville, 1996)

Curve B: Atti's (2006)

Curve C: CDA

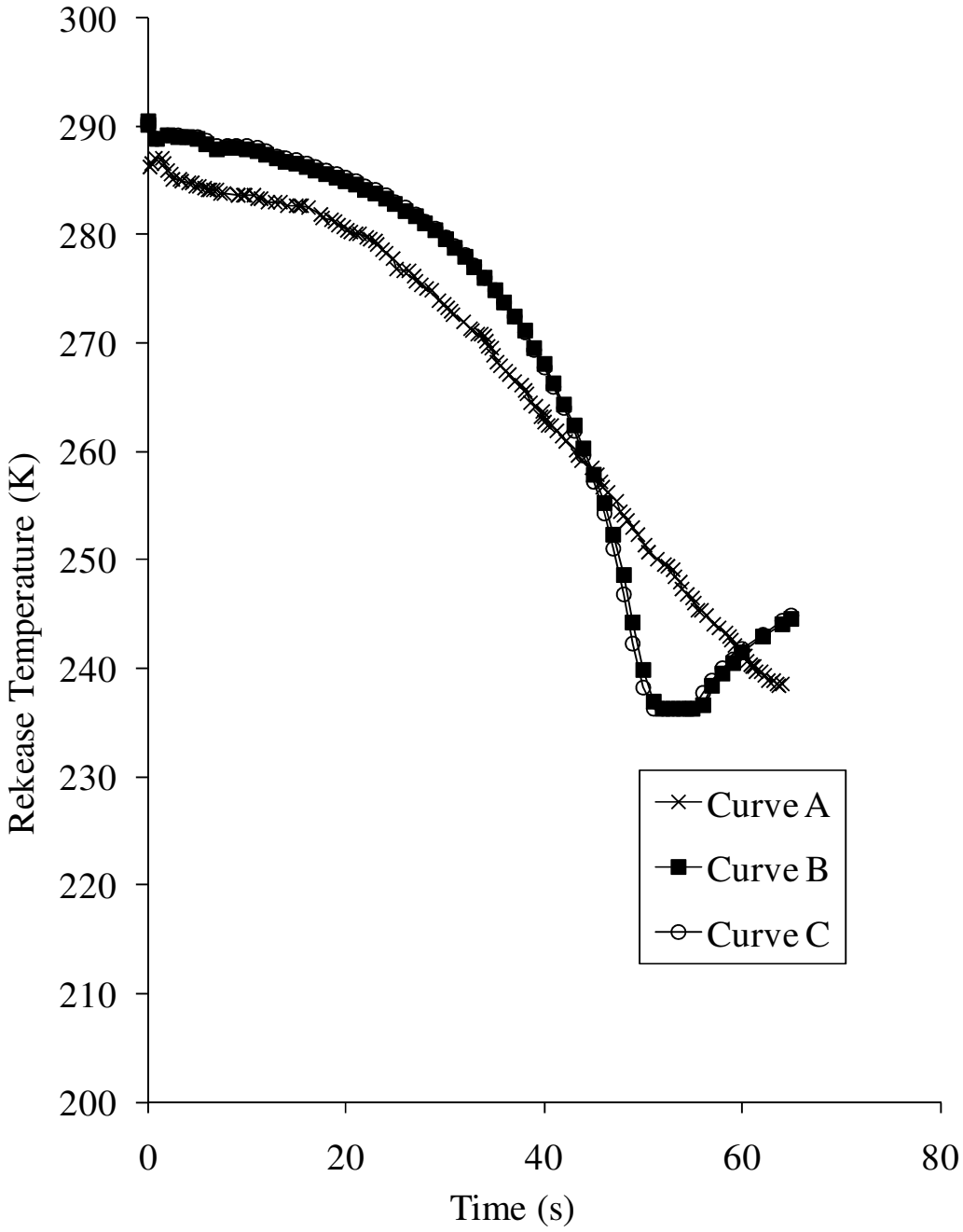

Figure 7.7: Variation of open end temperature with time following a 95 mm diameter axisymmetric puncture for test P45.

Curve A: Experimental data (Richardson and Saville, 1996)

Curve B: Atti's (2006)

Curve C: CDA

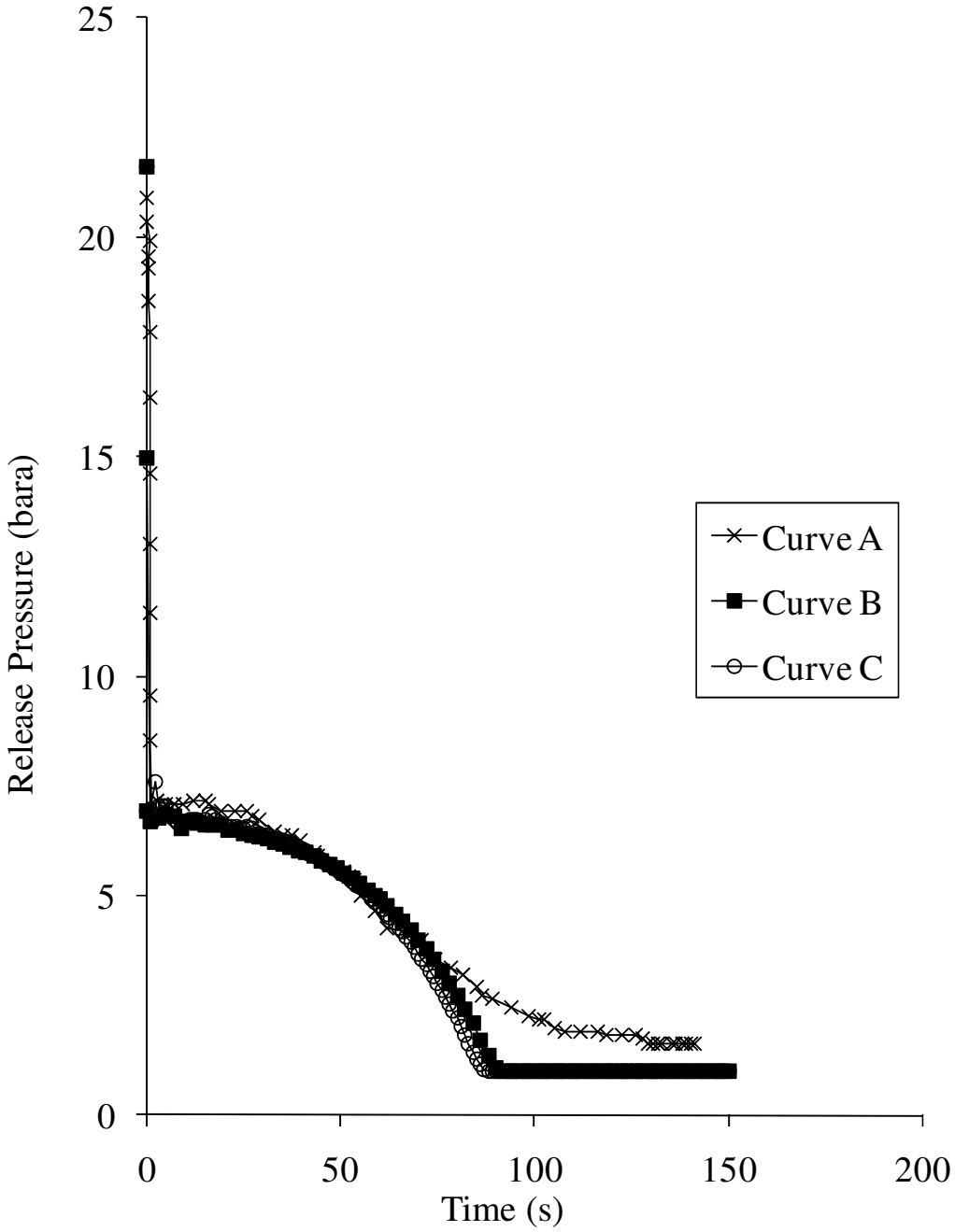

Figure 7.8: Variation of open end pressure with time following a 70 mm diameter axisymmetric puncture for test P47.

Curve A: Experimental data (Richardson and Saville, 1996)

Curve B: Atti's (2006)

Curve C: CDA

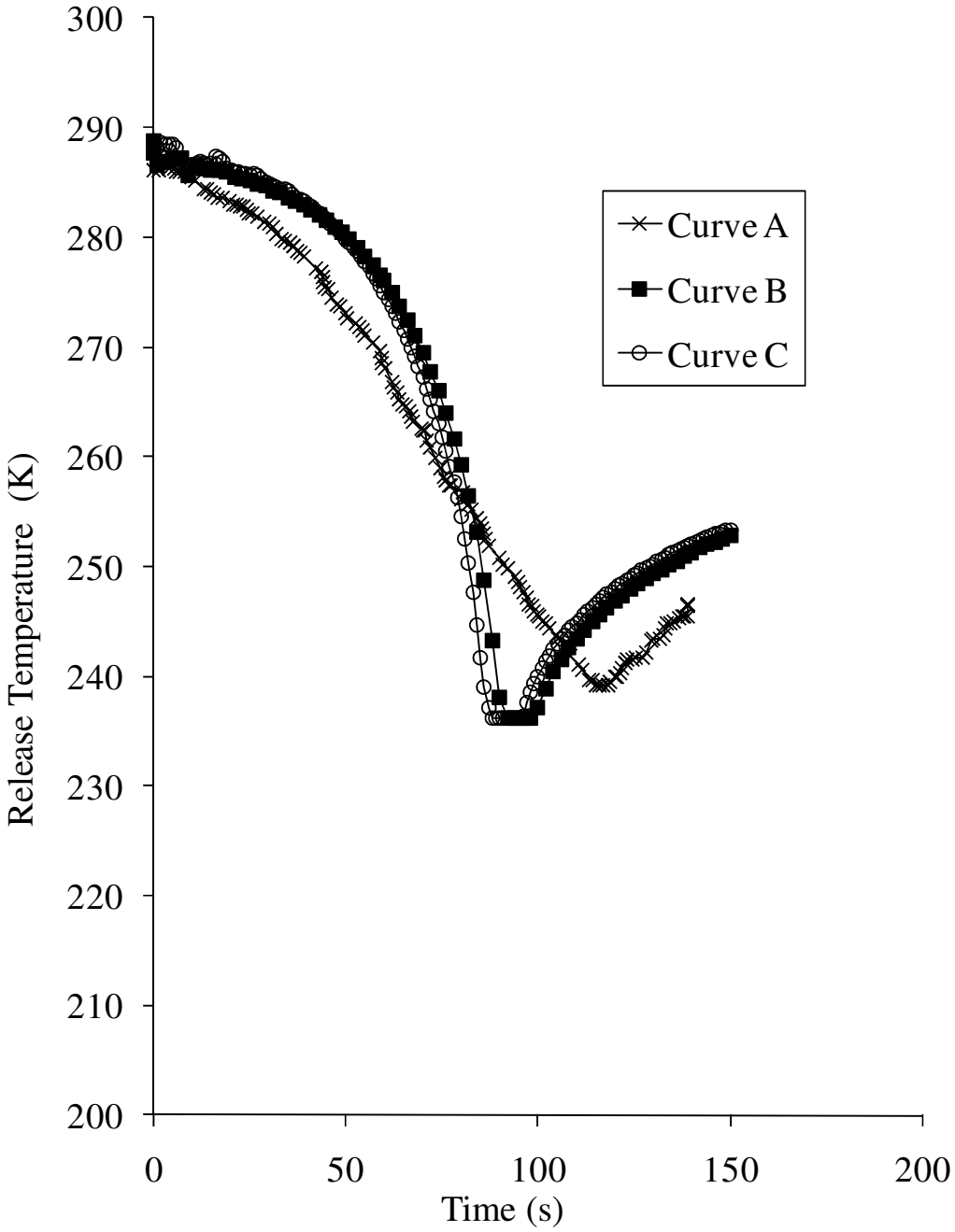

Figure 7.9: Variation of open end temperature with time following a 70 mm diameter axisymmetric puncture for test P47.

Curve A: Experimental data (Richardson and Saville, 1996)

Curve B: Atti's (2006)

Curve C: CDA

7.3.3 Applicability of the Critical Discharge Algorithm to Ultra High Pressure Pipelines

The following presents a comparison of Atti's (2006) critical discharge model predictions against those using the CDA for an hypothetical 2.4 km, 154 mm i.d. ultra high pressure pipeline transporting ethane at 760 bara. Table 7.6 shows the pipeline characteristics and the prevailing ambient conditions prior to failure.

Table 7.6: Ultra High pressure pipeline test conditioning.

Input		
Inlet Parameters	Number of components	1
	Feed composition (mole %)	Ethane - 100
	Feed inlet temperature (K)	317
	Feed inlet pressure (bara)	760
	Ambient temperature (K)	283
	Ambient pressure (bara)	1.01
Pipeline Characteristics	Length (m)	2400
	External diameter (mm)	168.6
	Wall thickness (mm)	7.3
	Roughness (mm)	0.05
	Orientation to the horizontal plane (deg)	0
Rupture Conditions	Failure mode	FBR
	Failure location relative to high pressure end (m)	2400
	Rupture diameter (mm)	154
	Discharge coefficient	1
Other Parameters	Feed flow rate prior to rupture (m^3/s)	0
	Pumping cessation time following pipeline failure (s)	0
	Pump shut-off head (bara)	110
	Grid system used	Simple
	Number of grid points specified	500
	Equation of State	PR
	Friction factor correlation	Chen
	Heat transfer coefficient (W/m^2K)	Automatically determined
	Total depressurisation time (s)	30

Figure 7.10 shows the variation of discharge rate with time obtained using Atti's (2006) model. For clarity the CDA predictions are presented separately in figure 7.11. As may be observed in figure 7.10, Atti's (2006) model produces large oscillations from 0 to ca. 3500 kg/s in the first few seconds. It is postulated that this behaviour is a result of the rapid change in the thermo-physical properties and phase behaviour induced by the extreme decompression. This results in the failure of the Brent (2002) algorithm to converge to a solution of equation (4.26). These spurious oscillations in the boundary conditions affect the flow of the remaining inventory and inevitably undermine the validity of the model predictions.

In contrast, the results obtained from the CDA (figure 7.11) show the hyperbolic decline synonymous with FBR. The small instabilities observed in figure 7.11 between 3 to 5 s are again probably due to the discontinuity in the thermo-physical properties induced by a similar phase transition.

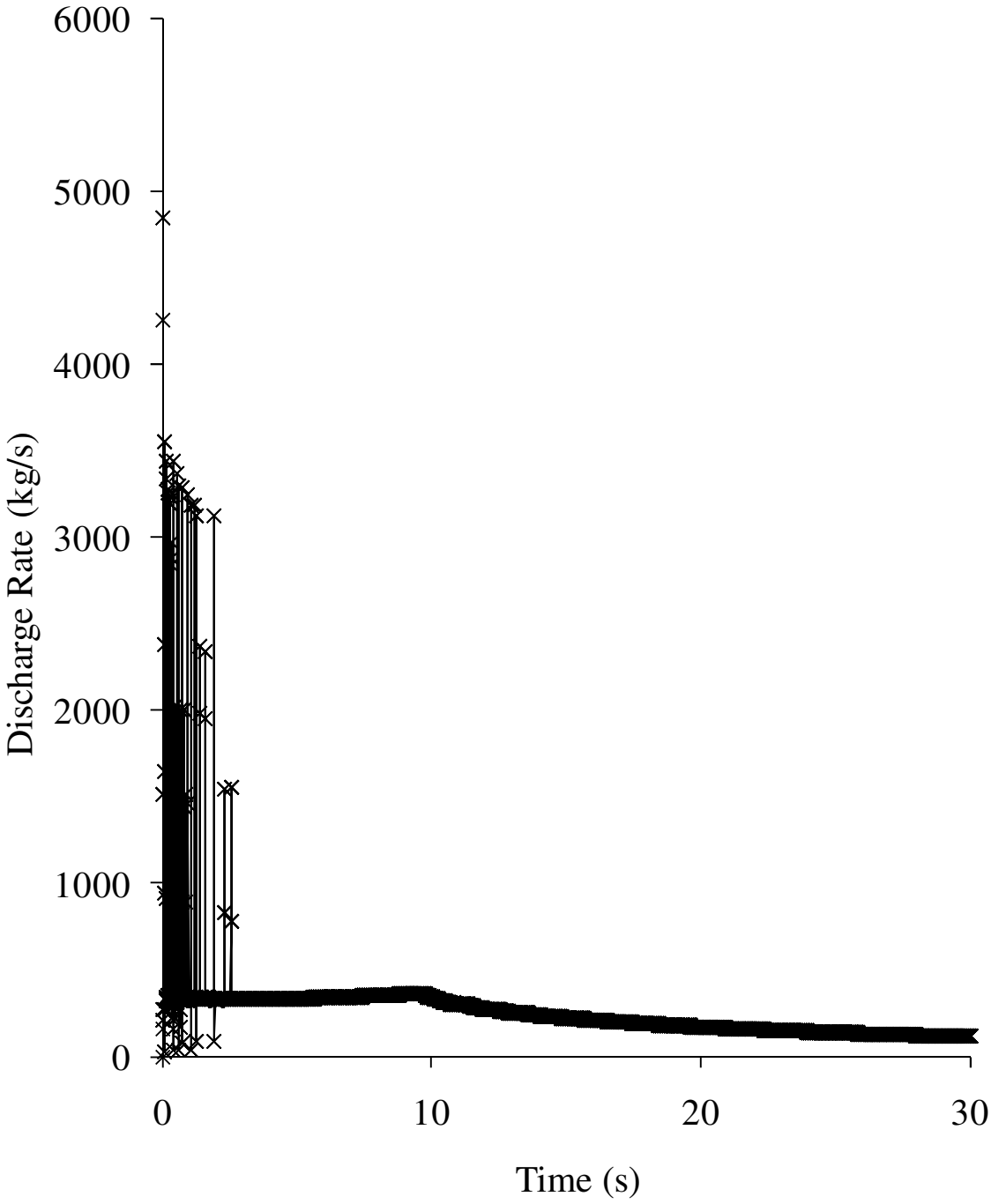

Figure 7.10: Variation of discharge rate with time for the hypothetical FBR of a 2.4 km, 154 mm i.d. pipeline containing 100 % ethane using Atti's (2006) model.

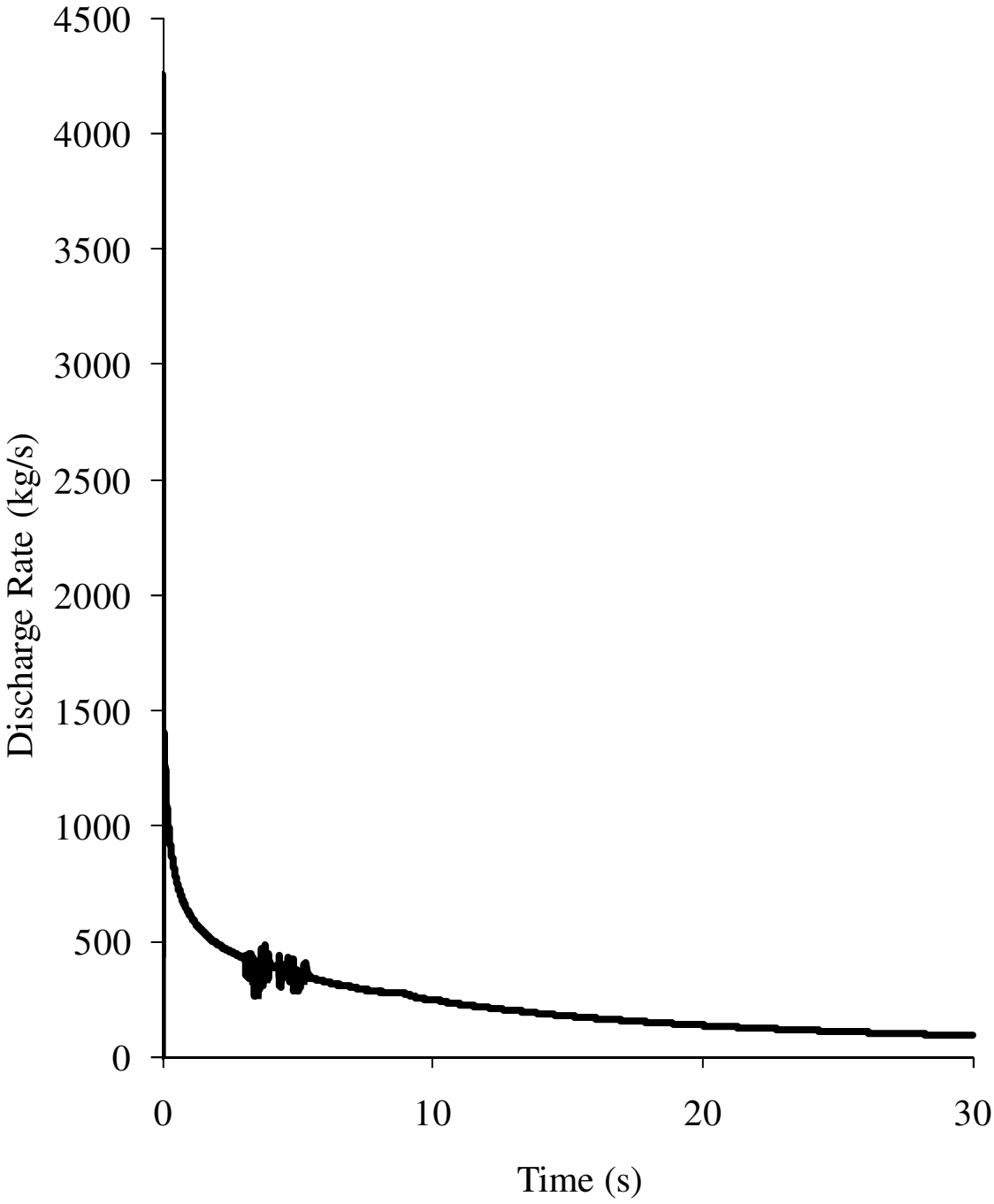

Figure 7.11: Variation of discharge rate with time for the hypothetical FBR of a 2.4 km, 154 mm i.d. pipeline containing 100 % ethane using the Critical Discharge Algorithm (CDA).

7.4 Conclusion

This chapter addressed two of the main shortcomings associated with previous work in modelling pipeline rupture. The first dealt with the inability of Oke's (2004) steady state model to handle non-isothermal flow conditions as a result of any temperature differences between the pipeline inventory and the surrounding ambient. The second addressed the rupture plane instabilities encountered in Atti's (2006) model when simulating outflow following the rupture of ultra high pressure pipelines.

The development of the non-isothermal flow model involved the addition of an energy equation accounting for heat transfer and friction to the continuity and momentum equations followed by their numerical solution. The performance of the model was tested against published measured data for two long pipelines transporting multi-component hydrocarbon mixtures for a range of inlet temperatures and pressures. Since the ambient temperatures were not given, they were assumed to be the same as the feed temperature.

The excellent agreement between the non-isothermal model predictions of the outlet pressure and the measured data supported the validity of the isothermal flow assumption. Surprisingly, despite this, Oke's (2004) isothermal flow model produced significant errors in predicting the discharge pressure for all conditions involving two-phase flow. For vapour phase flows however, the model produced a similar level of accuracy as that using the non-isothermal flow model suggesting that the problem has its root in the two-phase flow formulation of Oke's (2004) model.

Although the performance of the non-isothermal steady state model presented in this chapter was encouraging, its absolute credibility can only be fully established based on comparison with real data involving flows where the pipeline inventory and surrounding ambient are at different temperatures.

In the second part of the study, the limitations of the critical flow model employed by Atti (2006) with respect to the rupture of ultra high pressure pipelines was highlighted.

Given the economic incentives in operating pipelines at ultra high pressures (e.g. above 600 bara: Urbaniak et al., 2007), the ability to model the failure of such pipelines is becoming increasingly important.

An alternative methodology hereby termed the Critical Discharge Algorithm (CDA) based on the isentropic HEM critical flow model of Elias and Lellouche (1994) was developed. To establish credibility, the performance of the CDA at moderate pressures was first evaluated by comparison of its predictions against the Isle of Grain pipeline rupture tests (Chen, 1993; Richardson and Saville, 1996) as well as those based on Atti's (2006) model. With the exception of minor differences observed at the onset of phase transition, generally good agreement between both models and the measured data were obtained in all cases.

Both the CDA and Atti's (2006) model predictions were next compared against one another for the hypothetical full bore rupture of an ultra high pressure 2.4 km, 154 mm i.d. pipeline containing ethane at 760 bara. Atti's (2006) model produced unrealistic large amplitude oscillations in the variation of the discharge mass with time during the first few second following rupture where most of the inventory is lost. These were caused by a failure of convergence in the numerical solution of the energy balance (equation (4.25)). No such oscillations were observed in the case of the CDA thus establishing its successes in modelling the particular case examined.

Clearly a future study testing the performance of the CDA for a number of ultra high pressure hydrocarbon mixtures would be very useful in establishing its full range of applicability particularly when examined against real data.

Chapter 8: Conclusions and Future Work

8.1 Conclusions

The key contributions of this work may be distilled as follows:

- State of the art review of the modelling of pipeline ruptures
- Reduction in the computational run times for modelling such failures through the development, testing and validation of an efficient numerical scheme based on the Finite Volume Method (FVM)
- Addressing the failure of the Method of Characteristics (MOC) based outflow model in:
    - handling non-isothermal steady state flow conditions prior to pipeline rupture
    - simulating outflow following the rupture of ultra-high pressure pipelines
- The development, testing and validation of a fluid-structure interaction model for investigating ductile fracture behaviour in CO_2 pipelines.

The key outcomes are improving safety and protecting the environment through a better understanding of the consequences associated with the accidental failure of pressurised pipelines.

The following is a summary of the main findings:

In chapter 2 a detailed review of the mathematical models available in the open literature for simulating pipeline failures was conducted. This highlighted the varying degrees of rigor of the models developed. For example, some concentrate only on the depressurisation induced expansion wave while ignoring outflow, or assume simple ideal gas behaviour. Others ignore frictional and heat transfer effects, which have been

found to have a significant impact on the decompression behaviour. These limitations inevitably undermine the efficacy of the model predictions.

It was found that the homogeneous equilibrium based models developed by Mahgerefteh et al. (1999) and Atti (2006) were the most robust with the latter performing best in terms of accuracy and computational runtime. Nonetheless, the CPU runtimes associated with the simulation of the blowdown of long pipelines (> 100 km) remain persistently long.

The review also highlighted the increasing application of pipeline decompression models to the prediction of fractures propagation. Currently, however, those models that are reported in the literature fail to account for the complex interaction between crack growth and the fluid decompression.

In chapter 3, the main assumptions used in the formulation of the homogeneous equilibrium fluid model were presented and discussed. The equations governing the conservation of mass, momentum and energy were presented, which were subsequently shown to be quasi-linear and hyperbolic in nature.

The essential thermodynamic equations and hydrodynamic correlations for the speed of sound in a two-phase fluid, fluid viscosity as well as phase and flow dependent friction coefficients were presented. Following this, the lumped body approach for modelling fluid/pipe wall and pipe wall/ambient heat transfer as well as the real fluid isothermal steady state model was outlined.

In chapter 4, the formulation of the MOC based on the Method of Specified Time Intervals employed in the numerical resolution of the conservation equations was outlined. Furthermore, the Euler predictor-corrector technique applied to the resultant compatibility equations was briefly described.

These compatibility equations were coupled with appropriate boundary conditions to simulate the outflow from a multi-segment pipeline following failure. These accounted for closed valves or dead-ended pipes (intact end point), centrifugal pumps (at the flow

source) and full-bore ruptures/punctures. The frictional losses in the case of the multi-segment pipelines due to valves and junctions (bends or connector) between pipe sections were accounted for by the introduction of a loss coefficient, K_{loss}.

In chapter 5, a FVM was presented as an alternative resolution technique for the system of conservation equations with the aim of further reducing the computational runtime. The particular FVM used was based on a deterministic re-formulation of the staggered grid Random Choice Method (Gottlieb, 1988) and was developed specifically for the non-conservative form of the equations.

The performance of the FVM was tested by comparison of its predictions against available field data as well as the hypothetical rupture of a realistic pipeline containing a full range of pressurised inventories including gas, two-phase and liquid hydrocarbons. In all cases the FVM predictions were also compared against those obtained using the MOC. It was found that in general, the FVM performed well. However, in cases where the pipeline inventory was initially in the liquid phase, the FVM exhibited numerical instabilities. This was found to be due to its inability to handle the large discontinuities encountered in the fluid properties at the rupture plane upon pipeline failure.

Importantly though, in the cases examined significant reductions ranging from 23 to 78 % in the CPU runtimes were observed using the FVM as compared to the MOC.

Given that the CPU times are at any rate generally insignificant in the case of the rupture simulation of liquid containing hydrocarbons due to the finite fluid compressibility, the MOC is recommended as an effective method of resolution for such failures.

In chapter 6 the HEM based outflow model was coupled with the well-established Drop Weight Tear Test energy fracture technique (Makino et al., 2001) to simulate ductile fracture propagation in CO_2 pipelines. This study was prompted given the significant interest and the associated safety concerns in the use of pressurised pipelines for transporting captured CO_2 from fossil fuel power plants as part of the Carbon Capture and Sequestration Chain.

Of all the possible modes of pipeline failure, long running ductile fractures are by far the most catastrophic. As such the development of reliable quantitative techniques for predicting such failures for CO_2 pipelines in the presence of the likely impurities is of significant value.

Based on the application of the model to a hypothetical 500 m pipeline with a realistic fracture toughness transporting dense phase pure CO_2 as well as those based on pre-combustion, post combustion and oxy-fuel capture technologies, the following general conclusions may be made:

1. In the case of pure CO_2, the starting line temperature has a profound effect on the fracture behaviour. Whereas in the temperature range 0 – 20 ^{o}C the fracture length is limited to very short distances, only a 10 ^{o}C rise in the temperature from 20 to 30 ^{o}C results in a fracture propagating through the entire pipeline length. Given the relatively small amounts of impurities present, the post-combustion pipeline behaves in much the same way. Clearly, the above finding has important implications for pipeline routes where the ambient temperatures may exceed 20 ^{o}C.

2. The transition to a long running fracture in the case of pre-combustion CO_2 is lower than that for the pure and post combustion CO_2. In this case, long running fractures is likely at any temperature above 10 ^{o}C.

3. The oxy-fuel composition represents the worst case scenario. Here long running fractures would be expected under all the temperatures under consideration.

Remarkably, the increase in the line pressure from 100 to 180 barg reduced the pipeline's propensity to fracture propagation. All of the above findings were successfully explained by examining the CO_2 and its mixtures depressurisation trajectories during fracture propagation relative to the corresponding phase envelopes.

Chapter 7 addressed two of the main shortcomings associated with previous work in modelling pipeline rupture. The first dealt with the inability of Oke's (2004) steady state

model to handle non-isothermal flow conditions in situations where the feed inventory was at a different temperature from the surrounding ambient. The second addressed the rupture plane instabilities encountered in Atti's (2006) model when simulating outflow following the rupture of ultra high pressure pipelines.

The development of the non-isothermal flow model involved the addition of an energy equation accounting for heat transfer and friction to the continuity and momentum equations followed by their numerical solution. The performance of the model was tested against published measured data for two long pipelines transporting multi-component hydrocarbon mixtures for a range of inlet temperatures and pressures. Since the ambient temperatures were not given, they were assumed to be the same as the feed temperature.

The excellent agreement between the non-isothermal model predictions of the outlet pressure and the measured data supported the validity of the isothermal flow assumption. Surprisingly, despite this, Oke's (2004) isothermal flow model produced significant errors in the predicting the discharge pressure for all conditions involving two-phase flow. For vapour phase flows however, the model produced a similar level of accuracy as that using the non-isothermal flow model suggesting that the problem has its root in the two-phase flow formulation of Oke's model.

Although the performance of the non-isothermal steady state model presented was encouraging, its absolute credibility can only be fully established based on comparison with real data involving flows where the pipeline inventory and surrounding ambient are at different temperatures.

In the second part of the study, the limitations of the critical flow model employed by Atti (2006) with respect to the rupture of ultra high pressure pipelines was highlighted. Given the economic incentives in operating pipelines at ultra high pressures (e.g. above 600 bara: Urbaniak et al., 2007), the ability to model the failure of such pipelines is becoming increasingly important.

An alternative methodology referred to as the Critical Discharge Algorithm (CDA) based on the isentropic HEM critical flow model of Elias and Lellouche (1994) was developed. To establish credibility, the performance of the CDA at moderate pressures was first evaluated by comparison of its predictions against the Isle of Grain pipeline rupture tests (Chen, 1993; Richardson and Saville, 1996) as well as those based on Atti's (2006) model. With the exception of minor differences observed at the onset of phase transition, generally good agreement between both models and the measured data were obtained in all cases.

Both the CDA and the Atti's (2006) model predictions were next compared against one another for the hypothetical full bore rupture of an ultra high pressure 2.4 km, 154 mm i.d. pipeline containing ethane at 760 bara. Atti's (2006) model produced unrealistic large amplitude oscillations in the variation of the discharge mass with time during the first few second following rupture where most of the inventory is lost. These were caused by the failure of the numerical solution of the energy balance (equation (4.25)) to converge. No such oscillations were observed in the case of the CDA thus establishing its successes in modelling the particular case examined.

It should be noted out that almost all of the findings presented in this work are based on the validity of the Homogenous Equilibrium Model (HEM) where the constituent phases are assumed to be at thermal and mechanical equilibrium. Although the reasonably good agreement with the real pipeline data available support this assumption, given their very limited number it is impossible to ascertain the range of applicability of the HEM. Certainly in the case of vertically inclined pipelines, phase slip will be an important consideration and the development of an heterogeneous model becomes necessary. The FVM presented in this work lays the foundation for developing such a model.

In conclusion it is hoped that the key outcome of this PhD study is improving safety and protecting the environment through a better understanding of the consequences associated with the accidental failure of pressurised pipelines.

8.2 Suggestions for Future Work

Heterogeneous Two-phase Model

As mentioned above, the development of a heterogeneous flow model accounting for phase slip and temperature gradients between the constituent phases is considered as a very useful extension of the FVM presented in this work. This will require the formulation of separate conservation equations for each constituent phase and their coupling through the appropriate empirically determined source terms. The latter will require the design of realistic experiments for the investigation of the various flow regimes and their transitions during pipeline failure.

Reduction in Computational Runtime

The following investigations and models are recommended to reduce the computational workload of the model:

1. The use of Adaptive Grid Refinement (AMR) in which the grid system is continually redistributed and refined where required will be investigated. This may allow for the use of an optimum number of grids points thereby reducing computational runtime and improving accuracy.
2. The reduction of terms in the governing equations which become insignificant in some limiting cases may help to reduce the computational workload associated with long simulations. For example, where pressure gradients are no longer important and outflow is dominated by momentum effects the pressure may be ignored in the conservation equations thereby reducing the complexity of the model.

Shock Capturing Schemes

Despite the success of the Finite Volume Method (FVM) based model in predicting outflow, as was found in the chapter 5, this numerical method is unable to predict the outflow of liquids. In order to capture the discontinuities in the fluid properties which cause the FVMs failure a shock capturing scheme may be employed. Such a scheme requires the reformulation of the governing equations in terms of the conservative variables.

Additionally, the ability to capture shocks may extend the applicability of the model to, for example, the unsteady blowdown through initially empty vents.

Behaviour of Underwater Fracture

In the present study, a model describing the fracturing of high pressure pipelines into ambient air has been presented. However, in the UK the vast majority of CO_2 must inevitably be transported through sub-sea pipelines to the sequestration point. The behaviour of fractures in sub-sea pipelines is not well understood and presents an important extension of this work.

References

Al-Khomairi, A. (2003). Use of steady-state pump head-discharge curve for unsteady pipe flow applications. *Journal of Hydraulic Engineering*, (December), 1001-1006.

Assael, M. J., Trusler, J. P. M., and Tsolakis, T. F. (1996). *Thermophysical properties of fluids*.

Atti, O. (2006). *Modelling Outflow and Low Temperature Induced Crack Propagation in Pressurised Pipelines*. University College London.

Bendiksen, K., Maines, D., and Moe, R. (1991). The dynamic two-fluid model OLGA: Theory and application. *SPE production*, *6*(6), 171–180. Society of Petroleum Engineers.

Bilio, M., Brown, S., Fairwheather, M., and Mahgerefteh, H. (2009). CO2 pipelines material and safety considerations. *IChemE Symposium Series: HAZARDS XXI Process Safety and Environmental Protection* (Vol. 155, p. 423–429). Manchester: IChemE.

Botros, K. K., Geerligs, J., and Eiber, R. J. (2010a). Measurement of Decompression Wave Speed in Rich Gas Mixtures at High Pressures (370 bars) Using a Specialized Rupture Tube. *Journal of Pressure Vessel Technology*, *132*(5), 051303.

Botros, K.K., Geerligs, J., Rothwell, B., Carlson, L., Fletcher, L., and Venton, P. (2010b). Transferability of decompression wave speed measured by a small-diameter shock tube to full size pipelines and implications for determining required fracture propagation resistance. *International Journal of Pressure Vessels and Piping*, *87*(12), 681-695. Elsevier.

Botros, K.K., Studzinski, W., Geerligs, John, and Glover, Alan. (2004). Determination of decompression wave speed in rich gas mixtures. *The Canadian Journal of Chemical Engineering*, *82*(5), 880–891. John Wiley & Sons.

Botros, K. K, Geerligs, J., and Given, R. (2004). Decompression Response of High-Pressure Natural Gas Pipelines Under Rupture or Blowdown Conditions, *PRCI report*.

Botros, K. K, Geerligs, J, Glover, A, and Rothwell B, A. (2001). Expansion Tube for Determination of the Wave Speed for Dense/Rich Gases at Initial Pressure of up to 22 MPa. *Proceedings of the International Gas Research Conference*. Amsterdam.

Brankin, R. W. (1989). Algorithm 670: a Runge-Kutta-Nystrom code. *ACM transactions on mathematical software*, *15*(1), 31.

Brent, R. P. (2002). *Algorithms for minimization without derivatives*.

Brown, S., and Mahgerefteh, H. (2009). From Cradle to Burial: High Pressure Phase Equilibrium Behaviour of CO_2 during CCS. *Proceedings of the 2009 AIChE Annual meeting*. Nashville.

Chen, J., Richardson, S., and Saville, G. (1995a). Modelling of two-phase blowdown from pipelines—I. A hyperbolic model based on variational principles. *Chemical Engineering Science*, *50*(4), 695–713. Elsevier.

Chen, J. R., Richardson, S. M., and Saville, G. (1995b). Modelling of Two-Phase Blowdown from Pipelines - II. A simplified numerical method for method for multi-component mixtures. *Chem. Eng. Sci.*, *50*(13), 2173-2187.

Chen, J., Richardson, S., and Saville, G. (1993). A simplified numerical method for transient two-phase pipe flow. *Trans IChemE*, *71*(3), 304–306. Institution of Chemical Engineers.

Chen, N. H. (1979). An Explicit Equation for Friction Factor in Pipe. *Industrial & Engineering Chemistry Fundamentals*, *18*(3), 296-297.

Cleaver, R., Cumber, P. S., and Halford, A. (2003). Modelling outflow from a ruptured pipeline transporting compressed volatile liquids. *Journal of Loss Prevention in the Process Industries*, *16*(6), 533-543.

Cosham, A., and Eiber, R. (2008). Fracture propagation in CO_2 pipelines. *Journal of Pipeline Engineering*, *7*, 115-124.

Courant, R., Friedrichs, K., and Lewy, H. (1967). On the Partial Difference Equations of Mathematical Physics. *IBM Journal of Research and Development*, *11*(2), 215-234.

Cullen, W. D. (1990). *The public inquiry into the Piper Alpha disaster*.

Cumber, P. (2007). Outflow from fractured pipelines transporting supercritical ethylene. *Journal of Loss Prevention in the Process Industries*, *20*(1), 26-37.

Daubert, T. E., and Danner, R. P. (1990). Data Compilation - Physical and Thermodynamic Properties of Pure Compounds. Taylor and Francis (extant).

De Visser, E., Hendriks, C., Barrio, M., Molnvik, M., De Koeijer, G., Liljemark, S., et al. (2008). Dynamis CO_2 quality recommendations. *International Journal of Greenhouse Gas Control*, *2*(4), 478-484.

Denton, G. (2009). *CFD Simulation of Highly Transient Flows*. University College London.

Eiber, R. J., Bubenik, T. A., and Maxey, W. A. (1993). *GASDECOM, computer code for the calculation of gas decompression speed that is included fracture control technology for natural gas pipelines*.

Elias, E., and Lellouche, G. (1994). Two-phase critical flow. *International Journal of Multiphase Flow*, *20*(94), 91-168.

Ely, J. F., and Hanley, H. J. M. (1981). Prediction of transport properties. 1. Viscosity of fluids and mixtures. *Industrial & Engineering Chemistry Fundamentals*, *20*(4), 323-332.

Ely, J. F., and Hanley, H. J. M. (1983). Prediction of transport properties. 2. Thermal conductivity of pure fluids and mixtures. *Industrial & Engineering Chemistry Fundamentals*, *22*(1), 90-97.

Fairuzov, Y. V. (1998). Blowdown of Pipelines Carrying Flashing Liquids. *AIChE Journal*, *44*(2), 245-254.

Fearnehough, G. (1974). Fracture propagation control in gas pipelines: A survey of relevant studies. *International Journal of Pressure Vessels and Piping*, *2*(4), 257-282.

Flatt, R. (1986). Unsteady compressible flow in long pipelines following a rupture. *International Journal for Numerical Methods in Fluids*, *6*(2), 83-100. John Wiley & Sons, Ltd Sussex.

Geurst, J. (1986). Variational principles and two-fluid hydrodynamics of bubbly liquid/gas mixtures. *Physica A: Statistical and Theoretical Physics*, *135*(2-3), 455-486. Elsevier.

Gottlieb, J. (1988). Staggered and nonstaggered grids with variable node spacing and local time stepping for the random choice method. *Journal of Computational Physics*, *78*(1), 160-177.

Greenshields, C., Venizelos, G., and Ivankovic, A. (2000). A fluid-structure model for fast brittle fracture in plastic pipes. *Journal of Fluids and Structures*, *14*(2), 221–234. Elsevier.

Haque, A., Chamberlain, G., Saville, G., Richardson, S. M., and Shirvil, L. (1992). Blowdown of pressure vessels. Pt. 2: experimental validation of computer model and case studies (BLOWDOWN program). *Process Safety and Environmental Protection*, *70*, 10-17.

Hall, A. R. W., Butcher, E. R., and Teh, C. E. (1993). Transient simulation of two-phase hydrocarbon flows in pipelines. *Proceedings of the European Two-Phase Flow Group Meeting* (pp. 73-82).

Heggum, G., Weydahl, T., Roald, W., Mølnvik, M., and Austegard, A. (2005). CO2 conditioning and transportation. In D. C. Thomas and S. M. Benson (Eds.), *Carbon Dioxide Capture for Storage in Deep Geologic Formations* (Vol. 2).

HSE. (1996). A guide to the Pipelines Safety Regulations 1996. *Interpretation A Journal Of Bible And Theology*.

Hyprotech (2003). ProFES - Reference Guide. Houston: Aspentech.

ICF International (2010). *Implementation of Directive 2009 / 31 / EC on the Geological Storage of Carbon Dioxide*.

I.E.A. (2011). *World Energy Outlook 2010 Factsheet*.

Inoue, T., Makino, Hiroyuki, Endo, S., Kubo, T., and Matsumoto, T. (2003). Simulation method for shear fracture propagation in natural gas transmission pipelines. *International Offshore and Polar engineering Conference* (Vol. 5, pp. 121-128). Honululu.

Johnson, D. M., Horner, N., Carlson, L., and Eiber, R. (2000). Full scale validation of the fracture control of a pipeline designed to transport rich natural gas. *Pipeline Technology*, *1*, 331.

Jones, D., and Gough, D. (1981). Rich Gas Decompression Behavior in Pipelines. - *EPRG Linepipe Research Seminar IV, BRITISH GAS*. Duisberg.

Keenan, J. H., and Nuemann, E. P. (1946). Measurement of friction in a pipe for subsonic and supersonic flow of air. *Journal of applied mechanics*, *13*(2).

King, G., and Kumar, S. (2010). How to Select Wall Thickness, Steel Toughness, and Operating Pressure for Long CO_2 pipelines. *Journal of Pipeline Engineering*, *9*(4), 253-264.

Kruse, H., and Tekiela, M. (1996). Calculating the consequences of a CO_2-pipeline rupture. *Energy Conversion and Management*, *37*(95), 1013-1018.

Kunz, O., Klimeck, R., and Wagner, W. (2007). The GERG-2004 wide-range equation of state for natural gases and other mixtures. *GERG TM15, Fortschritt-Berichte VDI*.

Leis, B. N. (1997). Relationship Between Apparent (Total Charpy Vee- Notch Toughness) and the Corresponding Dynamic Crack-Propagation Resistance. *Proceedings International Pipeline Conference*. Calgary: ASME.

Lemmon, E. W., Huber, M. L., and McLinden, M. O. (2007). NIST Standard Reference Database 23: Reference Fluid Thermodynamic and Transport Properties-REFPROP. Gaithesburg: National Institute of Standards and Technology.

Leveque, R. J. (2002). *Finite Volume Methods for Hyperbolic Problems*. Cambridge University Press.

Li, H., and Yan, J. (2006). Impact of impurities in CO_2-fluids on CO_2 transport process. *Proceedings of GT2006* (pp. 367-375). Barcelona.

Li, H., and Yan, J. (2009). Evaluating cubic equations of state for calculation of vapor–liquid equilibrium of CO_2 and CO_2-mixtures for CO_2 capture and storage processes. *Applied Energy*, *86*(6), 826-836.

Mahgerefteh, H, Atti, O., and Denton, G. (2007). An Interpolation Technique for Rapid CFD Simulation of Turbulent Two-Phase Flows. *Process Safety and Environmental Protection*, *85*(1), 45-50.

Mahgerefteh, H, Oke, A, and Rykov, Y. (2006). Efficient numerical solution for highly transient flows. *Chemical Engineering Science*, *61*(15), 5049-5056.

Mahgerefteh, H., Denton, G., and Rykov, Y. (2008). A hybrid multiphase flow model. *AIChE Journal*, *54*(9), 2261–2268.

Mahgerefteh, H, Denton, G., and Rykov, Y. (2008). CO_2 Pipeline Rupture. *IChemE Symposium Series: HAZARDS XX Process Safety and Environmental Protection* (pp. 869 - 879). Manchester: IChemE.

Mahgerefteh, H., Rykov, Y., and Denton, Garfield. (2009). Courant, Friedrichs and Lewy (CFL) impact on numerical convergence of highly transient flows. *Chemical Engineering Science*, *64*(23), 4969-4975.

Mahgerefteh, H., Saha, P., and Economou, I.G. (1999). Fast numerical simulation for full bore rupture of pressurized pipelines. *AIChE Journal*, *45*(6), 1191–1201.

Mahgerefteh, H., Saha, P., and Economou, I. G. (1997). A study of the dynamic response of emergency shutdown valves following full bore rupture of gas pipelines. *Process safety and environmental protection*, *75*(4), 201–209. Institution of Chemical Engineers.

Mahgerefteh, H, Saha, P., and Economou, I. G. (2000). Modeling fluid phase transition effects on dynamic behavior of ESDV. *AIChE Journal*, *46*(5), 997-1006.

Makino, H., Takeuchi, I., and Higuchi, R. (2008). Fracture Propagation and Arrest in High-Pressure Gas Transmission Pipeline by Ultra Strength Line Pipes. *7th International Pipeline Conference*. Calgary.

Makino, H., Sugie, T., Watanabe, H., Kubo, T., Shiwaku, T., Endo, S., et al. (2001). Natural Gas Decompression Behavior in High Pressure Pipelines. *ISIJ International*, *41*(4), 389-395.

Makino, H., Sugie, T., Watanabe, H., Kubo, T., Shiwaku, T., Endo, S., et al. (2001). Natural Gas Decompression Behavior in High Pressure Pipelines. *ISIJ International*, *41*(4), 389-395.

Maxey, W. A. (1974). Fracture initiation, propagation and arrest. *Proceedings of the 5th symposium in Line Pressure Research*. Houston.

Myers, G. E. (1987). *Analytical Methods in Conduction Heat Transfer*. Genium.

Nordsveen, M., and Haerdig, A. (1997). Simulations of severe slugging during depressurization of an oil/gas pipeline. *Modeling, identification and control*, *18*(1), 61-73.

Oke, A. (2004). *An efficient numerical simulation for modelling outflow following rupture or puncture of pressurised pipeline networks*. University College London.

Oke, A., Mahgerefteh, H, Economou, I. G., and Rykov, Y. (2003). A transient outflow model for pipeline puncture. *Chem Eng Sci*, *58*, 4591-4694.

Oosterkamp, A., and Ramsen, J. (2008). *State-of-the-Art Overview of CO_2 Pipeline Transport with relevance to offshore pipelines*. *Security*.

Peng, D. Y., and Robinson, D. B. (1976). A New Two-Constant Equation of State. *Industrial & Engineering Chemistry Fundamentals*, *15*(1), 59-64.

Perry, R. H., and Green, D. W. (1997). Perry's Chemical Engineers' Handbook (7th Edition). McGraw-Hill.

Peterson, C. E., Chexal, V. K., and Clements, T. B. (1985). Analysis of a hot-leg small break in a three loop Westinghouse PWR plant. *Nuclear Technology*, *70*(1), 104.

PHMSA. (2010). Pipeline Incidents and Mileage Reports. Retrieved October 31, 2010, from http://primis.phmsa.dot.gov/comm/reports/safety/PSI.html.

Philips, A. G., and Robinson, C. G. (2005). *Gas Decompression Behaviour Following the Rupture of High Pressure Pipelines - Phase 2: Modeling Report*.

Picard, D. J., and Bishnoi, P. R. (1988). The Importance of Real-Fluid Behaviour and Non-Isentropic Effects in Modeling Decompression Characteristics of Pipeline Fluids for Application in Ductile Fracture Propagation Analysis. *Canadian Journal of Chemical Engineering*, *66*(1), 3-12.

Picard, D., and Bishnoi, P. (1987). Calculation of the thermodynamic sound velocity in two-phase multicomponent fluids. *International Journal of Multiphase Flow*, *13*(3), 295–308. Elsevier.

Prasad, P., and Ravindran, R. (1985). *Partial Differential Equations*. New Delhi: Wiley Eastern Ltd.

Popescu, M. (2009). Modeling of fluid dynamics interacting with ductile fraction propagation in high pressure pipeline. *Acta Mechanica Sinica*, *25*(3), 311–318. Springer.

Richardson, S., and Saville, G. (1996). Blowdown of LPG pipelines. *Process Safety and Environmental Protection*, *74*(4), 235–244. Elsevier.

Roe, P. L. (1981). Approximate Riemann Solvers, Parameter and Difference Schemes. *Journal of Computational Physics*, *372*, 357-372.

Rohsenow, W. M., Hartnett, J. P., and Cho, Y. I. (Eds.). (1998). *Handbook of heat transfer* (3rd ed.). New York: McGraw-Hill.

Shapiro, A. H. (1953). *The Dynamics and Thermodynamics of Compressible fluid flow* (Vol. 1, p. 672). Wiley.

Shoup, G., Xiao, J., and Romma, J. (1998). Multiphase pipeline blowdown simulation and comparison to field data. *BHR Group Conference Series Publication* (Vol. 31, p. 3–16).

Soave, G. (1972). Equilibrium constants from a modified Redlich-Kwong equation of state. *Chemical Engineering Science*, *27*(6), 1197–1203. Elsevier.

Starling, K. (1973). Fluid thermodynamic properties of light petroleum systems. Houston: Gulf Publishing Company.

Starling, K. E., and Savidge, J. L. (1992). *Compressibility Factors for Natural Gas and Other Related Hydrocarbon Gases*.

Sugie, M., Akiyama, T., Tanake, K., Kawaguchi, Y., and Matsuoka, E. (1987). Notch Ductility Requirements of Line Pipes for Arresting Propagating Shear Fracture. *Journal of pressure vessel technology*, *109*(4), 428-434.

Takeuchi, I., Makino, H., Okaguchi, S., Takahashi, N., and Yamamoto, A. (2006). Crack arrestability of high-pressure gas pipelines by X100 or X120. *23 rd World Gas Conference*. Amsterdam.

Tam, V., and Higgins, R. (1990). Simple transient release rate models for releases of pressurised liquid petroleum gas from pipelines. *Journal of Hazardous Materials*, *25*(1-2), 193–203. Elsevier.

Techo, R. (1965). An accurate equation for the computation of the friction factor for smooth pipes from the Reynolds number. *Journal of applied mechanics*, *32*, 443.

Terenzi, A. (2005). Influence of real-fluid properties in modeling decompression wave interacting with ductile fracture propagation. *Oil & Gas Science and Technology*, *60*(4), 711-719.

Thomson, G. H., Brobst, K. R., and Hankinson, W. (1982). Improved Correlation Compressed Liquids and Liquid Mixtures, *28*(4), 671-676.

Toro, E. F. (2009). *Riemann Solvers and Numerical Methods for Fluid Dynamics - A Practical Introduction* (3rd ed.). Springer - Verlag.

Tubb, R. (2010). Pipeline & Gas Journal's 2010 International Pipeline Construction Report. *Pipeline & Gas Journal*, *237*(2).

Urbaniak, D., Gerebizza, E., Wasse, G., and Kochladze, M. (2007). *Kashagan oil field development*.

Walas, S. M. (1985). *Phase equilibria in chemical engineering*. Boston: Butterworth.

Wu, D., and Chen, S. (1997). A Modified Peng-Robinson Equation of State. *Chemical Engineering Communications*, *156*(1), 215-225.

Wylie, E. B., and Streeter, V. L. (1993). *Fluid Transients in systems*. Englewood, NJ: Prentice-Hall

Zucrow, M. J., and Hoffman, J. D. (1975). *Gas Dynamics*. New York: Wiley.